UNIVERSITY OF SOUTHAMPTON

Faculty of Engineering and Physical Sciences
Institute of Sound and Vibration Studies

Extension and Application of the Eigen Analysis in General Curvilinear Coordinates Method for Acoustic Propagation in Aero-Engine Intakes

by

Rhiannon Hawkins

A thesis for the degree of
Doctor of Philosophy

April 2024

University of Southampton

Abstract

Faculty of Engineering and Physical Sciences
Institute of Sound and Vibration Studies

Doctor of Philosophy

Extension and Application of the Eigen Analysis in General Curvilinear Coordinates Method for Acoustic Propagation in Aero-Engine Intakes

by Rhiannon Hawkins

Numerical methods are utilised in the industrial design process of aero-engines to model the acoustic properties of proposed designs. The Eigen Analysis in General Curvilinear Coordinates (EAGCC) method is a numerical method developed to predict acoustic propagation in aero-engine ducts.

This PhD thesis aims to validate and develop the EAGCC method such that it can be used to predict the far-field linear acoustic propagation from a representative fully three-dimensional aero-engine intake.

This has been demonstrated by applying the method to a non-axisymmetric intake and cross-validated against published ACTRAN/TM results. The cross-validation includes predictions of induct and far-field propagation for both hard wall and lined configurations.

The extension of the method has led to the development of guidance to rationalise the modal classification approach for non-axisymmetric intakes and to the re-formulation of the propagation framework for lined cases to reduce the impact of liner discontinuity.

A comprehensive error analysis study has identified the mechanisms by which mesh-related error occurs. Two local error terms have been derived, quantified, and validated in one dimension.

Further efforts have been made to explore ways of developing the method that broadens future applicability within the industrial design process. Progress towards this goal includes the reduction in computation time through the parallelisation of the generalised eigenvalue problem formulation and the introduction of a new approximation method for predicting sensitivities to small changes in mean flow.

Contents

List of Figures

List of Tables

Declaration of Authorship

I declare that this thesis and the work presented in it is my own and has been generated by me as the result of my own original research.

I confirm that:

1. This work was done wholly or mainly while in candidature for a research degree at this University;
2. Where any part of this thesis has previously been submitted for a degree or any other qualification at this University or any other institution, this has been clearly stated;
3. Where I have consulted the published work of others, this is always clearly attributed;
4. Where I have quoted from the work of others, the source is always given. With the exception of such quotations, this thesis is entirely my own work;
5. I have acknowledged all main sources of help;
6. Where the thesis is based on work done by myself jointly with others, I have made clear exactly what was done by others and what I have contributed myself;
7. Parts of this work have been published as: R. Hawkins and A. G. Wilson, "A fast method for calculating sensitivities of acoustic propagation in ducts to small changes in geometry and mean flow," in *28th AIAA/CAES Aeroacoustics Conference*, no. AIAA 2022-3018, (Southampton, UK), American Institute of Aeronautics and Astronautics, June 2022
   R. Hawkins and A. G. Wilson, "Error analysis for 1D propagation using eigen analysis in general curvilinear coordinates," in *AIAA AVIATION*, no. AIAA 2021-2298, American Institute of Aeronautics and Astronautics, July 2021

Signed:..... Date:.....

Acknowledgements

I would like to take the opportunity to thank my supervisor Prof Alec Wilson for his help and support throughout the PhD. I particularly appreciate his patience and willingness to help tackle problems hands-on.

I would also like to express my gratitude to Dr Rie Sugimoto for her guidance and meticulous feedback. As well as for providing ACTRAN/TM results referred to in Chapter V.

Finally, I would like to thank my partner, friends, family and colleagues for their continued support and patience throughout the last five years!

Nomenclature

Abbreviations

BLAS	Basic Linear Algebra Subroutines
BPF	Blade Passing Frequency
CAA	Computational Aero Acoustics
CFD	Computational Fluid Dynamics
CPU	Central Processing Unit
dB	Decibel
DRP	Dispersion-Relation-Preserving
EAGCC	Eigen Analysis in General Curvilinear Coordinates
EO	Engine Order
EPNL	Effective Perceived Noise Level
FD	Finite Difference
FEM	Finite-Element Method
FWH	Ffowcs-Williams and Hawkings
GB	gigabytes
GEP	Generalised Eigenvalue Problem
HW	Hard Wall
IATA	International Air Transport Association
ICAO	International Civil Aviation Organisation
KH	Kelvin-Helmholtz
LEE	Linearised Euler Equations
MUMPS	Multi-front Massively Parallel sparse direct Solver
NGV	Nozzle Guide Vanes
OGV	Outlet Guide Vanes
PDE	Partial Differential Equation

RAM	Random Access Memory
RANS	Reynolds Averaged Navier Stokes
RK	Runge-Kutta
SPL	Sound Pressure Level
SW	Soft Wall
UHBR	Ultra High Bypass Ratio

Symbols

$\bar{\rho}, \rho'$	$\bar{\rho}, \rho'$ time average and perturbation density normalised by $\bar{\bar{\rho}}$
$(\Delta\zeta)^3 \frac{J'''}{J}$	Third local error term
$(\Delta\zeta)^3 \tilde{\omega}^2 J J'$	First local error term
$(\Delta\zeta)^3 i\tilde{\omega}^2 J''$	Second local error term
(ξ, η, ζ)	Curvilinear coordinate system
$\%Mn+$	Percentage Mach number increase
α	Cut-on ratio
$\bar{\bar{\rho}}$	Representative density (kg/m^3)
$\bar{\bar{c}} = \frac{\gamma \bar{\bar{p}}}{\bar{\bar{\rho}}}$	Representative speed of sound (m/s)
$\bar{\bar{p}}$	Representative pressure (Pa) - for aerodynamic scaling
$\bar{\mathbf{u}}$, $\mathbf{u'}$	Time average and perturbation velocity vector normalised by $\bar{\bar{c}}$
$\bar{c} = \frac{\bar{p}}{\bar{\rho}}$	Local speed of sound
$\Delta\zeta$	Distance between ζ surfaces
ΔMn	Magnitude of the change in Mach number
Δz	Distance between z surfaces
ϵ^{ljk}	Permutation tensor
η	Pseudo-radial coordinate
γ	Ratio of specific heats
κ	Axial wavenumber
$\lambda_{jr}, \lambda_{jl}$	Right and left travelling eigenvalues at surface j
μ	Radial order
∇	Grad operator
ω	Angular frequency
Ψ_{kr}, Ψ_{kl}	Propagated source terms, subscripts denote right and left travelling

$\psi_{kr},\ \psi_{kl}$	Local source terms at surface$k$, subscripts denote right and left travelling
σ_j	$\frac{1}{2\tilde{\omega}J_j^2}\frac{\partial J_j}{\partial \zeta}$
$\mathbf{E}_k = (\mathbf{E}_{kl}, \mathbf{E}_{kr}, \mathbf{E}_{kh})^T$	Eigenvalue vector at surface k where r - right-travelling, l - left-travelling, h - higher-order
$\mathbf{e}_{jr}, \mathbf{e}_{jl}$	Right and left running eigenvectors at surface j
$\mathbf{f} = \begin{pmatrix} u_\xi \\ u_\eta \\ u_\zeta \\ p \end{pmatrix}$	Solution vector $\mathbf{f}$
$\mathbf{u}^*$	Transformation of velocity vector $\mathbf{u}$ by the Jacobian matrix
$\tilde{\sigma}$	Standard deviation
$\tilde{c}_{jr}\tilde{c}_{jl}$	Right and left running amplitude coefficients at mid point
$\tilde{\omega}$	$\frac{\omega}{c}$ Non-dimensionalised angular frequency
ξ	Pseudo-circumferential coordinate
ζ_j	Pseudo-axial analysis surface j
ζ	Pseudo-axial coordinate
$\zeta_c = \frac{\zeta_k + \zeta_{k+1}}{2}$	Midpoint pseudo-surface between adjacent analysis surfaces k and $k+1$
A_{rr},B_{rl}...	Submatrices of change-of-basis matrices, subscripts denote direction of travel between two adjacent surfaces. r - right-travelling, l - left-travelling, h - higher-order
c	Speed of sound
c_{jr}, c_{jl}	Right and left running amplitude coefficients at surface j
$Error_{local,2r} Error_{local,1l}$	Right and left running local error terms
$f(x_i)$	Shift function
g^{ij}	Contravariant metric tensor
g_1	Gaussian height
g_2	Gaussian width
G_k	Global transfer matrix at surface k
g_{ij}	Covariant metric tensor
i	$\sqrt{-1}$
J', J'', J'''	First, second and third derivatives of the Jacobian (with respect to ζ)

J_j	Jacobian matrix at surface j, $\frac{\partial z}{\partial \zeta}$ in 1D
L_{mod}	Length of modified region
m	Circumferential wavenumber
Mn	Mach number
n_m	Number of circumferential points
n_r	Number of radial points
p'	Perturbation pressure
P_k	Propagation matrix from surface 1 to k, with entries $P_{rr}, P_{ll}, P_{rl}, P_{lr}$
$p_{ds,j}$,$p_{us,j}$	Complex pressure amplitudes at surface j, downstream and upstream travelling respectively
p_{exact_j}	Exact pressure at surface j
Q_k	Local transfer matrix from surface k to $k+1$, with entries $Q_{rr}, Q_{ll}, Q_{rl}, Q_{lr}$
r_1,r_2	Reflections captured in the local propagation process
r_{in}	Inner radius
r_{out}	Outer radius
S_{k+1}	Local transfer matrix from surface 1 to $k+1$, with entries $S_{rr}, S_{ll}, S_{rl}, S_{lr}$
t	Time
T_N	Local transfer matrix from surface N to 1, with entries $T_{rr}, T_{ll}, T_{rl}, T_{lr}$
u_{exact_j}	Exact velocity at surface j
X_{basis}	Change-of-basis matrix at midpoint pseudo-surface
X_{in}	Propagation matrix taking incoming information from surface to mid-point pseudo-surface
$X_{j,j+1}$	Local transfer matrix from surface $j+1$ to j
X_{out}	Propagation matrix taking outcoming information from pseudo-midpoint surface to surface
(r, θ, z)	Cylindrical polar coordinates
A,B	Matrices in the Generalised Eigenvalue Problem
o/w	Outer wall

Chapter 1

Introduction

The Eigen Analysis in General Curvilinear Coordinates (EAGCC) method is a numerical method developed by Wilson [6] to predict the acoustic propagation in aero-engine ducts. Numerical methods are utilised in the industrial design process of aero-engines to both understand the mechanisms through which noise is created and to quantify the noise impact of the designs. This requires methods that can meet the unique demands of computational aero-acoustics (CAA) problems in timescales appropriate to the design process. This project looks to investigate the applicability of the EAGCC method for such uses and, where possible, extend the method towards this goal.

1.1 Social Background

Prior to the COVID-19 outbreak, for over a decade, there had been a constant growth of between four and eight percent in air traffic. In 2018 the International Civil Aviation Organisation (ICAO) reported that 4.3 billion passengers were carried by scheduled air transport services [7]. This growth was predicted to continue at a compound rate of approximately 3.5 percent, which the International Air Transport Association (IATA) suggested would lead to double the number of passengers by 2037, estimated around 8.2 billion [8].

COVID-19 has had a significant impact on the aviation sector, with around a 60 percent decrease in passengers globally in 2020 compared to 2019 [9]. However, by 2022 this had improved to a 28 percent decrease from 2019 and the year-on-year growth is expected to continue. Ultimately, it is expected that the decline from COVID-19 will not have an effect on the planned regulatory developments set out prior to the COVID-19 outbreak [10].

Aviation noise has a detrimental effect on communities situated around airports, in fact the ICAO state that: *"Aircraft noise is one, if not the most detrimental environmental effects of aviation. It can cause community annoyance, disrupt sleep, adversely affect the academic performance of children, and could increase the risk for cardiovascular disease of people living in the vicinity of airports."*[11].

1.1.1 Negative Effects of Aircraft Noise

There is significant research to show that aircraft noise negatively impacts children's cognition. The RANCH (road traffic and aircraft noise and children's cognition and health) study looked at 9-10 year olds in schools surrounding three international airports, including Heathrow, and found that the aircraft noise led to poorer comprehension and cognition [12]. Furthermore, there is evidence that these negative effects can be reversed by reducing aircraft noise. A longitudinal study in Munich looked at school children exposed to airport noise, during the transition of the New Munich International airport being opened and the old airport closing. The school children's cognition was observed to improve with the closure of the old airport and to worsen with the opening of the new airport [13].

There is also some evidence to suggest aircraft noise can negatively affect health. It can impair sleep quality [14] and an association between aviation noise and hospitalisation or mortality from cardiovascular disease has been noted [15]. Whilst these are small studies and only limited conclusions can be made, a negative relationship between health and aviation noise is indicated.

Aircraft passengers and crew also experience noise during their flight. A study in 2018 measured the sound pressure levels on 200 flights across six different types of aircraft and at each stage of flight. The study found that passengers and crew spent 72 percent of their flight time exposed to sound pressure levels (SPL) higher than 80 dBA [16]. The noise at work act sets limits of 80-85 dBA, averaged over an 8 hour work day, as repeated exposure to sound levels this high can be harmful to hearing. Furthermore, exposure to cabin noise can reduce passenger comfort [17] as well as, increase stress and impair the memory and sleep of passengers and crew, even just from short-term exposure.

As the demand for air transport increases, so does the need for reducing the impact of the associated noise. The ICAO have set out four areas in their 'Balanced Approach' to achieve this, which include: local measures such as land use planning; noise abatement operational procedures such as take-off and landing; and limited use of noise-quotas such as restrictions on night-time flying. Considering the anticipated growth of air traffic and an increasing population, it seems likely that the development of airport expansions, increased scheduling, and increasing populations

surrounding airports will continue. Therefore, these three measures are not enough on their own, which leads to the fourth and most significant (to this project) measure: **noise reduction at source**. [18].

1.2 Sources of Aircraft Noise

Aircraft noise can be classified as tonal or broadband. Tonal noise consists of dominant frequencies and harmonics; broadband noise contains an almost even spread of energy over the frequency spectrum and is caused by random events. Aircraft noise propagates to the far-field with an associated directivity pattern, affected by factors such as: geometry, mean flow, frequency, and other associated characteristics of the source.

Aircraft noise can be classified as airframe or engine noise, both of which are caused by fluctuations in pressure that propagate to observers on the ground or to the cabin. Airframe noise is caused by turbulent flow around the body of the aircraft; the components that contribute to airframe noise are those that are not involved in the propulsion system such as: landing gear; openings such as fuel tank vents; flaps and slats; wings; and the fuselage [19]. Airframe noise is at its most prominent at approach (landing) as this is when many of these components are engaged and the engine noise is at its lowest as it is operating at low power. During the flight the main source of airframe noise is from the wing [20].

Airframe noise is typically broadband and propagates to the far-field or through the fuselage to the cabin. As the plane climbs and accelerates, the turbulent boundary layer around the fuselage creates cabin noise, which increases in intensity the further back one is in the cabin [21].

Some tonal airframe noise is created by interactions with cavities and discontinuities such as landing-wheel bays, and from vortex-shedding at the trailing edge of slats in the wing. Airframe noise is dependent on the dimensions of the plane and the flight speed and can be affected by environmental conditions in the atmosphere.

Engine noise sources consist of: jet, fan, combustion, and turbine noise [21]. Fig. 1.1 shows the cross-section of a Rolls-Royce turbofan engine. In an aeroplane engine a large volume of air is compressed and injected into the combustion chamber where it is ignited with fuel. Once ignited it travels through the turbine and is ejected out of the exhaust at high velocity creating thrust that propels the aircraft.

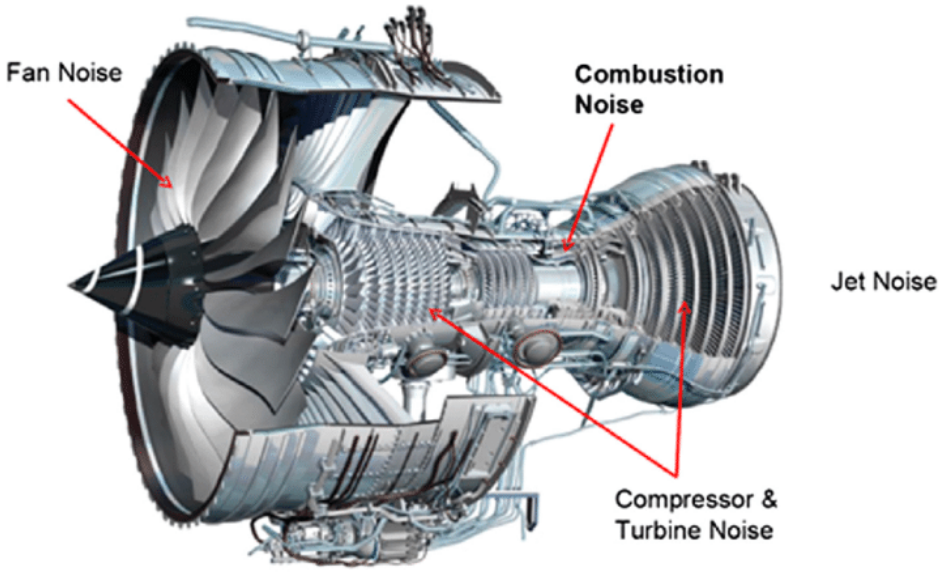

FIGURE 1.1: Rolls-Royce Trent 1000 Turbo-Fan Engine Diagram. Image taken from [1]

1.2.1 Jet Noise

Jet noise is caused by high velocity exhaust flows, ejected out from the engine, mixing with the atmosphere. Lighthill [22] demonstrated that acoustic intensity from a turbulent jet is proportional to velocity which is why jet noise is loudest at take off.

In a turbojet engine the thrust needed to propel the aircraft forward comes solely from the jet, hence jet noise is the dominant noise source. In a turbofan engine, however, the addition of the fan creates a secondary source of thrust by pushing air through the bypass duct; this increases the mean thrust per unit mass flow. The higher the ratio of air bypassed, the lower the jet velocity and reduction in the intensity of the jet mixing noise can be achieved. In a high-bypass ratio turbofan there will also be mixing noise created by the interaction of the air from the bypass duct and the jet. The transition from turbojet to turbofan engines was both fuel efficient and noise reducing. Only in low-bypass ratio engines is jet noise the dominant source, and nowadays most commercial planes are high-bypass turbofans [23], with a move to Ultra High Bypass Ratio (UHBR) turbofans expected in the future.

1.2.2 Fan Noise

Fan noise is consistently one of the dominant noise sources in all flight stages and it creates both tonal and broadband components. At relative supersonic tip speeds shocks are created near the tips of each fan blade and propagate upstream against the mean flow in a helical pattern. This is known as the rotor-locked pressure field. After interacting with the flow and any acoustic treatment in the intake the rotor-locked

pressure field radiates to the far field with a spectrum dominated by discrete tones. The frequency of the tones range from first shaft order to Blade Passing Frequency (BFP) and higher harmonics. Observers, however, are likely to hear mostly lower tones produced by the stronger dominant shocks, referred to as 'buzz-saw' noise [24].

At both supersonic and subsonic tip speeds the movement of the fan blades through the air creates a boundary layer on the blade. These form vortical disturbances that travel with the mean flow, called wakes. The wakes lead to both tonal and broadband noise sources [25].

Tonal noise is created by wakes from rotor blades hitting stator vanes (Schulten, 1993) and is dependent on: the ratio of rotor blades to stator vanes, the rotation speeds, and flow velocities. The 'Tyler and Sofrin selection rule' [26] had been used to reduce this noise by indicating the number of rotor and stator blades needed such that the first harmonic of the interaction noise is cut-off and therefore does not propagate [27]. However, the rule is based on radially symmetric mean flow and is not as useful for realistic geometry and flow of modern aero-engines.

Wakes are also created through vortex shedding where acoustic waves hit the trailing edge of a blade creating vortices that travel with the mean flow. Broadband noise is created through the interactions of these two mechanisms. Additionally, rotating blades cause turbulence against the nacelle inner walls creating a boundary layer. Generally, all interactions between turbulent flow and solid bodies contribute to the broadband spectrum.

1.2.3 Combustion Noise

The combustion process requires the mixing of the fuel with the compressed air to be exceptionally quick, resulting in high levels of turbulence. The burning of the fuel causes particles to expand and contract, creating non-uniform variations in the rate of heat release. This creates direct combustion noise.

Indirect combustion noise, a consequence of direct combustion noise, is created by the unsteady flow accelerating the entropy waves, the hotspots from the combustion process, into the turbine where they face a change in mean flow. This creates changes in pressure that propagate as acoustic waves. It is unclear what proportion of combustion noise is occupied by these two mechanisms or if there are indeed others [1]. Combustion noise has always been a minor source of engine noise, however, owing to the reduction of other sources and from next-generation combustion modes burning more unsteadily, it is expected to become a more prominent noise source [1].

1.2.4 Turbine Noise

Both broadband and tonal combustion noise travels through the Nozzle Guide Vanes (NGV) into the turbine. The flow field released from the NGV is circumferentially non-uniform, interactions with the turbine tones [21] generate noise that propagates out the exhaust and through a shear layer that is formed by the mixing of the jet with the atmosphere. The tonal noise spectrum is spread by the shear layer which can cause it to resemble that of a broadband source. The amount of spreading is dependent on the geometry of the exhaust nozzle, as well as the wavelength and shear layer thickness.

1.2.5 Overall Contributions

At different stages of flight, the overall noise observed from the aircraft is composed of different proportions of the noise sources mentioned. At sideline (take off) and cutback the engine is at full capacity so the fan and jet are the dominant sources of noise. At approach (landing) the engine is producing lower thrust and landing components are deployed resulting in fan and airframe noise being dominant. Fig 1.2 shows the contribution of different noise sources from a typical high-bypass ratio turbofan aircraft; it shows the 'Effective Perceived Noise Level' EPNL from the certification reference point. For more information on EPNL see Appendix 4, Smith [21]. Fig. 1.3 shows a typical noise spectrum of the engine of a high by-pass ratio

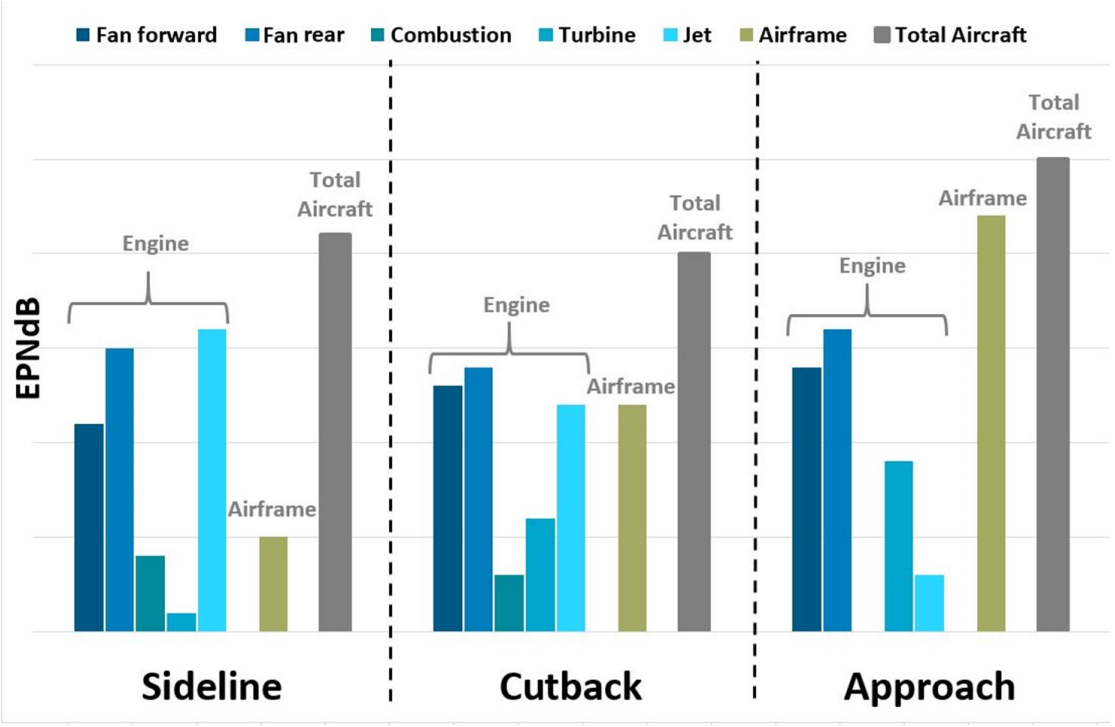

FIGURE 1.2: Relative EPNL contributions from different aircraft sources at the noise certification reference points. Data are representative of a modern aircraft powered by high-bypass-ratio turbofan engines. Data taken and reproduced from Figure 3 [2]

engine. As indicated in the figure, in future UHBR engines the fan, turbine and combustion noise is expected to increase. Tonal noise is predominantly interactions in the turbomachinery stages and from inlet and outlet perturbations, whereas the broadband noise is created by the combination of combustion and jet noise at low frequencies [3].

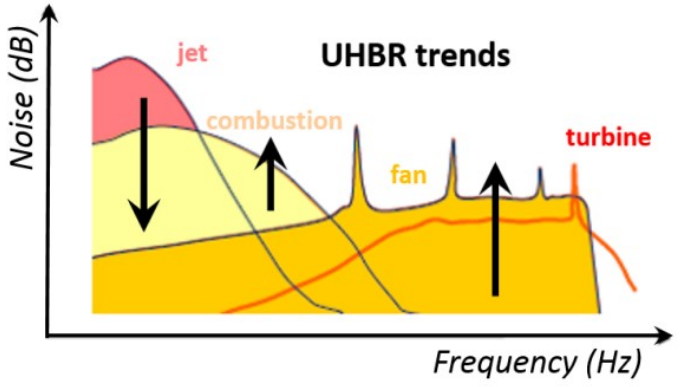

FIGURE 1.3: Typical turbo engine spectrum and future trends for UHBR architectures. Figure taken from [3].

1.3 Numerical Methods in Industry

1.3.1 Challenges to CAA

Computational Aeroacoustics (CAA) faces a unique set of problems that make it distinct from CFD and linear acoustics [28] [29], characterised by Tam [29] as a need for numerical methods that are sensitive to the physics of the problem.

The existence of multiple disparate length scales, and a dependency on both time and space, lead to fundamental problems in computational size. Any numerical scheme that discretises time creates dissipation from this discontinuity causing computed amplitudes to decrease. This error must be considered when choosing the time step. Furthermore, meshes must be sufficiently fine (spatially) at the noise source, which requires similarly small time steps to maintain numerical stability. However, this can lead to unnecessarily long computation times, particularly as coarser meshes are appropriate for regions further away from the source [29][30].

CAA often predicts propagation over long distances, so the scheme cannot be overly dissipative or dispersive [28], once more resulting in a high number of mesh points needed and the need for high-order schemes. Computational domains require artificial truncated boundaries with radiation and outflow boundary conditions that prevent reflections [29].

1.3.2 Modern demands

To optimise the design of aero-engine intakes for noise, models must account for the mechanisms that can affect the acoustic radiation in the far-field such as installation effects from the wing and fuselage [31], complex geometries, and acoustic liners.

The next generation Ultra-High-Bypass-Ratio (UHBR) engines will have much larger nacelles which bring with them additional acoustic challenges. To reduce drag, the increase in width will be offset by a reduction in length, achieved by reducing the length of the air-inlet and the distance between the fan and OGV [32][33]. However, reducing the length of the air-inlet reduces the area available for acoustic treatment [31]. Furthermore, circumferentially non-uniform flow distortion is intensified in shorter intakes [34], which can significantly affect the far-field SPL and directivity [34] [35][32].

Reducing the distance between the fan and the OGV will also create distortion and will lead to rotor-stator interaction noise becoming a prominent source of fan intake noise [32][33]. Capturing these effects can require models with higher fidelity and accuracy than previously required, which can lead to more computational expense.

1.3.3 Computational Approach

A direct approach can be used to approach these problems, using Direct Numerical Simulations (DNS) [36] [37]. These schemes include all scales of the problem, but as a result, can be computationally prohibitive for use within the industrial design process. Other high-fidelity methods include Large Eddy Simulations (LES), where the largest turbulent scales are computed whilst the rest are modelled [38]. However, this is still computationally prohibitive at high Reynolds numbers. Lattice-Boltzmann methods reduce the computational expense further and feature low dissipation and dispersion properties, but are still too computationally expensive for the early design stage [39].

In general, the resolution requirements often needed for full 3D predictions including multiple acoustic sources and frequencies are too computationally demanding to be solved directly, or included in the design and optimisation process.

There are a range of commercial and proprietary solvers that can be applied to CAA problems; including specialist solvers like ACTRAN/TM, which have been developed specifically for CAA. When selecting one of these tools to use, often there is a trade-off between speed and accuracy. In general, simplifications can be made to, for example, the mean flow, or geometry, in order to speed up the prediction time of the model, but this can limit wider use.

Hybrid methods are often used to break down CAA problems, to assign appropriate methods and/or simplifications to relevant parts of the problem (that may not be applicable to the problem as a whole) [31], ultimately optimising the computation time [40] [35]. In the example of UHBR, the need to model distortion, include new source terms such as rotor-stator interaction, and radiate to the far-field calls for a hybrid approach [33] [35]. Common setups include using CFD solvers to compute the non-linear source terms and then coupling this with a CAA solver such as ACTRAN to compute the upstream induct and far-field propagation [41] [42].

Ultimately, there is a requirement to balance the accuracy of predictions with the computational expense in order to utilise computational methods in the industrial design process of aero-engine intakes.

This project will explore the potential application of the Eigen Analysis In General Curvilinear Coordinates (EAGCC) method within this landscape. The application of the method to representative non-axisymmetric geometries will be considered both in terms of accuracy and computational expense. An understanding of the limitations of the method and areas for future development will be established through the extended application of the method.

1.4 Project Aim and Objectives

The key research aim of this PhD project is:

- To validate and develop the EAGCC method such that it can be used to predict the far-field linear acoustic propagation from a representative fully three-dimensional aero-engine intake.

The project aim will be met through these objectives:

- Identify the mechanisms that cause mesh-related error. Utilise the results when applying the method.
- Validate the application of the EAGCC method to aero-engine intakes through comparison with published results.
- Explore ways of developing the method that broadens future applicability within the industrial design process.

1.5 Original Contributions

The EAGCC method was created and implemented by Wilson [6], details of how the EAGCC method is formulated can be found in Chapter 3. The original contributions of this project come in the form of extended application of and developments to the method detailed below:

- Characterisation and quantification of mesh-related error terms for one dimensional cases.
- The application, and validation, of the EAGCC method to modelling the linear acoustic propagation and far-field directivity of a fully representative 3D non-axisymmetric aero-engine intake, with and without an acoustic liner.
- The development of guidance and a new approach towards applying the method to large intakes to reduce the memory requirement, improve the modal classification, and tackle liner discontinuity.
- The introduction of a new approximation method for predicting the results associated with small changes to the mean flow, with reduced computation time compared to the full EAGCC method. The work includes quantification of the error for axisymmetric geometry and the expected limitations of this approximation.

- Parallelisation of the function that forms the Generalised Eigenvalue Problem, leading to a reduction in the computation time of the method to 3D intakes.

1.6 Publications

- R. Hawkins and A. G. Wilson, "A Fast Method For Calculating Sensitivities Of Acoustic Propagation In Ducts To Small Changes In Geometry And Mean Flow" in *28th CEAS/AIAA Aeroacoustics Conference*, June 2022, AIAA 2022-3018
- R. Hawkins and A. G. Wilson, "Error Analysis for 1D Propagation Using Eigen Analysis in General Curvilinear Coordinates", in *AIAA AVIATION*, July 2021, AIAA 2021-2298

1.7 Outline of Contents

- Chapter 2 presents a literature review focussing on semi-analytic eigen-based and numerical CAA methods primarily considering linear propagation but with commentary on wider non-linear applications.
- Chapter 3 introduces the EAGCC method and provides a detailed explanation of each step that underpins the initial framework. Where developments have been made to the method in this project, these will be introduced in the relevant chapters.
- Chapter 4 looks at mesh-related discretisation error in one dimension, starting with the analytical derivation of local error terms. The mesh-related error is then explored numerically, and the presence of the error terms is validated by a set of one-dimensional test cases. This chapter also provides a discussion of how the results from this analysis can be applied more broadly within the EAGCC method.
- Chapter 5 validates the application of the EAGCC method to predicting the linear propagation from a non-axisymmetric aero-engine intake. Results are initially presented for a simplified axisymmetric geometry, with and without a liner, at several circumferential harmonics. The method is then applied to the non-axisymmetric intake and validated against a reference solution produced by ACTRAN/TM. This chapter also introduces new approaches towards the implementation of the EAGCC method to such geometries, and identifies areas for future work.
- Chapter 6 introduces an extension to the EAGCC method. This extension is a linear approximation method that is initially demonstrated with an analytical

one-dimensional example. It is then validated through a series of numerical test cases including a realistic axisymmetric intake. The limits of application are identified for axisymmetric annular ducts.

- Chapter 7 provides a summary of the work in this project and identifies areas of future work.

Chapter 2

Literature Review

This literature review looks at the development of a variety of methods for modelling acoustic propagation and far-field radiation from aero-engine ducts. The body of work exploring aero-acoustic propagation problems is vast, therefore this review concentrates on a subset relevant to the project. This includes semi-analytical eigen-based methods such as multiple-scales and common numerical computational aero-acoustic (CAA) models used for modelling fan noise. As the focus of this work has been on linear propagation problems, this literature review will reflect this.

2.1 Linear Duct Acoustics

Introduced by Tyler and Sofrin [26], duct modes are used as mathematical 'building blocks' to construct the acoustic pressure field as a weighted sum of modes. Linearised governing equations, such as the linearised Euler equations (LEE) are solved to give eigen-solutions or modes and corresponding mode-shapes. A comprehensive discussion around modal behaviour will be given in the following chapter.

Linear acoustics often relies on simplifications/approximations to be made to realistic intake problems, such as annular duct geometry and uniform flow; and assumes that all acoustic perturbations are to be small in amplitude [43]. Boundary conditions, such as Ingard [44] and Ingard-Myers [45], have been implemented to model the modal behaviour around acoustic liners. Eversman [23] provides a review of linear duct acoustic methods.

2.2 Semi-Analytical Approaches Based on Eigen-analysis

2.2.1 Multiple Scales

The multiple scales method considers an annular or cylindrical duct with constant cross-section and slowly varying radius. The acoustic field is considered as a perturbation problem with a general form of solutions. The amplitudes and wavenumbers are slowly varying functions dependent on a small parameter that denotes the rate of change of the slowly varying radius.

Many researchers have tried to utilise the small parameter changes in the geometry of ducts to model the acoustic field including Van Dyke [46] who considered many 2D and thin 3D cases.

The method of multiple scales is a perturbation method where multiple parameters within the same domain, for example: a fast and small spatial scale, are treated independently. By treating them independently, the solution does not contain non-periodic time-dependent terms. Nayfeh *et al.* [47] [48] applied this method to a hard-walled circular duct with slowly varying radius and no mean flow, which led to an exact solution for the differential equation to describe the slowly varying amplitude.

Rienstra [49] [50] improved upon this method determining an exact solution with and without flow, and implementing the Ingard-Myers boundary condition [45] into the formulation [51].

Rienstra and Eversman [52] implemented the slowly varying method numerically on a duct with slowly varying mean flow and geometry (cylindrical to annular), representative of an aero-engine inlet, and compared the results to finite element method (FEM). Overall the results were consistent across the two methods, including the predicted liner attenuation. One fundamental difference, however, was that the finite element model contained modal scattering, which is intrinsically built into this type of propagation model as it considers many modes at once. The multiple-scales method is implemented tonally, so does not include modal interaction. Furthermore, the multiple-scales assumes that any modal scattering in the slowly varying part of the duct is small and, thus not included in the analysis.

The method was developed more generally for ducts of arbitrary cross-section and slowly varying area [53] including non-axisymmetric ducts. Features of the generalised method include:

- The mean flow (considered isentropic irrotational) is assumed to be nearly uniform, with axial variations only [54], [55], [56].

- The acoustic field solution is approximated with an ansatz, and the amplitude function is expanded up to second order.
- The amplitude function and the full solution of the first order equation rely on a solvability condition, that the associated eigenvalue problem must be self-adjoint.
- The leading order equation gives an eigenvalue problem to be solved for each axial analysis plane that is complex requiring the method must be implemented numerically.

In this method the analysis planes used are parallel to each other and the x-axis but not necessarily normal to the wall. A locally orthogonal coordinate system at each analysis plane is established, which allows the boundary condition to be applied in the same way as it would be for a straight duct, this is only acceptable due to the slowly varying condition.

Problems were found to occur at turning points where modes approach the cut-on/cut-off boundary. At the point of which they transition, the wavenumber is zero (changing from real to imaginary), and as a result, the amplitude function becomes singular. This means the slowly varying assumption fails in the local boundary layer around the turning point. Rienstra [53] found that a different approximation for the boundary layer is appropriate whereby the axial variation of the mode satisfies Airy's equation.

Cooper and Peake [55] extended the method to a slowly varying duct with mean swirling flow. They found that the inclusion of vorticity led to an eigenvalue problem that is not self-adjoint and thus, the previous solvability condition no longer applies. Furthermore, as the swirling flow moves modes closer to cut-off, the same singularities at turning points are seen as in [51] [53]. They too used Airy functions to solve this problem.

Ovenden [57] incorporated an Airy function into a composite multiple-scales solution for modes transitioning from cut-on to cut-off, broadening the applicability of the multiple scales approximation.

This composite solution was applied by Ovenden, Eversman and Rienstra [58] to a duct of slowly varying arbitrary cross-section with and without mean flow and compared to FEM results. The multiple scales results agreed with the FEM results at low radial order modes, where there is little to no scattering. At high radial order modes, there is a large amount of modal scattering, which is captured by the FEM results but is not a feature of the multiple-scales prediction. It was shown that modes that transition from cut-on to cut-off were successfully captured by the composite multiple-scales method, but the method falls at high frequencies or high radial order modes as it cannot predict modal scattering.

Peake and Cooper [54] also adapted Rienstra's [59] method to hard-wall elliptical slowly varying ducts. They demonstrated that ducts that transition from elliptical to circular cannot be approximated as slowly varying circular ducts, as the eccentricity of the elliptical cross-section has a large effect on the propagation.

Brambley and Peake [56] applied the multiple-scales method to a strongly curved cylindrical duct with mean potential flow and slowly varying radius, with a curved centreline that ran through the duct. They used analysis planes that were not parallel, but instead normal to the centreline by using a curvilinear axial coordinate, s, the arclength along the centreline. The radii and curvature of the centreline are functions of the slowly varying parameter. Therefore, the duct can be strongly curved whilst the changes in curvature and cross-sectional area remain slowly varying. The curvature of the duct means the sound field can no longer be expressed in terms of Bessel functions. A generalised eigenvalue problem is formed at each analysis surface and solved numerically using a pseudo-spectral method, to give the amplitude and wavenumbers. It is found that the curvature causes asymmetry between upstream and downstream propagating modes creating a more complex eigen-mode spectrum than that of a straight duct.

Smith, Ovenden and Bowles [60] adapted the multiple-scales approach to capture modal scattering, and validated their approach against the FEM results [58].

2.2.2 Waveguides

Stevenson [61] derived exact equations for propagation in horns of arbitrary shape following on from his work on electromagnetic horns. This was achieved by projecting the Helmholtz equation on a set of normalised orthogonal eigen-functions.

Pagneux *et al.* [62] built on this by projecting the Helmholtz equation with Dirichlet boundary conditions onto orthogonal, but not normalised, eigen-functions. Axisymmetric waveguides were split into cylindrical segments with varying cross-sections. Pressure and velocity are written as projections of eigen-functions on either side of each segment boundary, which are functions of the roots of Bessel functions, waveguide radius, and height. The presence of evanescent modes prevents integrating the resultant differential equation, so it is solved by matching the pressure and velocity at the segment boundaries.

Pagneux *et al.* find that the correct number of modes must be chosen to form a complete basis for the solution to converge, including higher order evanescent modes. This method is applied to a circular cross-section exponential horn and validated against FEM solutions.

Further extension was made to the multimodal method by Pagneux *et al.*[63], leading to the application to three-dimensional bends with a circular cross-section [64]. In this form, local scattering matrices composed of transmission and reflection matrices are calculated by matching the upstream pressure values found on either side of the lined segment. The local scattering matrices are combined iteratively to form a global scattering matrix. The global scattering matrices characterise the behaviour throughout the duct [65].

Félix and Pagneux [66] applied the multimodal method to lined 2D and 3D waveguides both straight and with a bend, through the addition of an admittance matrix. Pagneux *et al.* [67] validated the multimodal method against FEM for two realistic turbofan intakes. The first, a 3D duct with azimuthal scattering induced by a spliced intake liner with two hard-walled diametrically opposed splices at BPF. The second, a 2D infinite rectangular duct, with a liner with axially and circumferentially varying impedance.

In the applications of the multimodal method discussed a hard-wall Neumann boundary condition was used for the eigen-solutions, for lined applications the modal basis did not satisfy the boundary condition at the liner. This in turn decreased the radial convergence of the solution, and it was shown that the accuracy of the lined section related to the number of modes included.

Maurel *et al.* [68] developed the multimodal method into the Improved Multimodal Method (IMM) through the addition of a supplementary mode called the boundary mode. It improved the method by fulfilling the boundary condition at the liner, thus improving the convergence of the method. Furthermore, it is orthogonal to the first N modes in the expansion and avoids the divergence caused by evanescent modes.

When applied to a 3D axisymmetric waveguide, and compared to the original multimodal method, the IMM improved the convergence of the solution and achieved the same level of accuracy with a much smaller number of modes in the expansion. The number of modes needed for the improved method is proportional to frequency, as it is the number of propagating modes and two additional modes corresponding to the first evanescent mode and the supplementary mode.

Maurel *et al.* [69] extended the IMM to more complex geometries through the introduction of a geometrical transformation defined by a Jacobian matrix. This approach is applied to a Serpent Billiard (waveguide made up of a succession of semi-circular rings connecting two straight ducts).

Félix *et al.* [70] tried improving the convergence of the original multimodal method by replacing the Neumann condition with a Robin boundary condition for the liner. However, it was found that the IMM still performed the best.

Mercier and Maurel [71] developed both multimodal methods further to include the presence of flow. A Prandtl-Glauert transformation is used to transform the wave equation into the form of the Helmholtz equation with mean flow. Both methods are validated against FEM solutions for a 2D waveguides with potential mean flow for Mach numbers 0 to 1. Similarly to the no mean flow case, the supplementary mode improves convergence and reaches the same level of accuracy with 4 modes in the expansion as the standard does with 50.

2.2.3 Other semi-analytic eigen-based methods

Moinier and Giles [72] developed a numerical method for computing eigenmodes for axially and circumferentially uniform mean flow (non-uniform radially) - both viscous and inviscid. The method was validated against an analytical solution for an annular duct with uniform inviscid mean flow. The linearised Navier Stokes equations were discretised forming a generalised eigenvalue problem and boundary conditions were applied by replacing the relevant rows/columns. The eigenvalue problem was solved by using a commercial linear algebra solver, LAPACK, and the modes are classified.

The modes with the largest pressure magnitude are classified as acoustic, the remaining modes with the largest entropy perturbations are classified as entropy modes and the remaining are classified as vortical. For 'cut-off' evanescent acoustic modes, the direction of travel is classified by the sign of the imaginary part of the wavenumber. If positive, then they are decaying with increasing axial direction and are therefore downstream travelling. Similarly, if negative then upstream travelling. For modes that are cut on, as the imaginary part of the wavenumber is zero, Moinier and Giles [72] used the sign of the group velocity, to identify the direction of travel. This was done by adding a small negative imaginary component to the frequency of the modes giving the cut on modes imaginary parts that indicate their direction of travel. Fourth-order smoothing is shown to alter the pressure and radial variation in some modes, this can cause them to be misclassified but can also be used as a tool for highlighting spurious modes.

Moinier and Giles [72] modelled the propagation around the cascade of flat plate stator vanes in an annular duct where the mean flow can be considered inviscid and uniform and the propagation around Outlet Guide Vanes (OGV) where incoming acoustic waves create unsteady viscous flows. For axisymmetric geometries and/or uniform mean flows this classification method is sufficient, in non-uniform mean flows and in non-axisymmetric geometries, however, the direction of travel is not always as easy to discern.

Kousen [73] used an eigen-based method to model the propagation in annular and cylindrical ducts with uniform and non-uniform shear flow; with and without a liner.

Kousen compared two finite difference schemes: of second and fourth order. The eigenvalue problem is formulated such that the governing Euler equations are transformed into a discretised generalised eigenvalue problem and eigen-solutions are found using an eigensolver through QR factorisation. The results indicate that in non-uniform mean flow, axial wavenumbers are split into two sets; a discrete set of acoustic modes that correspond to those of uniform mean flow and then a second continuous set along the local convected speeds of the mean flow.

Maldonado [74] looked at modal propagation in swirling flows solving the LEE. The eigenvalue problem is discretised using a central fourth-order Finite Difference (FD) scheme, as used by Kousen [73], and the GEP is solved with the LAPACK QZ algorithm solver. Similarly to Moiner and Giles [72], a subset of the modes are not well resolved and dominated by point-to-point oscillations. Here a filter developed by Tam [29] consisting of a 15-point stencil Dispersion-Relation-Preserving (DRP) scheme was used to separate the physical and numerical modes. It was found that convective modes were also removed by this filter due to the fact they are highly oscillatory.

2.3 Numerical Approaches

2.3.1 Finite Difference

Finite difference (FD) schemes solve differential equations by approximating derivatives with discrete difference equations based on Taylor expansions. The space and time domains are discretised over structured grids. FD schemes have been applied to a multitude of CAA problems [75] [75] [76] [77].

2.3.1.1 Dispersion-Relation-Preserving Schemes

Tam and Webb introduced the Dispersion-Relation-Preserving (DRP) scheme [78] and illustrated how it could address many of the CAA issues which are reviewed in Tam's later publication[29]. The idea behind DRP schemes is that if the finite difference scheme has the same dispersion-relation as the original PDE, then it will also have the same number of modes and the same propagation characteristics: non-dispersive and non-dissipative.

To define the scheme, the Fourier transform of the partial derivatives is considered equal to the Fourier transform of the finite difference approximation, and approximated by fourth-order Taylor's series. This differs from the standard approach of taking Taylor's series approximations of the derivatives themselves. This approach preserves the wavenumber, and therefore, the dispersion relation. The spatial

discretisation is optimised by choosing a stencil coefficient that minimises the integrated error. If the time step chosen is sufficiently small, the group velocity stays consistent too. High-frequency waves can contaminate the solution but are damped through artificial damping. This idea has been widely employed and developed subsequently [79] [80] [81].

The DRP scheme uses radiation and outflow boundary conditions that effectively carry the signals out of the domain with little reflection. At the walls, ghost mesh points that fall outside of the boundary are used to accommodate the extra non-physical boundary conditions created by the high-order scheme[82]. This idea was also applied to curved walls of elliptical and circular cylinders to accurately predict modal scattering [83].

Structured grids are difficult to model complex geometries, due to the multiple length and time scales faced in aero-acoustics problems. If the spatial mesh spacing and, by consequence, the time step are dictated by the finest mesh spacing needed over the whole domain then the scheme will be computationally inefficient. However, it is often only a small part of the domain that requires such a fine mesh [84].

Tam and Kurbatskii [85] introduced a multi-size-mesh for DRP schemes. The multi-size-mesh divides the computational domain into subdomains, each with a uniform mesh of different spacing. At every interface between subdomains discontinuities are created causing erroneous numerical waves. Special stencils were devised in order to dampen the spurious waves caused by the discontinuity.

The multi-mesh DRP scheme was applied to a test-case with turbulent boundary layer flow over a cavity and validated against experimental measurements. The mesh was divided into six subdomains with the finest mesh around the cavity opening region. The spatial and time steps double at each interface, and the outer subdomain is 32 times larger than the finest. The multi-size mesh is shown to drastically reduce the computation time without sacrificing accuracy.

Schoenwald and Panek [86] have utilised overlapping grids when applying DRP schemes to realistic intakes including a 3D scarfed intake using a high-order FD code TUBA [87].

2.3.1.2 Compact-Differencing Schemes

Compact differencing schemes, first introduced by Lele [88], benefit from being more accurate for their stencil size than a normal explicit FD scheme. Lele [88] presented a high-order scheme with a spectral-like resolution, a modified Padé scheme. Spectral methods approximate functions globally rather than locally, and Padé schemes have this same global dependence making them ‘spectral-like’ in nature. Whereas, in a

standard FD scheme, derivative approximations at a given node only depend on neighbouring nodes included in the stencil. The spectral-like resolution of Lele's scheme leads to small dispersive errors and improved representation of shorter length scales, making it highly applicable to CAA problems.

It is restricted in application to problems with smooth solutions as there is no artificial dissipation added as it is a central scheme. Lele [88] successfully applied the scheme to the examples of a resolving structure of a shock wave and a compressible mixing layer between two supersonic streams. The resolution of the scheme, not the order of accuracy, is directly related to how well the shock is captured.

Kim and Lee [89] optimised the compact schemes for higher resolution by minimising dispersion error over a wide wavenumber domain. The integrated error equation they used is similar to that of Tam and Webb [78] with the addition of a weighting function and optimisation range factor. The weighting function weights the integrand towards the higher wavenumber range, where the most dispersive error exists in the original compact schemes.

Hixon [90] introduced the idea of pre-factorisation, taking the compact central-difference methods of Lele [88] and reducing the stencils by factoring them into two low-order biased stencils. These pre-factored schemes have the advantage of having smaller independent matrices to solve, including smaller boundary stencils, whilst keeping the non-dissipative nature of central-difference schemes and spectral-like resolution of implicit compact schemes.

Ashcroft and Zhang [91] combined the work of Hixon [90] and of Kim and Lee [89] by optimising the pre-factored schemes for the prediction of wave propagation. When compared to Tam's explicit DRP scheme [78] and Hixon's pre-factored scheme [90], the optimised pre-factored schemes have lower dispersion error across the whole wavenumber range. The improved resolution of the optimised schemes does require more computational operations than the DRP scheme.

The optimised and pre-factored compact schemes have been applied extensively to 2.5D and 3D intakes and exhaust problems demonstrating their suitability for CAA applications [28] [77] [92] [93] [94].

2.3.1.3 Finite Differences Schemes on General Curvilinear Meshes

Finite-difference schemes require structured meshes, but this causes a problem when applying to CAA problems due to complex geometry. One way to overcome this is to use General Curvilinear Coordinates, a curvilinear mesh with pseudo-orthogonal coordinates can be fitted to the geometry and the Jacobian matrix describes the

transformation between the general curvilinear coordinate system and a given orthogonal system, such as cylindrical polar coordinates.

Lau [95] [96] presented the use of general curvilinear coordinates in a FD scheme for 3D potential problems. The governing equations are transformed into a system of linear equations and expressed in terms of curvilinear coordinates determined by a transformation by the inverse Jacobian. The boundary condition requires that the normal derivative is zero on the wall, so the curvilinear mesh is designed such that one of the coordinate lines matches the orientation of the normal. By doing so, the normal derivative on the curved surface can be approximated by a central difference expression without any transformation. The governing equations are solved using an iterative Gauss-Seidel method.

Lau [96] applied the method to three applications, with a range of mesh densities, and compared the results to the solutions obtained using Finite Element Method (FEM). In all the test cases the finer meshes gave good agreement to the analytical solution. It was also shown that similar accuracy could be achieved with a coarser mesh if the mesh points were concentrated around where the changes in temperature occur. The FD method required significantly less arithmetic operations and storage than the FEM required for similar accuracy.

Daiguji and Shin [97] presented a series of numerical schemes applied to 2D and 3D applications utilising a curvilinear coordinate grid to solve the Navier-Stokes (N-S) equations. The governing N-S equations used contain physical velocities and derivatives of the curvilinear coordinates with dependence on the Jacobian used to describe the transformation from the Cartesian to the Curvilinear coordinates. Daiguji and Shin note that smooth grids must be used due to the various dependencies between the contravariant velocities, the Jacobian, and the grid spacing. The computational procedures are similar to that of Lau [96], a set of simultaneous equations from the coordinate transformation and governing equations are formed and solved iteratively.

Visbal and Gaitonde [98] developed high-order compact-differencing schemes based on the compact schemes of Lele [88] for use on general curvilinear stretching and deforming meshes for CAA applications [98] [99]. The compact-differencing schemes used were Padé -like schemes coupled with implicit high-order low-pass filters. For implementation on general curvilinear 3D meshes, the importance of freestream preservation is demonstrated and a new formulation is presented. To avoid the creation of metric cancellation errors, before discretising the governing equations, the metric relations must be written in conservative form and then evaluated with high order formulas. For deforming meshes a further identity is required to meet the geometric conservation law [98][100].

Visbal and Gaitonde [99] also demonstrate the effect of freestream preservation with the example of modelling a spherical pulse on a 3D curvilinear mesh by applying a fourth-order compact-differencing scheme with a tenth-order implicit filter. When the metrics are evaluated without the new formulation the wave is highly distorted, due to metric cancellation errors. For the same scheme, with the new metrics, the solution shows no distortion and is in good agreement with the exact solution.
Compact-differencing methods are non-dissipative as they are centred [88], however, this can lead them to be susceptible to numerical instabilities from the growth of high-frequency modes caused by mesh non-uniformities [98]. Therefore, the compact scheme must be coupled with a high-order low-pass filter, which is shown to prevent reflections from infecting the global solution and to act as an outflow boundary condition when applied to a 2D pressure pulse on a stretched grid [99].

Visbal and Gaitonde [99] developed a multi-domain method where adjacent meshes have overlapping stencils. Information from the neighbouring domains is exchanged at the overlapping regions, but otherwise the domains are independent of each other and can be computed in parallel to improve computational efficiency.

2.3.2 Finite Element Method

Finite Element Method (FEM) is based on the weak formulation of a partial differential equation (PDE) [101]. The test function allows for the sampling of the differential function at small sections of the domain. This is integrated over the whole domain for a set of test functions. The solution is described as a linear combination of globally continuous basis functions and their coefficients on unstructured meshes [102].

FEM has been successfully applied to many CAA problems in the frequency domain [103] solving linear governing equations such as LEE or the convected Helmholtz equation [104] [105] [106]. Although using linear governing equations eliminates the capability of capturing non-linear effects expected at high engine speeds, the non-linear effects are less significant at modest power settings.

In traditional high-bypass ratio intakes, the mean flow is largely irrotational and realistic problems have been modelled with the convected Helmholtz equation by using high-order finite and infinite elements [107] [108] [109].

Gabard *et al.* [110] analysed the dispersion properties of FEM time-harmonic solutions of the convected Helmholtz equation. It is shown that suitable grid resolutions are needed to minimise dispersion and aliasing errors.

2.3.2.1 ACTRAN/TM

ACTRAN/TM is a commercial FEM solver widely used for the propagation and radiation of Turbomachinery noise. Developed in the late 1990s - early 2000s, originally based on the Convected Helmholtz equation. Recent versions solve the Möhring formulation [111] in the frequency domain. The Möhring formulation reduces to the convected Helmholtz equation for isentropic flow [112].

ACTRAN/TM can be applied to duct propagation with source terms added at the end of the duct to represent incoming acoustic modes. ACTRAN/TM supports the inclusion of an acoustic liner, which is incorporated by the use of an impedance or admittance boundary condition based on the Ingard-Myers boundary condition [45].

As ACTRAN/TM is a FEM code it is a domain-based method restricted to bounded domains. To extend the model to predict radiation a non-reflecting boundary condition is required which truncates the domain.

Perfectly Match Layer (PML) can be applied to prevent reflections at the end of the truncated domain and can be used in conjunction with FW-H to project the predicted solution to the far-field.

Alternatively, infinite elements (IE) at the outer boundary of the truncated domain can both provide a non-reflecting boundary condition and be used to reconstruct the far-field radiation [107].

ACTRAN/TM has been widely used for modelling the propagation and far-field radiation for bypass ducts [113] [114] [115] [116] and intakes [117] [118] [119].

ACTRAN/TM has been applied to the propagation and radiation of fan noise from several 3D intake models [120] [121], including investigation into the effects of mean flow distortion [122] [123] [34] in non-axisymmetric intakes.

Although ACTRAN/TM cannot predict non-linear effects, as it is a linear code, it has been used in hybrid schemes coupled to CFD sources to approximate the propagation from 3D intakes including non-linear effects and buzz-saw noise [42] [41] [124].

2.3.3 Discontinuous Galerkin Method

First developed by Reed and Hill to solve the neutron transport equation [125], Discontinuous Galerkin Methods (DGM) are a class of FEM that use discontinuous piecewise polynomials as basis and test functions [30]. The basis functions used in FEM are globally continuous, whereas DGM uses piecewise-continuous basis functions which allow for explicit integration resulting in a computationally less expensive method.

Atkins and Shu [126] introduced the quadrature-free implementation which significantly improves the computational demand by simplifying the way the temporal terms are expressed and how volume and surface integrals are evaluated.

DGM is most commonly used in the time domain and has been applied to many CAA problems including modelling the propagation and acoustic scattering in realistic 3D intakes, and from the wing and fuselage [127] [128].

For the time domain schemes the computation time scales linearly with the number of time steps. Therefore a large time step must be selected, but one that is not so large that it will lead to instabilities. Several methods have been developed to achieve this balance for DGM. These include: Multi rate time step [129], [130]; Implicit time march [131], [132]; and variable order elements [133].

Several comparisons have shown that DGM has lower dispersion error and dissipation than FD schemes [134] [30].

Similarly to FD, time domain DGM models can also suffer from KH instabilities excited by thin shear layers, particularly at low frequencies [135]. These instabilities are exacerbated by time-domain impedance boundary conditions, Fung and Ju [136] provide a review of this.

ACTRAN/DGM is an extended quadrature-free RK-DGM [137] packaged in a commercial solver. ACTRAN/DGM solves the LEE in the time-domain on axisymmetric and full 3D unstructured coarse grids, with the option to include acoustic liners. The computation is fully in-core and the computation time can be reduced by optimising the modelling parameters and parallelisation, examples of this are given [135]. The domain is surrounded by a buffer zone with a non-reflecting boundary and the far-field and predictions are given by a FWH surface.

ACTRAN/DGM has been applied to several CAA problems, including realistic intakes and exhaust configurations [135] [138] for tonal and broadband predictions. In the latter an alternative, computationally quicker, approach was used where all radial modes are injected at once with a random amplitude and phase until the solution converges.

ACTRAN/DGM also features an automatic adaptive spatial order which allows the same mesh to be used for different flows and frequencies [135] [138] [139] [140].

Rarata *et al.* [40] used a hybrid approach for modelling fan noise in far-field by coupling CFD source prediction with CAA propagation and radiation. The CFD solution from Rolls-Royce HYDRA, a second-order finite volume code, is coupled to linear ACTRAN/DGM. Modal source terms are matched to give the equivalent acoustic pressure field in the aeroengine intake to encompass the 'non-linear' effects

but are represented in the linear model. Computation time was considerably reduced compared to the full CFD solution.

Chapter 3

Technical background underpinning the Eigen Analysis in General Curvilinear Coordinates method, and new developments

Sections 3.1 to 3.8 of this chapter provide an overview of how the EAGCC method is implemented including any relevant technical background information required to understand how the method works. No development made to the method is detailed here, only work already published by Wilson [6] [141] [65] [142], though the purpose of these sections is to provide a more detailed explanation of the method than previous publications, particularly where relevant to the work contained in the later chapters of this thesis.

Section 3.9, however, does introduce new developments to the method made by the author that differ from the original configuration.

3.1 Overview of Method Implementation

To apply the Eigen Analysis in General Curvilinear Coordinates (EAGCC) method to a given duct, a single body-fitted mesh with: pseudo-axial, ζ; pseudo-radial, ξ; and pseudo-circumferential, η; coordinates is created to represent the duct. The mean flow parameters of velocity, pressure, and density are interpolated onto the curvilinear mesh.

A finite-difference scheme is used to compute the Jacobian and metric tensor, allowing for easy exchange between the generalised curvilinear coordinate system and a chosen orthogonal coordinate system.

The governing linearised Euler equations (LEE), expressed in relation to the Jacobian and metric tensor, are formed into a generalized eigenvalue problem (GEP) with the inclusion of appropriate boundary conditions.

Eigen-solutions are computed at each pseudo-axial analysis surface [1], at fixed ζ positions. The computed eigen-values, or modes, are sorted into right-running acoustic, left-running acoustic, vortical, and higher order modes.

Local transfer matrices match incoming and outgoing modal coefficients between neighbouring axial surfaces through the use of change-of-basis matrices defined at the mid-point between each adjacent pair. Input signals from either, or both, ends are propagated through the duct, marching once forwards and once backwards (axially), combining local transfer matrices to form a global transfer matrix. This global transfer matrix relates the modal coefficient at any position in the duct, to the global input. The final solution is given by the product of the global transfer matrix and the input coefficients, forming amplitude coefficients to the base eigenvectors.

The prediction has been extended to include the far-field radiation through the use of a Ffowcs-Williams and Hawkings surface [65].

Fig. 3.1 illustrates the steps that take place when implementing the EAGCC method. Each step corresponds to a following section which will discuss the corresponding process in greater detail.

[1] it can be assumed throughout that any reference to axial analysis surfaces are in reference to pseudo-axial surfaces

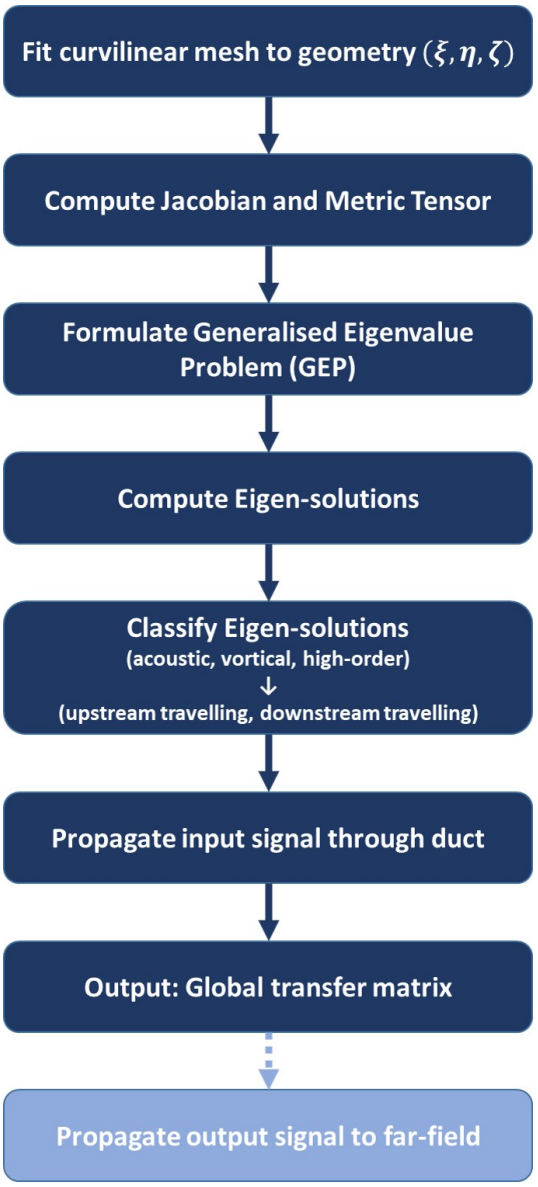

FIGURE 3.1: Flowchart of the EAGCC method

The EAGCC method is implemented through an Object-Oriented code designed and written, in MATLAB, by Wilson [6]. The inputs include: the mesh (implicitly defines the duct geometry); mean flow; input frequency/frequencies; range of circumferential harmonics (needed to describe the acoustic modes of interest); and boundary condition - including any necessary impedance values of lined regions.

3.2 Mesh

Many modern aero-engine intake designs are non-axisymmetric with complex geometries. The EAGCC method utilises a generalised curvilinear coordinate system. This type of coordinate system is not necessarily orthogonal, which makes it possible to fit a structured curvilinear mesh to any smooth duct geometry, such as those of non-axisymmetric aero-engine intakes.

The method uses a global body-fitted general curvilinear coordinate system which is used to fit a smooth mesh to the duct geometry. The coordinate system consists of: 'pseudo-axial', ζ; 'pseudo-radial', ξ; and 'pseudo-circumferential',η coordinates.

The mesh is formulated with the following characteristics:

- The mesh is fitted to the duct geometry and extends smoothly to the near-field (far enough such that uniform mean flow is expected)
- Minimum and maximum axial and radial spacing is set in relation to the outer radius (to ensure sufficient radial and axial definition)
- Axial points are equispaced along the inner and outer walls of the duct
- The radial points are equispaced along the outer axial mesh line, whereas at the fanface Chebyshev polynomials are used to map the radial points, resulting in a higher concentration towards to outer wall
- A smooth transition from the axial surface at the fanface to the curved outer axial surface at the near-field is given by defining a gradient vector that gradually transforms the shape of the surfaces from one to the other. Different gradients can be set in different dimensions. A similar process is used to give a gradual transition of the radial surfaces from the inner to outer wall.

The mesh must be smooth enough to ensure there are only gradual changes to the mesh spacing even if there are harsh changes in geometry. This is important as the Jacobian matrix is considered constant between axial surfaces. The effects of mesh definition are discussed in further detail in Chapter 4.

3.3 Jacobian and Metric Tensor

Due to the non-orthogonal nature of the mesh defined by general curvilinear coordinates, it is necessary to compute the Jacobian matrix and corresponding metric tensor. The Jacobian matrix acts as a transformation matrix between the curvilinear coordinate system and a chosen orthogonal system. Whilst the Jacobian matrix allows

for any output to be expressed in terms of an orthogonal coordinate system, all the information calculated (velocity, pressure etc.) is calculated with respect to the curvilinear system. Due to the non-orthogonality of this system, operators such as derivatives, grad, and curl include extra terms with respect to the Jacobian (and metric tensor).

The Jacobian matrix consists of a 3x3 matrix where the rows and columns correspond to the 3 orthogonal cartesian coordinate directions, x, y, z, and the 3 curvilinear coordinates, ξ, η, ζ.

$$J = \frac{\partial x^j}{\partial \xi^i} = \begin{pmatrix} \frac{\partial x}{\partial \xi} & \frac{\partial x}{\partial \eta} & \frac{\partial x}{\partial \zeta} \\ \frac{\partial y}{\partial \xi} & \frac{\partial y}{\partial \eta} & \frac{\partial y}{\partial \zeta} \\ \frac{\partial z}{\partial \xi} & \frac{\partial z}{\partial \eta} & \frac{\partial z}{\partial \zeta} \end{pmatrix} \tag{3.1}$$

The Jacobian matrix is considered constant between adjacent analysis surfaces, this results in a form of discretisation, the effects of which will be explored further in Chapter 4.

The Jacobian matrix, and corresponding determinant and derivatives, as well as the metric tensor, are calculated at each mesh point using a central finite-difference (FD) scheme with a five or seven-point stencil. In the radial direction the FD scheme forms a derivative matrix. For a 5-point stencil, the matrix gives a third-order approximation of the derivatives at each point.

3.4 Generalised Eigenvalue Problem

3.4.1 Governing Equations

For most of the EAGCC applications considered so far, the mean flow is (or is close to) homentropic, therefore, the homentropic linearised Euler equations (LEE) are appropriate governing equations, introduced below [6].

Momentum

$$\frac{\partial \mathbf{u}'}{\partial t} + \bar{\mathbf{u}} \cdot \nabla \mathbf{u}' + \mathbf{u}' \cdot \nabla \bar{\mathbf{u}} = -\frac{1}{\bar{\rho}} \nabla p' + \frac{p'}{\gamma \bar{\rho}^2 \bar{c}^2} \nabla \bar{p}. \tag{3.2}$$

Mass

$$\frac{1}{\bar{c}^2} \frac{\partial p'}{\partial t} + \bar{\mathbf{u}} \cdot \nabla (\frac{p'}{\bar{c}^2}) + \mathbf{u}' \cdot \nabla \bar{\rho} = -\bar{\rho} \nabla \cdot \mathbf{u}' - (\frac{p'}{\bar{c}^2}) \nabla \cdot \bar{\mathbf{u}} \tag{3.3}$$

where

$$\bar{c} = \sqrt{\frac{\bar{p}}{\bar{\rho}}}. \tag{3.4}$$

Note that terms with bars denote time-averaged quantities and terms with apostrophes denote the perturbations from the time average. All terms are non-dimensional, the mean pressure $\bar{p}$ is normalised by the reference pressure $\bar{\bar{p}}$, and

perturbation pressure p' is normalised by $\gamma\bar{\bar{p}}$, $\bar{c}$ is a local correction to the speed of sound $\bar{\bar{c}}$.

It is noted that although the governing equations stated here are non-dimensional, and are handled as such throughout the method. The output of the EAGCC method itself can be expressed both non-dimensionally or dimensionally utilising the same normalisation terms stated above.

3.4.1.1 Tensor form

Due to the non-orthogonality of the coordinate system, the governing equations must be represented in tensor form where derivatives and other operators are expressed with respect to the metric tensor.

The covariant metric tensor, g_{ij}, represents the metric tensor of the coordinate system, and the contravariant metric tensor, g^{ij}, is the inverse of the covariant metric tensor and g the determinant.

To formulate the momentum and mass equations, 3.2 and 3.3, into tensor form, common vector and tensor calculus identities taken from [143] [144] are introduced below.

First it is noted that

$$(\mathbf{u}\cdot\nabla\mathbf{u}) = \nabla(\frac{1}{2}\mathbf{u}\cdot\mathbf{u}) - \mathbf{u}\times(\nabla\times\mathbf{u}). \tag{3.5}$$

The tensor formulation of the cross-product

$$(\mathbf{a}\times\mathbf{b})_i = g_{ij}\epsilon^{ljk}a_j b_k \tag{3.6}$$

and curl,

$$(\nabla\times\mathbf{u}) = g_{il}\epsilon^{ljk}\frac{\partial u_k}{\partial x^j} \tag{3.7}$$

include the permutation tensor ϵ^{ljk} which is related to the permutation symbol e^{ljk}, such that $\epsilon^{ljk} = \frac{1}{\sqrt{(g)}}e^{ljk}$.

Substituting Eqn. 3.6 and 3.7 into Eqn. 3.5 leads to,

$$(\mathbf{u}\cdot\nabla\mathbf{u})_i = \frac{1}{2}\frac{\partial}{\partial x^i}(g^{jk}u_j u_k) - \epsilon^{ljk}\epsilon^{mnp}g_{il}g_{km}u_j\frac{\partial u_p}{\partial x^n}. \tag{3.8}$$

Substituting this identity into Eqn. 3.2, the momentum equation with respect to the metric tensor is given as

$$\frac{\partial u_i'}{\partial t} + \frac{1}{2}\frac{\partial}{\partial x^i}(g^{jk}[u_j'\bar{u}_k + \bar{u}_j u_k']) - \epsilon^{ljk}\epsilon^{mnp}g_{il}g_{km}[u_j'\frac{\partial \bar{u}_p}{\partial x^n} + \bar{u}_j\frac{\partial u_p'}{\partial x^n}] = -\frac{1}{\bar{\rho}}\frac{\partial \rho'}{\partial x^i} - \frac{p'}{\gamma\bar{\rho}^2}\frac{\partial \bar{\rho}}{\partial x^i} \tag{3.9}$$

For the mass equation the identity

$$\nabla \cdot \mathbf{u} = \frac{1}{\sqrt{g}}\frac{\partial}{\partial x^i}(\sqrt{g}g^{ij}u^j) \tag{3.10}$$

where g^{ij} is the inverse of the metric tensor matrix g_{ij}, is introduced. Substituting this identity in Eqn. 3.3, the mass equation with respect to the metric tensor is given as

$$\frac{1}{\bar{c}}\frac{\partial p_i'}{\partial t} + g^{ij}\bar{u}_j\frac{\partial}{\partial x^i}(\frac{p'}{\bar{c}^2}) + g^{ij}u_j'\frac{\partial \bar{\rho}}{\partial x^i} = -\frac{p'}{\sqrt{g}\bar{c}^2}\frac{\partial}{\partial x^i}(\sqrt{g}g^{ij}\bar{u}_j) + \frac{\bar{\rho}}{\sqrt{g}}\frac{\partial}{\partial x^i}(\sqrt{g}g^{ij}u_j'). \tag{3.11}$$

3.4.2 Forming the Generalised Eigenvalue Problem

To demonstrate how the generalised eigenvalue problem (GEP) is formed, first the governing equations can be simplified. This does not alter the general form of the matrices but reduces the number of terms included and therefore easier to understand.

Starting from the homentropic linearised Euler equations, if uniform axial velocity is assumed, then $\bar{\rho}$, $\bar{p}$, $\bar{c}^2$ are all constants and, for simplicity, are set to 1. The mean flow velocity only varies axially, z direction, such that

$$\bar{\mathbf{u}} \cdot \nabla\bar{\mathbf{u}}' = M\frac{\partial \bar{\mathbf{u}}'}{\partial z} \tag{3.12}$$

where M is the local mean flow Mach number. The equations for conservation of momentum and mass can now be written as

Momentum:

$$\frac{\partial \mathbf{u}'}{\partial t} + M\frac{\partial \mathbf{u}'}{\partial z} = -\nabla p' \tag{3.13}$$

Mass:

$$\frac{\partial p'}{\partial t} + M\frac{\partial p'}{\partial z} = -\nabla \cdot \mathbf{u} \tag{3.14}$$

Taking a Fourier transform in time, a solution of the form

$$p' = p(r)e^{i\omega t}e^{-im\theta}e^{-ik_z z} \tag{3.15}$$

$$u' = u(r)e^{i\omega t}e^{-im\theta}e^{-ik_z z} \tag{3.16}$$

is assumed, where m is the circumferential mode number and ω is the angular frequency. From the equations above

$$\frac{\partial p'}{\partial t} = i\omega p' \tag{3.17}$$

and

$$\frac{\partial u'}{\partial \theta} = -imu'. \tag{3.18}$$

Thus the generalised eigenvalue problem

$$A\frac{\partial f}{\partial z} = Bf \tag{3.19}$$

is formed of

$$A = \begin{bmatrix} M & 0 & 0 & 0 \\ 0 & M & 0 & 0 \\ 0 & 0 & M & 1 \\ 0 & 0 & 1 & M \end{bmatrix} \tag{3.20}$$

and

$$B = \begin{bmatrix} -i\omega & 0 & 0 & -\frac{\partial}{\partial r} \\ 0 & -i\omega & 0 & -im \\ 0 & 0 & -i\omega & 0 \\ (-\frac{1}{r} - \frac{\partial}{\partial r}) & -im & 0 & -i\omega \end{bmatrix}. \tag{3.21}$$

The GEP is formed at each axial analysis surface. The size of the A and B matrices are $4 \times n_r \times n_m$ where n_r is the number of radial points and n_m is the number of circumferential modes included in the solution basis. The solution vector $f = \begin{pmatrix} u'_r \\ u'_\theta \\ u'_z \\ p' \end{pmatrix}$ is defined for every radial point at every circumferential mode.

3.4.2.1 GEP in Tensor Form

The GEP is complex to formulate in the tensor form due to many of the terms being with respect to various derivative operators, therefore it has been formulated symbolically [6].

3.4.3 Boundary Conditions

The boundary conditions replace the pseudo-momentum equation in the rows of the A and B matrices that correspond to points on the duct walls. For example, if there is a hard wall condition then the radial velocity at the wall is zero, so the $A_{1,1}$ entry (the

first row and column of matrix A) that corresponds to the wall is set to 0. For lined ducts, the momentum equation is replaced by the Ingard [44] boundary condition,

$$\mathbf{u'} \cdot \mathbf{n} = (i\omega + \bar{\mathbf{u}} \cdot \nabla) \frac{p'}{i\omega Z} \tag{3.22}$$

where $\mathbf{u'}$ is the unsteady velocity, $\bar{\mathbf{u}}$ is the mean flow velocity, and $\mathbf{n}$ is the unit normal vector. The boundary condition is expressed in terms of the curvilinear coordinates in the same way the LEE equations are formed, and the unit normal is the pseudo-radial basis vector $\hat{\xi}$, [65]. For ducts with curved surfaces and non-uniform mean flow the Myers' extension [45] can be implemented in the same manner, however, this is outside the scope of this project.

3.5 Computing Eigen-Solutions

To demonstrate the eigenanalysis process analytically, here is a simple 1D example. Starting with the 1D homentropic linearised Euler equations

$$M\frac{\partial u'}{\partial z} + \frac{\partial p'}{\partial z} = -\frac{\partial u'}{\partial t} \tag{3.23}$$

and

$$\frac{\partial u'}{\partial z} + M\frac{\partial p'}{\partial z} = -\frac{\partial p'}{\partial t} \tag{3.24}$$

where $M = \frac{\bar{u}}{c}$ is the mean flow Mach number.

To express these equations in the frequency domain, a solution of the form $p(z)e^{i\omega t}$ is assumed. Thus, the equations become

$$M\frac{\partial u'}{\partial z} + \frac{\partial p'}{\partial z} = -i\tilde{\omega}u' \tag{3.25}$$

and

$$\frac{\partial u'}{\partial z} + M\frac{\partial p'}{\partial z} = -i\tilde{\omega}p' \tag{3.26}$$

where $\tilde{\omega} = \frac{\omega}{c}$.

The generalised eigenvalue problem, Eqn. 3.19, is formed such that $\mathbf{f} = \begin{pmatrix} u' \\ p' \end{pmatrix}$ and $A, B \in \mathcal{M}^{2\times 2}$ are

$$A = \begin{bmatrix} M & 1 \\ 1 & M \end{bmatrix}, \quad B = \begin{bmatrix} -i\tilde{\omega} & 0 \\ 0 & -i\tilde{\omega} \end{bmatrix}. \tag{3.27}$$

Assuming A is invertible, to find the eigen-solutions the system is re-arranged

$$\frac{\partial \mathbf{f}}{\partial z} = A^{-1}BF \tag{3.28}$$

$$= \frac{i\tilde{\omega}}{1-M^2}\begin{bmatrix} M & -1 \\ -1 & M \end{bmatrix}\mathbf{f}. \tag{3.29}$$

By definition $\left|A^{-1}B - \lambda I\right| = 0$, where λ are the eigenvalues. Expressing Eqn. 3.28 in this form leads to

$$\begin{vmatrix} \frac{Mi\tilde{\omega}}{1-M^2} - \lambda & \frac{-i\tilde{\omega}}{1-M^2} \\ \frac{-i\tilde{\omega}}{1-M^2} & \frac{Mi\tilde{\omega}}{1-M^2} - \lambda \end{vmatrix} = 0. \tag{3.30}$$

Taking the determinant produces a quadratic equation for λ

$$\lambda^2 - 2\frac{Mi\tilde{\omega}}{1-M^2}\lambda + \left(\frac{i\tilde{\omega}}{1-M^2}\right)^2\left(1+M^2\right) = 0. \tag{3.31}$$

Solving Eqn. 3.31 using the quadratic formula, the eigenvalues are found as

$$\lambda_r = \frac{-i\tilde{\omega}}{1+M}, \quad \lambda_l = \frac{i\tilde{\omega}}{1-M} \tag{3.32}$$

the subscripts r and l denote right and left travelling in the axial direction. Throughout this thesis, right-traveling will be considered downstream (with the mean flow) and left-traveling as upstream (against the mean flow) [2]

It is noted that, in three dimensions there would be four eigenvalues, two corresponding to acoustic modes (right and left- travelling), and the additional two corresponding to vortical and entropy modes.

To find the corresponding eigenvectors to Eqn. 3.32 the two eigenvalues are substituted back into the system of equations. Firstly, for λ_r

$$\begin{bmatrix} \frac{i\tilde{\omega}M}{1-M^2} + \frac{i\tilde{\omega}}{1+M} & \frac{-i\tilde{\omega}}{1-M^2} \\ \frac{-i\tilde{\omega}}{1-M^2} & \frac{i\tilde{\omega}M}{1-M^2} + \frac{i\tilde{\omega}}{1+M} \end{bmatrix}\begin{bmatrix} u' \\ p' \end{bmatrix} = \begin{bmatrix} 0 \\ 0 \end{bmatrix}. \tag{3.33}$$

As the two rows are linearly dependent the pressure is fixed to 1, $p' = 1$. Therefore, the top row can be written as

$$i\tilde{\omega}\left(\frac{M}{1-M^2} + \frac{1}{1+M}\right)u' - \frac{i\tilde{\omega}}{1-M^2} = 0. \tag{3.34}$$

[2] Further information related to the direction of travel of acoustic modes can be found in Rienstra and Hirschberg [43], chapter 7.

As $1 - M^2 = (1 + M)(1 - M)$ it follows that

$$i\tilde{\omega}\Big(\frac{M}{(1-M)(1+M)} + \frac{1}{(1+M)}\Big)u' = \frac{i\tilde{\omega}}{(1-M)(1+M)} \tag{3.35}$$

$$i\tilde{\omega}\Big(\frac{M+(1-M)}{(1-M)(1+M)}\Big)u' = \frac{i\tilde{\omega}}{(1-M)(1+M)} \tag{3.36}$$

$$i\tilde{\omega}\Big(\frac{1)}{(1-M)(1+M)}\Big)u' = \frac{i\tilde{\omega}}{(1-M)(1+M)}. \tag{3.37}$$

$$\tag{3.38}$$

Therefore, $u' = 1$.

Following the same process for λ_l, the two corresponding eigenvectors are

$$\mathbf{e}_r = \begin{pmatrix} 1 \\ 1 \end{pmatrix}, \quad \mathbf{e}_l \begin{pmatrix} -1 \\ 1 \end{pmatrix}. \tag{3.39}$$

The first entry in the eigenvectors above corresponds to the velocity and the second to the pressure, hence the right-running velocity is positive as it is travelling with the mean flow and the left-running value is negative as it travels against the mean flow. This example is in 1D, in three dimensions the eigenvectors have 4 entries corresponding to the velocity in each direction and the pressure.

3.5.1 GEP in generalised curvilinear coordinate system

The GEP in curvilinear coordinate is of the form $A^* \frac{\partial \mathbf{f}^*}{\partial \zeta} = B^* \mathbf{f}^*$ where $\mathbf{f}^* = \begin{pmatrix} u^* \\ p^* \end{pmatrix}$. The previous equations are written in terms of Cartesian/orthogonal coordinate system. In curvilinear coordinates the velocity $\mathbf{u}^*$ is a transformation of $\mathbf{u}$ by the Jacobian matrix J.

$$\mathbf{u}^* = J\mathbf{u} \tag{3.40}$$

In 1D $J = \frac{\partial z}{\partial \zeta}$, therefore

$$\frac{\partial u}{\partial z} = \frac{\partial (\frac{u^*}{J})}{J\,\partial \zeta} \tag{3.41}$$

$$= \frac{1}{J}\frac{\partial}{\partial \zeta}(\frac{u^*}{J}) \tag{3.42}$$

$$= \frac{1}{J^2}\frac{\partial u^*}{\partial \zeta} + \frac{1}{J^3}\frac{\partial J}{\partial \zeta}u^*. \tag{3.43}$$

This can be rearranged to give

$$\frac{\partial u^*}{\partial \zeta} = J^2\frac{\partial u}{\partial z} + \frac{1}{J}\frac{\partial J}{\partial \zeta}u^*. \tag{3.44}$$

The GEP is solved in the same manner as shown above, but the resulting eigen-solutions will include terms relating to the Jacobian.

3.5.2 Implementation

The previous example in 1D demonstrates how eigenvalues and eigenvectors are computed analytically. Within the EAGCC code the generalised eigenvalue problem is solved using the built-in MATLAB solver 'eig' [145]. This solver uses a QR (specifically QZ or 'generalised Schur decomposition') algorithm to solve the GEP. It is based upon QR factorisation which factorises matrices into the product of an orthogonal matrix, 'Q', and a (right) upper triangular matrix, 'R'. The solver includes many variations of the QR algorithm to handle symmetric, non-symmetric matrices, and singular value problems [146].

The GEP is formed at each axial analysis surface. The size of the matrices scales with the number of radial points , n_r, and the number of circumferential modes considered, n_m, such that in 3D the matrix row and column size is equal to $4 \times n_r \times n_m$. The computation time of the 'eig' solver does not scale linearly with the size of these matrices, this is investigated further in Chapter 5 section 5.4.

3.6 Mode Classification

The eigen-solutions are sorted into three categories: right-running, left-running, and high order, where right-running are downstream travelling and left-running are upstream travelling. High-order modes are those with high absolute eigenvalues or those with 'noisy' eigenvectors (high number of oscillations).

The right/ downstream and left/ upstream running are sorted through linear programming based on the real and imaginary parts of the eigenvalue in relation to the expected cut on/off boundary approximated using the dispersion relation. The correct classification of modes into these three categories is essential to the method.

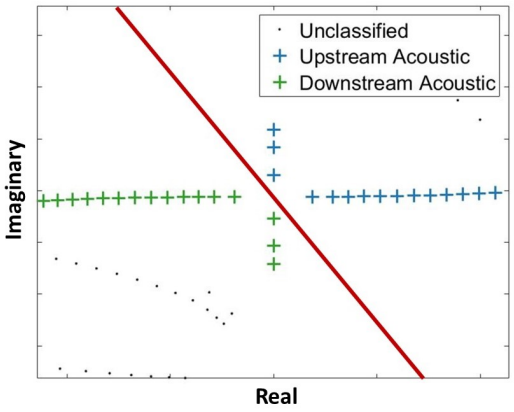

FIGURE 3.2: Eigenvalue plot, real on the horizontal axis, imaginary on the vertical axis. The red line demonstrates the split between upstream and downstream eigenvalues positioned on the argand diagram

The downstream/ right-running modes are sorted further into acoustic, vortical, and entropy modes based on their eigenvector pressure and velocity profiles. Whilst this secondary sorting is useful for analysis and understanding, only the direction of travel is essential for the method to work correctly.

However, most of the cases in this thesis have potential flow. As such, the vortical modes have been removed from the propagation, which does require accurate secondary sorting to ensure that an incorrectly reduced set of modes are not used.

The current method for mode classification still requires a level of manual intervention, particularly with the identification of high-order modes. A 'roughness' parameter is used to identify the modes with high numbers of oscillations. It utilises the fourth-order derivatives of the pressure profile with respect to the radial and circumferential directions to reveal the high-frequency content of the pressure functions. The higher the 'roughness' the more 'noise' or high-frequency oscillations there are on the function. A tolerance for the 'roughness' is manually set such that any modes that fall above it are classified as high order. Fig. 3.3 provides an example of such mode.

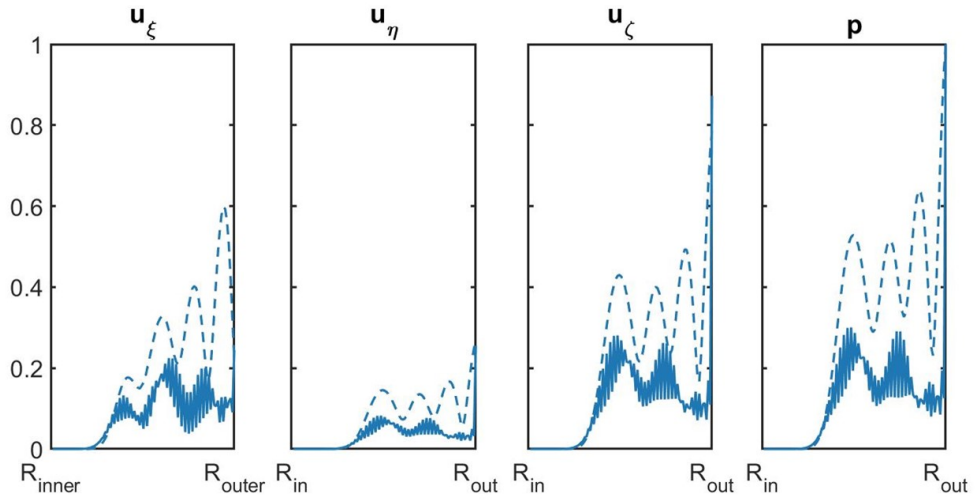

FIGURE 3.3: Mode shape/eigenvector of two modes with similar eigenvalues. The dashed line shows an acoustic mode that would be kept in the modal sum, the solid line shows a highly oscillatory mode that would be filtered out of the modal sum using the 'roughness' parameter

For cases with more complex geometries and mean flows, the optimal threshold of the 'roughness' parameter can change for different sections of the duct. Therefore, at present this process can require considerable additional set-up time. For the method to be utilised within the commercial design process this process would need to be improved. Further discussion on this is included in Chapter 5 section 5.4.

3.7 Propagation

Inside EAGCC models, acoustic sources are represented as coefficients of the eigenvectors at either or both the upstream and downstream ends of the domain, and are propagated through the duct. This process is described in detail in the following section.

3.7.1 Local Transfer Matrices

At any axial surface, k, the eigenvalues can be expressed as a vector $\mathbf{E}_k = (\mathbf{E}_{kl}\ \mathbf{E}_{kr}\ \mathbf{E}_{kh})^T$ with a corresponding amplitude coefficients denoted as c_{kl}, c_{kr} and c_{kh}. Local transfer matrices propagate the signals described by these coefficients from each analysis surface to the next, through the use of change-of-basis matrices. This acts as a form of mode-matching.

The mode-matching must account for all the upstream and downstream travelling information, including reflections. At the mid-point between adjacent analysis

surfaces, the coefficients of the incoming eigen-modes (expressed in relation to their incoming basis) are matched to their corresponding outgoing eigen-modes (expressed in relation to their outgoing basis). The signal is then propagated in the direction it leaves towards the next surface.

At this stage of the process, the eigen-solutions form a complete basis for the numerical problem and, therefore, no approximation is necessary in the matching process.

Considering the two neighbouring surfaces, ζ_1 and ζ_2, this relationship can be written as a matrix equation

$$\begin{pmatrix} c_{2r} \\ c_{1l} \end{pmatrix} = X_{12} \begin{pmatrix} c_{1r} \\ c_{2l} \end{pmatrix} \tag{3.45}$$

where c_{2r},c_{2l},c_{1r},c_{1l} are vectors of complex amplitude coefficients corresponding to the eigenvectors found at the analysis surfaces, 2 and 1, travelling in the upstream/ left and downstream/ right directions, denoted l and r.

Matrix, X_{12} is the local transfer matrix, relating the information at surface 1 to the information at surface 2; it is the product of three matrices, $X_{out}X_{basis}X_{in}$, as shown below.

The intermediate coefficients, $\tilde{c}$, calculated at the pseudo-midpoint surface, ζ_c, are the coefficients at surfaces 1 and 2 propagated to and from the midpoint by matrices X_{in}, and X_{out}.

X_{in} and X_{out} are formed of diagonal matrices, X_{kr}. These diagonal matrices contain the axial variation of each mode, this is the change in amplitude expected during the transition from surface k to the mid-point, and is given by the eigenvalues of the modes and the pseudo-axial distance travelled. The diagonal entries of X_{kr} at row and column n are given by $e^{i\lambda_{kr_n}\frac{\zeta_c-\zeta_k}{2}}$, where this is the axial variation for the n^{th} right-running mode at surface k.

$$\begin{pmatrix} \tilde{c}_{1r} \\ \tilde{c}_{2l} \end{pmatrix} = X_{in} \begin{pmatrix} c_{1r} \\ c_{2l} \end{pmatrix} = \begin{pmatrix} X_{1r} & 0 \\ 0 & X_{2l} \end{pmatrix} \begin{pmatrix} c_{1r} \\ c_{2l} \end{pmatrix} \tag{3.46}$$

$$\begin{pmatrix} c_{2r} \\ c_{1l} \end{pmatrix} = X_{out} \begin{pmatrix} \tilde{c}_{2r} \\ \tilde{c}_{1l} \end{pmatrix} = \begin{pmatrix} X_{2r} & 0 \\ 0 & X_{1l} \end{pmatrix} \begin{pmatrix} \tilde{c}_{2r} \\ \tilde{c}_{1l} \end{pmatrix}. \tag{3.47}$$

The change-of-basis matrix relates the signals travelling into the midpoint pseudo-surface, $\tilde{c}_{lr}, \tilde{c}_{2l}$, with the signals travelling out of the midpoint, $\tilde{c}_{1l}, \tilde{c}_{2r}$.

$$\begin{pmatrix} \tilde{c}_{2r} \\ \tilde{c}_{1l} \end{pmatrix} = X_{basis} \begin{pmatrix} \tilde{c}_{1r} \\ \tilde{c}_{2l} \end{pmatrix}. \tag{3.48}$$

This matching process is illustrated in Fig. 3.4.

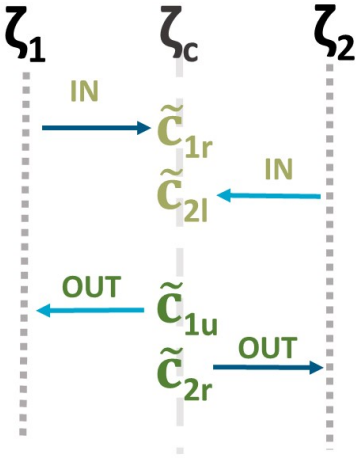

FIGURE 3.4: Matching at mid-point pseudo surface ζ_c

The change-of-basis matrix accounts for scattering and reflections, making sure that information is not 'double counted' if it is reflected. The full calculation process is shown by Wilson [65] and further details are included in the next section.

Substituting Eq. 3.46 into Eq. 3.48 leads to

$$\begin{pmatrix} \tilde{c}_{2r} \\ \tilde{c}_{1l} \end{pmatrix} = X_{basis} X_{in} \begin{pmatrix} c_{1r} \\ c_{2l} \end{pmatrix}. \tag{3.49}$$

Left multiplying both sides of Eq. 3.47 by the inverse of X_{out}

$$X_{out}^{-1} \begin{pmatrix} c_{2r} \\ c_{1l} \end{pmatrix} = \begin{pmatrix} \tilde{c}_{2r} \\ \tilde{c}_{1l} \end{pmatrix} \tag{3.50}$$

and substituting this into Eqn. 3.49 gives

$$X_{out}^{-1} \begin{pmatrix} c_{2r} \\ c_{1l} \end{pmatrix} = X_{basis} X_{in} \begin{pmatrix} \tilde{c}_{1r} \\ \tilde{c}_{2l} \end{pmatrix}. \tag{3.51}$$

Finally left multiplying both sides by X_{out} leads to a formula that captures the local propagation process between two adjacent surfaces

$$\begin{pmatrix} c_{2r} \\ c_{1l} \end{pmatrix} = X_{12} \begin{pmatrix} c_{1r} \\ c_{2l} \end{pmatrix} = X_{out} X_{basis} X_{in} \begin{pmatrix} c_{1r} \\ c_{2l} \end{pmatrix}. \tag{3.52}$$

This local propagation process is illustrated in Fig. 3.5.

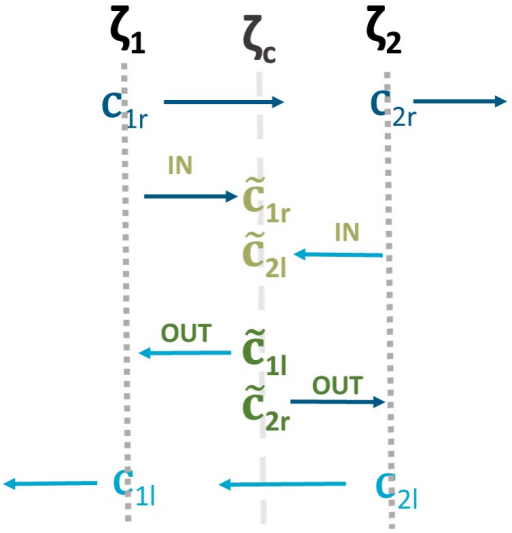

FIGURE 3.5: Local propagation between analysis surfaces 1 and 2

3.7.2 Change-of-basis matrices

At the mid-point surface, ζ_c, the change-of-basis matrix matches the ingoing and outgoing information, such that

$$E_1 c_1 = E_2 c_2. \tag{3.53}$$

Thus, the coefficients can be expressed as

$$c_2 = E_2^{-1} E_1 c_1 \tag{3.54}$$

where $E_2^{-1}E_1$ is a change-of-basis matrix from ζ_1 to ζ_2. Similarly, $E_1^{-1}E_2$ is a change-of-basis matrix from ζ_2 to ζ_1. These two matrices are the inverses of each other and can be expressed as

$$E_2^{-1} E_1 = \begin{pmatrix} A_{rr} & A_{rl} & A_{rh} \\ A_{lr} & A_{ll} & A_{lh} \\ A_{hr} & A_{hl} & A_{hh} \end{pmatrix} \tag{3.55}$$

$$E_1^{-1} E_2 = \begin{pmatrix} B_{rr} & B_{rl} & B_{rh} \\ B_{lr} & B_{ll} & B_{lh} \\ B_{hr} & B_{hl} & B_{hh} \end{pmatrix} \tag{3.56}$$

The subscripts denote the direction of travel of the information. For example: $A_{lr}\tilde{c}_{1r}$ describes a signal that is travelling right from ζ_1 but is reflected and exits travelling left at ζ_2. $\tilde{c}_{1r}$ is written with respect to the incoming basis of ζ_1, but when multiplied by the change-of-basis matrix, A_{lr}, it is now expressed with respect to the basis of ζ_2. There are also signals that continue in the same direction as they enter, such as $A_{rr}\tilde{c}_{1r}$ which describes signals that are travelling right from ζ_1 and continue to travel right through ζ_2.

The change-of-basis matrices include high-order modes, this is because the effects caused by scattering from acoustic modes to high-order modes must be included to retain a full solution, to prevent the incorrect modal scattering that can result from using an artificially reduced set. The scattered information itself, however, can be neglected from the propagation as the modes are highly cut-off. Backscattering from high-order modes to acoustic modes is neglected.

The change-of-basis matrices must also account for reflections. At the mid-point pseudo-surface, ζ_c, the outgoing coefficients travelling in a given direction are a combination of signals continuing in the same direction they entered and signals reflected back in the direction they entered from. For a given basis, k, signals are broken into right-travelling $\tilde{c}_{kr}$, left-travelling $\tilde{c}_{kl}$ and reflections r_k. Such that for surfaces 1 and 2

$$\tilde{c}_{2r} = A_{rr}(\tilde{c}_{1r} + r_1) \tag{3.57}$$

$$\tilde{c}_{1l} = B_{ll}(\tilde{c}_{2l} + r_2). \tag{3.58}$$

This is illustrated in Fig. 3.6.

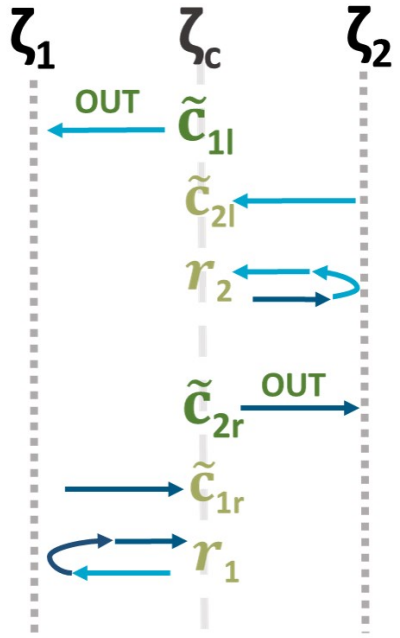

FIGURE 3.6: Matching between analysis surfaces ζ_1 and ζ_2, including the reflections r_1 and r_2.

To ensure reflections are not double counted, the following identities are obeyed

$$r_1 = -B_{rl}(\tilde{c}_{2l} + r_2) \tag{3.59}$$

$$r_2 = -A_{lr}(\tilde{c}_{1r} + r_1). \tag{3.60}$$

Substituting Eqn. 3.60 into Eqn. 3.59 leads to

$$r_1 = (I - B_{rl}A_{lr})^{-1}B_{rl}(\tilde{c}_{2l} - A_{lr}\tilde{c}_{1r}) \tag{3.61}$$

similarly,

$$r_2 = (I - A_{lr}B_{rl})^{-1}B_{rl}(\tilde{c}_{2l} - A_{lr}\tilde{c}_{r1}). \tag{3.62}$$

Substituting these two expressions into Eqn. 3.59 and Eqn. 3.60 and expressing this in the form of Eqn. 3.48 leads to

$$\begin{pmatrix} \tilde{c}_{2r} \\ \tilde{c}_{1l} \end{pmatrix} = \begin{pmatrix} A_{rr}(I + (I - B_{rl}A_{lr})^{-1}B_{rl}A_{lr}) & -A_{rr}(I - B_{rl}A_{lr})^{-1}B_{rl} \\ -B_{ll}(I - A_{lr}B_{rl})^{-1}A_{lr} & B_{ll}(I + (I - A_{lr}B_{rl})^{-1}A_{lr}B_{rl}) \end{pmatrix} \begin{pmatrix} \tilde{c}_{1r} \\ \tilde{c}_{2l} \end{pmatrix}. \tag{3.63}$$

The terms $A_{lr}B_{rl}$ etc represent 'double reflections' and are therefore assumed sufficiently small such that $(I - B_{rl}A_{lr})$ etc are invertible.

3.7.3 Global Transfer Matrix

The output of the method is a global transfer matrix, G_k, that relates the output modal coefficients at any surface, k, to the global input given as right-running coefficients at surface 1 and left-running coefficients at the last surface, N, such that

$$\begin{pmatrix} c_{kr} \\ c_{kl} \end{pmatrix} = G_k \begin{pmatrix} c_{1r} \\ c_{Nl} \end{pmatrix}. \tag{3.64}$$

Wilson [65] demonstrates that the local transfer matrices can be combined, through a process of induction, to relate the incoming and outgoing information for a larger set of consecutive analysis surfaces, starting from either end.

Marching forwards, it is assumed a transfer matrix from surface 1 to k is known such that

$$\begin{pmatrix} c_{kr} \\ c_{1l} \end{pmatrix} = \begin{pmatrix} P_{rr} & P_{rl} \\ P_{lr} & P_{ll} \end{pmatrix} \begin{pmatrix} c_{1r} \\ c_{kl} \end{pmatrix}. \tag{3.65}$$

Reflections within the region between surfaces 1 and k are accounted for with the P_{rl}, P_{lr} terms, but it is noted that the reflections can occur at any unspecified two adjacent surfaces in this region, this is illustrated in Fig. 3.7.

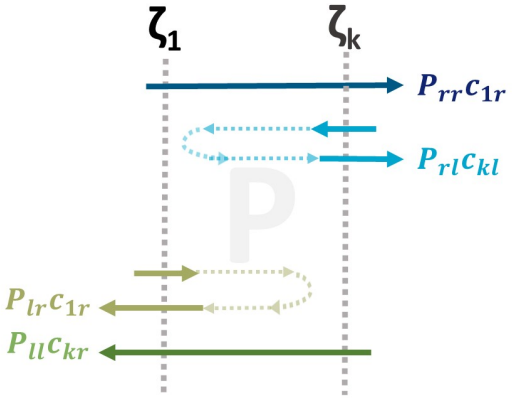

FIGURE 3.7: Matching surfaces 1 to k, blue right-running from k and green left-running from 1

Stepping forward to surface $k+1$, the local transfer matrix, Q,

$$\begin{pmatrix} c_{(k+1)r} \\ c_{kl} \end{pmatrix} = \begin{pmatrix} Q_{rr} & Q_{rl} \\ Q_{lr} & Q_{ll} \end{pmatrix} \begin{pmatrix} c_{kr} \\ c_{(k+1)l} \end{pmatrix} \tag{3.66}$$

describes the information travel between the two adjacent surfaces k and $k+1$, Fig. **??**.

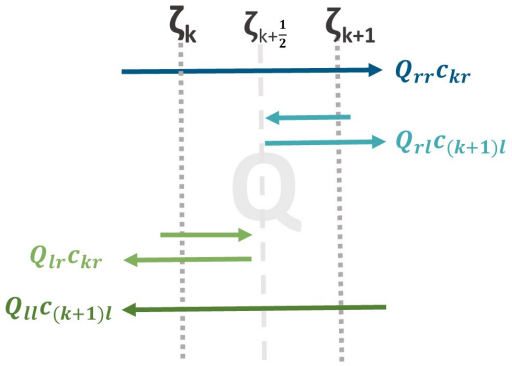

FIGURE 3.8: Matching surfaces between k and $k+1$

To combine the two steps the intermediate terms c_{kl} and c_{kr} must be eliminated. The linear system of equations given by Eqns. 3.66 and 3.65 is

$$c_{(k+1)r} = Q_{rr}c_{kr} + Q_{rl}c_{(k+1)l} \tag{3.67}$$
$$c_{kl} = Q_{lr}c_{kr} + Q_{ll}c_{(k+1)l} \tag{3.68}$$
$$c_{kr} = P_{rr}c_{1r} + P_{rl}c_{kl} \tag{3.69}$$
$$c_{1l} = P_{lr}c_{1r} + P_{ll}c_{kl}. \tag{3.70}$$

The expression for c_{kl} (Eqn. 6.30) is substituted into the formula for c_{kr} (Eqn.)

$$c_{kr} = P_{rr}c_{1r} + P_{rl}c_{kl} \tag{3.71}$$
$$= P_{rr}c_{1r} + P_{rl}(Q_{lr}c_{kr} + Q_{ll}c_{(k+1)l}). \tag{3.72}$$
$$\tag{3.73}$$

Gathering the c_{kr} terms to the left-hand side leads to

$$(I - P_{rl}Q_{lr})c_{kr} = P_{rr}c_{1r} + P_{rl}Q_{ll}c_{(k+1)l} \tag{3.74}$$
$$c_{kr} = (I - P_{rl}Q_{lr})^{-1}(P_{rl}Q_{ll}c_{(k+1)l} + P_{rr}c_{1r}). \tag{3.75}$$

Similarly, substituting the expression for c_{kr} (Eqn. 6.31) into the formula for c_{kl} (Eqn. 6.30)

$$c_{kl} = Q_{lr}c_{kr} + Q_{ll}c_{(k+1)l} \tag{3.76}$$
$$= Q_{lr}(P_{rr}c_{1r} + P_{rl}c_{kl}) + Q_{ll}c_{(k+1)l} \tag{3.77}$$
$$= (I - Q_{lr}P_{rl})^{-1}(Q_{lr}(P_{rr}c_{1r}) + Q_{ll}c_{(k+1)l}). \tag{3.78}$$

These new equations for c_{kr} (Eqn. 3.75) and c_{kl} (Eqn. 3.78) are substituted into the formulas given for $c_{(k+1)r}$ (Eqn. 3.67) and c_{1l} (Eqn. 6.32).Therefore eliminating these intermediate terms

$$c_{(k+1)r} = Q_{rr}c_{kr} + Q_{rl}c_{(k+1)l} \tag{3.79}$$
$$= Q_{rr}[(I - P_{rl}Q_{lr})^{-1}(P_{rl}(Q_{ll}c_{(k+1)l}) + P_{rr}c_{1r})] + Q_{rl}c_{(k+1)l} \tag{3.80}$$
$$= Q_{rr}(I - P_{rl}Q_{lr})^{-1}P_{rr}c_{1r} + (Q_{rr}(I - P_{rl}Q_{lr})^{-1}P_{rl}Q_{ll} + Q_{rl})c_{(k+1)l}, \tag{3.81}$$

and

$$c_{1l} = P_{lr}c_{1r} + P_{ll}c_{kl} \tag{3.82}$$
$$= P_{lr}c_{1r} + P_{ll}[(I - Q_{lr}P_{rl})^{-1}(Q_{lr}(P_{rr}c_{1r}) + Q_{ll}c_{(k+1)l})] \tag{3.83}$$
$$= [P_{lr} + P_{ll}(I - Q_{lr}P_{rl})^{-1}(Q_{lr}P_{rr})]c_{1r} + P_{ll}(I - Q_{lr}P_{rl})^{-1}Q_{ll}c_{(k+1)l}. \tag{3.84}$$

Thus, the transfer matrix for travelling from surfaces 1 to $k+1$ is

$$\begin{pmatrix} c_{(k+1)r} \\ c_{1l} \end{pmatrix} = \begin{pmatrix} S_{rr} & S_{rl} \\ S_{lr} & S_{ll} \end{pmatrix} \begin{pmatrix} c_{1r} \\ c_{(k+1)l} \end{pmatrix} \tag{3.85}$$
$$= \begin{pmatrix} Q_{rr}(I - P_{rl}Q_{lr})^{-1}P_{rr} & Q_{rl} + Q_{rr}(I - P_{rl}Q_{lr})^{-1}P_{rl}Q_{ll} \\ P_{lr} + P_{ll}(I - Q_{lr}P_{rl})^{-1}Q_{lr}P_{rr} & P_{ll}(I - Q_{lr}P_{rl})^{-1}Q_{ll} \end{pmatrix} \begin{pmatrix} c_{1r} \\ c_{(k+1)l} \end{pmatrix}. \tag{3.86}$$

The process of stepping forward, each time adding on the next local transfer matrix is repeated until the end, surface N, is reached.

Marching backwards from N to 1 a similar process is followed, a transfer matrix from N to any k is found such that

$$\begin{pmatrix} c_{Nr} \\ c_{kl} \end{pmatrix} = \begin{pmatrix} T_{rr} & T_{rl} \\ T_{lr} & T_{ll} \end{pmatrix} \begin{pmatrix} c_{kr} \\ c_{Nl} \end{pmatrix}. \tag{3.87}$$

Finally by eliminating c_{1l} and c_{Nr} from Eqns 3.85 and 3.87 in a similar manner to above, the global transfer matrix, G_k, is derived as

$$\begin{pmatrix} c_{kr} \\ c_{kl} \end{pmatrix} = G_k \begin{pmatrix} c_{1r} \\ c_{Nl} \end{pmatrix} \tag{3.88}$$

$$= \begin{pmatrix} I - S_{rl}T_{lr} & 0 \\ 0 & I - T_{lr}S_{rl} \end{pmatrix}^{-1} \begin{pmatrix} S_{rr} & S_{rl}T_{ll} \\ T_{lr}S_{rr} & T_{ll} \end{pmatrix} \begin{pmatrix} c_{1r} \\ c_{Nl} \end{pmatrix}. \tag{3.89}$$

3.8 Far-Field Radiation

The EAGCC propagation prediction can be projected to the far-field using a Ffowcs-Williams and Hawkings surface. The surface must be positioned away from the intake such that the mean flow is uniform and homentropic. The unsteady far-field pressure equation used is detailed in Wilson [65] and agrees with the formulation 1C introduced by Najafi-Yazdi *et al.* [147] which includes the presence of mean flow for problems where sound is received by a stationary observer in a moving medium.

3.9 Developments to the EAGCC method

This section introduces two developments made to the EAGCC method as part of the work of this thesis. The first of which is a new approach to modelling lined intakes, and was found to be essential to produce the 3D lined results presented in Chapter 5. The second is an optimisation of the function that forms the generalised eigenvalue problem, which significantly reduces the run time for 3D intake cases and is fundamental to the approximation method introduced in Chapter 6.

3.9.1 Methodology for lined cases

The mesh is designed such that the start and end of the liner correspond to axial mesh points on the outer wall, the impedance boundary condition is also defined at each axial mesh position. The mode-matching, however, occurs at the mid-point between surfaces. Therefore, at the ends of the liner, there is a disparity between the boundary conditions of the two sets of incoming modes and the physical position of the mode matching.

It has been observed that the optimal mode sorting for the surfaces corresponding to the liner ends is dependent on whether the section upstream or downstream is being considered (hard wall or lined). When propagating across sections, this can lead to poor results and dissipation upstream.

To overcome this problem a new approach to modelling the lined duct has been devised. First, the domain is split into three sections, as shown in Fig. 3.9. These sections are determined by the position of the liner and overlap by one surface on either side corresponding to the ends of the liner.

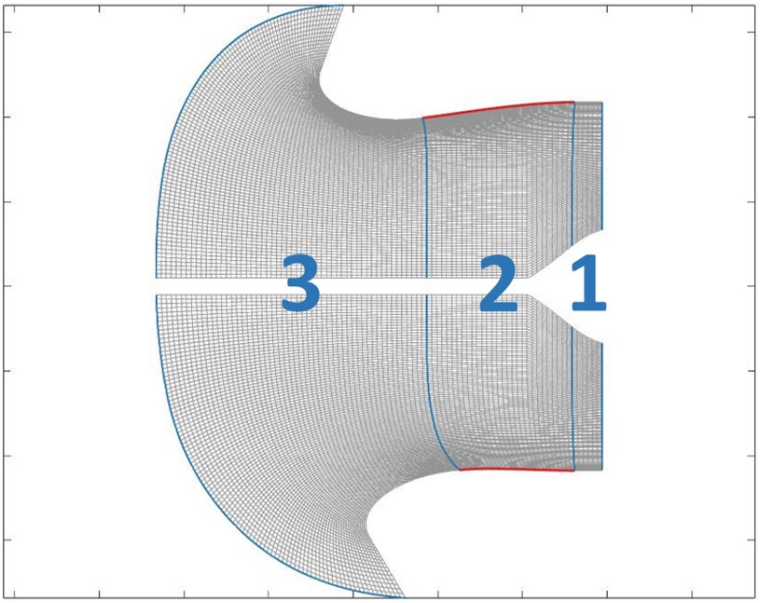

FIGURE 3.9: Mesh of 3D intake, cut taken from top (circumferential position 90 degrees). Blue lines indicate the start and end surfaces of the three sections, and the red line indicates the position of the acoustic liner.

By overlapping the sections, the surfaces at the liner ends can be treated both as hard wall (in a hard wall section) and lined (in a lined section), and the eigen-solutions for both boundary conditions are computed.

The mode sorting can be refined for each section individually, starting downstream and using the upstream output as the upstream input to the adjacent upstream section, represented as a sum of coefficients of the modes at that surface using the inverse of the eigenvector matrix.

3.9.1.1 Propagation

Referring to section 3.7, the propagation process travels forwards and backwards through the duct, combining local transfer matrices, Q, into S and T matrices.

In the new methodology, the same propagation process as described in section 3.7 takes place in each section individually. The local transfer matrices are combined into final S and T matrices, given by Eqns. 3.85 and 3.87, and stored per section. Fig. 3.10 tries to capture this step visually, the three sections are shown with distinct boundaries due to the overlapping surfaces at the liner ends.

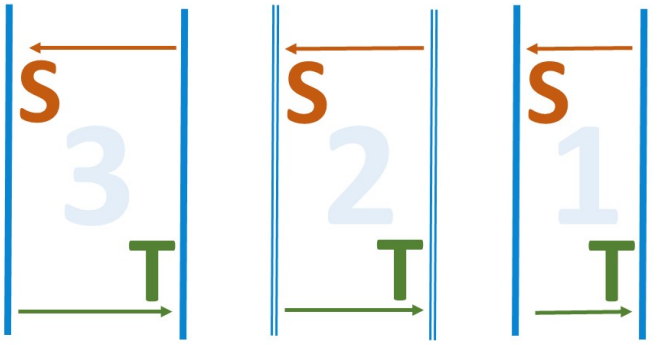

FIGURE 3.10: Three sections, 1 and 3 hard wall, section 2 is lined. Solid lines indicate hard wall axial surface boundaries and the double lines indicate lined surface boundaries. S and T matrices are shown for each individual section.

New local transfer matrices, Q (Eqn. 3.66), between the overlapping surfaces, are calculated to perform a change of basis between the hard wall and lined modes of these surfaces, as illustrated in Fig. 3.11.

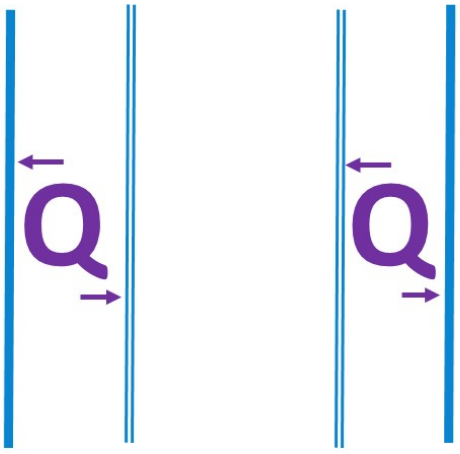

FIGURE 3.11: Local transfer matrices are computed to match the hard wall and lined information at the overlapping surfaces ('between' sections 2 and 3 as well as 1 and 2).

These additional transfer matrices allow for the transmission of information across the liner that accounts for reflections and represents the incoming signals with respect to the appropriate hard wall or lined basis, depending on the direction of travel.

A new domain is defined by just the axial surfaces at the end of each section (including the two overlapping surfaces). The final S and T matrices of each individual section are now treated as local transfer matrices, Q (Eqn. 3.66). The forward and backwards propagation procedure is now applied to this new domain, illustrated in Fig. 3.12.

This forms a global transfer matrix, G (Eqn. 3.88), for the whole domain, relating the global input to the outputs at each of the section boundaries with respect to the hard wall or lined boundary conditions of that section, Fig. 3.13.

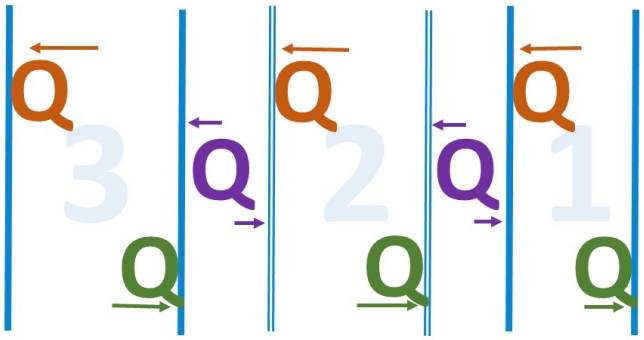

FIGURE 3.12: Treating the domain as a whole, with just 6 surfaces. S and T matrices now act as local Q matrices.

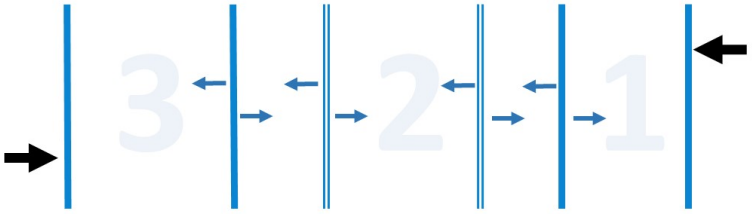

FIGURE 3.13: Global transfer matrix G is formed, with upstream and downstream travelling outputs at each surface.

The relevant outputs from the global transfer matrix, indicated in Fig. 3.14, can then be used as inputs for each section individually.

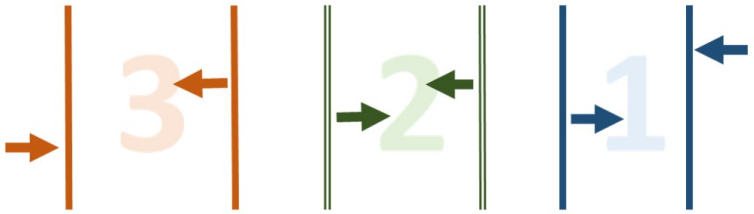

FIGURE 3.14: Sections treated individually again, with the relevant outputs from the global transfer matrix used as inputs.

In summary this new methodology does not change the existing propagation formulation but alters the way it is applied to lined cases. Such that

- Intakes are split into sections which are treated as individual domains
- Axial surfaces corresponding to liner ends are decomposed into both lined and hard wall modes
- Local transfer matrices are computed to transition between the hard wall and lined sections.

3.9.2 Parallelisation of the matriculate function

Within the EAGCC eigen-analysis framework there is a function, 'matriculate', that has been designed to formulate the generalised eigenvalue problem (GEP).

The A and B matrices of Eqn. 3.19, are formed of components from each of the governing equations. The Momentum equation (Eqn. 3.2) in (ξ, η, ζ) and the Mass equation (Eqn. 3.3). The matriculate function formulates these components from each of the four equations individually before combining them to form the GEP.

In the original version of the matriculate function, this process was performed for each equation in serial. For large matrices, this can be time-consuming. However, to reduce this computation time the matriculate function has been developed such that the components corresponding to each equation are formulated in parallel. All the cases featured in this project have four governing equations, thus requiring four cores per surface.

For larger A and B matrices such as those found in non-axisymmetric intake cases, this change substantially reduces the computation time required to formulate the GEP. This is demonstrated further in Chapter 5 section 5.4.

Chapter 4

Error Analysis

The method of propagation, described in Chapter 3, of forming local transfer matrices at mid-points between pseudo-axial analysis surfaces assumes that the Jacobian is constant between mesh points. As changes in geometry, or mean flow, between two analysis surfaces weakens this assumption, it can be deduced that this pseudo-discretisation of the duct will introduce numerical errors in the way of non-physical reflection and transmission. Each time local transfer matrices are formed, small numerical errors could contribute to the coefficients given at each surface, and these local errors are then propagated into neighbouring surfaces where more error can arise. Because errors are effectively sources of noise that themselves propagate, an error analysis in three dimensions is complex. Therefore, this chapter is limited to/ starts with an error analysis for acoustic propagation in one dimension.

This chapter considers a plane wave at unit amplitude propagating in a one-dimensional duct with no mean flow. Local error terms are approximated for this case and then compared and validated to the results of a numerical study.

4.1 Error Analysis

In cartesian, or *physical* , coordinates the 1D Euler equations are of the form

$$\begin{aligned} \frac{\partial u}{\partial z} &= -i\tilde{\omega}p \\ \frac{\partial p}{\partial z} &= -i\tilde{\omega}u \end{aligned} \tag{4.1}$$

where $\tilde{\omega} = \frac{\omega}{c}$.

These equations can be formed into the generalised eigenvalue problem

$$\frac{d\mathbf{F}}{\partial z} = -ik \begin{pmatrix} 0 & 1 \\ 1 & 0 \end{pmatrix} \mathbf{F} \tag{4.2}$$

where $\mathbf{F} = \begin{pmatrix} u \\ p \end{pmatrix}$.
In curvilinear coordinates the velocity, u^*, is a transformation of u by the Jacobian matrix, J, such that

$$u^* = Ju \ , \ \ J = \frac{\partial z}{\partial \zeta}.$$

To write Eqn. 4.1 in terms of curvilinear coordinates, u^* and p^*,

$$\begin{aligned} \frac{\partial u}{\partial z} = \frac{\partial (\frac{u^*}{J})}{J \partial \zeta} &= \frac{1}{J} \frac{\partial}{\partial \zeta} (\frac{u^*}{J}) \\ &= \frac{1}{J^2} \frac{\partial u^*}{\partial \zeta} + \frac{1}{J^3} \frac{\partial J}{\partial \zeta} u^*. \end{aligned} \tag{4.3}$$

Thus,

$$\frac{\partial u^*}{\partial \zeta} = -i\tilde{\omega} p J^2 + \frac{1}{J} \frac{\partial J}{\partial \zeta} u^*. \tag{4.4}$$

As $p^* = p$,

$$\frac{1}{J} \frac{\partial p^*}{\partial \zeta} = \frac{-i\tilde{\omega} u^*}{J}.$$

Therefore,

$$\frac{\partial p^*}{\partial \zeta} = -i\tilde{\omega} u^*. \tag{4.5}$$

4.1.1 Eigen-solutions

The generalised eigenvalue problem in curvilinear coordinates is

$$\frac{\partial \mathbf{F}^*}{\partial \zeta} = i\tilde{\omega} \begin{pmatrix} \frac{1}{i\tilde{\omega} J} \frac{\partial J}{\partial \zeta} & -J^2 \\ -1 & 0 \end{pmatrix} \mathbf{F}^* \tag{4.6}$$

where

$$\mathbf{F}^* = \begin{pmatrix} u^* \\ p^* \end{pmatrix}.$$

The eigenvalues are denoted by

$$\lambda^* = J\hat{\lambda}, \tag{4.7}$$

λ^* are the eigenvalues in the curvilinear space and $\hat{\lambda}$ are the eigenvalues in the cartesian space. Now,

$$i\tilde{\omega}\begin{vmatrix} \frac{1}{i\tilde{\omega}J}\frac{\partial J}{\partial \tilde{\zeta}} - \lambda^* & -J^2 \\ -1 & 0-\lambda^* \end{vmatrix} = i\tilde{\omega}\Big((\frac{1}{i\tilde{\omega}J}\frac{\partial J}{\partial \tilde{\zeta}} - \lambda^*)(-\lambda^*) - J^2\Big) = 0. \tag{4.8}$$

The quadratic expression for λ^* is

$$i\tilde{\omega}\Big(\lambda^{*2} - \frac{1}{i\tilde{\omega}J}\frac{\partial J}{\partial \tilde{\zeta}}\lambda^* - J^2\Big) = 0. \tag{4.9}$$

Using the quadratic formula,

$$\begin{aligned} \lambda^* &= i\tilde{\omega}\Big(\frac{\frac{1}{i\tilde{\omega}J}\frac{\partial J}{\partial \tilde{\zeta}} \pm \sqrt{(-\frac{1}{i\tilde{\omega}J}\frac{\partial J}{\partial \tilde{\zeta}})^2 + 4J^2}}{2}\Big) \\ &= i\tilde{\omega}\Big(\frac{1}{2i\tilde{\omega}J}\frac{\partial J}{\partial \tilde{\zeta}} \pm \sqrt{((\frac{1}{2i\tilde{\omega}J}\frac{\partial J}{\partial \tilde{\zeta}})^2 + J^2}\Big) \\ &= i\tilde{\omega}J(-i\sigma \pm \sqrt{1-\sigma^2}) \end{aligned} \tag{4.10}$$

where

$$\sigma = \frac{1}{2\tilde{\omega}J^2}\frac{\partial J}{\partial \tilde{\zeta}}. \tag{4.11}$$

The positive and negative square root terms give expressions for upstream and downstream travelling waves. The convention used throughout this thesis, for induct propagation, is that upstream is left travelling and downstream is right travelling. Therefore the eigenvalues for downstream and upstream travelling waves are:

$$\lambda^*_{jr} = i\tilde{\omega}J_j(-i\sigma_j - \sqrt{1-\sigma^2}) \tag{4.12}$$

$$\lambda^*_{jl} = i\tilde{\omega}J_j(-i\sigma_j + \sqrt{1-\sigma^2}) \tag{4.13}$$

respectively, where subscripts r and l denote right and left travelling and subscript j denotes the respective surface.

The cartesian/physical equivalent is

$$\hat{\lambda} = i\tilde{\omega}(-i\sigma \pm \sqrt{1-\sigma^2}),$$

as the physical velocity has no dependence on the Jacobian term. In further calculations, unless stated otherwise, the curvilinear forms are used.

To find the corresponding eigenvectors, the eigenvalues from Eqn. 4.10 are substituted into the generalised eigenvalue problem (Eqn. 4.6),

$$\begin{pmatrix} \frac{1}{J}\frac{\partial J}{\partial \tilde{\zeta}} - (i\tilde{\omega}J(-i\sigma \pm \sqrt{1-\sigma^2})) & -i\tilde{\omega}J^2 \\ -i\tilde{\omega} & -(i\tilde{\omega}J(-i\sigma \pm \sqrt{1-\sigma^2})) \end{pmatrix}\begin{pmatrix} u^* \\ p^* \end{pmatrix} = 0. \tag{4.14}$$

Therefore,

$$\Big(\frac{1}{J}\frac{\partial J}{\partial \zeta} - \big(i\tilde{\omega}J(-i\sigma \pm \sqrt{1-\sigma^2})\big)\Big)u^* - i\tilde{\omega}J^2 p^* = 0$$
$$-i\tilde{\omega}u^* - i\tilde{\omega}J(-i\sigma \pm \sqrt{1-\sigma^2}\,)p^* = 0 \tag{4.15}$$

Re-arranging the second equation provides an expression for u^* in terms of p^*

$$u^* = -J(-i\sigma \pm \sqrt{1-\sigma^2}\,)p^*, \tag{4.16}$$

therefore, the eigenvectors are

$$\mathbf{e} = \begin{pmatrix} -J(-i\sigma \pm \sqrt{1-\sigma^2}\,) \\ 1 \end{pmatrix}. \tag{4.17}$$

The eigenvector matrix at surface j is given by

$$E_j = \begin{pmatrix} \frac{-\lambda^*_{jr}}{ik} & \frac{-\lambda^*_{jl}}{ik} \\ 1 & 1 \end{pmatrix} = \begin{pmatrix} -J_j(-i\sigma_j - \sqrt{(}1-\sigma_j^2)) & -J_j(-i\sigma_j + \sqrt{(}1-\sigma_j^2)) \\ 1 & 1 \end{pmatrix}. \tag{4.18}$$

For the following error analysis, all terms are approximated to first order in $\sigma, \sigma', \sigma'', J', J'', J'''$..., the eigenvalues and eigenvectors are

$$\lambda^*_{jr} = i\tilde{\omega}J_j(-i\sigma_j - 1) \tag{4.19}$$

$$\lambda^*_{jl} = i\tilde{\omega}J_j(-i\sigma_j + 1) \tag{4.20}$$

and

$$E_j = \begin{pmatrix} -J_j(-i\sigma_j - 1) & -J_j(-i\sigma_j + 1) \\ 1 & 1 \end{pmatrix}. \tag{4.21}$$

4.1.2 Approximation of change-of-basis matrix

Coefficients are given with respect to the basis at each analysis surface. As $E_j c_j = E_{j+1}c_{j+1}$ then $E^{-1}_{j+1}E_j c_j = c_{j+1}$ which is the change of basis matrix from surface j to $j+1$. As defined in Wilson [65],[6] the change of basis matrix is

$$\mathbf{E}^{-1}_{j+1}\mathbf{E}_j = \begin{pmatrix} A_{rr} & A_{rl} \\ A_{lr} & A_{ll} \end{pmatrix}. \tag{4.22}$$

The subscripts correspond to the direction of information travel with respect to the different basis, for example, the term A_{rl} acts as a change of basis for information that is left traveling at surface j and is right traveling at surface $j+1$.

From Eqn.4.21,

$$E_j^{-1} = \frac{1}{2J_j}\begin{pmatrix} 1 & J_j(-i\sigma_j+1) \\ -1 & -J_j(-i\sigma_j-1) \end{pmatrix}. \tag{4.23}$$

Therefore,

$$\begin{aligned} E_{j+1}^{-1}\mathbf{E}_j &= \frac{1}{2J_{j+1}}\begin{pmatrix} 1 & J_{j+1}(-i\sigma_{j+1}+1) \\ -1 & -J_{j+1}(-i\sigma_{j+1}-1) \end{pmatrix}\begin{pmatrix} -J_j(-i\sigma_j-1) & -J_j(-i\sigma_j+1) \\ 1 & 1 \end{pmatrix} \\ &= \frac{1}{2J_{j+1}}\begin{pmatrix} -J_j(-i\sigma_j-1)+J_{j+1}(-i\sigma_{j+1}+1) & -J_j(-i\sigma_j+1)+J_{j+1}(-i\sigma_{j+1}+1) \\ J_j(-i\sigma_j-1)-J_{j+1}(-i\sigma_{j+1}-1) & J_j(-i\sigma_j+1)-J_{j+1}(-i\sigma_{j+1}-1) \end{pmatrix}. \end{aligned} \tag{4.24}$$

These terms with respect to J and σ are

$$\begin{aligned} A_{rr} &= \frac{1}{2J_{j+1}}(-J_j(-i\sigma_j-1)+J_{j+1}(-i\sigma_{j+1}+1)) \\ &= \frac{-1}{2J_{j+1}}J_j(-i\sigma_j-1)+\frac{1}{2}(-i\sigma_{j+1}+1) && (4.25) \\ A_{rl} &= \frac{1}{2J_{j+1}}(-J_j(-i\sigma_j+1)+J_{j+1}(-i\sigma_{j+1}+1)) \\ &= \frac{-1}{2J_{j+1}}J_j(-i\sigma_j+1)+\frac{1}{2}(-i\sigma_{j+1}+1)) && (4.26) \\ A_{lr} &= \frac{1}{2J_{j+1}}(J_j(-i\sigma_j-1)-J_{j+1}(-i\sigma_{j+1}-1)) \\ &= \frac{1}{2J_{j+1}}J_j(-i\sigma_j-1)-\frac{1}{2}(-i\sigma_{j+1}-1) && (4.27) \\ A_{ll} &= \frac{1}{2J_{j+1}}(J_j(-i\sigma_j+1)-J_{j+1}(-i\sigma_{j+1}-1)) \\ &= \frac{1}{2J_{j+1}}J_j(-i\sigma_j+1)-\frac{1}{2}(-i\sigma_{j+1}-1)). && (4.28) \end{aligned}$$

Similarly, looking at the change of basis matrix from surface $j+1$ to surface j we have

$$E_j^{-1}E_{j+1} = \begin{pmatrix} B_{rr} & B_{rl} \\ B_{lr} & B_{ll} \end{pmatrix}, \tag{4.29}$$

and

$$\begin{aligned} B_{rr} &= \frac{1}{2J_j}(-J_{j+1}(-i\sigma_{j+1}-1)+J_j(-i\sigma_j+1)) && (4.30) \\ &= \frac{-1}{2J_j}J_{j+1}(-i\sigma_{j+1}-1)+\frac{1}{2}(-i\sigma_j+1) && (4.31) \\ B_{rl} &= \frac{1}{2J_j}(-J_{j+1}(-i\sigma_{j+1}+1)+J_j(-i\sigma_j+1)) && (4.32) \\ &\frac{1}{2J_j}J_{j+1}(-i\sigma_{j+1}+1)+\frac{1}{2}(-i\sigma_j+1) && (4.33) \end{aligned}$$

$$B_{lr} = \frac{1}{2J_j}(J_{j+1}(-i\sigma_{j+1} - 1) - J_j(-i\sigma_j - 1)) \tag{4.34}$$

$$= \frac{1}{2J_j}J_{j+1}(-i\sigma_{j+1} - 1) - \frac{1}{2}(-i\sigma_j - 1) \tag{4.35}$$

$$B_{ll} = \frac{1}{2J_j}(J_{j+1}(-i\sigma_{j+1} + 1) - J_j(-i\sigma_j - 1)) \tag{4.36}$$

$$= \frac{1}{2J_j}J_{j+1}(-i\sigma_{j+1} + 1) - \frac{1}{2}(-i\sigma_j - 1). \tag{4.37}$$

To approximate these terms to first order, the Taylor's expansion for J_{j+1} is taken as

$$J_{j+1} \approx J_j + \Delta\zeta J_j' + \frac{(\Delta\zeta)^2 J_j''}{2} + \frac{(\Delta\zeta)^3 J_j'''}{6}. \tag{4.38}$$

Substituting this approximation into A_{rr} (Eqn. 4.25)

$$A_{rr} = \frac{-J_j(-i\sigma_j - 1)}{2}\Big(J_j + \Delta\zeta J_j' + (\Delta\zeta)^2\frac{J_j''}{2} + (\Delta\zeta)^3\frac{J_j'''}{6}\Big) + \frac{1}{2}(-i\sigma_{j+1} + 1). \tag{4.39}$$

Factoring out J_j leads to

$$\Big(J_j + \Delta\zeta J_j' + (\Delta\zeta)^2\frac{J_j''}{2} + (\Delta\zeta)^3\frac{J_j'''}{6}\Big) = J_j\Big(1 + \Delta\zeta\frac{J_j'}{J_j} + (\Delta\zeta)^2\frac{J_j''}{2J_j} + (\Delta\zeta)^3\frac{J_j'''}{6J_j}\Big). \tag{4.40}$$

Taking the approximation

$$(1+\epsilon)^{-1} \approx 1 - \epsilon + \epsilon^2 - \epsilon^3 + ... \tag{4.41}$$

and setting

$$\epsilon = \Delta\zeta\frac{J_j'}{J_j} + (\Delta\zeta)^2\frac{J_j''}{2J_j} + (\Delta\zeta)^3\frac{J_j'''}{6J_j}, \tag{4.42}$$

Substituting ϵ into Eqn. 4.41

$$(1+\epsilon)^{-1} = \Big(1 + \Big(\Delta\zeta\frac{J_j'}{J_j} + (\Delta\zeta)^2\frac{J_j''}{2J_j} + (\Delta\zeta)^3\frac{J_j'''}{6J_j}\Big)\Big)^{-1}. \tag{4.43}$$

Therefore, to first order

$$\Big(J_j\Big(1 + \Delta\zeta\frac{J_j'}{J_j} + (\Delta\zeta)^2\frac{J_j''}{2J_j} + (\Delta\zeta)^3\frac{J_j'''}{6J_j}\Big)\Big)^{-1} \approx J_j^{-1}\Big(1 - \Delta\zeta\frac{J_j'}{J_j} - (\Delta\zeta)^2\frac{J_j''}{2J_j} - (\Delta\zeta)^3\frac{J_j'''}{6J_j}\Big). \tag{4.44}$$

Substituting this into A_{rr} (Eqn. 4.39)

$$A_{rr} = \frac{1}{2}\Big(\big(-J_j(-i\sigma_j - 1)\big)J^{-1}\big(1 - \frac{\Delta\zeta J_j'}{J_j} - \frac{(\Delta\zeta)^2 J_j''}{2J_j} - \frac{(\Delta\zeta)^3 J_j'''}{6J_j}\big)\Big) + \frac{1}{2}(-i\sigma_{j+1} + 1). \tag{4.45}$$

Using the identity

$$\sigma_j = \frac{1}{2J_j^2\tilde{\omega}}\frac{\partial J_j}{\partial \zeta}, \tag{4.46}$$

we have that

$$\begin{aligned}
\sigma_{j+1} &= \frac{1}{2J_{j+1}^2\tilde{\omega}}\frac{\partial J_{j+1}}{\partial \zeta} && (4.47)\\
&= \frac{1}{2(J_j + \Delta\zeta J_j' + ...)^2\tilde{\omega}}\frac{\partial (J_j + \Delta\zeta J_j' + ...)}{\partial \zeta} && (4.48)\\
&= \sigma_j + \Delta\zeta\sigma_j'. && (4.49)
\end{aligned}$$

Using the Taylor's series expansion,

$$\begin{aligned}
A_{rr} &= \frac{1}{2}\Big(\big(-J_j(-i\sigma_j - 1)\big)J^{-1}\big(1 - \Delta\zeta\frac{J_j'}{J_j} - (\Delta\zeta)^2 f12\frac{J_j''}{J_j} - (\Delta\zeta)^3\frac{1}{6}\frac{J_j'''}{J_j}\big)\Big)\\
&\quad + \frac{1}{2}\Big(1 - i\sigma_j - i\Delta\zeta\sigma_j' - (\Delta\zeta)^2\frac{1}{2}i\sigma_j'' - (\Delta\zeta)^3\frac{1}{6}i\sigma_j'''\Big)\\
&= \frac{1}{2}\Big(2 + \Delta\zeta(\frac{-i\sigma_j J_j'}{J_j} - \frac{J_j'}{J_j} - i\sigma_j') + \frac{(\Delta\zeta)^2}{2}(\frac{-i\sigma_j J_j''}{J_j} + \frac{J_j''}{J_j} - i\sigma_j'') + \frac{(\Delta\zeta)^3}{6}(\frac{-i\sigma_j J_j'''}{J_j} - \frac{J_j'''}{J_j} - i\sigma_j''')\Big).
\end{aligned} \tag{4.50}$$

To first order, this simplifies to,

$$\begin{aligned}
A_{rr} &= 1 - \frac{\Delta\zeta}{2}(\frac{J_j'}{J_j} + i\sigma_j') - \frac{(\Delta\zeta)^2}{4}(\frac{J_j''}{J_j} + i\sigma_j'') - \frac{(\Delta\zeta)^3}{12}(\frac{J_j'''}{J_j} + i\sigma_j''')\\
&= 1 + \frac{\Delta\zeta}{2}(\frac{-J_j'}{J_j} - i\sigma_j') + \frac{(\Delta\zeta)^2}{4}(\frac{-J_j''}{J_j} - i\sigma_j'') + \frac{(\Delta\zeta)^3}{12}(\frac{-J_j'''}{J_j} - i\sigma_j''').
\end{aligned} \tag{4.51}$$

Similarly, to first order, the other terms in the change-of-basis matrix are:

$$\begin{aligned}
A_{rl} &= \frac{-1}{2J_{j+1}}J_j(-i\sigma_j + 1) + \frac{1}{2}(-i\sigma_{j+1} + 1)) && (4.52)\\
&= \frac{\Delta\zeta}{2}(\frac{J_j'}{J_j} - i\sigma_j') + \frac{(\Delta\zeta)^2}{4}(\frac{J_j''}{J_j} - i\sigma_j'') + \frac{(\Delta\zeta)^3}{12}(\frac{J_j'''}{J_j} - i\sigma_j''') && (4.53)\\
A_{lr} &= \frac{1}{2J_{j+1}}J_j(-i\sigma_j - 1) - \frac{1}{2}(-i\sigma_{j+1} - 1) && (4.54)\\
&= \frac{\Delta\zeta}{2}(\frac{J_j'}{J_j} + i\sigma_j') + \frac{(\Delta\zeta)^2}{4}(\frac{J_j''}{J_j} + i\sigma_j'') + \frac{(\Delta\zeta)^3}{12}(\frac{J_j'''}{J_j} + i\sigma_j''') && (4.55)\\
A_{ll} &= \frac{1}{2J_{j+1}}J_j(-i\sigma_j + 1) - \frac{1}{2}(-i\sigma_{j+1} - 1)) && (4.56)\\
&= 1 + \frac{\Delta\zeta}{2}(\frac{-J_j'}{J_j} + i\sigma_j') + \frac{(\Delta\zeta)^2}{4}(\frac{-J_j''}{J_j} + i\sigma_j'') + \frac{(\Delta\zeta)^3}{12}(\frac{-J_j'''}{J_j} + i\sigma_j'''). && (4.57)
\end{aligned}$$

(4.58)

For the entries B in the other change-of-basis matrices we have

$$B_{rr} = \frac{-1}{2J_j} J_{j+1}(-i\sigma_{j+1} - 1) + \frac{1}{2}(-i\sigma_j + 1). \tag{4.59}$$

Similarly J_{j+1} is approximated such that

$$J_{j+1} \approx J_j + \Delta\zeta J_j' + \frac{(\Delta\zeta)^2}{2} J_j'' + \frac{(\Delta\zeta)^3}{6} J_j''' \tag{4.60}$$

$$-i\sigma_j \approx -i\sigma_j - i\sigma_j'\Delta\zeta - i\sigma_j''\frac{(\Delta\zeta)^2}{2} - i\sigma_j'''\frac{(\Delta\zeta)^3}{6}. \tag{4.61}$$

Therefore,

$$B_{rr} = \frac{1}{2J_j}\Big(\big(-J_j - \Delta\zeta J_j' \frac{(\Delta\zeta)^2}{2} J_j'' - \frac{(\Delta\zeta)^3}{6} J_j''' \big) \big(-1 - i\sigma_j - i\sigma_j'\Delta\zeta - i\sigma_j''\frac{(\Delta\zeta)^2}{2} - i\sigma_j'''\frac{(\Delta\zeta)^3}{6} \big) - i\sigma_j + 1 \Big), \tag{4.62}$$

to first order

$$B_{rr} = 1 + \frac{\Delta\zeta}{2}\big(\frac{J_j'}{J_j} + i\sigma_j'\big) + \frac{(\Delta\zeta)^2}{4}\big(\frac{J_j''}{J_j} + i\sigma_j''\big) + \frac{(\Delta\zeta)^3}{12}\big(\frac{J_j'''}{J_j} + i\sigma_j'''\big). \tag{4.63}$$

Similarly,

$$B_{rl} = \frac{\Delta\zeta}{2}\big(\frac{-J_j'}{J_j} + i\sigma_j'\big) + \frac{(\Delta\zeta)^2}{4}\big(\frac{-J_j''}{J_j} + i\sigma_j''\big) + \frac{(\Delta\zeta)^3}{12}\big(\frac{-J_j'''}{J_j} + i\sigma_j'''\big) \tag{4.64}$$

$$B_{lr} = \frac{\Delta\zeta}{2}\big(\frac{-J_j'}{J_j} - i\sigma_j'\big) + \frac{(\Delta\zeta)^2}{4}\big(\frac{-J_j''}{J_j} - i\sigma_j''\big) + \frac{(\Delta\zeta)^3}{12}\big(\frac{-J_j'''}{J_j} - i\sigma_j'''\big) \tag{4.65}$$

$$B_{ll} = 1 + \frac{\Delta\zeta}{2}\big(\frac{J_j'}{J_j} - i\sigma_j'\big) + \frac{(\Delta\zeta)^2}{4}\big(\frac{J_j''}{J_j} - i\sigma_j''\big) + \frac{(\Delta\zeta)^3}{12}\big(\frac{J_j'''}{J_j} - i\sigma_j'''\big). \tag{4.66}$$

The change of basis matrix, as shown in Chapter 3 and Wilson [65], is

$$\begin{pmatrix} A_{rr}(I + (I - B_{rl}A_{lr})^{-1}B_{rl}A_{lr}) & -A_{rr}(I - B_{rl}A_{lr})^{-1}B_{rl} \\ -B_{ll}(I - A_{lr}B_{rl})^{-1}A_{lr} & B_{ll}(I + (I - A_{lr}B_{rl})^{-1}A_{lr}B_{rl}) \end{pmatrix}. \tag{4.67}$$

From the first order approximations, it is known that $B_{rl} = -A_{rl}$ and $B_{lr} = -A_{lr}$. Therefore,

$$\begin{aligned} B_{rl}A_{lr} = -A_{rl}A_{lr} = -\Big(&\frac{\Delta\zeta}{2}\big(\frac{J_j'}{J_j} - i\sigma_j'\big) + \frac{(\Delta\zeta)^2}{4}\big(\frac{J_j''}{J_j} - i\sigma_j''\big) + \frac{(\Delta\zeta)^3}{12}\big(\frac{J_j'''}{J_j} - i\sigma_j'''\big)\Big) \\ &\times \Big(\frac{\Delta\zeta}{2}\big(\frac{J_j'}{J_j} + i\sigma_j'\big) + \frac{(\Delta\zeta)^2}{4}\big(\frac{J_j''}{J_j} + i\sigma_j''\big) + \frac{(\Delta\zeta)^3}{12}\big(\frac{J_j'''}{J_j} + i\sigma_j'''\big)\Big). \end{aligned} \tag{4.68}$$

To first order this is equal to 0. Therefore, $(I - B_{rl}A_{lr})^{-1}$ and $(I - A_{lr}B_{rl})^{-1}$ are both equal to 1 and the change-of-basis matrix

$$\begin{pmatrix} A_{rr}(1 + B_{rl}A_{lr}) & -A_{rr}B_{rl} \\ -B_{ll}A_{lr} & B_{ll}(1 + A_{lr}B_{rl}) \end{pmatrix} = \begin{pmatrix} A_{rr} & -A_{rr}B_{rl} \\ -B_{ll}A_{lr} & B_{ll} \end{pmatrix}. \tag{4.69}$$

Furthermore,

$$\begin{aligned} A_{rr}B_{rl} = \Big(1 + \frac{\Delta\zeta}{2}\big(\frac{-J_j'}{J_j} - i\sigma_j'\big) + \frac{(\Delta\zeta)^2}{4}\big(\frac{-J_j''}{J_j} - i\sigma_j''\big) + \frac{(\Delta\zeta)^3}{12}\big(\frac{-J_j'''}{J_j} - i\sigma_j'''\big)\Big) \\ \times \Big(\frac{\Delta\zeta}{2}\big(\frac{-J_j'}{J_j} + i\sigma_j'\big) + \frac{(\Delta\zeta)^2}{4}\big(\frac{-J_j''}{J_j} + i\sigma_j''\big) + \frac{(\Delta\zeta)^3}{12}\big(\frac{-J_j'''}{J_j} + i\sigma_j'''\big)\Big). \end{aligned} \tag{4.70}$$

To first order this is equal to B_{rl}. Similarly, $B_{ll}A_{lr} = A_{lr}$, and therefore,

$$\begin{pmatrix} A_{rr} & -B_{rl} \\ -A_{lr} & B_{ll} \end{pmatrix}. \tag{4.71}$$

The propagation from one surface to the next adjacent surface can be expressed by 3.49:

$$\begin{pmatrix} c_{2r} \\ c_{1l} \end{pmatrix} = X_{out}X_{basis}X_{in}\begin{pmatrix} c_{1r} \\ c_{2l} \end{pmatrix}.$$

Written explicitly

$$\begin{pmatrix} c_{2r} \\ c_{1l} \end{pmatrix} = \begin{pmatrix} e^{\lambda_{(j+1)r}(\frac{\Delta\zeta}{2})} & 0 \\ 0 & e^{-\lambda_{jl}(\frac{\Delta\zeta}{2})} \end{pmatrix}\begin{pmatrix} A_{rr} & -B_{rl} \\ -A_{lr} & B_{ll} \end{pmatrix}\begin{pmatrix} e^{\lambda_{jr}(\frac{\Delta\zeta}{2})} & 0 \\ 0 & e^{-\lambda_{(j+1)l}(\frac{\Delta\zeta}{2})} \end{pmatrix}\begin{pmatrix} c_{1r} \\ c_{2l} \end{pmatrix}. \tag{4.72}$$

Re-writing the X_{in} and X_{out} matrices by adding $0 = e^{-i\tilde{\omega}J_j\frac{\Delta\zeta}{2}} - e^{-i\tilde{\omega}J_j\frac{\Delta\zeta}{2}}$ to the diagonal entries gives

$$\begin{aligned} &\left[\begin{pmatrix} e^{-i\tilde{\omega}J_j\frac{\Delta\zeta}{2}} & 0 \\ 0 & e^{-i\tilde{\omega}J_j\frac{\Delta\zeta}{2}} \end{pmatrix} + \begin{pmatrix} (e^{\lambda_{(j+1)r}\frac{\Delta\zeta}{2}} - e^{-i\tilde{\omega}J_j\frac{\Delta\zeta}{2}} & 0 \\ 0 & (e^{\lambda_{jl}\frac{\Delta\zeta}{2}} - e^{-i\tilde{\omega}J_j\frac{\Delta\zeta}{2}}) \end{pmatrix}\right] \\ &\qquad X_{Basis}\left[\begin{pmatrix} e^{-i\tilde{\omega}J_j\frac{\Delta\zeta}{2}} & 0 \\ 0 & e^{-i\tilde{\omega}J_j\frac{\Delta\zeta}{2}} \end{pmatrix} + \begin{pmatrix} (e^{\lambda_{jr}\frac{\Delta\zeta}{2}} - e^{-i\tilde{\omega}J_j\frac{\Delta\zeta}{2}}) & 0 \\ 0 & (e^{-\lambda_{(j+1)l}\frac{\Delta\zeta}{2}} - e^{-i\tilde{\omega}J_j\frac{\Delta\zeta}{2}}) \end{pmatrix}\right]. \end{aligned}$$

Labelling the matrices a, b, c, d respectively, with $a = c$

$$\begin{aligned} (a + b)X_{Basis}(c + d) &= aX_Bc + aX_Bd + bX_Bc + bX_Bd & (4.73)\\ &= aX_Ba + aX_Bd + bX_Ba + bX_Bd & (4.74)\\ &= aX_Ba + a(d + b) + bX_Bd. & (4.75) \end{aligned}$$

Separating the three terms,

$$aX_Ba = 2aX_B = e^{-i\tilde{\omega}J_j\Delta\zeta}X_{Basis}, \tag{4.76}$$

bX_Bd goes to higher order and

$$a(d+b) = e^{-i\tilde{\omega}J_j\frac{\Delta\zeta}{2}}\begin{pmatrix} P_{1A}+P_{1B} & 0 \\ 0 & P_{2A}+P_{2B}\end{pmatrix} \tag{4.77}$$

where

$$P_{1A}+P_{1B} = (e^{\lambda_{(j+1)r}\frac{\Delta\zeta}{2}} - e^{-i\tilde{\omega}J_j\frac{\Delta\zeta}{2}}) + (e^{\lambda_{jr}\frac{\Delta\zeta}{2}} - e^{-i\tilde{\omega}J_j\frac{\Delta\zeta}{2}}) \tag{4.78}$$

$$P_{2A}+P_{2B} = (e^{\lambda_{jl}\frac{\Delta\zeta}{2}} - e^{-i\tilde{\omega}J_j\frac{\Delta\zeta}{2}}) + (e^{-\lambda_{(j+1)l}\frac{\Delta\zeta}{2}} - e^{-i\tilde{\omega}J_j\frac{\Delta\zeta}{2}}). \tag{4.79}$$

Thus, the local propagation between adjacent surfaces 1 and 2

$$\begin{pmatrix} c_{2r} \\ c_{1l}\end{pmatrix} = M\begin{pmatrix} c_{1r} \\ c_{2l}\end{pmatrix} \tag{4.80}$$

$$= \left[e^{-i\tilde{\omega}J_j\Delta\zeta}X_{Basis} + e^{-i\tilde{\omega}J_j\frac{\Delta\zeta}{2}}\begin{pmatrix} P_{1A}+P_{1B} & 0 \\ 0 & P_{2A}+P_{2B}\end{pmatrix}\right]\begin{pmatrix} c_{1r} \\ c_{2l}\end{pmatrix}. \tag{4.81}$$

Now an approximation of the P entries is required.

$$P_{1A} = e^{\lambda_{(j+1)r}\frac{\Delta\zeta}{2}} - e^{-i\tilde{\omega}J_j\frac{\Delta\zeta}{2}} \tag{4.82}$$

$$= e^{i\tilde{\omega}J_{(j+1)r}(1+i\sigma_j)\frac{(\Delta\zeta)}{2}} - e^{-i\tilde{\omega}J_j\frac{\Delta\zeta}{2}} \tag{4.83}$$

$$= e^{i\tilde{\omega}\frac{(\Delta\zeta)}{2}(J_{(j+1)r}(1+i\sigma_j)-J_j)}, \tag{4.84}$$

and as

$$J_{(j+1)}(1+i\sigma_{(j+1)}) - J_j = J_{(j+1)} - J_j + J_{(j+1)}i\sigma_{(j+1)} \tag{4.85}$$

$$= J_j'\Delta\zeta + \frac{1}{2}J_j''(\Delta\zeta)^2 + \frac{1}{6}J_j'''(\Delta\zeta)^3 + iJ_j\sigma_j + iJ\sigma_j'\Delta\zeta + iJ_j\sigma_j''\frac{(\Delta\zeta)^2}{2}, \tag{4.86}$$

it can be surmised that

$$P_{1A} = e^{J_j'\Delta\zeta+\frac{1}{2}J_j''(\Delta\zeta)^2+\frac{1}{6}J_j'''(\Delta\zeta)^3+iJ_j\sigma_j+iJ\sigma_j'\Delta\zeta+iJ_j\sigma_j''\frac{(\Delta\zeta)^2}{2}}. \tag{4.87}$$

Factoring out the $e^{-i\tilde{\omega}J_j\frac{\Delta\zeta}{2}}$ term, by adding 0,

$$e^{-i\tilde{\omega}J_j\frac{\Delta\zeta}{2}}[e^{i\tilde{\omega}\frac{(\Delta\zeta)}{2}(J_{(j+1)r}(1+i\sigma_j)-J_j)} - 1]. \tag{4.88}$$

Taking the Taylor's approximation of these exponential terms leads to

$$\begin{aligned} P_{1A} =& -i\tilde{\omega}J_j\frac{\Delta\zeta}{2}\big(1-i\tilde{\omega}J_j\frac{\Delta\zeta}{2}-\frac{1}{8}\tilde{\omega}^2(\Delta\zeta)^2J_j^2+\frac{1}{48}i\tilde{\omega}^3(\Delta\zeta)^3J_j^3\big) \\ &\times\big(J_j'\Delta\zeta+\frac{1}{2}J_j''(\Delta\zeta)^2+iJ_j\sigma_j'\Delta\zeta+\frac{1}{2}iJ_j\sigma_j''(\Delta\zeta)^2+iJ_j\sigma_j\big) \qquad (4.89) \\ =&(\Delta\zeta)\Big(\frac{i^2\tilde{\omega}}{2}J_j\sigma_j\Big)+(\Delta\zeta)^2\Big(\frac{i\tilde{\omega}}{2}J_j'-\frac{i^2\tilde{\omega}}{2}J_j\sigma_j'+\frac{-i\tilde{\omega})^2}{4}J_jiJ_j\sigma_j\Big) \\ &+(\Delta\zeta)^3\Big(\frac{-i\tilde{\omega}}{4}J_j''-\frac{i^2\tilde{\omega}}{4}J_j\sigma_j''+\frac{1}{16}i^2\tilde{\omega}^3J_j^3\sigma_j+\frac{(i\tilde{\omega})^2}{4}J_jJ_j'+\frac{-i\tilde{\omega})^2}{4}J_j^2i\sigma_j'\Big). \qquad (4.90) \end{aligned}$$

This can be simplified by eliminating the σ and higher derivative terms, instead writing them with respect to J and higher derivatives. First, the derivatives of σ with respect to J_j and to first order are:

$$\sigma_j=\frac{J_j'}{2J_j^2\tilde{\omega}} \qquad (4.91)$$

$$\sigma_j'=\frac{J_j''}{2J_j^2\tilde{\omega}} \qquad (4.92)$$

$$\sigma_j''=\frac{J_j'''}{2J_j^2\tilde{\omega}} \qquad (4.93)$$

$$\sigma_j'''=\frac{J_j''''}{2J_j^2\tilde{\omega}}. \qquad (4.94)$$

Therefore, P_{1A} can be simplified to

$$\begin{aligned} P_{1A} =& (\Delta\zeta)(\frac{1}{4}\frac{J_j'}{J_j})+(\Delta\zeta)^2(\frac{-5}{8}i\tilde{\omega}J_j'+\frac{1}{4}\frac{J_j''}{J_j}) \\ &+(\Delta\zeta)^3(\frac{J_j'''}{8J_j}-\frac{9}{32}J_jJ_j'\tilde{\omega}^2-\frac{3}{8}i\tilde{\omega}J_j''). \qquad (4.95) \end{aligned}$$

Similarly,

$$\begin{aligned} P_{2A} =&(e^{\lambda_{jl}\frac{\Delta\zeta}{2}}-e^{-i\tilde{\omega}J_j\frac{\Delta\zeta}{2}}) \qquad (4.96) \\ =&\frac{-i\tilde{\omega}\Delta\zeta}{2}\Big(1-\frac{1}{2}i\tilde{\omega}J_j\Delta\zeta-\frac{1}{8}\tilde{\omega}^2J_j^2(\Delta\zeta)^3\Big) \\ &\times\Big(J_j'\Delta\zeta+\frac{1}{2}J_j''(\Delta\zeta)^2-iJ_j\sigma_j-iJ_j\sigma_j'\Delta\zeta-\frac{1}{2}iJ_j\sigma_j''(\Delta\zeta)^2\Big) \qquad (4.97) \\ =&(\Delta\zeta)(\frac{1}{4}\frac{J_j'}{J_j})+(\Delta\zeta)^2(-\frac{3}{8}i\tilde{\omega}J_j'-\frac{1}{4}\frac{J_j''}{J_j}) \\ &+(\Delta\zeta)^3(-\frac{1}{8}\frac{J_j'''}{J_j}-\frac{7}{32}J_jJ_j'\tilde{\omega}^2-\frac{1}{8}i\tilde{\omega}J_j''), \qquad (4.98) \end{aligned}$$

and

$$P_{1B} = \Big(\frac{1}{4}\frac{J_j'}{J_j}\Delta\zeta - \frac{1}{8}i\tilde{\omega}J_j'(\Delta\zeta)^2 - \frac{1}{32}\tilde{\omega}^2 J_j J_j'(\Delta\zeta)^3\Big) \tag{4.99}$$

$$P_{2B} = \Big(-\frac{1}{4}\frac{J_j'}{J_j}\Delta\zeta + \frac{1}{8}i\tilde{\omega}J_j'(\Delta\zeta)^2 + \frac{1}{32}\tilde{\omega}^2 J_j J_j'(\Delta\zeta)^3\Big). \tag{4.100}$$

Therefore,

$$\begin{aligned} P_{1A} + P_{1B} = (\Delta\zeta)(\frac{1}{2}\frac{J_j'}{J_j}) &+ (\Delta\zeta)^2(-\frac{3}{4}i\tilde{\omega}J_j' + \frac{1}{4}\frac{J_j''}{J_j}) \\ &+ (\Delta\zeta)^3(-\frac{3}{8}i\tilde{\omega}J_j'' + \frac{1}{8}\frac{J_j'''}{J_j} - \frac{5}{16}\tilde{\omega}^2 J_j J_j') \end{aligned} \tag{4.101}$$

$$\begin{aligned} P_{2A} + P_{2B} = (\Delta\zeta)(-\frac{1}{2}\frac{J_j'}{J_j}) &+ (\Delta\zeta)^2(-\frac{1}{4}i\tilde{\omega}J_j' - \frac{1}{4}\frac{J_j''}{J_j}) \\ &+ (\Delta\zeta)^3(-\frac{1}{8}i\tilde{\omega}J_j'' - \frac{1}{8}\frac{J_j'''}{J_j} - \frac{3}{16}\tilde{\omega}^2 J_j J_j'). \end{aligned} \tag{4.102}$$

From Eqn. 4.80

$$\begin{pmatrix} c_{2r} \\ c_{1l} \end{pmatrix} = M \begin{pmatrix} c_{1r} \\ c_{2l} \end{pmatrix} \tag{4.103}$$

$$= \begin{pmatrix} e^{-i\tilde{\omega}J_j\Delta\zeta}A_{rr} + e^{-i\tilde{\omega}J_j\frac{\Delta\zeta}{2}}(P_{1A}+P_{1B}) & -e^{-i\tilde{\omega}J_j\Delta\zeta}B_{rl} \\ -e^{i\tilde{\omega}J_j\Delta\zeta}A_{lr} & e^{-i\tilde{\omega}J_j\Delta\zeta}B_{ll} + e^{-i\tilde{\omega}J_j\frac{\Delta\zeta}{2}}(P_{2A}+P_{2B}) \end{pmatrix} \begin{pmatrix} c_{1r} \\ c_{2l} \end{pmatrix}. \tag{4.104}$$

As seen before, to approximate the entries of M the approximation of the σ derivatives shown in Eqn. 4.91 are used to express the terms with respect to J and higher derivatives. To first order,

$$\begin{aligned} M_{11} =& \Big(1 - i\tilde{\omega}\Delta\zeta J_j + \frac{1}{2}(-i\tilde{\omega})^2(\Delta\zeta)^2 J_j^2 - \frac{1}{6}i\tilde{\omega}^3(\Delta\zeta)^3 J_j^3\Big) \\ &\Big(1 + \frac{\Delta\zeta}{2}(\frac{-J_j'}{J_j} - i\sigma_j') + \frac{(\Delta\zeta)^2}{4}(\frac{-J_j''}{J_j} - i\sigma_j'') + \frac{(\Delta\zeta)^3}{12}(\frac{-J_j'''}{J_j} - i\sigma_j''')\Big) \\ &+ \Big(1 - i\tilde{\omega}\frac{\Delta\zeta}{2}J_j + \frac{1}{8}(-i\tilde{\omega})^2(\Delta\zeta)^2 J_j^2 - \frac{1}{48}i\tilde{\omega}^3(\Delta\zeta)^3)\Big) \\ &\Big(\Delta\zeta(\frac{1}{2}\frac{J_j'}{J_j}) + (\Delta\zeta)^2(-\frac{3}{4}i\tilde{\omega}J_j' + \frac{1}{4}\frac{J_j''}{J_j}) + (\Delta\zeta)^3(-\frac{3}{8}i\tilde{\omega}J_j'' + \frac{1}{8}\frac{J_j'''}{J_j} - \frac{5}{16}\tilde{\omega}^2 J_j J_j')\Big) \end{aligned} \tag{4.105}$$

$$\begin{aligned} =& \Big(1 + (\Delta\zeta)(-i\tilde{\omega}J_j - \frac{1}{4}\frac{iJ_j''}{J_j^2\tilde{\omega}}) + (\Delta\zeta)^2(-\frac{1}{8}\frac{iJ_j'''}{J_j^2\tilde{\omega}} - \frac{1}{2}\tilde{\omega}^2 J_j^2 - \frac{1}{2}\frac{J_j''}{J_j} - \frac{1}{2}i\tilde{\omega}J_j') \\ &+ (\Delta\zeta)^3(-\frac{1}{2}\tilde{\omega}^2 J_j J_j' - \frac{1}{12}\frac{J_j'''}{J_j} - \frac{1}{8}i\tilde{\omega}J_j'' - \frac{1}{24}\frac{iJ_j''''}{J_j^2\tilde{\omega}} + \frac{1}{6}i\tilde{\omega}^3 J_j^3)\Big). \end{aligned} \tag{4.106}$$

Similarly,

$$M_{12} = (\Delta\zeta)\Big(\frac{1}{2}\frac{J_j'}{J_j} - \frac{1}{4}\frac{iJ_j''}{\tilde{\omega}J_j^2}\Big) + (\Delta\zeta)^2\Big(-\frac{1}{8}\frac{iJ_j'''}{J_j^2\tilde{\omega}} - \frac{1}{2}i\tilde{\omega}J_j'\Big) + (\Delta\zeta)^3\Big(-\frac{1}{24}\frac{J_j'''}{J_j} - \frac{1}{24}\frac{iJ_j''''}{J_j^2\tilde{\omega}} - \frac{1}{8}i\tilde{\omega}J_j'' - \frac{1}{4}iJ_j'\tilde{\omega}^2J_j\Big) \tag{4.107}$$

$$M_{21} = (\Delta\zeta)\Big(-\frac{1}{2}\frac{J_j'}{J_j} - \frac{1}{4}\frac{iJ_j''}{J_j^2\tilde{\omega}}\Big) + (\Delta\zeta)^2\Big(-\frac{1}{2}\frac{J_j''}{J_j} - \frac{1}{8}\frac{iJ_j'''}{J_j^2\tilde{\omega}} - \frac{1}{2}i\tilde{\omega}J_j'\Big) + (\Delta\zeta)^3\Big(-\frac{5}{24}\frac{J_j'''}{J_j} - \frac{1}{24}\frac{iJ_j''''}{J_j^2\tilde{\omega}} + \frac{3}{8}i\tilde{\omega}J_j'' + \frac{1}{4}i\tilde{\omega}^2J_jJ_j'\Big) \tag{4.108}$$

$$M_{22} = \Big(1 + (\Delta\zeta)\Big(-\frac{1}{4}\frac{iJ_j''}{J_j^2\tilde{\omega}} - i\tilde{\omega}J_j\Big) + (\Delta\zeta)^2\Big(-\frac{1}{8}\frac{iJ_j'''}{J_j^2\tilde{\omega}} - \frac{1}{2}\tilde{\omega}^2J_j^2 - \frac{1}{2}i\tilde{\omega}J_j' - \frac{J_j''}{4J_j}\Big) + (\Delta\zeta)^3\Big(-\frac{1}{6}\frac{J_j'''}{J_j} - \frac{1}{8}i\tilde{\omega}J_j'' + -\frac{1}{2}\tilde{\omega}^2J_jJ_j' - \frac{1}{24}\frac{iJ_j''''}{J_j^2\tilde{\omega}} + \frac{1}{6}i\tilde{\omega}^3J_j^3\Big)\Big). \tag{4.109}$$

To calculate local error terms, analytical coefficients at adjacent surfaces are taken and propagated with the change-of-basis matrix, M, and compared to the expected analytical coefficients at the same adjacent surfaces.

4.1.3 Local Error Terms

The exact velocity and pressure of the acoustic signal at each analysis surface can be expressed as the eigenvectors multiplied by complex pressure amplitudes, p_{ds} and p_{us},

$$\begin{pmatrix} u_{exact_j} \\ p_{exact_j} \end{pmatrix} = \mathbf{E}_j \begin{pmatrix} p_{ds,j} \\ p_{us,j} \end{pmatrix}. \tag{4.110}$$

In this case of 1D propagation without mean flow, the exact pressure at any given position, surface j, is known analytically and is related to the input pressure, $p_{us,end}$; the frequency/ wave number, $\tilde{\omega}$; and the axial distance travelled, (Δz),

$$p_{exact_j} = p_{us,end}e^{i\tilde{\omega}\Delta z}. \tag{4.111}$$

In the curvilinear system the tensor velocity and pressure have a curvilinear direction so must include Jacobian terms

$$u^* = Ju, u^* = -p^*J. \tag{4.112}$$

The physical velocity and pressure, however, do not have this dependence on J, thus, the physical velocity $u_{exact} = -p_{exact}$ and

$$\begin{pmatrix} u_{exact_j} \\ p_{exact_j} \end{pmatrix} = \begin{pmatrix} -p_{exact_j} \\ p_{exact_j} \end{pmatrix} = \begin{pmatrix} -p_{us,end} e^{i\tilde{\omega}(\Delta z)_j} \\ p_{us,end} e^{i\tilde{\omega}(\Delta z)_j} \end{pmatrix}. \tag{4.113}$$

Substituting this into Eqn. 4.110 ,

$$\begin{pmatrix} -p_{us,end} e^{i\tilde{\omega}(\Delta z)_j} \\ p_{us,end} e^{i\tilde{\omega}(\Delta z)_j} \end{pmatrix} = \mathbf{E}_{physical_j} \begin{pmatrix} p_{ds,j} \\ p_{us,j} \end{pmatrix}. \tag{4.114}$$

Multiplying both sides of Eqn. 4.114 by the inverse of the 'physical' eigenvectors gives an expression for the exact complex amplitudes that can be found analytically

$$\mathbf{E}^{-1}_{physical_j} \begin{pmatrix} -p_{us,end} e^{i\tilde{\omega}(\Delta z)_j} \\ p_{us,end} e^{i\tilde{\omega}(\Delta z)_j} \end{pmatrix} = \mathbf{E}^{-1}_{physical_j} \mathbf{E}_{physical_j} \begin{pmatrix} p_{ds,j} \\ p_{us,j} \end{pmatrix} \tag{4.115}$$

$$= \begin{pmatrix} p_{ds,j} \\ p_{us,j} \end{pmatrix}. \tag{4.116}$$

Substituting the approximation of the inverse eigenvector, to first order, leads to

$$\begin{pmatrix} p_{ds,j} \\ p_{us,j} \end{pmatrix} = \frac{1}{2} \begin{pmatrix} 1 & (1 - i\sigma_j) \\ -1 & (1 + i\sigma_j) \end{pmatrix} \begin{pmatrix} -p_{us,end} e^{i\tilde{\omega}(\Delta z)_j} \\ p_{us,end} e^{i\tilde{\omega}(\Delta z)_j} \end{pmatrix} \tag{4.117}$$

$$= \begin{pmatrix} -\frac{i\sigma_j}{2} p_{end} e^{i\tilde{\omega}(\Delta z)_j} \\ (1 + \frac{i\sigma_j}{2}) p_{end} e^{i\tilde{\omega}(\Delta z)_j} \end{pmatrix}. \tag{4.118}$$

Therefore, the expected pressure amplitudes, $p_{us,1}$ and $p_{ds,2}$ (assuming no error) are

$$p_{us,1} = (1 + \frac{i\sigma_1}{2}) \tag{4.119}$$

$$= (1 + \frac{1}{4} \frac{iJ_1'}{J_1^2 \tilde{\omega}}) \tag{4.120}$$

$$p_{ds,2} = \frac{-i\sigma_2}{2} \tag{4.121}$$

$$= -\frac{1}{4} \frac{iJ_1'}{J_1^2 \tilde{\omega}} + (\Delta\zeta)\big(-\frac{1}{4} \frac{iJ_1''}{J_1^2 \tilde{\omega}} + \frac{1}{4} \frac{J_1'}{J_1} \big) + (\Delta\zeta)^2 \big(-\frac{1}{8} \frac{iJ_1'''}{J_1^2 \tilde{\omega}} + \frac{1}{4} \frac{J_1''}{J_1} + \frac{1}{8} i\tilde{\omega} J_1' \big)$$

$$+ (\Delta\zeta)^3 \big(-\frac{1}{24} \frac{iJ_1''''}{J_1^2 \tilde{\omega}} + \frac{1}{8} \frac{J_1'''}{J_1} + \frac{1}{8} i\tilde{\omega} J_1'' - \frac{1}{24} \tilde{\omega}^2 J_1 J_1' \big). \tag{4.122}$$

The expected pressure coefficients $p_{us,2}$, $p_{ds,1}$, found in the same way as above, are substituted as c_{2l} and c_{1r} and propagated by matrix M to estimate numerical coefficients c_{2r} and c_{1l}

$$\begin{pmatrix} c_{2r} \\ c_{1l} \end{pmatrix} = M \begin{pmatrix} -\frac{1}{2} i\sigma_j e^{i\tilde{\omega}(\Delta z)_j} \\ (1 + \frac{1}{2} i\sigma_{(j+1)}) e^{i\tilde{\omega}(\Delta z)_{(j+1)}} \end{pmatrix}. \tag{4.123}$$

Setting $(\Delta z)_j = 1$ and for $(\Delta z)_{(j+1)}$ expanding to give the exponent $(J\Delta\zeta + \frac{1}{2}J'_j(\Delta\zeta)^2 + \frac{1}{6}J''_j(\Delta\zeta)^3)$.

Note, as surfaces 1 and 2 are considered, all terms $(J, J', \sigma_j ...)$ are written without subscripts but are all with respect to surface $j = 1$.

Expanding the $\sigma_{(j+1)}$ term and simplifying by using the identities for σ (Eqn. 4.91) gives

$$c_{1r} = -\frac{1}{4}\frac{iJ'}{J^2\tilde{\omega}} \tag{4.124}$$

$$\begin{aligned} c_{2l} =& \Big(1 + \frac{i}{2}\big(\sigma + \sigma'\Delta\zeta + \frac{1}{2}\sigma''(\Delta\zeta)^2 + \frac{1}{6}\sigma'''(\Delta\zeta)^3\big)\Big) \\ & \times \Big(1 + i\tilde{\omega}J\Delta\zeta + (\Delta\zeta)^2)(\frac{1}{2}i\tilde{\omega}J' - \frac{1}{2}\tilde{\omega}^2J^2) + (\Delta\zeta)^3(\frac{1}{6}i\tilde{\omega}J'' - \frac{1}{6}i\tilde{\omega}^2J^2 - \frac{1}{2}\tilde{\omega}^2JJ')\Big) \\ =& \Big(1 + \frac{1}{4}\frac{iJ'}{\tilde{\omega}J^2} + (\Delta\zeta)\big(i\tilde{\omega}J + \frac{1}{4}\frac{iJ''}{J^2\tilde{\omega}} - \frac{1}{4}\frac{J'}{J}\big) + (\Delta\zeta)^2\big(\frac{3}{8}i\tilde{\omega}J' - \frac{1}{2}\tilde{\omega}^2J^2 + \frac{1}{8}\frac{iJ'''}{J^2\tilde{\omega}} - \frac{1}{4}\frac{J''}{J}\big) \\ & + (\Delta\zeta)^3\big(\frac{1}{24}i\tilde{\omega}J'' - \frac{1}{6}i\tilde{\omega}^3J^2 - \frac{1}{2}\tilde{\omega}JJ' - \frac{1}{24}\tilde{\omega}^2J' + \frac{1}{24}\frac{iJ''''}{J^2\tilde{\omega}} - \frac{1}{8}\frac{J'''}{j}\big)\Big). \end{aligned} \tag{4.125}$$

The local transfer matrix Q is

$$Q = \begin{pmatrix} c_{2r} \\ c_{1l} \end{pmatrix} = M \begin{pmatrix} c_{1r} \\ c_{2l} \end{pmatrix} = \begin{pmatrix} M_{11}c_{1r} & M_{12}c_{2l} \\ M_{21}c_{1r} & M_{22}c_{2l} \end{pmatrix}. \tag{4.126}$$

To approximate the entries of Q to first order, the first order approximations of M and the coefficients calculated previously are used

$$\begin{aligned} Q_{11} =& M_{11}c_{1r} \\ =& \Big[1 + (\Delta\zeta)\big(-i\tilde{\omega}J - \frac{1}{4}\frac{iJ''}{J^2\tilde{\omega}}\big) + (\Delta\zeta)^2\big(-\frac{1}{8}\frac{iJ'''}{J^2\tilde{\omega}} - \frac{1}{2}\tilde{\omega}^2J^2 - \frac{1}{2}\frac{J''}{J} - \frac{1}{2}i\tilde{\omega}J'\big) \\ & + (\Delta\zeta)^3\big(-\frac{1}{2}\tilde{\omega}^2JJ' - \frac{1}{12}\frac{J'''}{J} - \frac{1}{8}i\tilde{\omega}J'' - \frac{1}{24}\frac{iJ''''}{J^2\tilde{\omega}} + \frac{1}{6}i\tilde{\omega}^3J^3\big)\Big] \times \Big[-\frac{1}{4}\frac{J'}{J^2\tilde{\omega}}\Big] \\ =& \Big(-\frac{1}{4}\frac{iJ'}{J^2\tilde{\omega}} - (\Delta\zeta)\frac{1}{4}\frac{J'}{J} + (\Delta\zeta)^2\frac{1}{8}i\tilde{\omega}J' + (\Delta\zeta)^3\frac{1}{24}\tilde{\omega}^2J'\Big). \end{aligned} \tag{4.127}$$

Similarly,

$$Q_{12} = \Big((\Delta\zeta)\big(\frac{1}{2}\frac{J'}{J} - \frac{1}{4}\frac{iJ''}{\tilde{\omega}J^2}\big) + (\Delta\zeta)^2\big(-\frac{1}{8}\frac{J'''}{J^2\tilde{\omega}} + \frac{1}{4}\frac{J''}{J}\big) + (\Delta\zeta)^3\big(-\frac{1}{12}\frac{J'''}{J} - \frac{1}{24}\frac{iJ''''}{J^2\tilde{\omega}}\Big) \tag{4.128}$$

$$Q_{21} = 0 \tag{4.129}$$

$$Q_{22} = 1 + \frac{1}{4}\frac{iJ'}{\tilde{\omega}J^2} + (\Delta\zeta)^3\big(-\frac{1}{12}i\tilde{\omega}J'' - \frac{1}{24}\frac{J'''}{J}\big). \tag{4.130}$$

Therefore, the coefficients given by propagating the analytical coefficients, c_{1r}, C_{2l} with the change of basis matrix are

$$\begin{aligned} c_{2r} =& Q_{11} + Q_{12} = -\frac{1}{4}\frac{iJ'}{J^2\tilde{\omega}} + (\Delta\zeta)\big(\frac{1}{4}\frac{J'}{J} - \frac{1}{4}\frac{iJ''}{\tilde{\omega}J^2}\big) \\ &+ (\Delta\zeta)^2\big(\frac{1}{8}i\tilde{\omega}J' - \frac{1}{8}\frac{J'''}{J^2\tilde{\omega}} + \frac{1}{4}\frac{J''}{J}\big) + (\Delta\zeta)^3\big(\frac{1}{24}\tilde{\omega}^2JJ' - \frac{1}{12}\frac{J'''}{J} - \frac{1}{24}\frac{iJ''''}{J^2\tilde{\omega}}\big) \\ c_{1l} =& Q_{21} + Q_{22} = 1 + \frac{1}{4}\frac{iJ'}{\tilde{\omega}J^2} + (\Delta\zeta)^3\big(-\frac{1}{12}i\tilde{\omega}J'' - \frac{1}{24}\frac{J'''}{J}\big). \end{aligned} \tag{4.131}$$

Now the local error terms can be calculated by comparing these coefficients with the analytical coefficients.

$$\begin{aligned} Error_{local,1l} = c_{1l} - p_{1,us} &= 1 + \frac{1}{4}\frac{iJ'}{\tilde{\omega}J^2} + (\Delta\zeta)^3\big(-\frac{1}{12}i\tilde{\omega}J'' - \frac{1}{24}\frac{J'''}{J}\big) - \big(1 + \frac{1}{4}\frac{iJ'}{\tilde{\omega}J^2}\big) \\ &= (\Delta\zeta)^3\big(-\frac{1}{12}i\tilde{\omega}J'' - \frac{1}{24}\frac{J'''}{J}\big). \end{aligned} \tag{4.132}$$

For the analytical coefficient $p_{2,ds}$ we must first expand the $2 = j + 1$ terms

$$\begin{aligned} p_{2,ds} = -\frac{1}{4}\frac{iJ'}{J^2\tilde{\omega}} &+ (\Delta\zeta)\big(-\frac{1}{4}\frac{iJ''}{J^2\tilde{\omega}} + \frac{1}{4}\frac{J'}{J}\big) + (\Delta\zeta)^2\big(-\frac{1}{8}\frac{iJ'''}{J^2\tilde{\omega}} + \frac{1}{4}\frac{J''}{J} + \frac{1}{8}i\tilde{\omega}J'\big) \\ &+ (\Delta\zeta)^3\big(-\frac{1}{24}\frac{iJ''''}{J^2\tilde{\omega}} + \frac{1}{8}\frac{J'''}{J} + \frac{1}{8}i\tilde{\omega}J'' - \frac{1}{24}\tilde{\omega}^2JJ'\big). \end{aligned} \tag{4.133}$$

Therefore,

$$\begin{aligned} Error_{local,2r} &= c_{2r} - p_{2,ds} \\ &= (\Delta\zeta)^3\big(-\frac{1}{24}\frac{J'''}{J} + \frac{1}{12}\tilde{\omega}^2JJ' - \frac{1}{8}i\tilde{\omega}J''\big). \end{aligned} \tag{4.134}$$

Here, two local error terms have been identified:

$$Error_{local,1l} = (\Delta\zeta)^3\big(-\frac{1}{12}i\tilde{\omega}J'' - \frac{1}{24}\frac{J'''}{J}\big) \tag{4.135}$$

$$Error_{local,2r} = (\Delta\zeta)^3\big(-\frac{1}{24}\frac{J'''}{J} + \frac{1}{12}\tilde{\omega}^2JJ' - \frac{1}{8}i\tilde{\omega}J''\big). \tag{4.136}$$

The two cumulative local errors consist of three leading order terms:

$$(\Delta\zeta)^3\tilde{\omega}^2 JJ' \tag{4.137}$$

$$(\Delta\zeta)^3 i\tilde{\omega}^2 J'' \tag{4.138}$$

$$(\Delta\zeta)^3 \frac{J'''}{J}. \tag{4.139}$$

4.2 Numerical Study

In this section a numerical study is presented, with the same conditions as presented in the error analysis.

4.2.1 Methodology

If the EAGCC method is implemented with a uniformly spaced mesh then it is believed that any error in the solution of the method is not a result of the propagation framework itself. This will be explored further in section 4.2.2.1. However, due to the complex geometry of intended applications of the method, such as aero-engine intakes, it is often not possible to use a regular equispaced mesh. Therefore, this chapter investigates the error created by the use of irregular meshes.

The numerical error in the propagation is expected to be dependent on the frequency of the input; as well as the mean mesh spacing and the rate of variation of the mesh spacing. The numerical test cases in this chapter have been designed to incorporate all these parameters. For the mesh-related parameters, this is achieved through the use of a Gaussian shift function described below. This study considers an upstream travelling wave on a one-dimensional mesh where the analysis surfaces [in this 1D case they are points] are not uniformly spaced throughout the duct.

The EAGCC method uses a curvilinear coordinate system. The mesh can be expressed with respect to orthogonal coordinates, (r, θ, z), and with respect to the pseudo-radial, circumferential and axial coordinates, (ξ, η, ζ). The Jacobian defines the transformation between the two coordinate systems. In this 1D case, the pseudo-axial spacing, $\Delta\zeta$, is considered as equispaced throughout. The orthogonal mesh is defined below, and the spacing is expressed as Δz.

Initially, the mesh consists of n+1 equispaced points, Fig. 4.1, then a proportion of the mesh points are shifted to the right, Fig. 4.2.

FIGURE 4.1: n+1 equispaced points on straight line

FIGURE 4.2: Equispaced points shifted, faded grey show equispaced placement, grey values denote amount shifted.

The distance they are shifted by gradually increases and then decreases, as shown in Fig. 4.2. This forces the spacing in z and ζ to differ; in turn forcing the Jacobian and derivatives of the Jacobian to change.

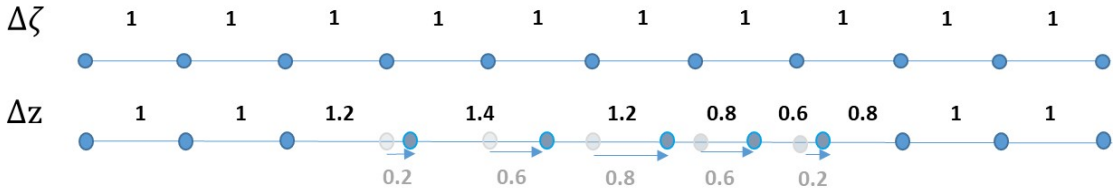

FIGURE 4.3: Equispaced (above) and shifted points (below) with the change in z and ζ noted in black

Fig. 4.3 demonstrates how the points get shifted and the Δz and $\Delta\zeta$ values for this example.

The distance by, and the overall proportion of the surfaces that are shifted, is determined by a chosen Gaussian shift function $f(x_i) = g_1 e^{-(\frac{x_i}{g_2})^2}$, where x_i is the position of the i^{th} equispaced point, $i \in [1, n+1]$, and g_1 and g_2 denote the 'Gaussian height' and 'Gaussian width' respectively.

This shift function represents a Gaussian profile, where the Gaussian width is comparable to the standard deviation of a traditional Gaussian distribution by $(g_2)^2 \approx 2\tilde{\sigma}^2$ and the Gaussian height simply gives the maximum distance by which the equispaced points are shifted.

The investigation looks at a one-dimensional duct of fixed length 1m and considers the four variables listed in Table. 6.1 below.

Fig. 4.4 shows the shift function, $f(x)$, plotted against the equispaced mesh positions, for every combination of Gaussian height, and Gaussian width at fixed spacing $\Delta\zeta = \frac{1}{128}$ from Table 6.1. The colours denote the Gaussian height and the line style denotes the Gaussian width, the wavenumber frequency does not alter the shift function as it is purely mesh-related.

The variation in the Gaussian profile for different $\Delta\zeta$ spacings are shown in Fig. 4.5.

TABLE 4.1: Variables included in numerical study

Description	Variable	Values	Units
Free field wavenumber (normalised)	$\tilde{\omega} = \frac{\omega}{c}$	4,8,16,32	m^{-1}
Equispaced spacing	$\Delta\zeta$	$\frac{1}{128}, \frac{1}{64}, \frac{1}{32}, \frac{1}{16}$	m
Gaussian height	g_1	0.001, 0.002, 0.004, 0.008, 0.016	m
Gaussian width	g_2	0.025, 0.05, 0.075, 0.1, 0.125, 0.15, 0.175	m

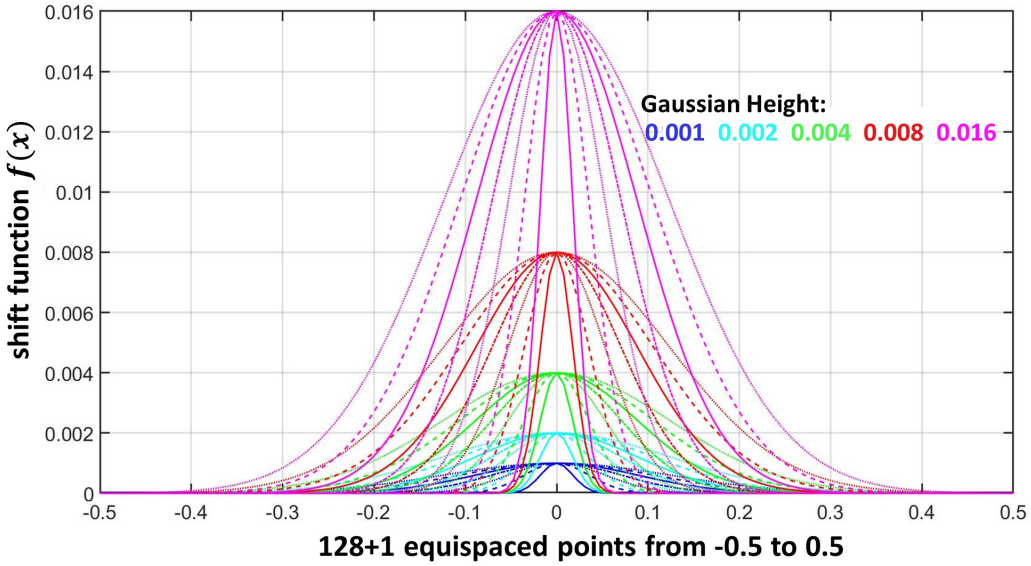

FIGURE 4.4: The equispaced points against the shift function resulting in a Gaussian profile. Fixed $\Delta\zeta = \frac{1}{128}$, line style represents the Gaussian width.

4.2.2 Numerical Results

This section discusses the results of the numerical error study. First the globally occurring error from the results is explored; then the local error terms relating the numerical results to the analytically derived error from the Error Analysis section are shown; and finally, it is shown how the numerical results can be predicted by propagating the local error terms determined by the error analysis.

4.2.2.1 Global error

The error metric used throughout this section is the root mean squared error of the numerical pressure when calculated at the mesh points, compared with the exact solution $p_{analytical} = p_{end}e^{i\tilde{\omega}\Delta z}$. All the figures in this section utilise a log scale.

Equispaced Mesh

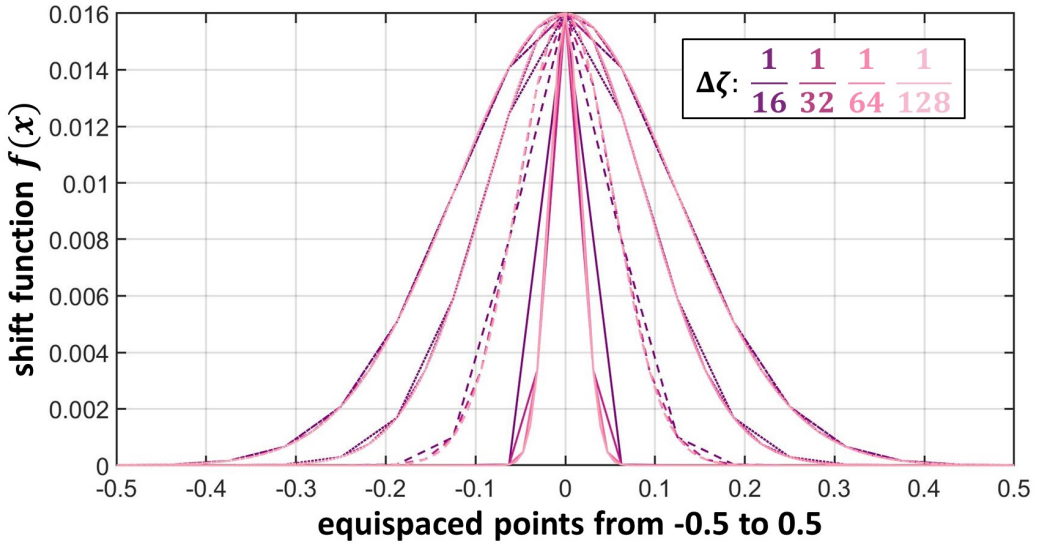

FIGURE 4.5: This figure plots the equispaced points against the shift function for fixed Gaussian height 0.016. The line style represents the Gaussian width: 0.025 0.075 0.125 0.175 solid to dotted respectively. The profiles for all $\Delta\zeta$ are over-layed and shown in colour, from darker to lighter $\Delta\zeta = \frac{1}{16}, \frac{1}{32}, \frac{1}{64}, \frac{1}{128}$ respectively.

When the equispaced mesh in z and ζ was used, the EAGCC method produced a result close to the exact solution. There is however a small, but negligible, numerical error given in this case, proportional to the frequency, $\tilde{\omega}$. This can be seen in Figs. 4.6 and 4.7. In this second figure, Fig. 4.7, the error is the same for all $\Delta\zeta$ therefore the small numerical error given in this base-case is not mesh dependent.

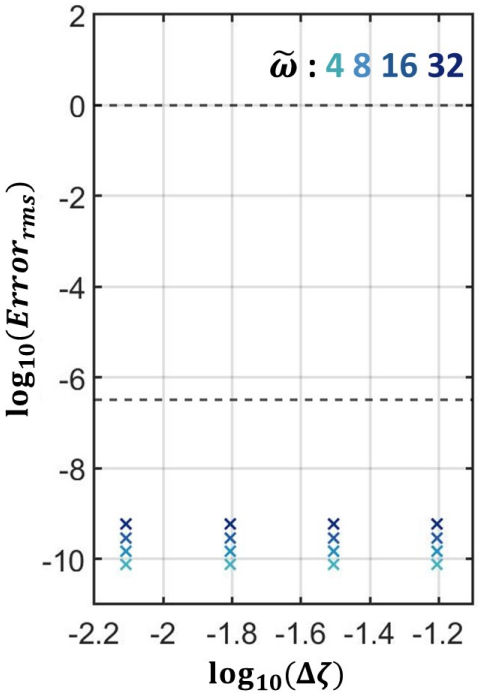

FIGURE 4.6: Root mean squared error against $\Delta\zeta$ on log_{10} scale. Dashed lines show the range of the error found in the numerical study, for the test cases with non-equispaced mesh points

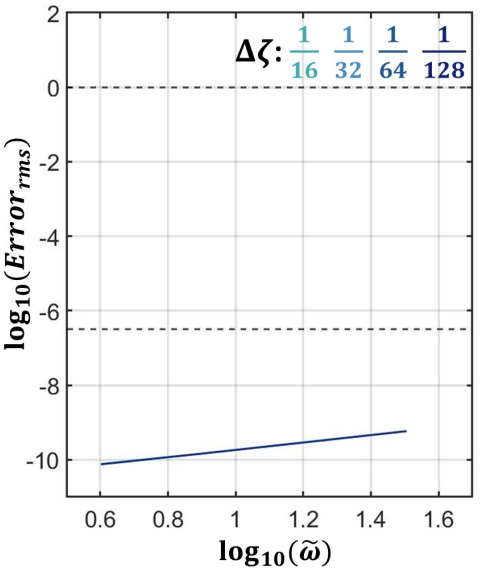

FIGURE 4.7: Root mean squared error against $\tilde{\omega}$ on log_{10} scale. Dashed lines show the range of the error found in the numerical study, for the test cases with non-equispaced mesh points

Frequency

Fig. 4.8 plots the error against the frequency for test cases with wide Gaussian widths

$g_2 = 0.125$ and $g_2 = 0.175$ with a coarse mesh spacing $\Delta\zeta = \frac{1}{16}$ and finer mesh spacing $\Delta\zeta = \frac{1}{64}$. For a fixed $\Delta\zeta$ the error is smaller for the wider Gaussian width, g_2; the cases with the coarser mesh spacing and narrower Gaussian width are shown to have the largest error. This is because the combination of the two results in more abrupt changes to the mesh distribution and therefore, the Jacobian and derivatives of the Jacobian.

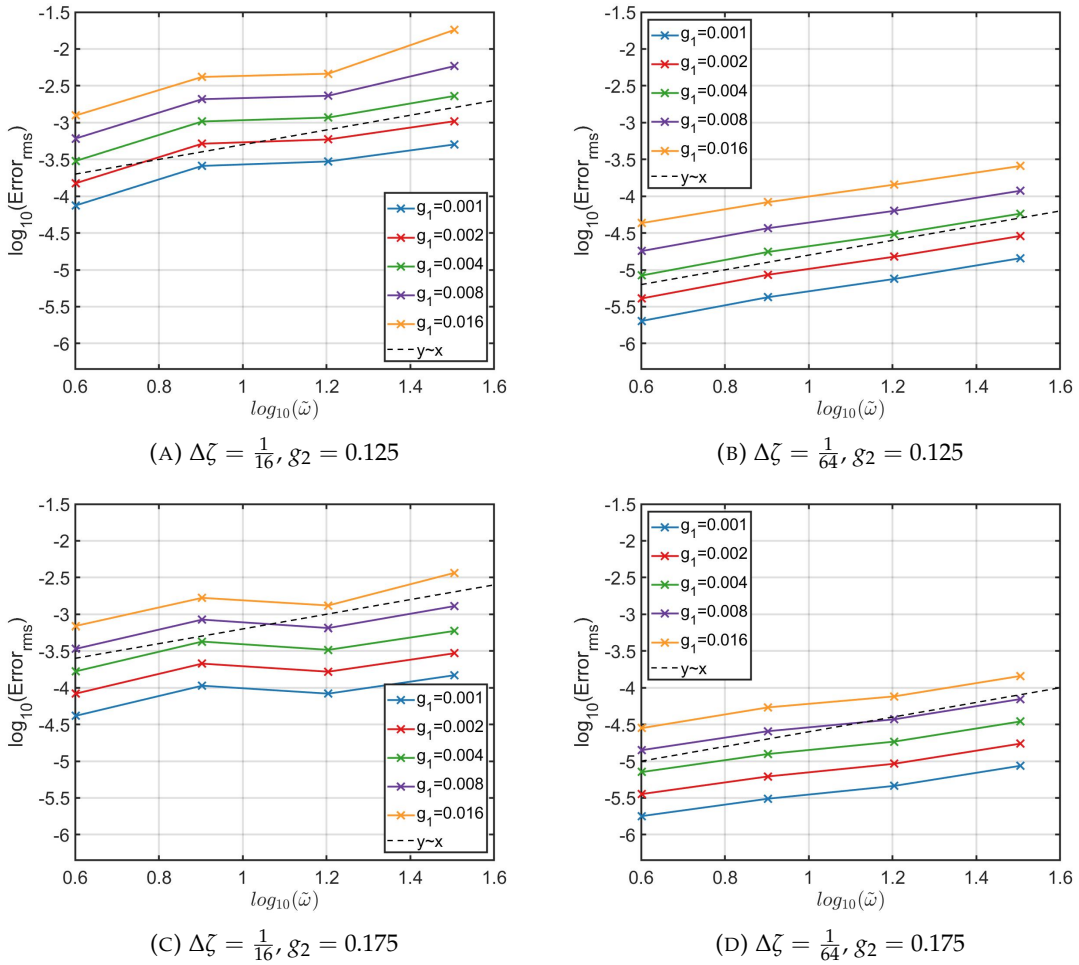

(A) $\Delta\zeta = \frac{1}{16}$, $g_2 = 0.125$

(B) $\Delta\zeta = \frac{1}{64}$, $g_2 = 0.125$

(C) $\Delta\zeta = \frac{1}{16}$, $g_2 = 0.175$

(D) $\Delta\zeta = \frac{1}{64}$, $g_2 = 0.175$

FIGURE 4.8: Error against Frequency on a log_{10} scale. Lines of constant Gaussian height, g_1.

For wide Gaussian widths, and small $\Delta\zeta$ (finer mesh spacing), the error is proportional to the frequency and increases with Gaussian height. For larger $\Delta\zeta$ (coarser mesh spacing) there is still a general positive relationship between the error and frequency but it is weaker.

Mesh spacing

Fig. 4.9 shows the error for fixed Gaussian width, $g_2 = 0.05$, at each of the four frequencies. At the smallest frequency $\tilde{\omega} = 4$ and the tallest Gaussian height $g_1 = 0.16$ the error is much higher, particularly for the finer mesh spacing. This is believed to be due to the severe change in the mesh spacing over this narrow Gaussian width and the smaller the $\Delta\zeta$ the bigger range in the Jacobian and higher derivatives, growing with order of derivative.

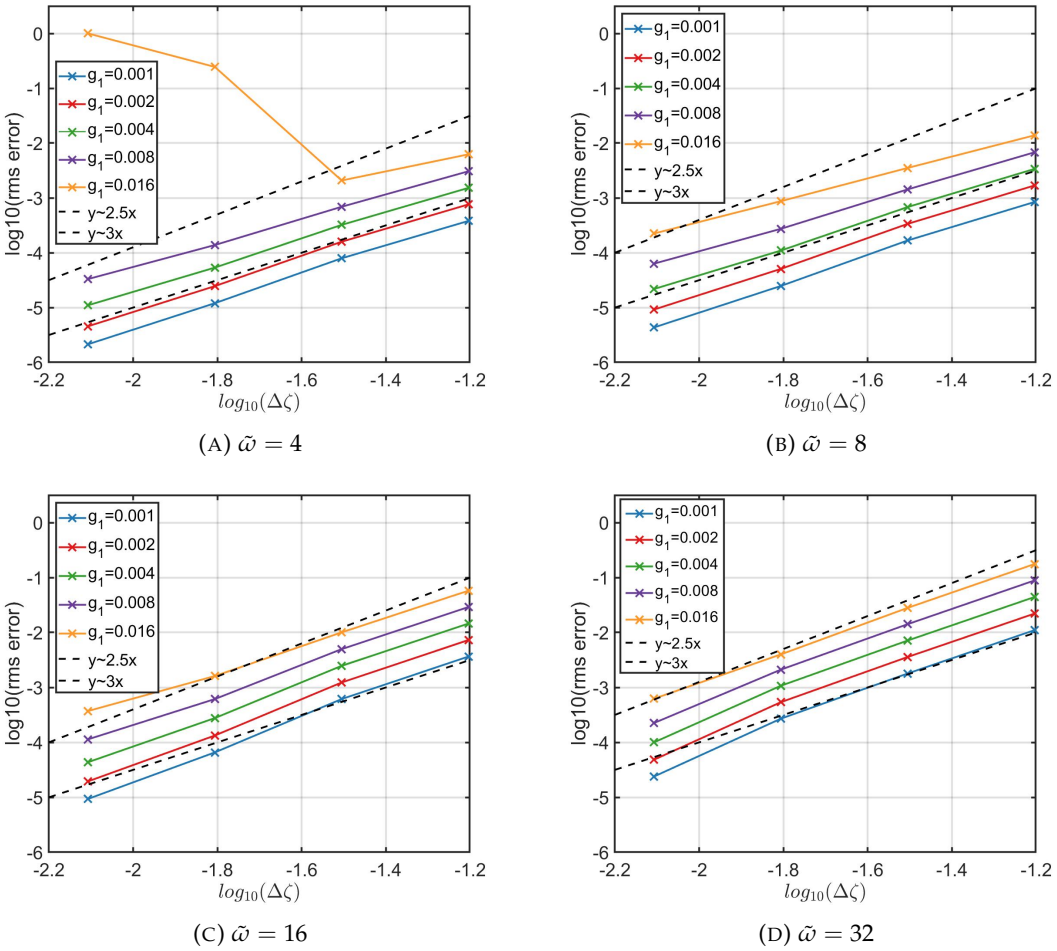

(A) $\tilde{\omega} = 4$ (B) $\tilde{\omega} = 8$

(C) $\tilde{\omega} = 16$ (D) $\tilde{\omega} = 32$

FIGURE 4.9: Error against $\Delta\zeta$ on a log_{10} scale. Fixed Gaussian width, $g_2 = 0.05$. Lines of constant Gaussian height, g_1.

Fig. 4.10 shows the error for test cases with fixed $g_2 = 0.075$. The error still looks mostly proportional to $\Delta\zeta^x$, with the exception of higher frequency and larger $\Delta\zeta$, where it is possible the constant of proportionality changes but as there is not enough data to determine this it could also be an effect of something else. In general, the data shows the error when considering constant Gaussian height to be proportional to $(\Delta\zeta)^x$ where $2 \leq x \leq 3$.

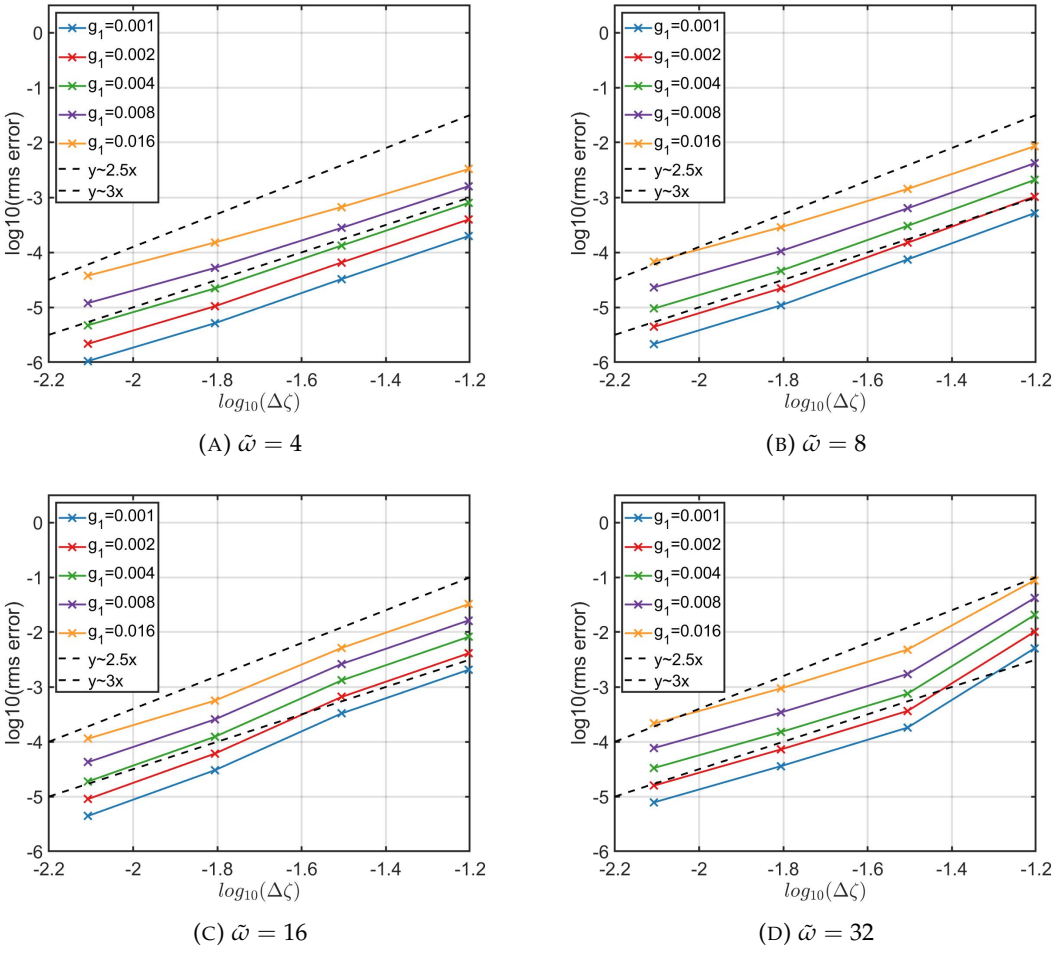

(A) $\tilde{\omega} = 4$ (B) $\tilde{\omega} = 8$

(C) $\tilde{\omega} = 16$ (D) $\tilde{\omega} = 32$

FIGURE 4.10: Error against $\Delta\zeta$ on a log_{10} scale. Fixed Gaussian width, $g_2 = 0.075$. Lines of constant Gaussian height, g_1.

Throughout all Figs. 4.8 to 4.10 the error increases with Gaussian height, g_1 and all Gaussian heights are in relative proportion (equispaced in the figures). This is not the case when considering Gaussian width.

Gaussian width

Figs. 4.11 and 4.12 show the error against Gaussian width for cases with fixed $\Delta\zeta = \frac{1}{16}$ and $\Delta\zeta = \frac{1}{32}$, respectively.

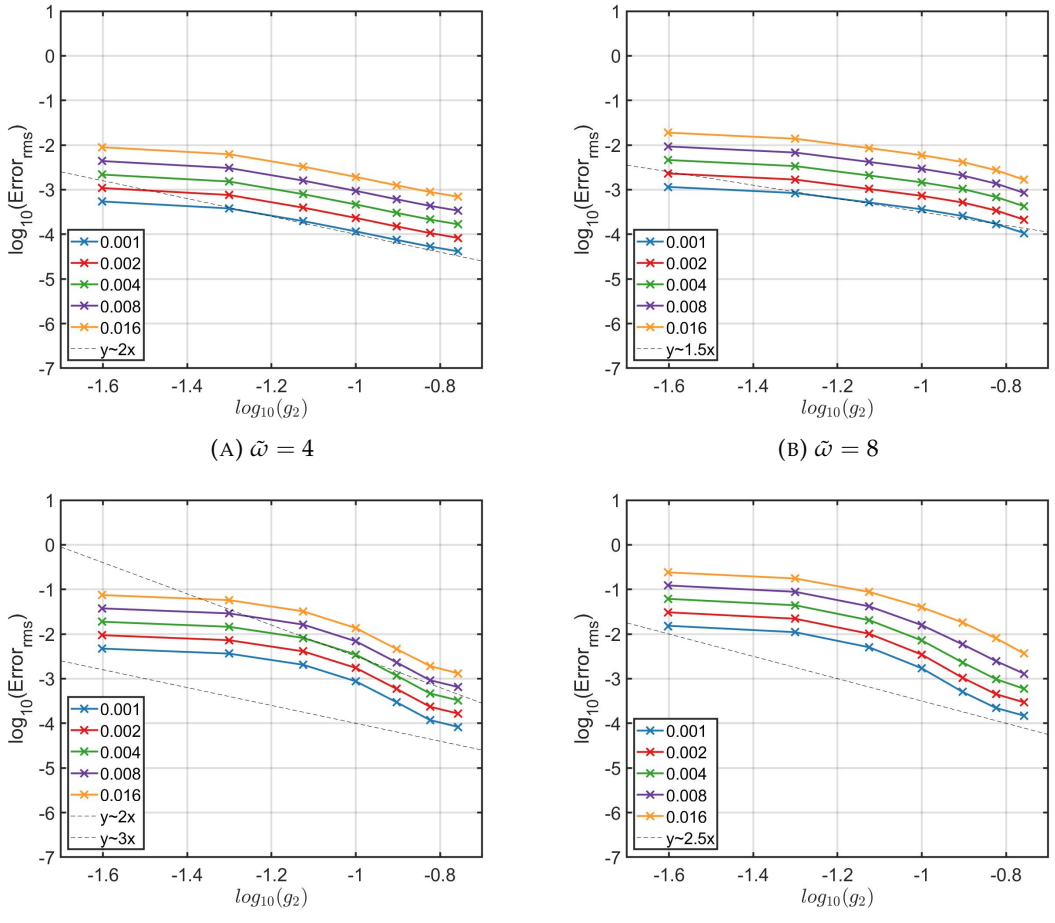

(A) $\tilde{\omega} = 4$

(B) $\tilde{\omega} = 8$

(C) $\tilde{\omega} = 16$

(D) $\tilde{\omega} = 32$

FIGURE 4.11: Error against Gaussian Width g_2 on a log_{10} scale. Fixed $\Delta\zeta = \frac{1}{16}$. Lines of constant Gaussian height, g_1.

The error decreases as Gaussian width increases. The error also decreases with mesh spacing $\Delta\zeta$ and increases with Gaussian height and frequency as seen previously.

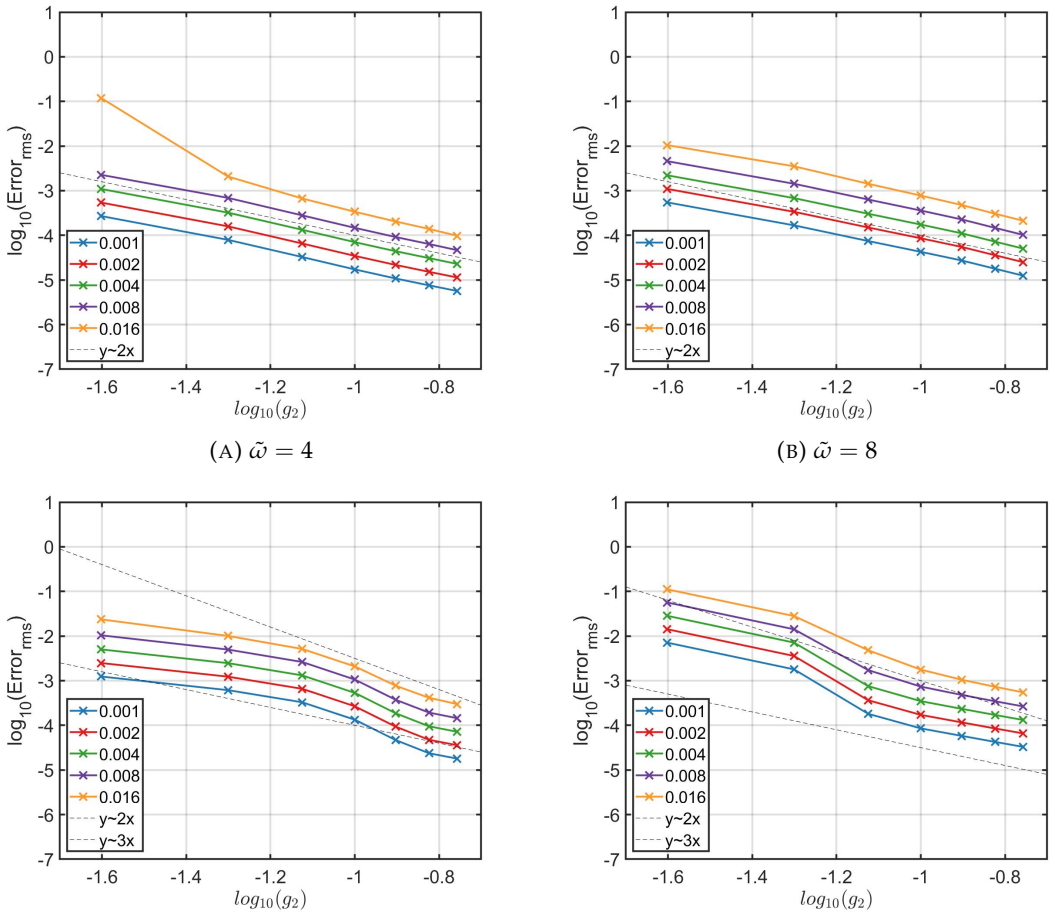

(A) $\tilde{\omega} = 4$

(B) $\tilde{\omega} = 8$

(C) $\tilde{\omega} = 16$

(D) $\tilde{\omega} = 32$

FIGURE 4.12: Error against Gaussian Width g_2 on a log_{10} scale. Fixed $\Delta\zeta = \frac{1}{32}$. Lines of constant Gaussian height, g_1.

Figs. 4.13 and 4.14 show the error against Gaussian width for $\Delta\zeta = \frac{1}{64}$ and $\Delta\zeta = \frac{1}{128}$ respectively.

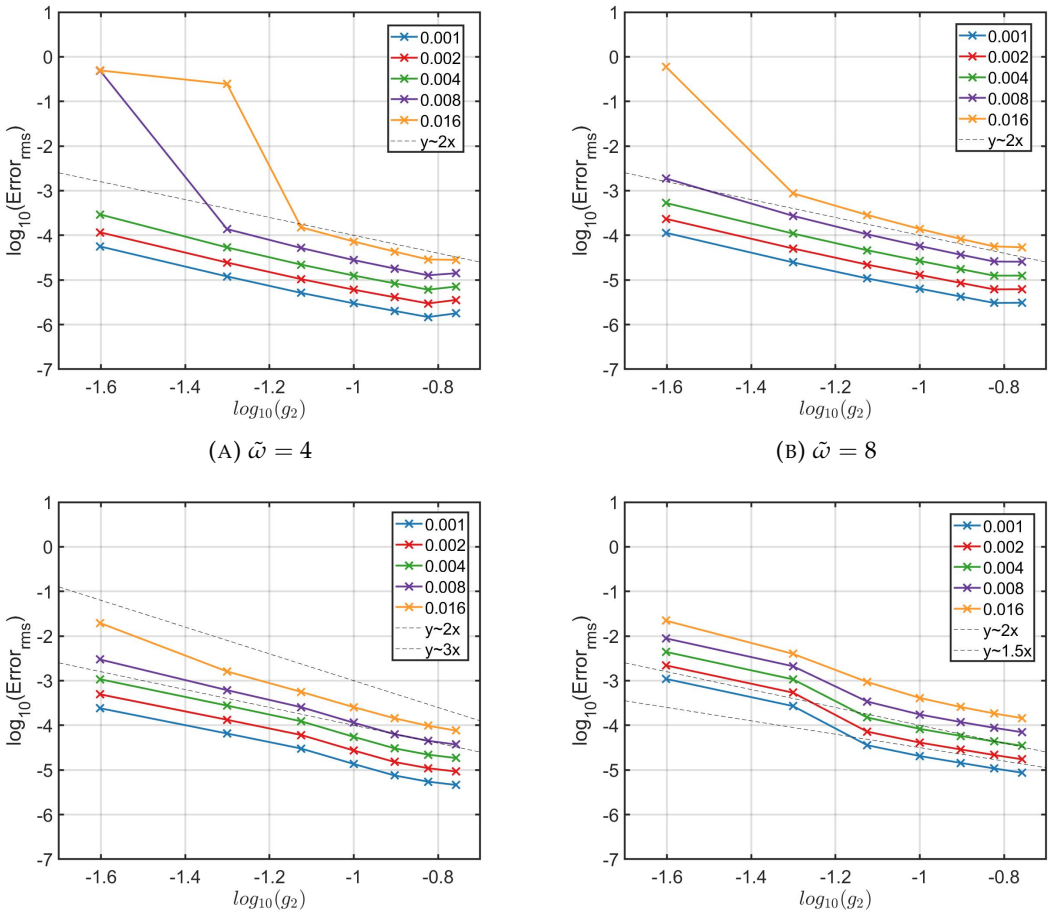

(A) $\tilde{\omega} = 4$

(B) $\tilde{\omega} = 8$

(C) $\tilde{\omega} = 16$

(D) $\tilde{\omega} = 32$

FIGURE 4.13: Error against Gaussian Width g_2 on a log_{10} scale. Fixed $\Delta\zeta = \frac{1}{64}$. Lines of constant Gaussian height, g_1.

The error is much larger at the smallest Gaussian widths coupled with larger Gaussian height, particularly in cases with small frequency (because frequency is low so the mesh-related error is more dominant) and at smaller mesh spacing, $\Delta\zeta$.

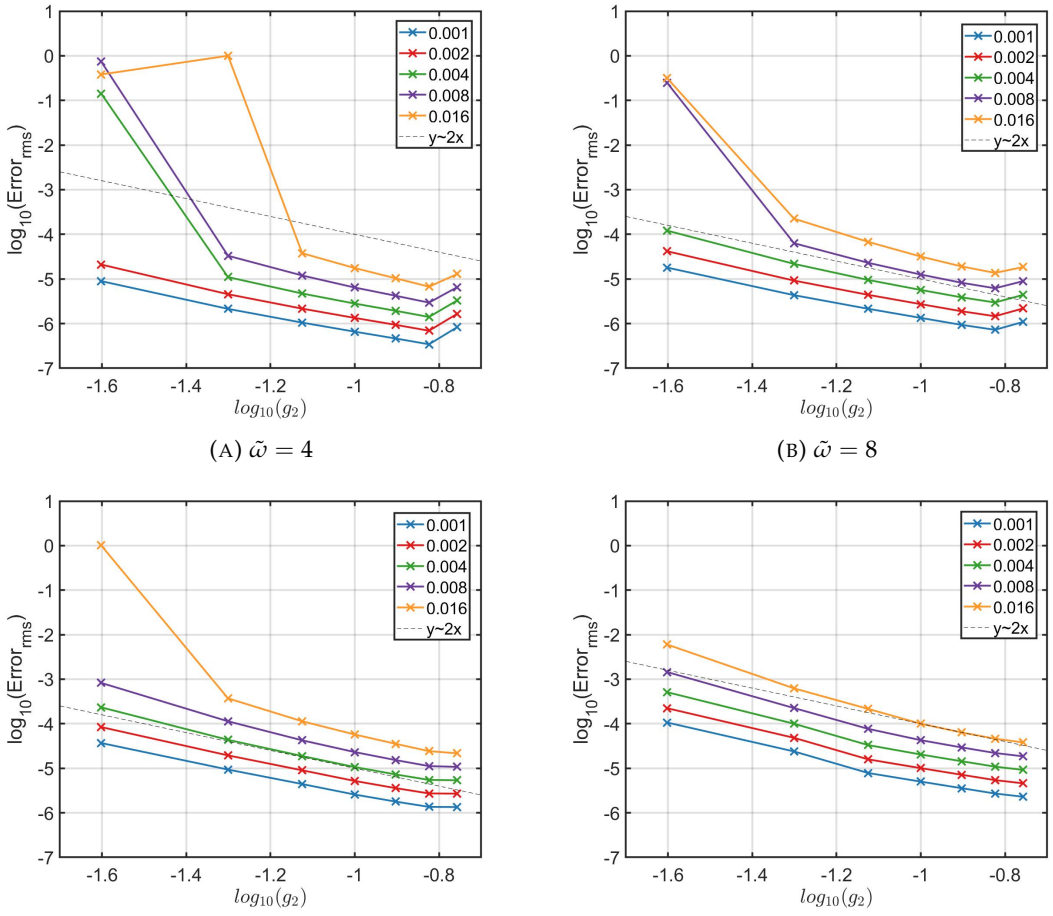

(A) $\tilde{\omega} = 4$ (B) $\tilde{\omega} = 8$

(C) $\tilde{\omega} = 16$ (D) $\tilde{\omega} = 32$

FIGURE 4.14: Error against Gaussian Width g_2 on a log_{10} scale. Fixed $\Delta\zeta = \frac{1}{128}$. Lines of constant Gaussian height, g_1.

Although the error generally decreases as Gaussian width increase, there are some exceptions seen at smaller frequencies and mesh spacing, Figs. 4.13 4.14, where there is a small increase in error at the largest Gaussian width. As the Gaussian width increases the proportion of the mesh that is shifted, this can allow for the change to be more gradual, hence reducing the global error. However, it is possible that if the Gaussian width is too wide there may not be a large enough proportion of equispaced points for the variation in mesh to reach equilibrium.

Overall, the error is negatively related to the Gaussian width, the general gradient varies between 1 and 3.5 and can often be higher for lower Gaussian width and lower for larger Gaussian widths. In general the error is related to the Gaussian width squared as shown by the $y = 2x$ trend lines.

All data

When considering all the data, a good representation of the error is given by

$$(\Delta\zeta)^3\tilde{\omega}\frac{g_1}{(g_2)^2}. \tag{4.140}$$

This is illustrated in Fig. 4.15 and will be investigated further in the next section.

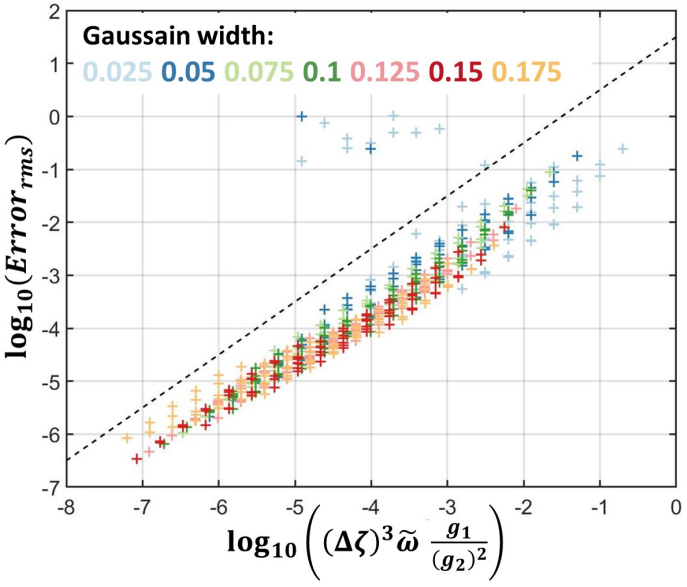

FIGURE 4.15: Scatter plot of the $Error_{rms}$ vs $(\Delta\zeta)^3\tilde{\omega}\frac{g_1}{(g_2)^2}$ on log_{10} scale

Fig. 4.15 includes all of the results from the numerical study, all three parts of this equation $(\Delta\zeta)^3$, $\tilde{\omega}$, and $\frac{g_1}{(g_2)^2}$ have been shown to individually relate globally to the error. Furthermore they relate to terms that are contained in the local error terms found in the error analysis. The anomalous data is at small Gaussian widths coupled with large Gaussian heights, therefore the mesh definition is poor resulting in much greater error.

The $(\Delta\zeta)^3$ part is consistent throughout all the local error terms found and is shown to be globally related to the error, Figs. 4.9 and 4.10. Frequency is also found in some of the local error terms and has also been shown to be related to the global error, Fig. 4.8. The error has also been shown to relate inversely to the Gaussian width squared, Figs. 4.11 to 4.14, and increase with Gaussian height.

Furthermore, the $\frac{g_1}{(g_2)^2}$ term is expected to scale with J and successive derivatives. The reasoning for this is as follows, firstly increasing the Gaussian height parameter increases the maximum J value. In addition, the smaller the Gaussian width then the greater the J' term as the change in J will be less gradual. From here it can be seen that the greatest value of $\frac{g_1}{(g_2)^2}$ would result from the maximum g_1 and minimum g_2 which

would also be expected to produce the greatest J, J'... (all assuming the $\Delta\zeta$ term is fixed). Therefore, these terms are expected to approximately scale.

4.2.2.2 Local Error

In the previous section Gaussian width and height terms were used as a proxy for the local error terms contained in $Error_{local,1l}$ and $Error_{local,2r}$ that were approximated in the error analysis. In this section, the actual derivatives of the Jacobian have been calculated in order to predict the error terms. The three local error terms have been propagated numerically for the specific test cases, giving the magnitude of all three terms along the duct (all pseudo-axial, ζ, positions).

In test cases where the frequency is small, such that $\tilde{\omega}^2 J' < J'''$, the first error term will not be prominent and the most dominant will be the third. As seen in Fig. 4.16 where $\tilde{\omega} = 4$. Therefore the first error term, seen exclusively in the right-running error Fig. 4.16, is particularly small and then the second error term is notably smaller than the third error term, the difference is bigger in the left-running error, Fig. 4.16. Contrast this with the same test-case parameters for $\Delta\zeta$,g_1, and g_2 but large $\tilde{\omega}$; where the first and second error terms are much more prominent. For the right-running error the first and second terms are both prominent with the third error term not negligible but smaller than the other two Fig. 4.17. For the left-running error the second error term, containing $\tilde{\omega}^2$ is the largest and dominant error term, Fig. 4.17.

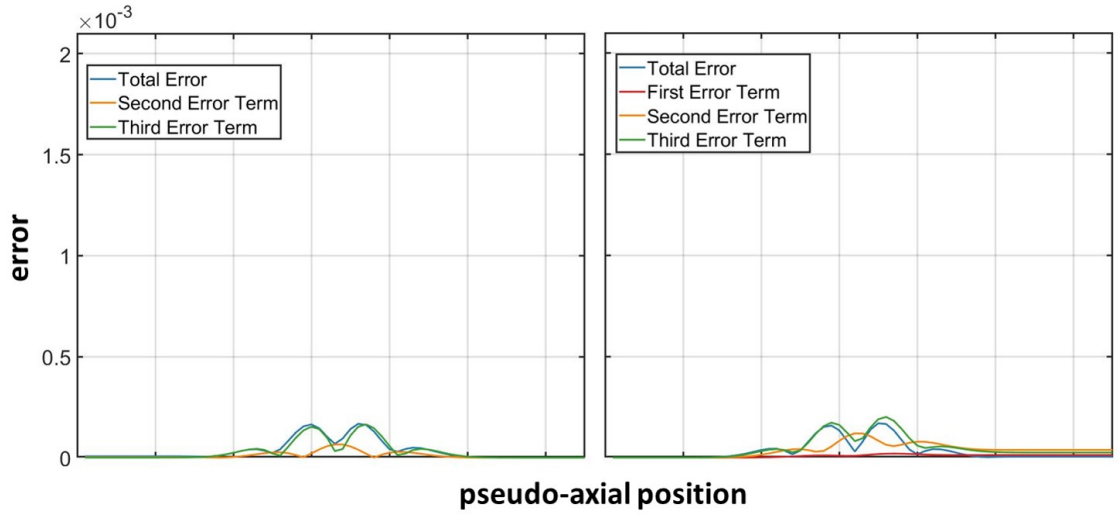

FIGURE 4.16: Left-hand side is the left travelling local error and on right-hand side is the right travelling local error, broken into total and three error terms for: $\tilde{\omega} = 4, \Delta\zeta = \frac{1}{64}, g_1 = 0.004, g_2 = 0.1$

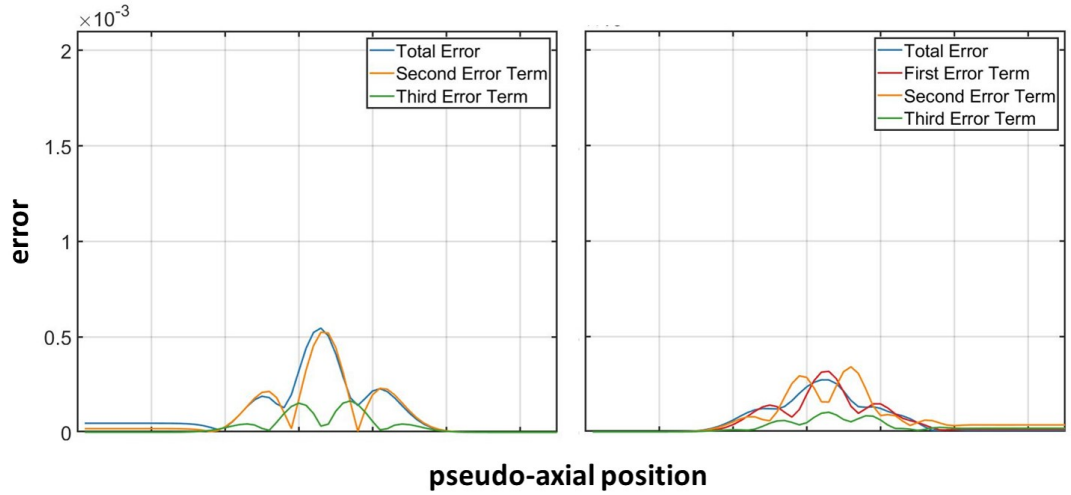

FIGURE 4.17: Left-hand side is the left travelling local error and on right-hand side is the right travelling local error, broken into total and three error terms for: $\tilde{\omega} = 32, \Delta\zeta = \frac{1}{64}, g_1 = 0.004, g_2 = 0.1$

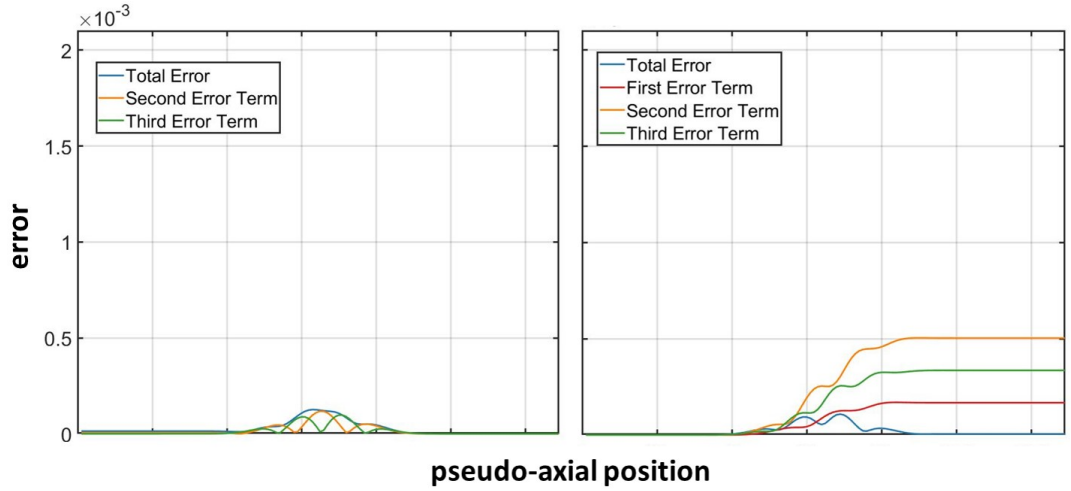

FIGURE 4.18: Left-hand side is the left travelling local error and on right-hand side is the right travelling local error, broken into total and three error terms for: $\tilde{\omega} = 16, \Delta\zeta = \frac{1}{128}, g_1 = 0.004, g_2 = 0.075$

Looking at the test cases with the largest Gaussian height, g_1, fixing other parameters, the total and local errors decrease with the increase of the Gaussian width, g_2, due to the larger proportion of shifted surfaces making the overall changes more gradual - it can also be said that this results in more gradual changes in the various derivatives of the Jacobian. Figs. 4.19 to 4.22 show a stepwise increase in the Gaussian width, g_2, from 0.075 to 0.0125 with all other parameters fixed. Note it is fixed at the largest Gaussian height $g_1 = 0.016$, so this results in the greatest maximum shift in the central planes.

Comparing Fig. 4.18 with Fig. 4.19 it is clear that increasing the Gaussian height results in an increase of the total error and all local errors, just as increasing the frequency does, but does not affect the relative magnitudes amongst the three errors, unlike the frequency.

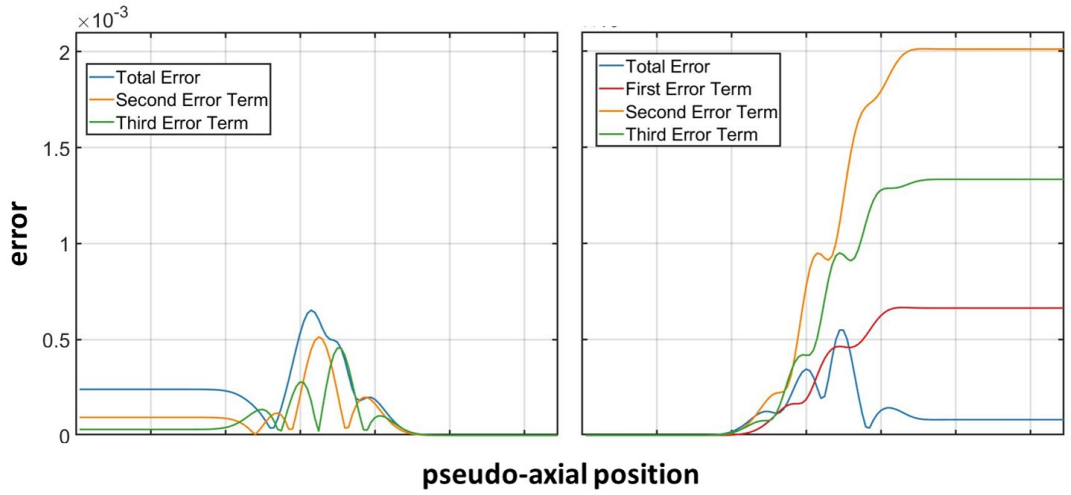

FIGURE 4.19: Left-hand side is the left travelling local error and on right-hand side is the right travelling local error, broken into total and three error terms for: $\tilde{\omega} = 16, \Delta\zeta = \frac{1}{128}, g_1 = 0.016, g_2 = 0.075$

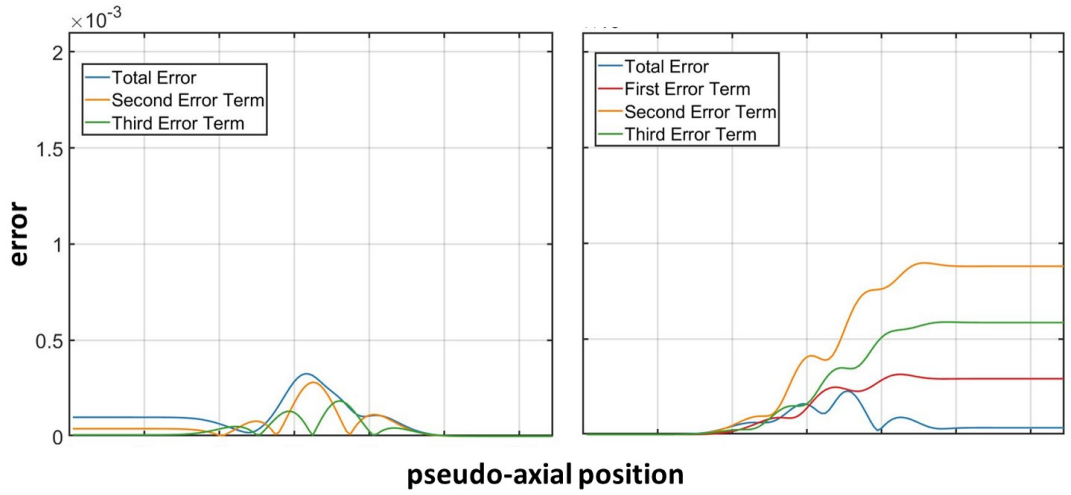

FIGURE 4.20: Left-hand side is the left travelling local error and on right-hand side is the right travelling local error, broken into total and three error terms for: $\tilde{\omega} = 16, \Delta\zeta = \frac{1}{128}, g_1 = 0.016, g_2 = 0.1$

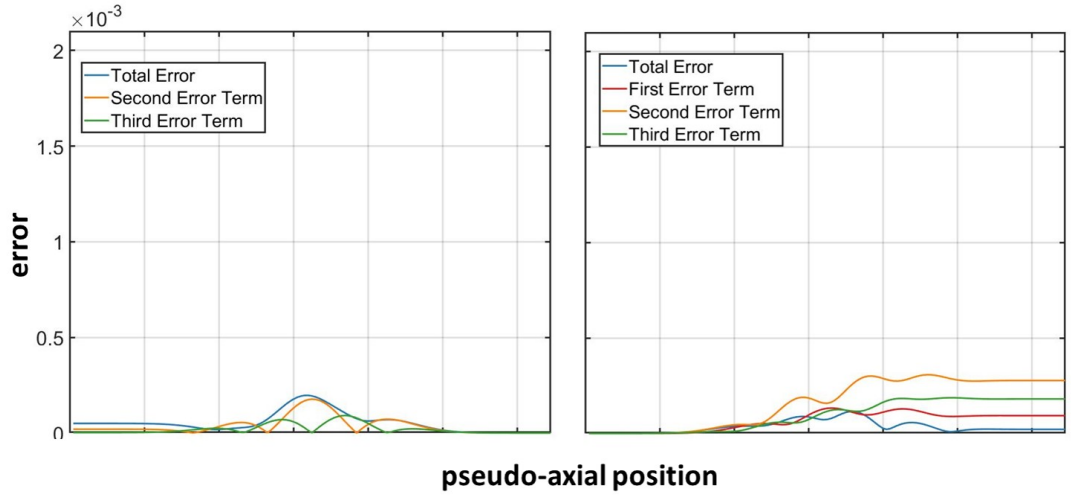

FIGURE 4.21: Left-hand side is the left travelling local error and on right-hand side is the right travelling local error, broken into total and three error terms for: $\tilde{\omega} = 16, \Delta\zeta = \frac{1}{128}, g_1 = 0.016, g_2 = 0.125$

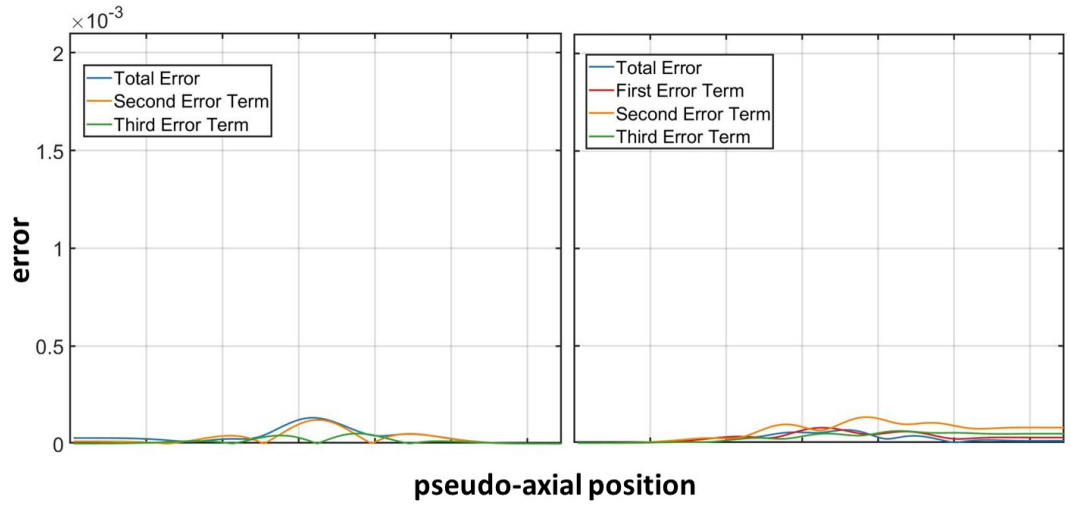

FIGURE 4.22: Left-hand side is the left travelling local error and on right-hand side is the right travelling local error, broken into total and three error terms for: $\tilde{\omega} = 16, \Delta\zeta = \frac{1}{128}, g_1 = 0.016, g_2 = 0.15$

Increasing the frequency reduces the magnitude of the right-running local error seen at the right-hand end of the duct, but increases the total errors and left-running local errors at the left-hand end of the duct due to the first and second error terms dependency on $\tilde{\omega}$. This can be seen from comparing Figs. 4.23 and 4.24 to Figs. 4.21 and 4.22.

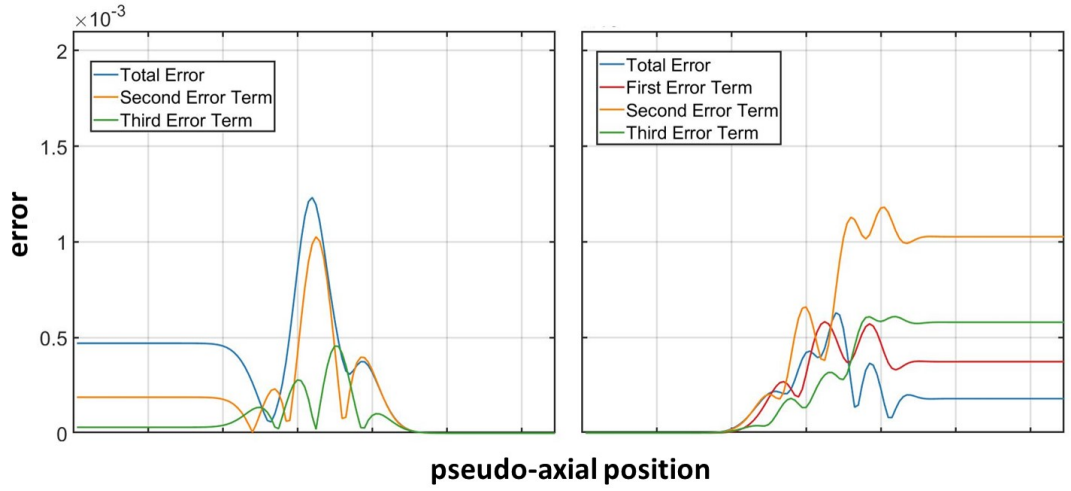

FIGURE 4.23: Left-hand side is the left travelling local error and on right-hand side is the right travelling local error, broken into total and three error terms for: $\tilde{\omega} = 32, \Delta\zeta = \frac{1}{128}, g_1 = 0.016, g_2 = 0.075$

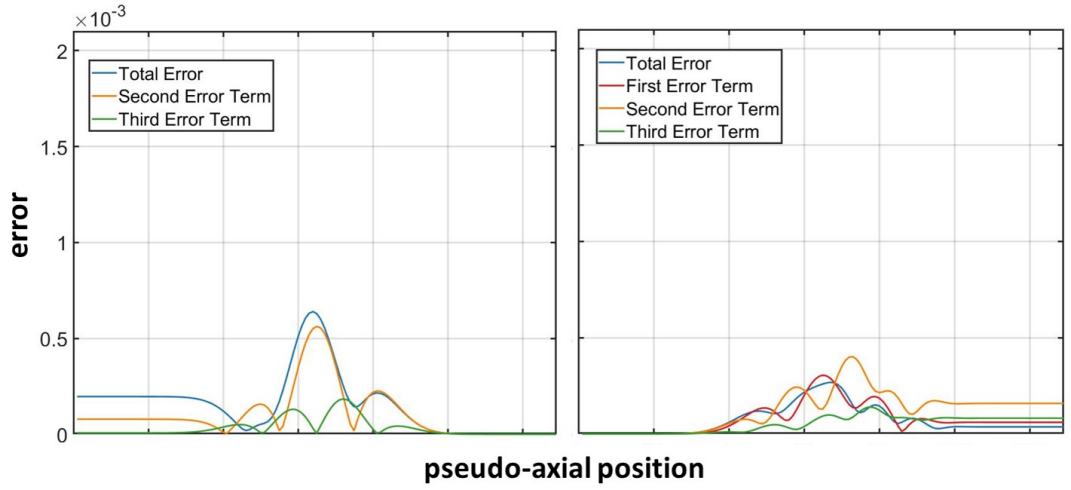

FIGURE 4.24: Left-hand side is the left travelling local error and on right-hand side is the right travelling local error, broken into total and three error terms for: $\tilde{\omega} = 32, \Delta\zeta = \frac{1}{128}, g_1 = 0.016, g_2 = 0.1$

4.2.2.3 Predicting numerical results

Using the local error terms derived in the error analysis and propagating them with the theoretical eigenvalues and eigenvectors, a signal of unit amplitude can be propagated upstream just as it is in the numerical study. This provides a prediction of the numerical EAGCC result given by the error analysis. If the two are in agreement then this suggests that the local error terms found in the error analysis are accurate in identifying the cause of the error. Comparing the prediction with the EAGCC result shows that the error analysis has effectively estimated the mesh-related errors in most cases. This is shown in Fig. 4.25 and Fig. 4.26, although in this second figure the

EAGCC result oscillates slightly more than the predicted result suggesting there are some higher order changes not captured by the first order approximation.

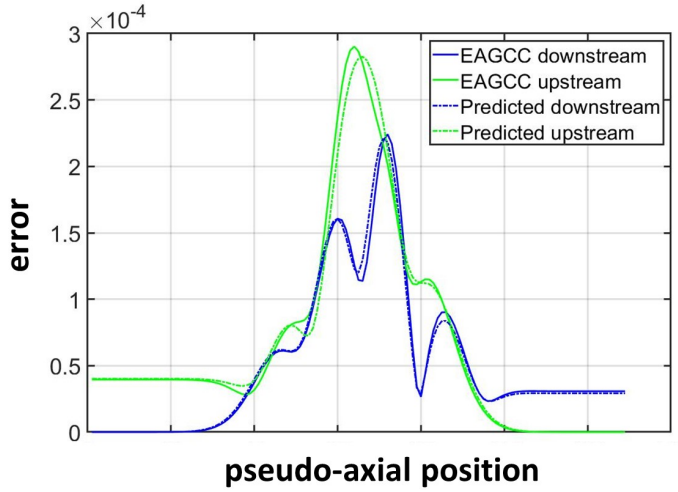

FIGURE 4.25: Predicted analytical result and EAGCC result, split into upstream and downstream travelling waves. For: $\tilde{\omega} = 16, \Delta\zeta = \frac{1}{128}, g_1 = 0.016, g_2 = 0.1$

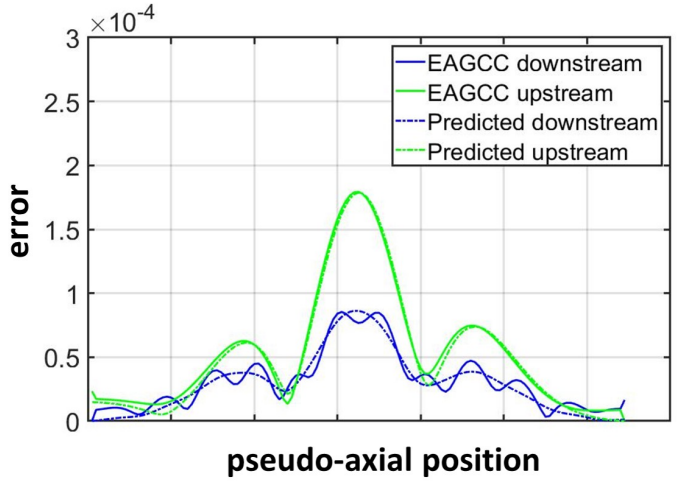

FIGURE 4.26: Predicted analytical result and EAGCC result, split into upstream and downstream travelling waves. For: $\tilde{\omega} = 16, \Delta\zeta = \frac{1}{128}, g_1 = 0.016, g_2 = 0.175$

Where the predicted result does not match up with the numerical result is in cases with larger $\Delta\zeta$. This is due to the mesh definition. One example of this is shown in Fig. 4.27. The predicted result did not capture the numerical result fully, this is possibly due to the combination of a large $\Delta\zeta$ and narrow Gaussian width creating poor mesh definition.

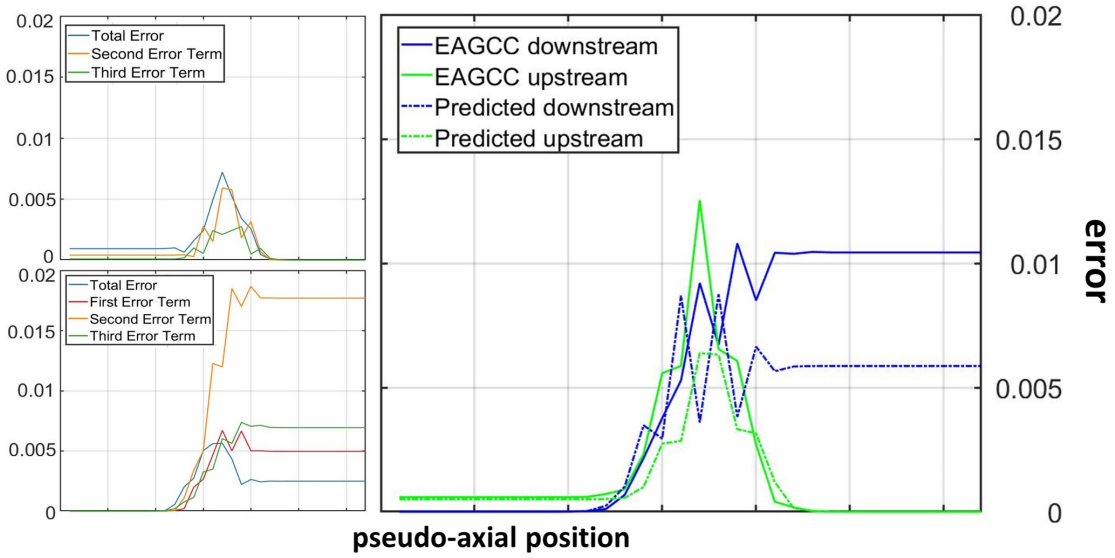

FIGURE 4.27: Error vs pseudo-axial position. Top left is the left travelling local error split into total and individual error terms, bottom left is the right travelling local error terms and the right hand side is the predicted analytical result and EAGCC result, split into upstream and downstream travelling waves. For: $\tilde{\omega} = 32\Delta\zeta = \frac{1}{32}, g_1 = 0.004, g_2 = 0.05$

4.3 Discussion - Application to 3D Meshes

A 3D analytic error calculation is prohibitively complex. However, the results given here still aid in the design of 3D meshes for the application of the EAGCC method.

Not all of the results of the present study are applicable to fully three-dimensional non-uniform meshes. However, some of the characteristics are expected to read across. It might be expected that:

- the error is still second order in mesh spacing
- the error terms relate to different orders of derivative of the Jacobian
- the relative importance of the errors scales with freefield wave number

Without a 3D error analysis, it is not possible to assess the effect of all of the terms of the Jacobian ($J_{z\xi}$, $J_{z\eta}$, $J_{x\zeta}$, $J_{y\zeta}$ etc.). Along a given pseudo-axial mesh line, however, the closest equivalent to the $J_{z\zeta}$ term in the one-dimensional analysis is $\frac{\partial s}{\partial \zeta}$ where s is the geometric distance along the mesh line.

The only way to remove these numerical errors would be to have a uniform mesh (constant Jacobian) but this is not possible in general. Instead to minimise the error it is important to use a smooth mesh such that the derivatives of the Jacobian (derivatives of $\frac{\partial s}{\partial \zeta}$) are small. Errors are likely to be most significant in areas where perturbation amplitudes are high. If this is known a priori then the mesh can be designed to be smooth in these areas.

In the application of an aero-engine intake, for example, for some noise sources the signal is strongest close to the outer wall. Therefore in these cases it is suggested that the points along the outer wall at a given circumferential position are equispaced such that the derivatives of the Jacobian are as small as possible in the high amplitude region.

4.4 Conclusions

The EAGCC method for acoustic propagation in one dimension, in the absense of flow, has been shown to be second-order accurate in mesh spacing.

Two local error equations have been derived relating to the leading order errors in the propagation and reverse direction respectively

$$Error_{local,1l} = (\Delta\zeta)^3\big(-\frac{1}{12}i\tilde{\omega}J'' - \frac{1}{24}\frac{J'''}{J}\big) \tag{4.141}$$

$$Error_{local,2r} = (\Delta\zeta)^3\big(\frac{1}{12}\tilde{\omega}^2JJ' - \frac{1}{8}i\tilde{\omega}J'' - \frac{1}{24}\frac{J'''}{J}\big) \tag{4.142}$$

These equations consist of three competing error terms which can be related to successive derivatives of the Jacobian matrix together with the freefield wave number in the direction of propagation.

At low wave numbers, such that $\tilde{\omega}^2J' << J'''$, it has been shown that the third error term is dominant. For higher wave numbers the first and second terms are more prominent.

The analysis is supported by a range of numerical test cases which confirm the predicted relationship between the wave number and mesh-related parameters and the error.

When the error terms are calculated using exact derivatives of the Jacobian and propagated numerically it is shown that the error terms accurately predict the error in the EAGCC method.

Finally, a discussion has been provided about how the results of this study can be applied to 3D meshes.

Chapter 5

Validation of the Eigen Analysis in General Curvilinear Coordinates Method Against ACTRAN/TM Solutions

The EAGCC method has been applied to a number of aero-engine inlet cases, however, the selection of cases falls short of a full validation. This chapter demonstrates the EAGCC method's capability to model the linear induct propagation, near-field radiation, and far-field directivity of a fully three-dimensional intake, and validates the results against published ACTRAN/TM results by Xiong and Sugimoto [34].

5.1 Reference Solution

5.1.1 Intake Rig

The reference solutions used throughout this chapter stem from the models used in [34], the three-dimensional results of which were validated against measured data from a scale rig test in AneCom Aero Test facility in Germany, as part of the EU fifth framework programme SILENCE(R) [148].

The drooped and scarfed rig intake is approximately 1/3 scale relative to a modern turbofan intake. The fan (not included in the model) has 24 blades and a diameter (D) of approximately 0.87m. The axial length of the intake liner is around 0.35D [34] [148].

The radius of the far-field microphone arc is approximately 20D, and the far-field measurements were taken at several rotation angles providing three-dimensional radiation reference data [34].

The operating condition considered by Xiong and Sugmimoto [34] is that of a high power setting Sideline condition, the fan plane Mach number is set at approximately 0.6 and the ambient Mach number is zero.

5.1.2 ACTRAN/TM Model

Sugimoto provided the ACTRAN/TM models used to produce the results published in [34], this included the meshes, virtual microphone positions (field points), input files, liner impedance, and output result files (mean flow, perturbation results induct and far-field).

The acoustic meshes used for the ACTRAN/TM models are unstructured, with finite elements in the near field and a layer of infinite elements to the outer boundary of this. The mesh resolution increases in areas of higher mean flow velocity.

In all of the original (published) ACTRAN/TM models a liner was included in the baffle region, with a non-dimensional impedance of $\frac{Z}{\rho c} = 1 + 0i$, where ρ is the fluid density of air and c the speed of sound.

The ACTRAN/TM models consider the circumferential modes 6 to 24, at the blade passing frequency (BPF) of 3475.7 Hz. At each of the circumferential modes, each of the cut-on modes are set with unit intensity at the fan plane and individually propagated to the far-field.

For the axisymmetric cases in this chapter, the reference solutions were produced by running the ACTRAN/TM models, provided by Sugimoto, for the circumferential modes of interest. However, the input files were edited to remove the baffle liner and the EAGCC mesh points were input as additional virtual microphone positions. The output unsteady velocity and pressure values at each virtual microphone position form the reference solution.

For the 3D cases, the original results files from the published work were used to create the reference solution. The unsteady velocity and pressure from the results nff file were read into MATLAB and the 'scattered interpolant' routine was used to interpolate the ACTRAN/TM solution onto the EAGCC mesh. The far-field results were taken from the virtual microphone output files.

5.1.3 Comparing results

To reduce the potential for un-accountable differences between the EAGCC and ACTRAN/TM solutions the following steps have been made:

- The reference solution was computed using ACTRAN/TM as described in section 5.1. This produced a reference solution interpolated onto the same mesh as used for the EAGCC calculation.
- The EAGCC solutions are output non-dimensionally, but have been expressed dimensionally for direct comparison against the ACTRAN/TM reference.
- The mean flow computed by ACTRAN/TM was interpolated onto the EAGCC mesh, using the ACTRAN iCFD package for axisymmetric cases and the MATLAB 'scattered interpolant' for 3D cases. This interpolated mean flow was used to produce the EAGCC solution.
- The ACTRAN/TM pressure profile at the fan face was used as the input signal for the EAGCC solution expressed as modal coefficients to the eigen-vector basis at this analysis surface. To do this the ACTRAN/TM solution vector was normalised, the velocity was normalised by the speed of sound and the pressure by the reference pressure and heat ratio, similarly to the normalisation of the governing equations shown in section 3.4.1.

5.2 Axisymmetric Validation Cases

An axisymmetric version of the intake was also considered by Xiong and Sugimoto [34], created by taking the side profile of the 3D intake and rotating round the engine shaft axis. The axisymmetric case is much simpler to set up, and quicker to run thus, it provides a great opportunity to interrogate the results before applying the EAGCC method to the more complex 3D intake.

All the following cases considered are at Blade Passing Frequency (BPF), a frequency of 3475.7 Hz (or 21838 rad/s). The induct and far-field SPL has been predicted for four incident modes (24,1),(31,1),(15,1),(8,1); that is by propagating the first upstream travelling radial harmonic at four fixed circumferential harmonics 8, 15, 24, and 31. This selection covers a range of scenarios in the acoustic modal breakdowns, mode (8,1) is highly cut on and there are 7 propagating acoustic modes at this circumferential harmonic; where as mode (31,1) is to close to the cut on/off boundary and no other propagating modes are present at this circumferential harmonic. Both hard wall and lined models are included for each circumferential mode. The liner impedance is the same as that used by Xiong and Sugimoto [34] (2.58 -0.75i).

5.2.1 Mesh

The axisymmetric mesh used for all the following cases is shown in Fig. 5.1. It is comprised of 132 points axially, and 101 points radially. The radial points are spaced

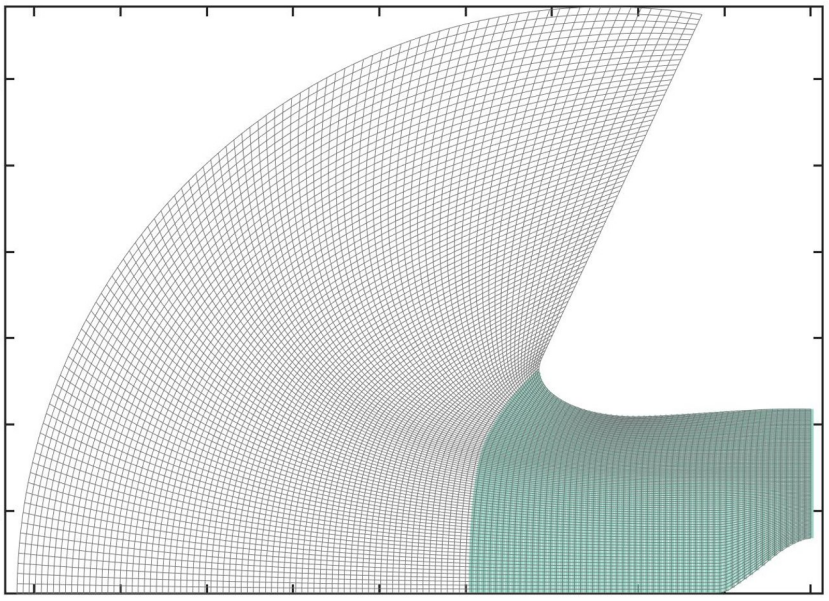

FIGURE 5.1: EAGCC axisymmetric mesh. Shaded area indicates induct region.

equally at the fan and at the outer arc, and the axial points are spaced equally at the inner wall. In the lined region, the axial points have been positioned such that the start and end of the liner coincide with axial mesh points. The shaded area in Fig. 5.1 indicates the 'induct' region, all figures restricted to induct correspond to the area shown.

5.2.2 Circumferential mode 24

Fig. 5.2 shows contour plots of the real part of the unsteady pressure for both methods. The EAGCC result for the hard wall case at blade passing frequency (BPF) for incident mode (24,1) generally agrees with the reference solution obtained from ACTRAN/TM.

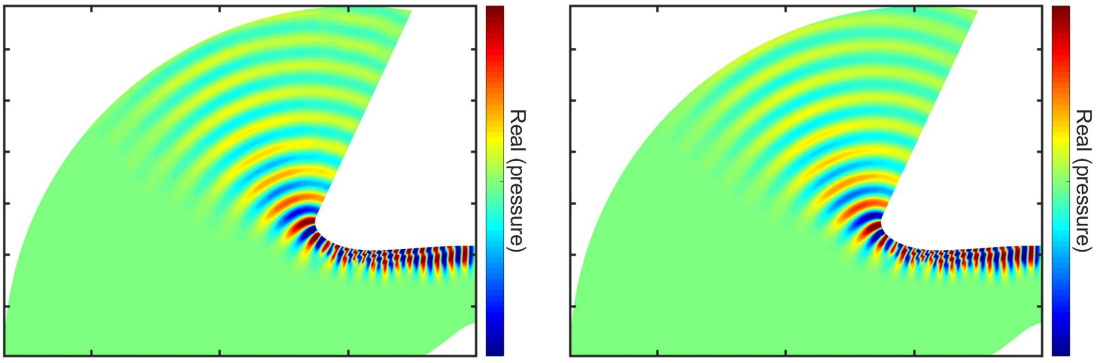

(A) EAGCC (B) ACTRAN/TM

FIGURE 5.2: Axisymmetric hard wall intake, incident mode (24,1). Real part of acoustic pressure.

The lined case results are shown in Fig. 5.3. It can be seen that the EAGCC method predicts the effects of the liner such as the change in radial amplitude profile in the lined region and modal scattering upstream of the liner.

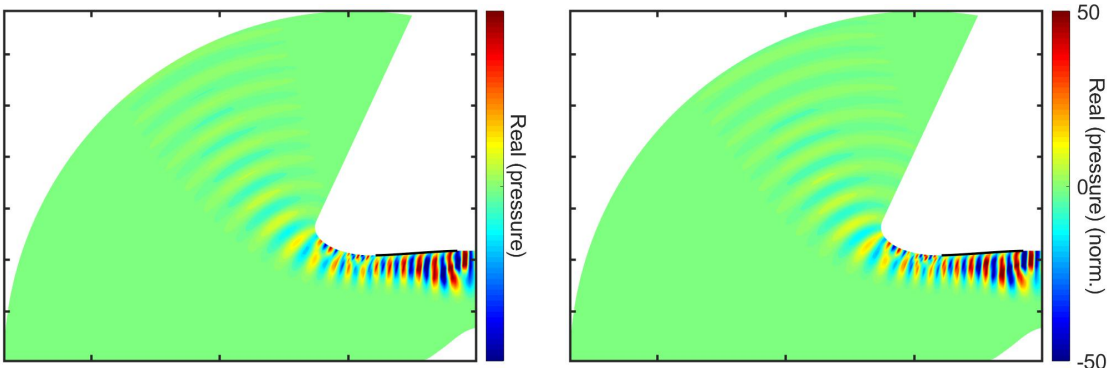

(A) EAGCC (B) ACTRAN/TM

FIGURE 5.3: Axisymmetric lined intake, incident mode (24,1). Real part of acoustic pressure.

Fig. 5.4 shows the pressure along the outer wall, in duct (as indicated in Fig. 5.1), for both the hard wall and lined cases. It shows that the hard wall predictions of the EAGCC and ACTRAN/TM methods agree within 1dB; and the lined predictions within 3 dB. The attenuation at the downstream end of the liner, followed by several oscillations are all well captured by the EAGCC method.

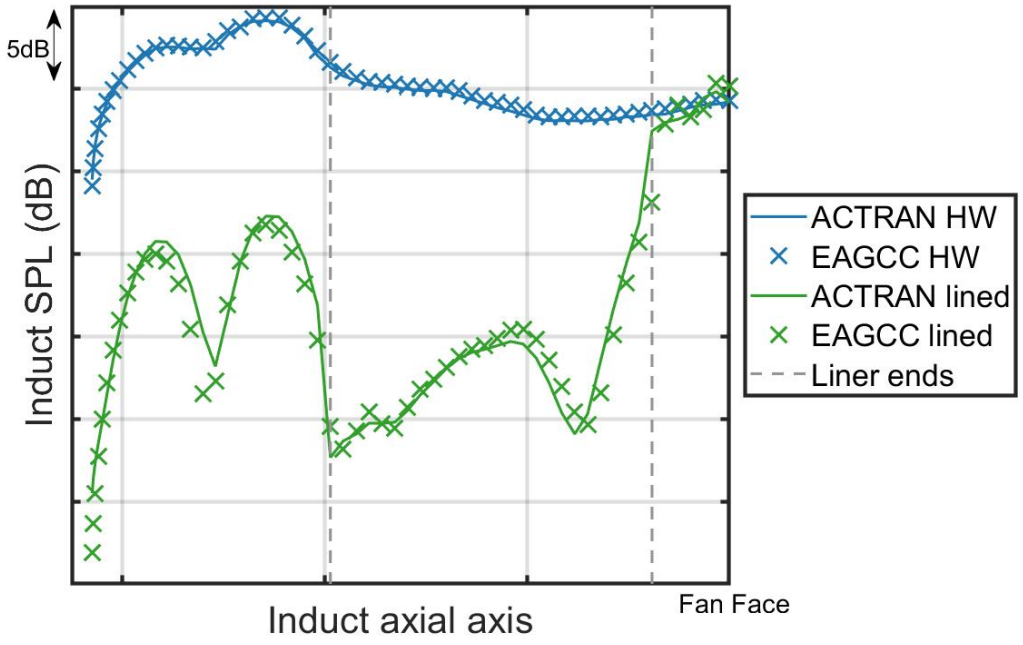

FIGURE 5.4: Axisymmetric intake, incident mode (24,1). Induct SPL (dB) along the outer wall.

Looking at the outer wall pressure alone, however, does not give the whole picture particularly as the maximum pressure often occurs away from the wall as seen in Fig. 5.3. Fig. 5.5 also plots the SPL against axial position in the induct region of the lined case, however, the different coloured lines show how this changes with distance from the outer wall (o/w) (this is achieved by plotting the pressure corresponding to different radial mesh positions). At all radial positions shown the results of both methods have a similar amplitude profile throughout the duct, the SPL is predicted within a tolerance of 3dB. Furthermore, the effects of the liner mentioned previously are shown in greater detail here. Inside the lined region, the pressure at the outer wall is attenuated by 10-15 dB whilst increased pressure amplitudes are seen at radial positions further away from the wall, in both solutions. Upstream of the liner the outer wall pressure and the pressure 20 nodes in from the wall almost alternate in phase, just as can be seen in Fig. 5.3.

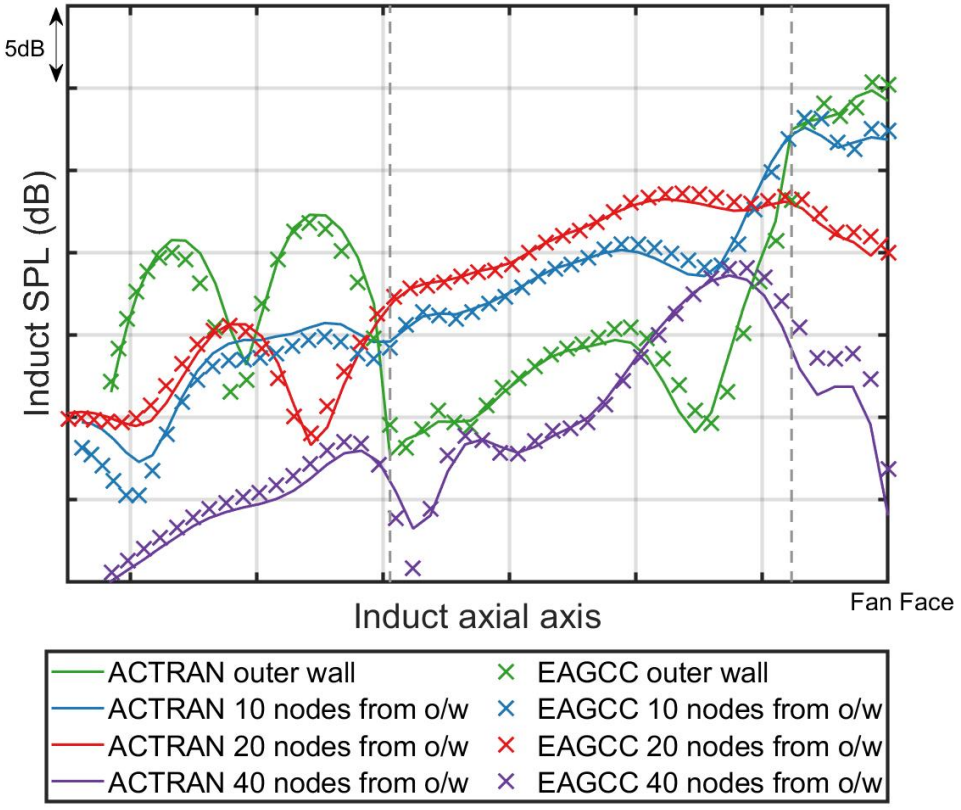

FIGURE 5.5: Axisymmetric lined intake, incident mode (24,1). Induct SPL (dB) at relative radial mesh positions to the outer wall (o/w). Grey dashed lines indicate liner ends

.

By using a FWH surface (section 3.8) set at the outer-most mesh surface in the near field, the EAGCC results have been propagated to the far-field. Fig. 5.6 shows the far-field sound pressure level for both the hard wall and lined cases at BPF. Both the

hard wall and lined cases have similar peak positions at around 70 degrees, the liner reduced the amplitude of this peak by around 10dB. The EAGCC hard wall prediction oscillates more than in the ACTRAN solution, both hard wall and lined results start to differ from the ACTRAN/TM result at higher polar angles. This is thought to be due to needing a higher radial resolution mesh in the near field to capture the range of radial harmonics.

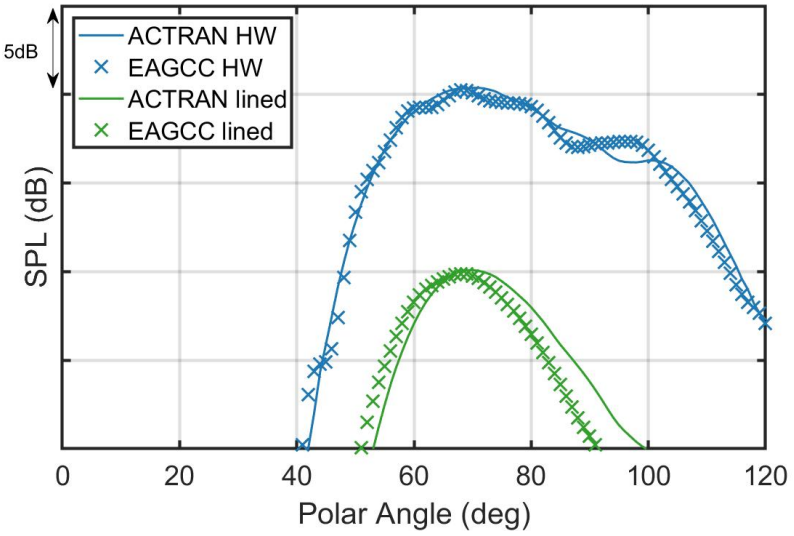

FIGURE 5.6: Axisymmetric intake, incident mode (24,1). Far-Field SPL (dB).

5.2.3 Circumferential mode 31

The EAGCC results for incident mode (31,1) are shown in Fig. 5.7 and Fig. 5.8. The EAGCC hard wall prediction looks similar to the ACTRAN/TM result induct, however, there is some difference in amplitude and phase of the propagating mode around the highlight and into the near field.

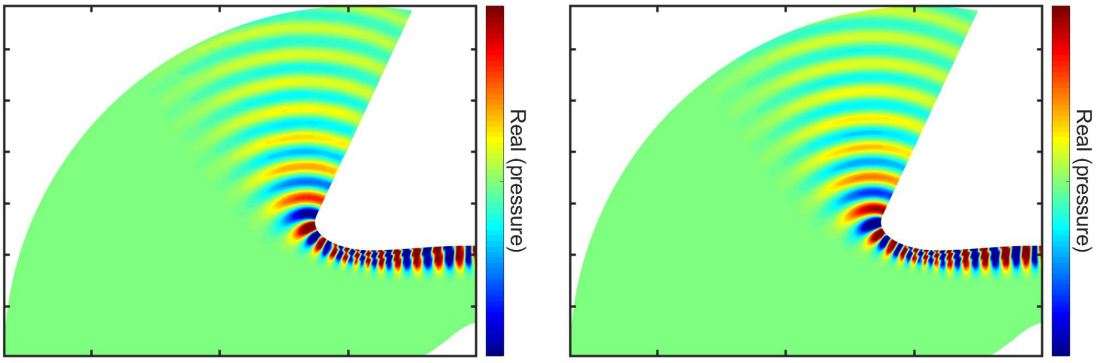

(A) EAGCC (B) ACTRAN/TM

FIGURE 5.7: Axisymmetric hard wall intake, incident mode (31,1). Real part of acoustic pressure.

As there is only one propagating mode upstream the liner is particularly effective, this has been captured in the EAGCC and ACTRAN/TM results, Fig. 5.8.

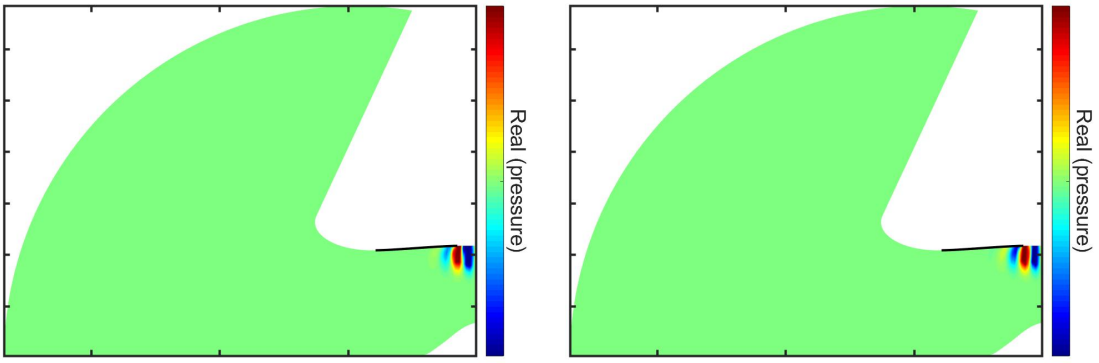

(A) EAGCC (B) ACTRAN/TM

FIGURE 5.8: Axisymmetric lined intake, incident mode (31,1). Real part of acoustic pressure.

Fig.5.9 shows the SPL along the outer wall in the induct region (as shown in Fig. 5.1) for the hard wall and lined cases. It can be seen that the outer wall pressure in the hard wall case agrees throughout the induct region. Fig. 5.9 also shows that that the liner reduces the amplitude of the propagating mode at the outer wall by over 100dB. The EAGCC result captures this reduction, however, upstream of the liner the ACTRAN/TM solution shows a higher increase in amplitude than the EAGCC solution, with a consistent difference of approximately 6dB.

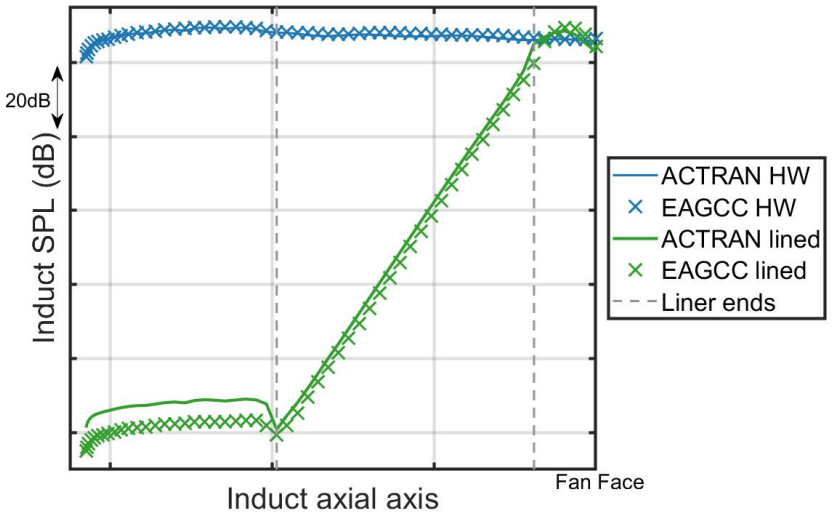

FIGURE 5.9: Axisymmetric intake, incident mode (31,1). Induct SPL (dB) along the outer wall.

The constant difference in pressure upstream of the liner is thought to be due to the fact that only one mode is propagating. Fig. 5.10 shows the radial pressure profile from both solutions, this difference in amplitude is consistent throughout the upstream section. The pressure amplitude of both solutions are non-dimensional as they are normalised by the heat ratio and reference pressure as described in 3.4.1 As the mode shapes captured by each of the schemes differ slightly in amplitude, this is then propagated through this upstream section. Although the difference in amplitude in both results is significant at 6 dB, both have been attenuated by around 100dB so this is not detrimental to the applicability of the EAGCC prediction.

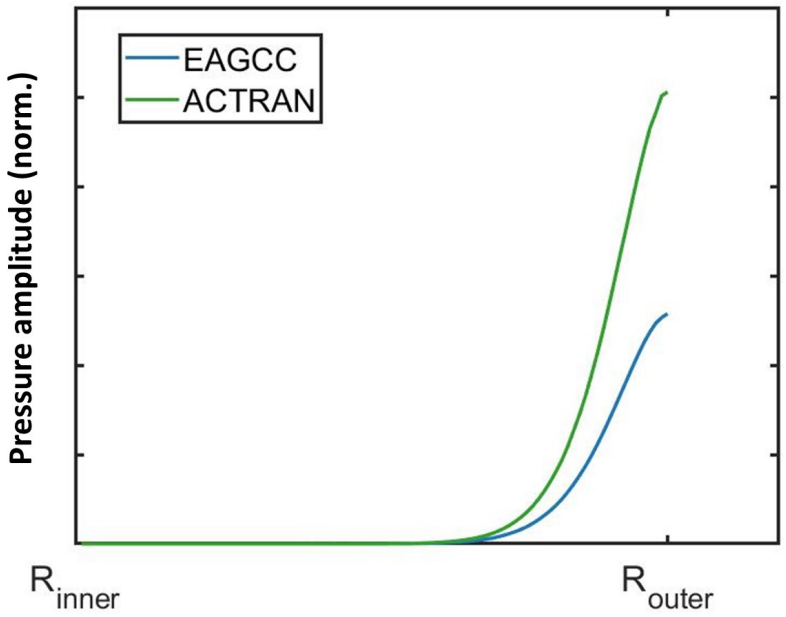

FIGURE 5.10: Axisymmetric lined intake, incident mode (31,1). Radial pressure profile upstream of the acoustic liner.

Fig. 5.11 shows the far-field SPL of the hard wall cases, the EAGCC and ACTRAN/TM SPL are within 2dB of each other. The EAGCC predicts the position of the peak angle, however, the overall profile has more oscillations than the ACTRAN prediction.

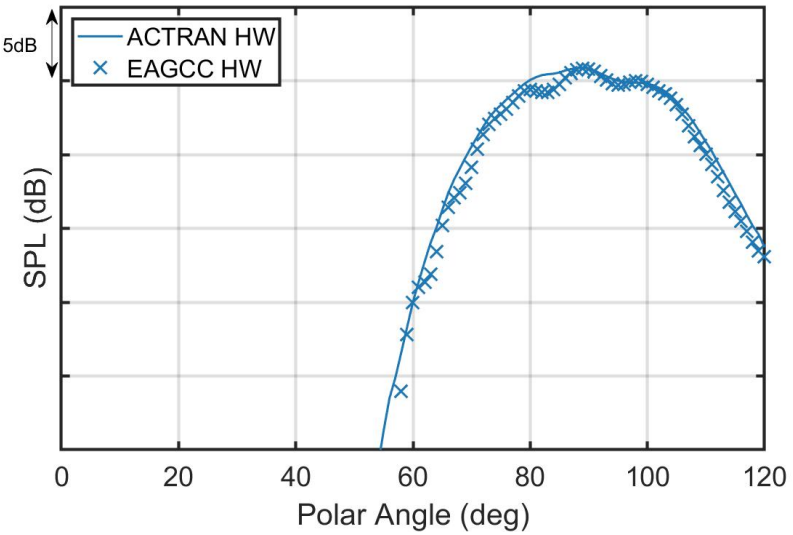

FIGURE 5.11: Axisymmetric hard wall intake, incident mode (31,1). Far-Field SPL (dB).

The lined case results, shown in Fig. 5.12, are not as good in amplitude with a difference of up to 6 dB. Given that this is the same magnitude as the difference seen induct, Fig. 5.9, it is likely that this is a direct consequence of the error upstream of the liner. The general shape of the far-field prediction, however, does agree with the ACTRAN/TM solution including the peak position. As with the hard wall case, the profile is more oscillatory. Both the hard wall and lined far-field results have similar peak positions at around 90 degrees, the liner substantially reduces the amplitude of this peak by over 100 dB.

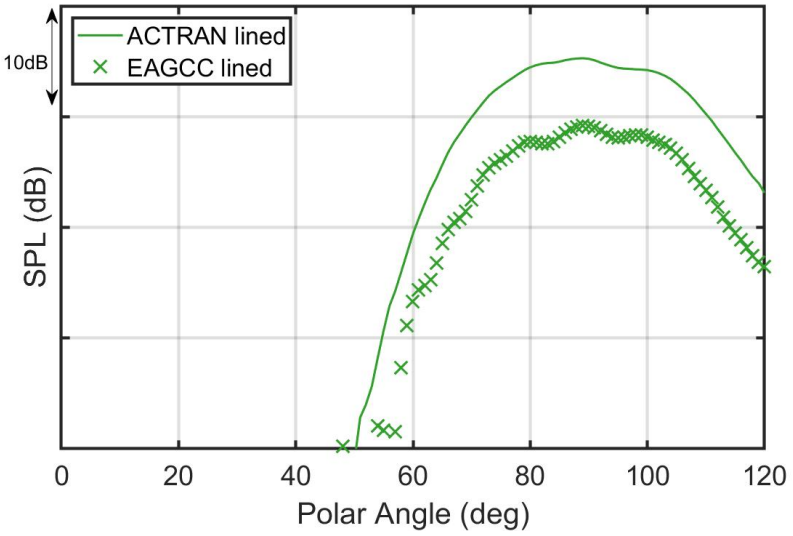

FIGURE 5.12: Axisymmetric lined intake, incident mode (31,1). Far-Field SPL (dB).

5.2.4 Circumferential mode 15

The EAGCC results for incident mode (15,1) are shown in Fig. 5.13 and Fig. 5.14 alongside ACTRAN/TM results for the same test case. In the hard wall case, both methods show a second radial mode propagating to the near field at low amplitude.

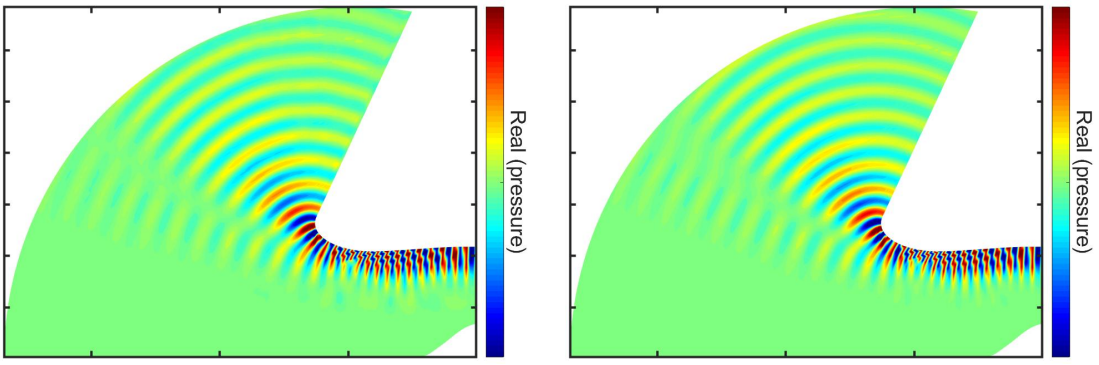

(A) EAGCC (B) ACTRAN/TM

FIGURE 5.13: Axisymmetric hard wall intake, incident mode (15,1). Real part of acoustic pressure.

For the lined case, as shown in Fig. 5.14, the EAGCC method captures the liner reducing the amplitude of the dominant mode and increasing the amplitude of the second radial mode just as in the ACTRAN/TM result.

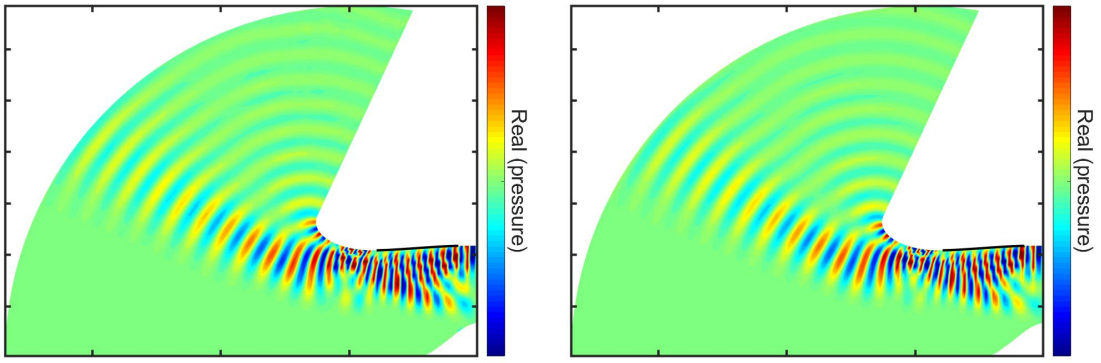

(A) EAGCC (B) ACTRAN/TM

FIGURE 5.14: Axisymmetric lined intake, incident mode (15,1). Real part of acoustic pressure.

Fig. 5.15 plots the outer wall pressure in the induct region for both the hard wall and lined cases. It is shown that the hard wall results agree almost exactly and the lined results generally agree in profile and within 2dB in amplitude (with one exception).

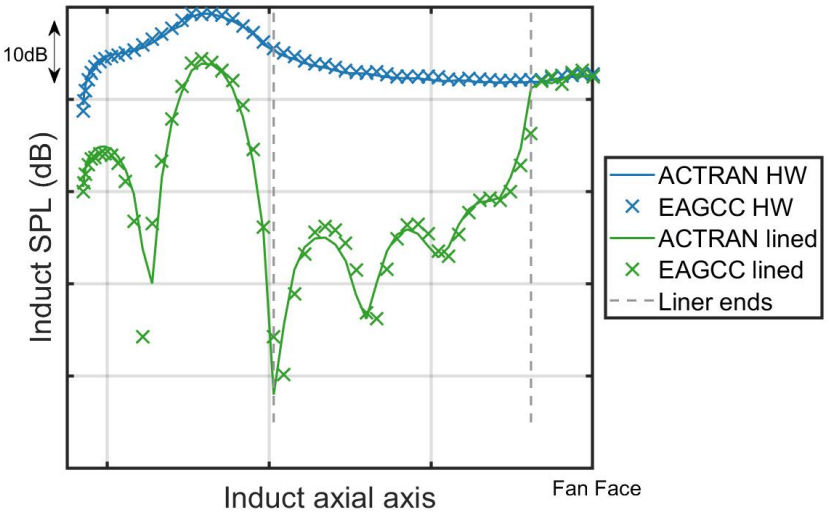

FIGURE 5.15: Axisymmetric intake, incident mode (15,1). Induct SPL (dB) along outer wall.

The far-field predictions for both hard wall and lined cases are shown in Fig. 5.16. The EAGCC predictions capture the general profile as well as the peak amplitude and position in both the hard wall and lined cases. However, for polar angles greater than 60 degrees the EAGCC result does not capture the higher-order peaks, with differences in amplitude of up to 5 dB throughout.

In contrast to the higher incident circumferential modes, the hard wall and lined peaks are similar in amplitude. The liner reduces the amplitude at higher polar angles but increases the amplitude at lower polar angles. Furthermore, the lined profile features a dominant narrow peak, at 20 to 70 degrees, followed by two smaller peaks at higher polar angles, whereas the hard wall peak profile spans a wider range of polar angles from 40 to 110 degrees. This is thought to be due to the changes in relative modal amplitudes caused by the liner as noted in Figs. 5.13 and 5.14.

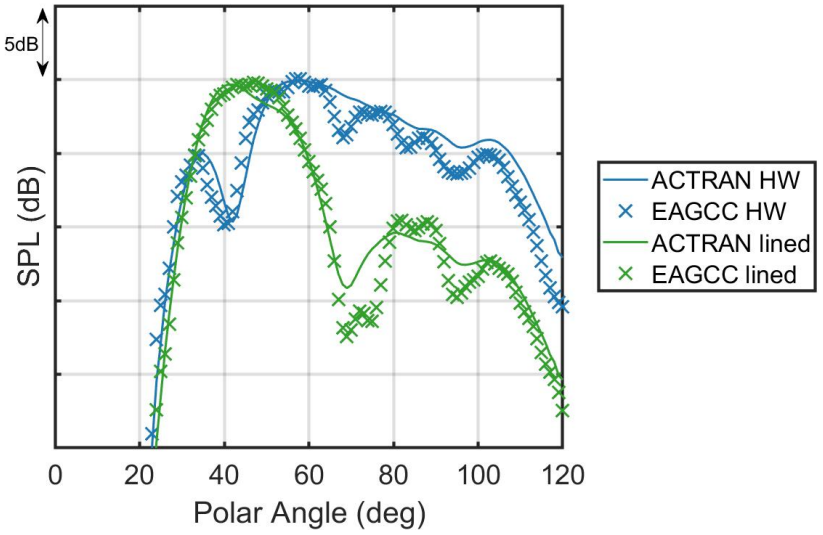

FIGURE 5.16: Axisymmetric intake, incident mode (15,1). Far-Field SPL (dB).

5.2.5 Circumferential mode 8

Fig. 5.17 shows the hard wall EAGCC and ACTRAN/TM solutions for incident mode (8,1). Both the EAGCC and ACTRAN/TM solutions show a wide polar arc of propagating pressure in the near field as a result of many cut-on modes propagating.

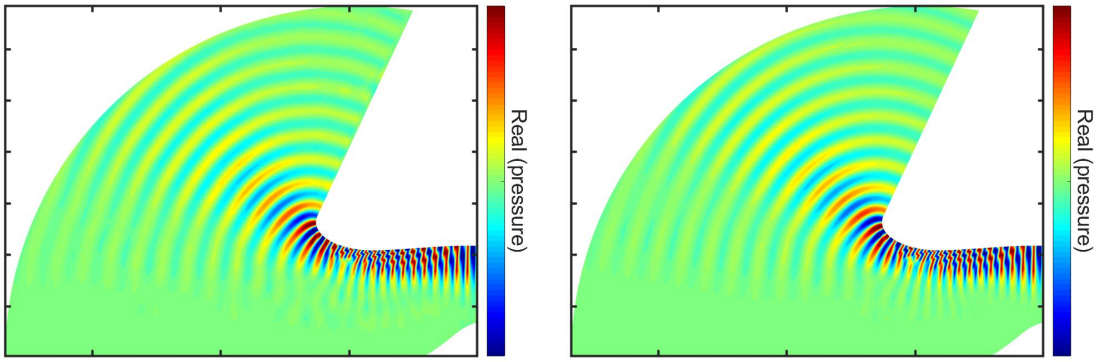

(A) EAGCC (B) ACTRAN/TM

FIGURE 5.17: Axisymmetric hard wall intake, incident mode (8,1). Real part of acoustic pressure.

Fig. 5.18 shows the solutions for the lined case. The EAGCC solution captures similar effects from the liner as the ACTRAN/TM solution including the significant modal scattering and attenuation in the higher order modes upstream of the liner and into the near-field.

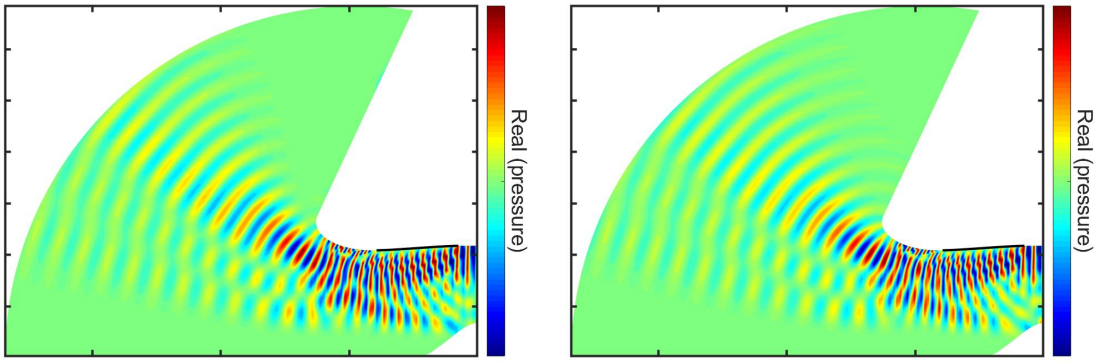

(A) EAGCC (B) ACTRAN/TM

FIGURE 5.18: Axisymmetric lined intake, incident mode (8,1). Real part of acoustic pressure.

Fig. 5.19 shows the outer wall SPL for both the hard wall and lined cases. The induct amplitude and profile of the hard wall solutions match almost entirely, and the lined predictions both show the same attenuation and oscillations inside the lined region as well as the increase in amplitude upstream of the liner. There is some discrepancy in the amplitudes in the lined case, with up to a 3 dB difference towards the highlight and in the lined region.

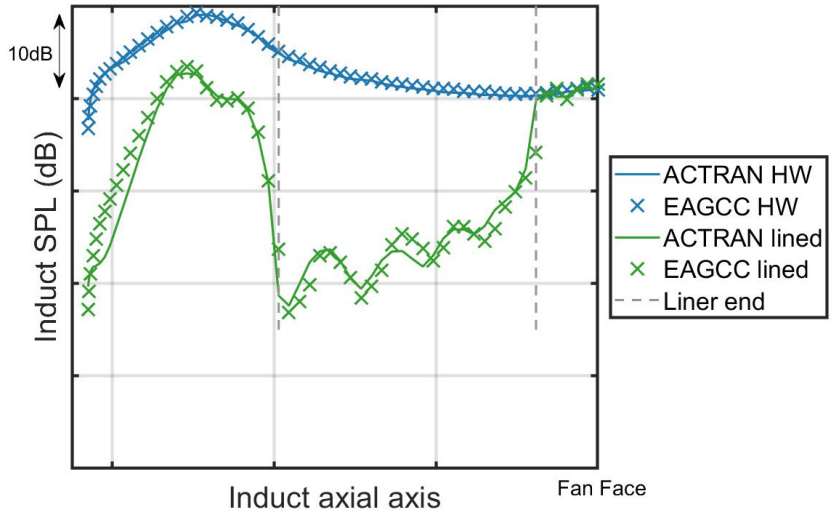

FIGURE 5.19: Axisymmetric intake, incident mode (8,1). Induct SPL (dB) along the outer wall.

Fig. 5.20 shows the far-field SPL for both the hard wall and lined cases, and it can be seen that there is some variation in the ACTRAN/TM and EAGCC far-field predictions. In the hard wall case, the highest peak at around 47 degrees match in position and amplitude, but at the lower polar angles the peak of the EAGCC result is higher in amplitude, and at the higher polar angle the EAGCC profile is more oscillatory than ACTRAN/TM and underpredicts the SPL. The amplitude difference is within 3 dB throughout and the general profiles agree.

For the lined case, the EAGCC result matches the ACTRAN/TM result at the two highest peaks in amplitude and position (around 50 degrees and 25 degrees), and the third peak in position (around 35 degrees) but lower amplitude. The general profile is well captured, though from 60 degrees and above the amplitude is lower. The greatest difference is around 3 dB. The lined far-field peak is slightly higher in amplitude than the hard wall, however, the higher amplitude region is narrower than the hard wall. This concurs with the pressure contours seen in Figs. 5.17 and 5.18.

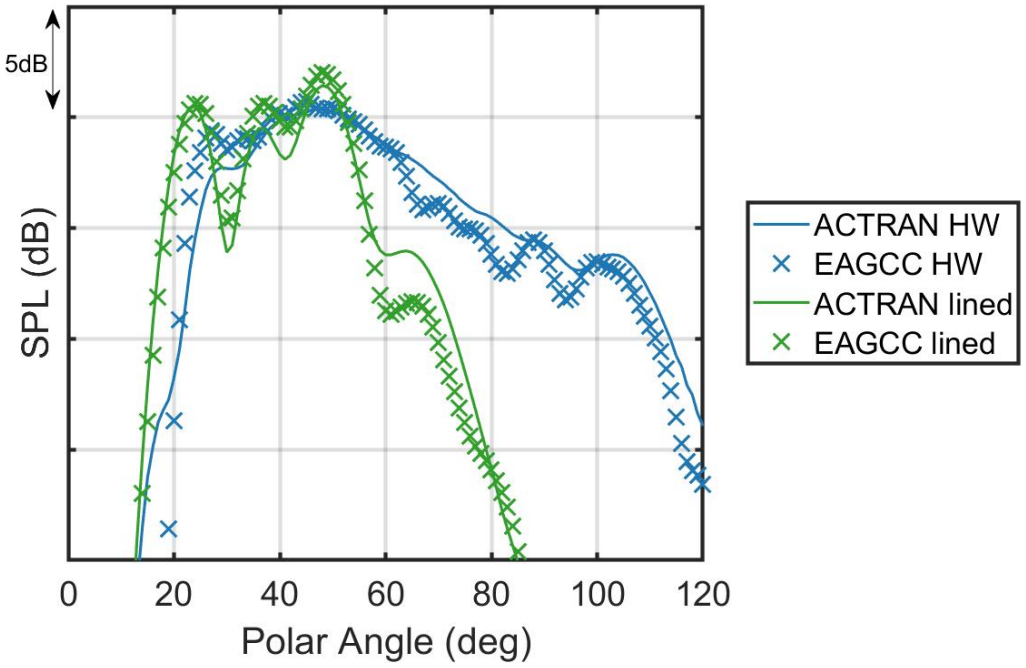

FIGURE 5.20: Axisymmetric intake, incident mode (8,1). Far-Field SPL (dB).

5.3 3D Intake Validation Cases

The following section sets out the methodology and results of the comparison between EAGCC and ACTRAN/TM for the non-axisymmetric 3D intake. The reference ACTRAN/TM solutions are formulated as described in 5.1.

5.3.1 Methodology

5.3.1.1 Mesh

The EAGCC mesh used to produce the results in this section was constructed as described in Chapter 3 section 3.2, and fitted to the same geometry used in the reference ACTRAN/TM results [34].

The mesh is defined in both cylindrical polar coordinates and generalised curvilinear coordinates. It has 101 radial points, 720 circumferential, and 130 axial; the circumferential points are equispaced, the radial points are spaced using a Chebyshev polynomial and the axial points are equispaced at the inner wall. The circumferential orientation is shown in Fig. 5.21, figures throughout the following sections will refer to these circumferential positions as reference points.

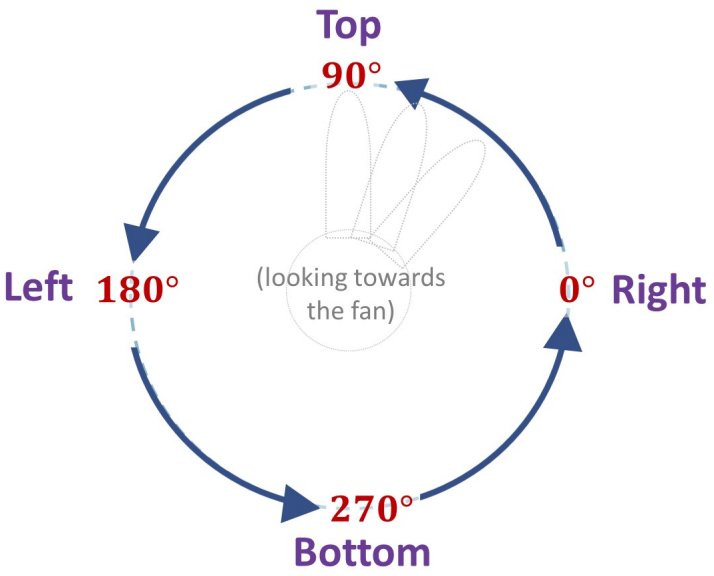

FIGURE 5.21: The circumferential mesh orientation, viewed from front looking downstream towards the fan.

Fig. 5.22 shows the mesh produced by taking a cut at a constant circumferential position of 90 degrees (top) to the central axis and through to 270 degrees (bottom) (ref. Fig. 5.21).

It is noted that the white space across the horizontal axis of Fig. 5.22 is purely a result of rotating the mesh to generate the figure and the centre of rotation is positioned away from the inner wall. This space is not present in the 3D mesh.

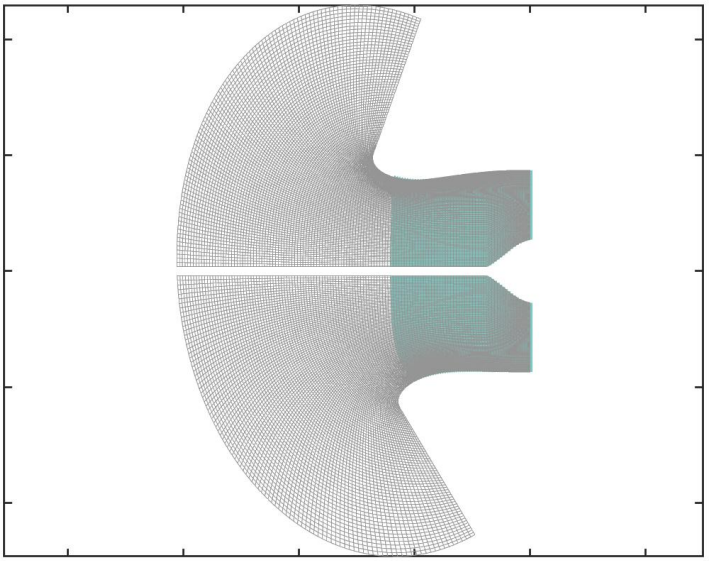

FIGURE 5.22: Side view of the mesh. Cut taken at constant circumferential plane at 90 degrees to 270 degrees (ref. 5.21)

5.3.1.2 Mean flow

The mean flow, already computed by ACTRAN/TM by Xiong and Sugimoto [34], was interpolated onto the EAGCC mesh using the built-in MATLAB interpolation function 'scattered interpolant' [149]. Fig. 5.23 shows the axial velocity component of the mean flow on a cross-section of the mesh.

5.3.1.3 Spectral resolution

It is important to include enough circumferential modes in the modal sum such that the modal scattering can be correctly captured. If too few are included then the presence of scattering will be represented through erroneous modal amplitudes in the circumferential modes that are included. However, due to computational demand, the number of circumferential modes included must be kept to a minimum.

For the case presented here the following steps were taken to determine the number of circumferential modes needed.

As reference solutions were readily available for this case it was possible to use a Fourier transform on the unsteady pressure of the ACTRAN/TM solution to see how the spectral energy changed throughout the duct. This indicated which circumferential modes had the highest amplitudes and were needed in the modal sum, and were used to compare against the EAGCC results. It is noted that the

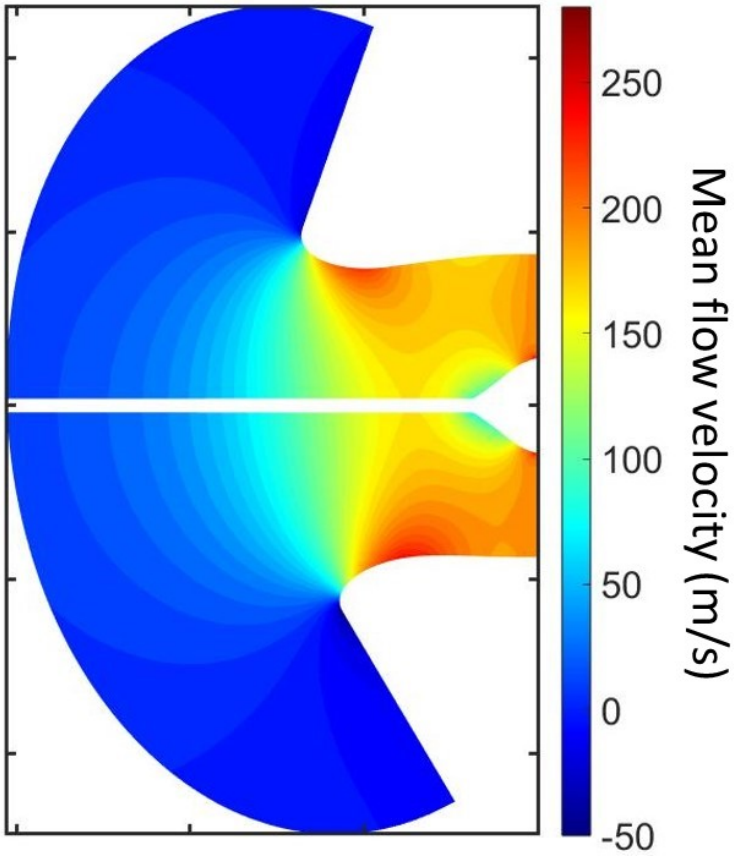

FIGURE 5.23: Mean flow velocity (m/s). Mesh cut at constant circumferential plane at 90 degrees to 270 degrees.

reference solution improved the efficiency of the next steps, however, it is not essential to the deductive process described below.

As the input mode considered is the first radial mode of circumferential mode 24, the circumferential modes included are expected to be approximately centred around mode 24. Initially, a small section of the duct was used to test the results of different ranges of input circumferential modes. A Fourier transform was used to look at the spectral amplitude/energy. The highest amplitudes are expected around circumferential mode 24 with very low amplitudes at the outer range of the sum. However, when an unsuitably reduced set is used energy can be seen building at the outer edges, as the energy cannot scatter to the higher/lower modes not included in the set. This can be used as an indication that more circumferential modes are needed, however, this process can be time-consuming and further work is required to establish a more efficient methodology or automated process.

5.3.1.4 Reduced domain

It was determined that 21 circumferential modes were needed to capture the modal scattering in this case, which results in large eigenvector matrices of 8484×8484

complex numbers that must be kept in working memory for use in the propagation. To lessen the computational demands of this test case, the domain size was reduced axially as shown in Fig. 5.24. In the reference ACTRAN intake model [34] acoustic treatment on the noise flare (baffle) is present, as shown in Fig. 5.24. Rather than include this additional liner in the EAGCC model, the reduced domain was defined such that it is not included in this region.

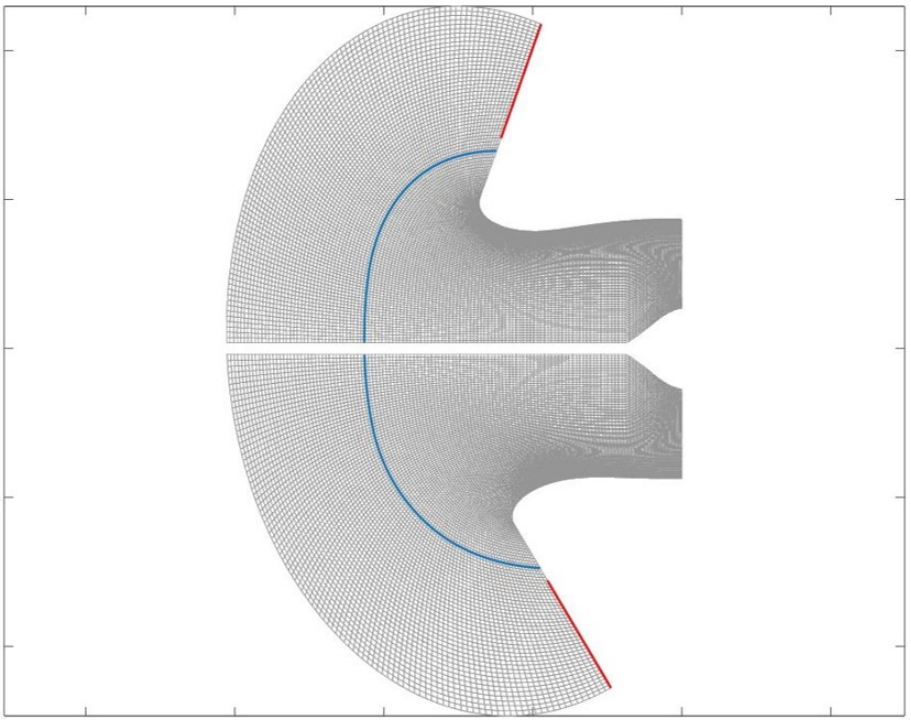

FIGURE 5.24: Mesh cut taken at constant circumferential plane 90 degrees to 270 degrees. Red lines indicate the baffle liner position, blue line indicates the upstream boundary of the reduced domain.

5.3.1.5 Far-field

The far-field directivity in the EAGCC method is given through the implementation of a FWH surface, as described in the technical background chapter section 3.8. The FWH surface is taken from an axial position, in the near-field, sufficiently far enough from the intake such that the mean flow is approximately uniform. From here, the upstream traveling information is propagated to the far-field. The accuracy of the far-field prediction is indicative of how well captured the upstream result is at the FWH surface.

The ACTRAN/TM far-field results, reported by Xiang and Sugimoto [34], are produced from the full domain which includes a baffle liner. The modal composition differs at any axial surface in this lined region to the hard wall surfaces downstream of the liner. Therefore, it is not expected that the far-field results taken from the reduced domain would necessarily match the reference ACTRAN/TM far-field results.

In order to compare the EAGCC and ACTRAN/TM far-field predictions, the far-field results presented in the next section are given by propagating both the EAGCC and interpolated ACTRAN/TM results from the furthest upstream axial surface of the reduced EAGCC domain to the far-field.

To demonstrate that the comparison is a true comparison of the EAGCC result with ACTRAN/TM, the FWH functionality was tested separately from the EAGCC model. The interpolated ACTRAN/TM solution taken from the furthest upstream axial surface of the original EAGCC domain was propagated to the far-field using a FWH surface. Fig. 5.25 shows the far-field directivity at 4 fixed circumferential positions produced by both methods. The results given by the FWH surface generally agree with the reference far-field results, obtained by the ACTRAN/TM model (using Infinite Elements), except at high polar angles ($>$ 100 degrees). There the FWH functionality of the EAGCC method is considered accurate and any differences between the far-field solutions going forward suggest a difference in the two solutions at the chosen FWH surface itself.

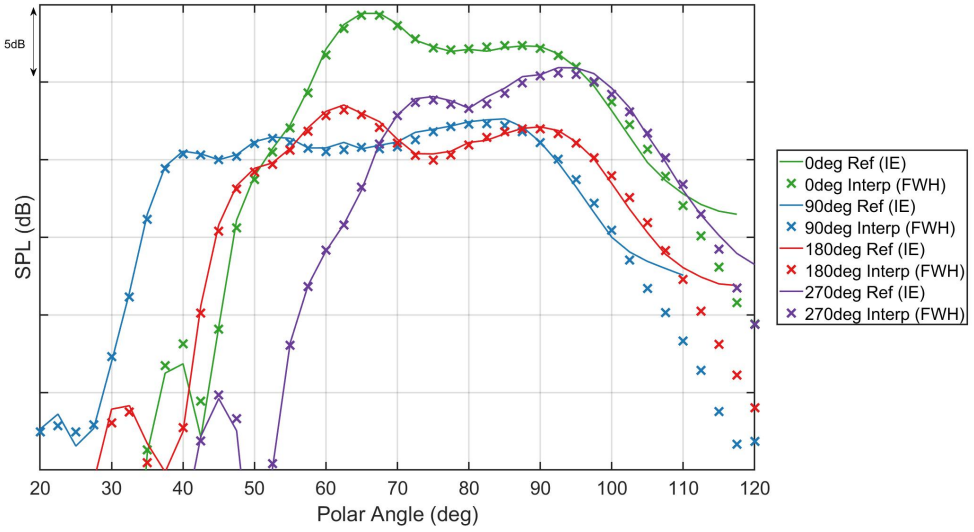

FIGURE 5.25: Far-field polar directivity at fixed circumferential positions. Lines indicate the results from the ACTRAN/TM model (IE). Symbols indicate the results from FWH.

To assess how far upstream the FWH surface needs to be implemented to achieve accurate results, this process of propagating the interpolated ACTRAN/TM results to the far-field was repeated at several axial positions. Fig. 5.26 shows the cross-section through the intake axis, and the FWH surfaces used to investigate are highlighted.

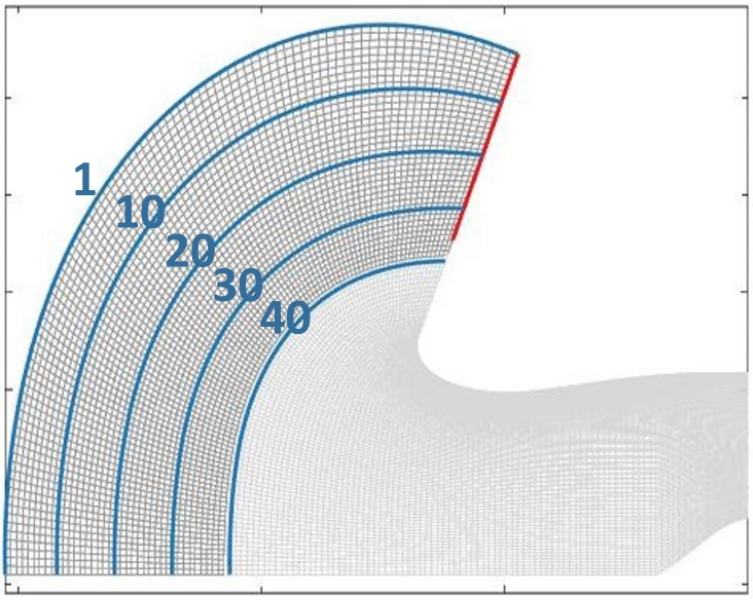

FIGURE 5.26: Mesh of original domain, cut taken at 90 degrees. Light grey mesh indicates the reduced domain. The blue lines indicate the axial surfaces used for the FWH surface. The red line indicates the baffle liner position.

Fig. 5.27 shows the mean flow velocity with the various trial FWH surfaces overlaid. There is little variation in the mean flow velocity in the outer range of FWH surfaces used (axial surface positions 1,10), particularly in the arc area closer to the outer wall where higher pressure changes are expected. There is more variation over the two surfaces further downstream (axial surface positions 30 and 40).

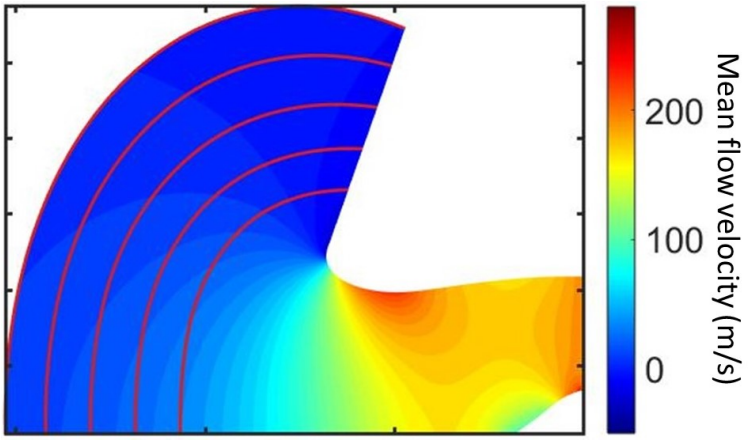

FIGURE 5.27: Mean flow velocity, cut at 90 degrees (top), with FWH axial surfaces at mesh positions: 1, 10, 20, 30, 40.

Fig. 5.28 shows how the accuracy of the far-field prediction worsens when the FWH surface is closer to the intake. The results from surfaces within the range of the baffle liner (positions: 1,10,20,30) all agree well with the reference solution, although the solution from surface 30 is less accurate at higher polar angles. The far-field result from surface 40 does resemble the general profile but there are visible differences such

as small differences in peak amplitudes and the loss of some definition including missing tertiary peaks and troughs.

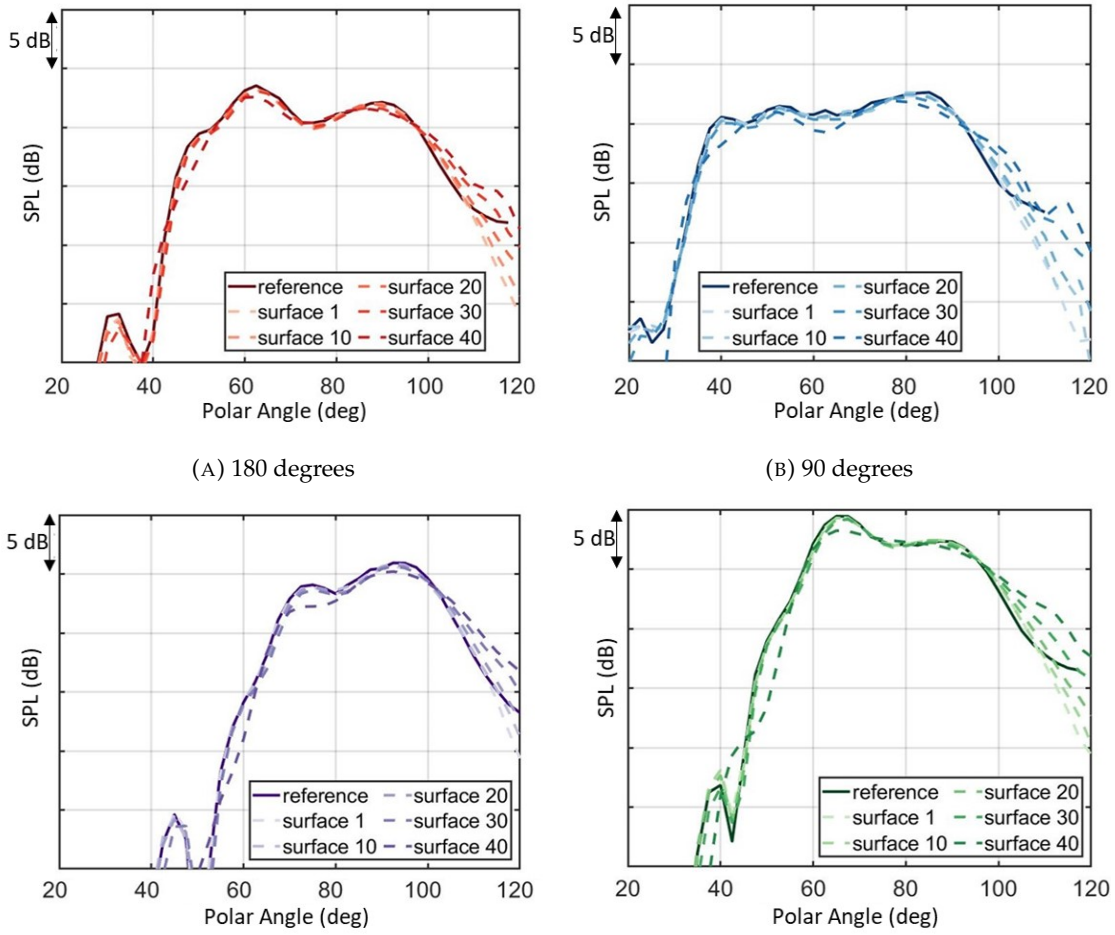

(A) 180 degrees

(B) 90 degrees

(C) 270 degrees

(D) 0 degrees

FIGURE 5.28: Far-field SPL (dB). Solid line indicates the reference AC- TRAN/TM result (IE), dashed lines show the results from using FWH from different axial surfaces, as indicated in Fig. 5.26.

5.3.1.6 Mode Sorting

Deciphering which modes to include or exclude from the acoustic modal sum is complex. For simpler applications, such as intakes with less or no modal scattering (particularly circumferential), modes that are poorly captured by the mesh are naturally excluded or insignificant to the sum. In this case, however, it was found that it is necessary to include such modes as they may have a significant effect on the overall solution.

The reason these modes are needed is considered to be because the solution is formed from an artificially reduced set of modes. These modes act as a substitute for modes not included in the reduced set, allowing scattering to and from these high-order

modes. Without this mechanism erroneous scattering into other (well-captured) modes takes place, resulting in incorrect/higher amplitude coefficients of the well-captured modes. This can be seen in the following examples showing areas of higher pressure amplitude and general noise in the solution; further resulting in poor far-field results.

In the current mode sorting arrangement, discerning the poorly captured modes has previously been possible through visual inspection of the axial wavenumbers and corresponding mode shapes/ eigenvectors. For the 3D case, however, due to the sheer number of modes and multiples of corresponding mode shapes/ eigenvectors, it is easiest to account for errors in mode sorting from inspecting the resulting solution. This was primarily through the consideration of the unsteady pressure inspected via contour plots, but also considered the accuracy of the far-field solution and other metrics included in the following sections.

However, propagating through the whole intake at once is computationally expensive. Therefore, for efficiency, the domain was divided axially into sections and the propagation process was applied to each of these smaller sections individually where they were inspected and altered iteratively. This allowed for the observation of changes to mode sorting to be made in greater detail and more efficiently.

Preliminary results for the whole intake had been initially produced, following the same mode sorting principles previously applied to the axisymmetric geometry. It was through dividing the domain, and iteratively refining the mode sorting (ultimately by expanding the modal sum), that the preliminary results were improved. This approach is recommended for future applications.

Figures 5.29 and 5.30 show examples of modes that were previously excluded (classified as high-order) from the modal sum, but were found to improve the overall result when included (classified as acoustic). In the top part of the figures a side-by-side comparison is shown of the axial wavenumbers at a fixed axial surface. The red box shows the corresponding radial pressure profiles for each circumferential mode corresponding to that wavenumber. The yellow box in the lower right corner of Fig. 5.29 shows a zoomed-in image of one of the radial pressure profiles.

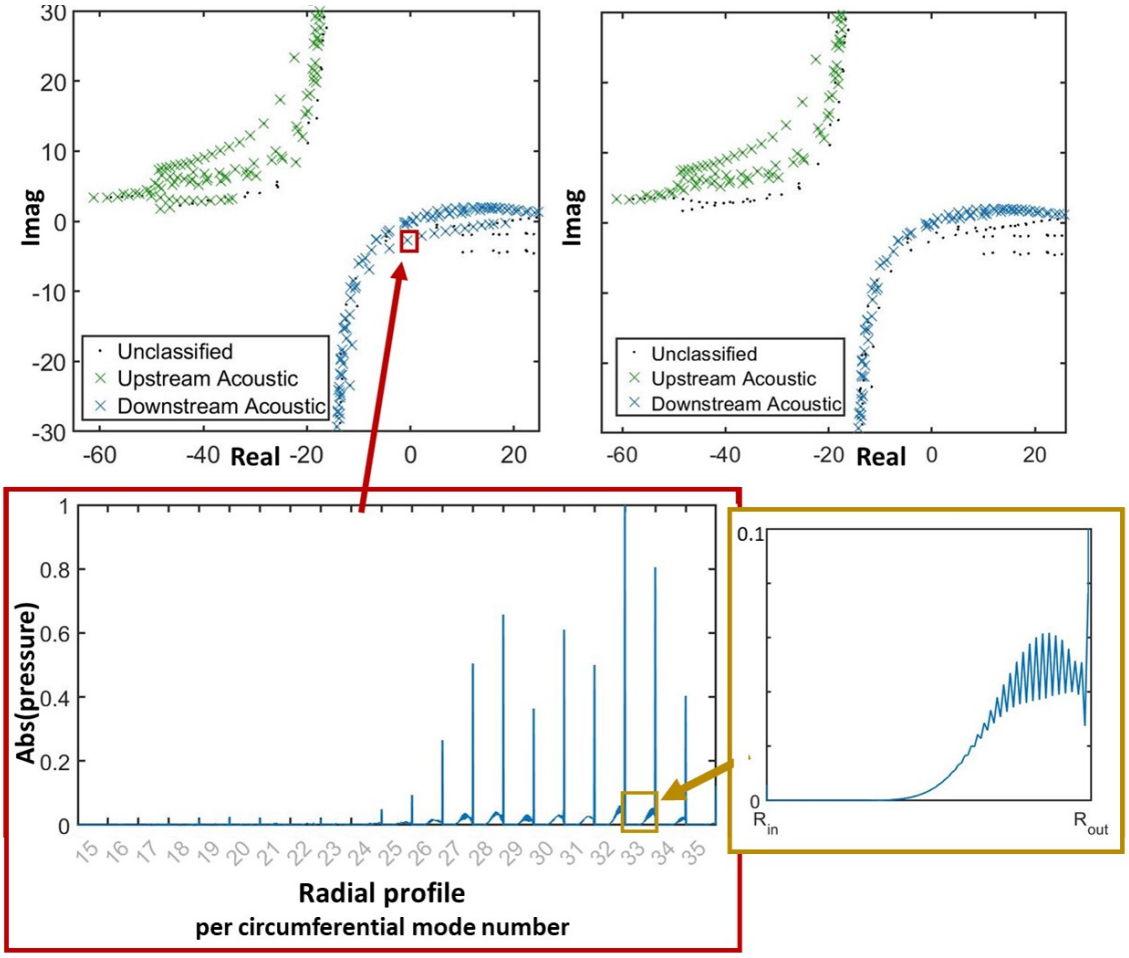

FIGURE 5.29: Axial wavenumbers at fixed axial surface, (top left) final version with more modes included, (top right) preliminary version with fewer modes included. (bottom left) Pressure profile of downstream mode representative of modes added to improve the result, (bottom right) zoomed-in radial profile of circumferential mode 33, amplitude on the vertical axis and radial position on the horizontal axis

It can be seen from Fig. 5.29 and 5.30 that these modes have highly oscillatory pressure profiles across the circumferential modal spectrum. Hence, why they were originally excluded from the modal sum.

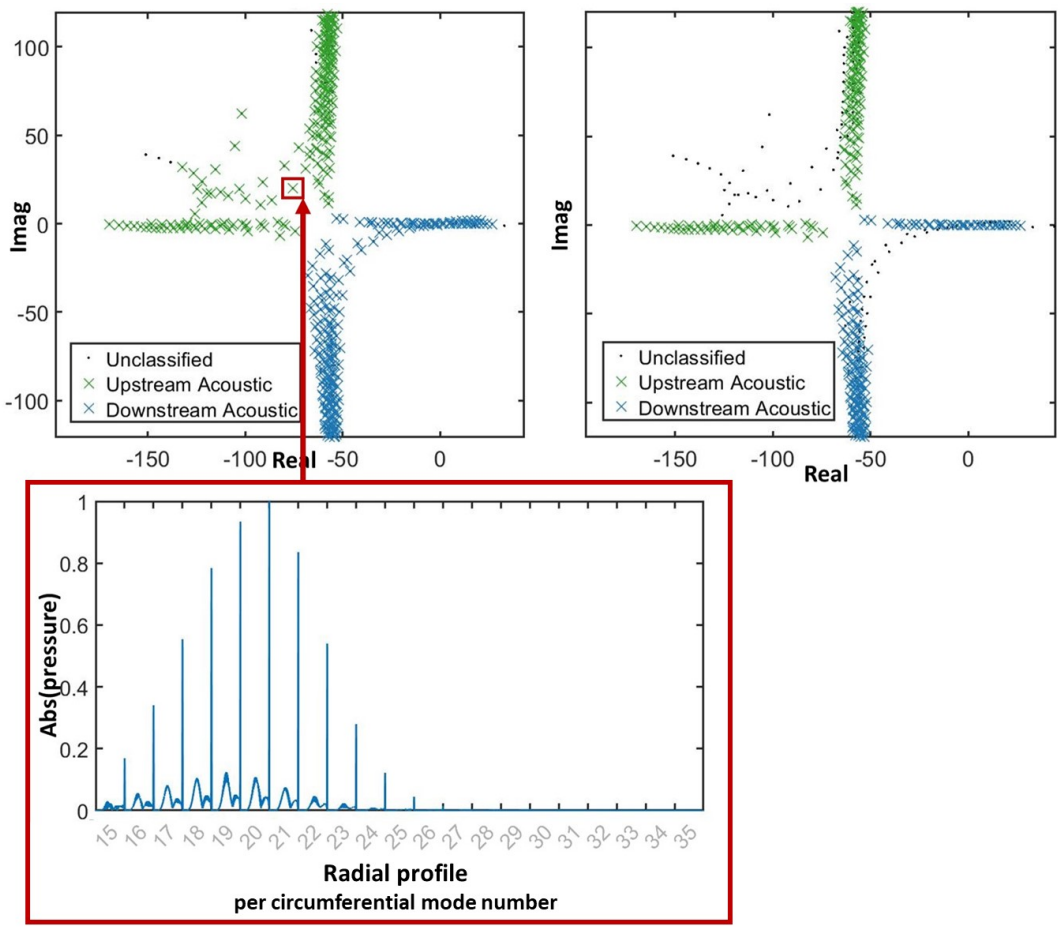

FIGURE 5.30: Axial wavenumbers at fixed axial surface, (top left) reported version with more modes included, (top right) preliminary version with less modes included. (bottom) Pressure profile of upstream mode representative of modes added to improve result

The following figures, 5.31 to 5.34, show contour plots of the real part of the acoustic pressure resulting from the two modal classification setups, the version on the right is the same as that used in the following results section and includes more modes classified as acoustic. They have been plotted on a narrow colour scale to deliberately accentuate the problem areas. It is evident that the final reported version still features some of these problem areas but to a lesser, non-detrimental, extent.

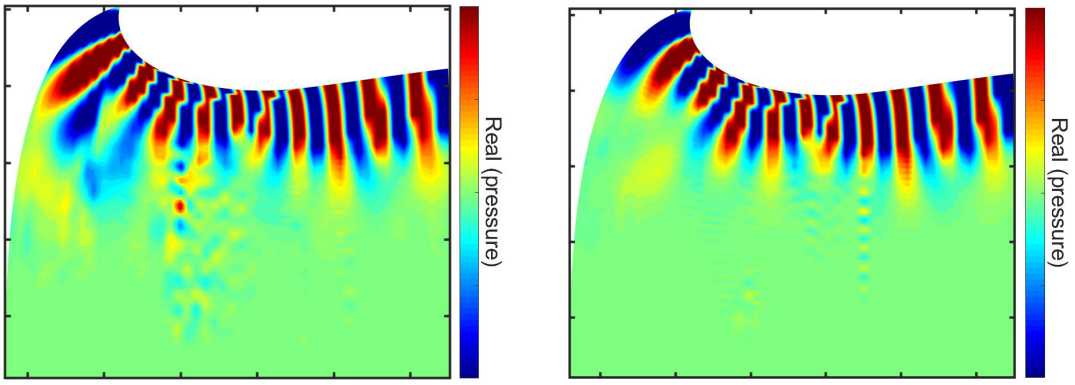

(A) preliminary result with less modes classified as acoustic

(B) reported result with more modes classified as acoustic.

FIGURE 5.31: 3D non-axisymmetric hard wall intake. Real part of acoustic pressure. Cut at fixed circumferential position 90 degrees.

Fig. 5.31 also shows an additional prominent region of high pressure at the upstream end of the duct section in the case with less acoustic modes included in the modal sum. It is thought that this is the result of high modal amplitude coefficients caused by modal scattering that would otherwise scatter to higher order modes not included in the modal sum; this appears to be confirmed by the right-hand figure where by more acoustic modes have been classified and this region of high amplitude no longer occurs.

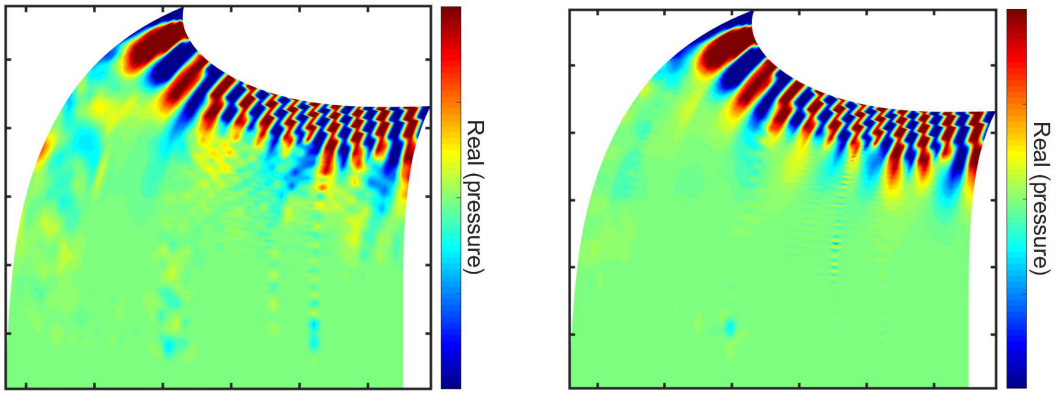

(A) preliminary result with less modes classified as acoustic

(B) reported result with more modes classified as acoustic.

FIGURE 5.32: 3D non-axisymmetric hard wall intake. Real part of acoustic pressure. Cut at fixed circumferential position 270 degrees.

Similarly to Fig. 5.31, Fig. 5.33 also shows areas of high pressure in the case with less acoustic modes. The areas of high amplitude both close to the outer wall and further inside the duct (radially) are removed once the number of acoustic modes is increased.

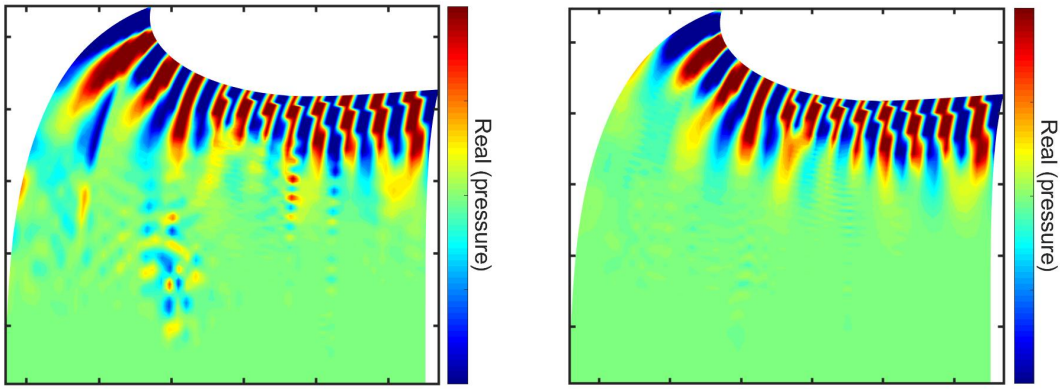

(A) preliminary result with less modes classified as acoustic

(B) reported result with more modes classified as acoustic.

FIGURE 5.33: 3D non-axisymmetric hard wall intake. Real part of acoustic pressure. Cut at fixed circumferential position 180 degrees.

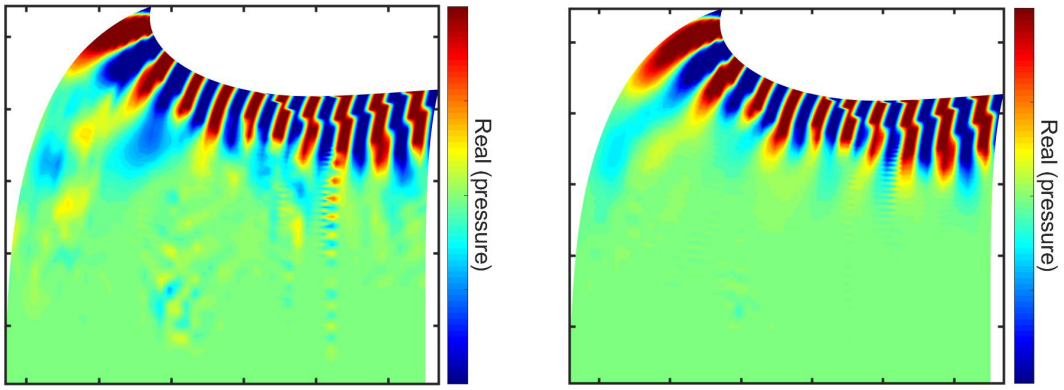

(A) preliminary result with less modes classified as acoustic

(B) reported result with more modes classified as acoustic.

FIGURE 5.34: 3D non-axisymmetric hard wall intake. Real part of acoustic pressure. Cut at fixed circumferential position 0 degrees.

Alternatively, it could be that the implementation of the EAGCC method on this intake requires more circumferential modes and/or increased mesh definition and this in turn could result in a lesser reliance on the poorly captured modes in the modal sum.

Ultimately further work is required to understand the modal behaviour, particularly of 3D non-axisymmetric modes, and to improve the modal sorting approach.

5.3.2 Hard wall duct results

Figs 5.35 shows the results for the 3D hard wall intake. The contour plots are shown as cuts taken at fixed circumferential positions to the centre axis (ref. Fig. 5.21). In the

result shown for 90 and 270 degrees, both the EAGCC and ACTRAN/TM results show the axial wavelength decreasing as the wave propagates upstream toward the highlight, before increasing again as it leaves the intake wall.

In the EAGCC results, there are some small pressure changes seen further radially from the outer wall that are not seen in the ACTRAN/TM result. This is likely to be a result of downstream reflections. There are small disparities in contour shapes throughout, most notably in the 270 degrees cut just upstream of the highlight. All these disparities, however, are subtle and assumed to be a result of incorrect mode sorting and therefore could be refined through improved mode sorting.

For the results shown at circumferential angles 180 and 0 degrees, the EAGCC results capture the circumferential variation in the pressure caused by the non-axisymmetric geometry and circumferential mean flow distortion, in agreement with the ACTRAN/TM results. Throughout Fig. 5.35 there are more areas of pressure change further away from the outer wall in the EAGCC results that are not visible in the ACTRAN/TM results.

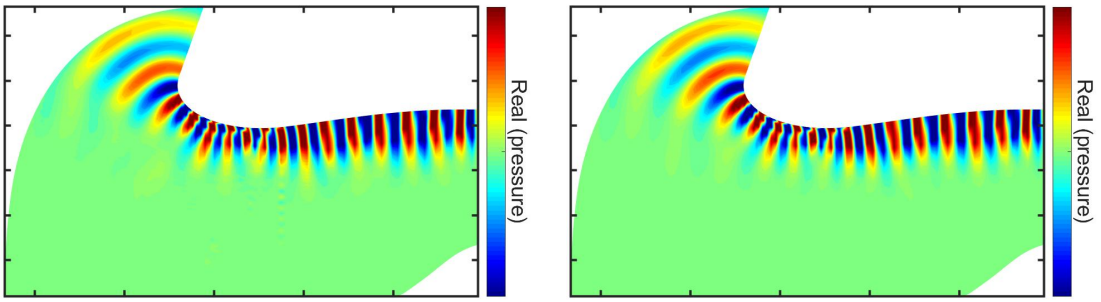

(A) EAGCC, cut at 90 degrees (B) ACTRAN/TM, cut at 90 degrees

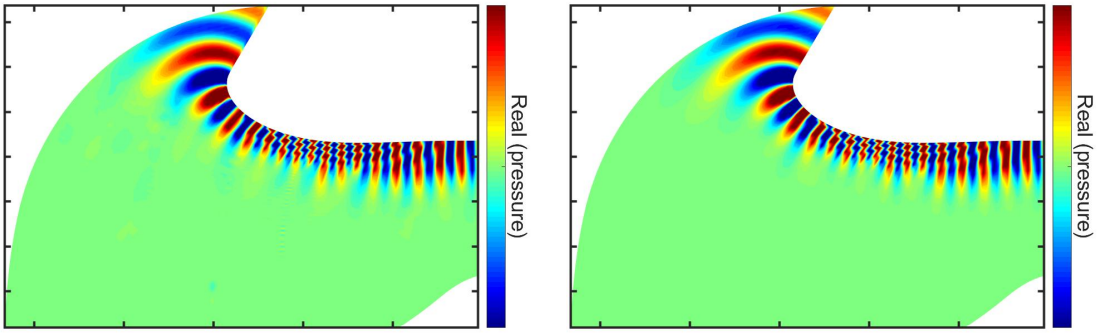

(C) EAGCC, cut at 270 degrees (D) ACTRAN/TM, cut at 270 degrees

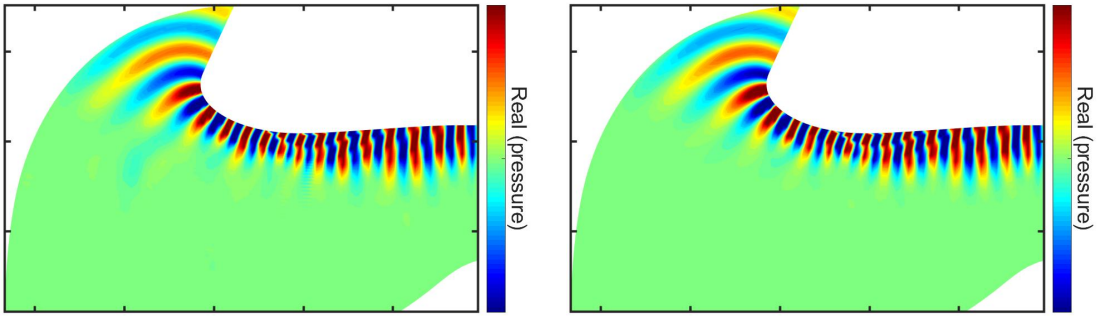

(E) EAGCC, cut at 0 degrees (F) ACTRAN/TM, cut at 0 degrees

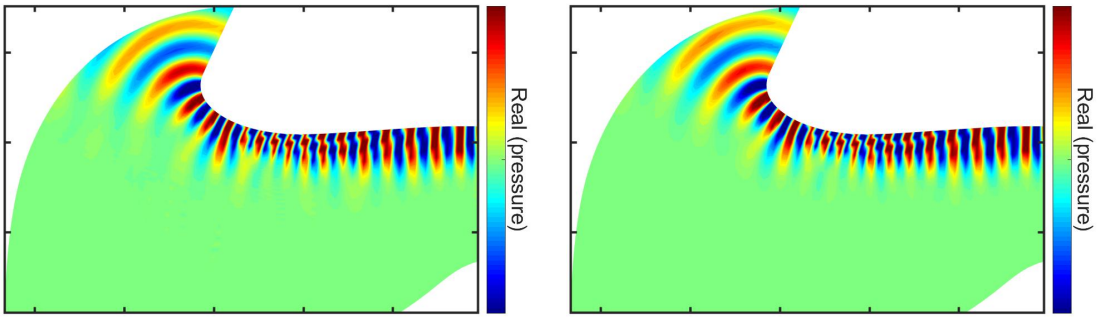

(G) EAGCC, cut at 180 degrees (H) ACTRAN/TM, cut at 180 degrees

FIGURE 5.35: 3D non-axisymmetric hard wall intake. Real part of acoustic pressure. Cuts taken at constant circumferential positions (ref. Fig. 5.21)

Fig. 5.36 and Fig. 5.3.2 plot the induct SPL (dB) along the outer wall and at two positions away from the outer wall, at fixed circumferential positions. For all circumferential positions, along the outer wall the EAGCC agrees with the ACTRAN/TM results within 2 dB. The general pressure profile along the outer wall, and at 20 radial points in from the outer wall, matches that of ACTRAN/TM.

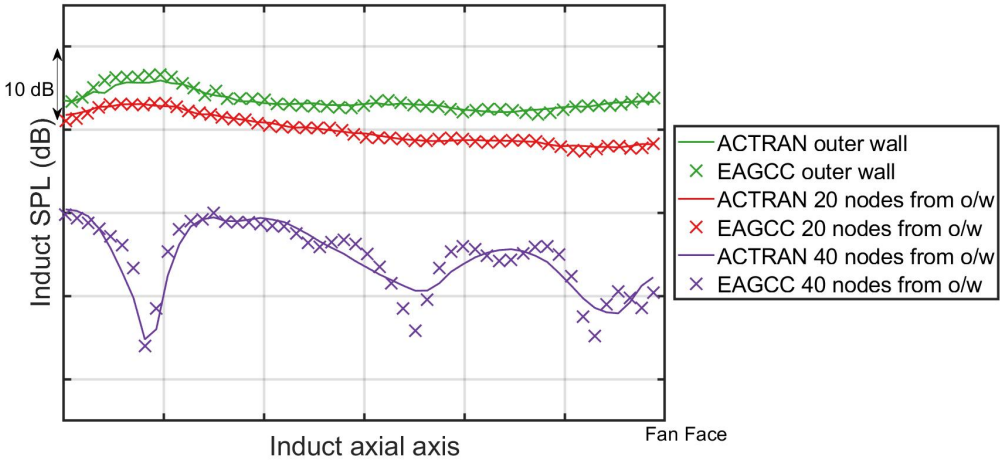

(A) 90 degrees

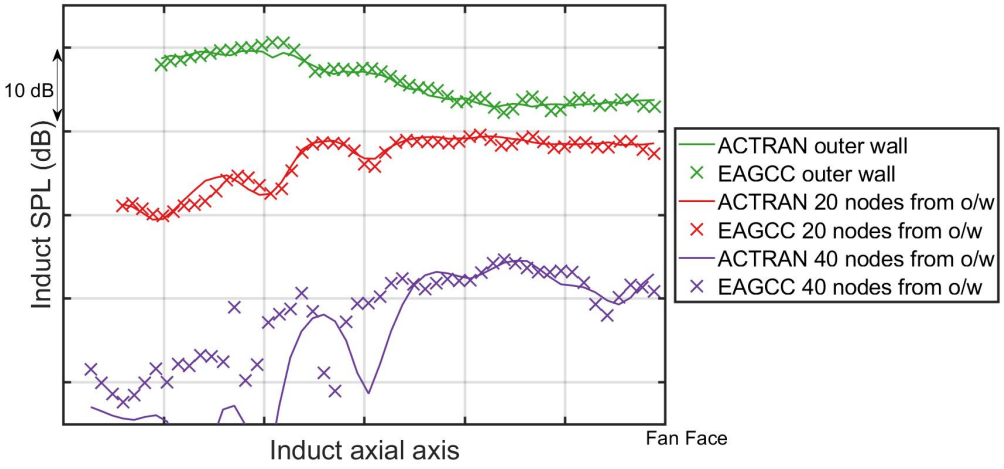

(B) 270 degrees

FIGURE 5.36: 3D non-axisymmetric hard wall intake. SPL (dB) induct, plotted at radial positions relative to outer wall. Taken at fixed circumferential positions 90 and 270 degrees.

At 40 radial points from the outer wall, there is the largest disparity between the two results. This is most pronounced at the circumferential position 270 degrees, where the biggest difference is just over 10 dB.

The EAGCC result is more oscillatory than ACTRAN/TM overall. This is thought to be a result of downstream reflections caused by incorrect mode sorting.

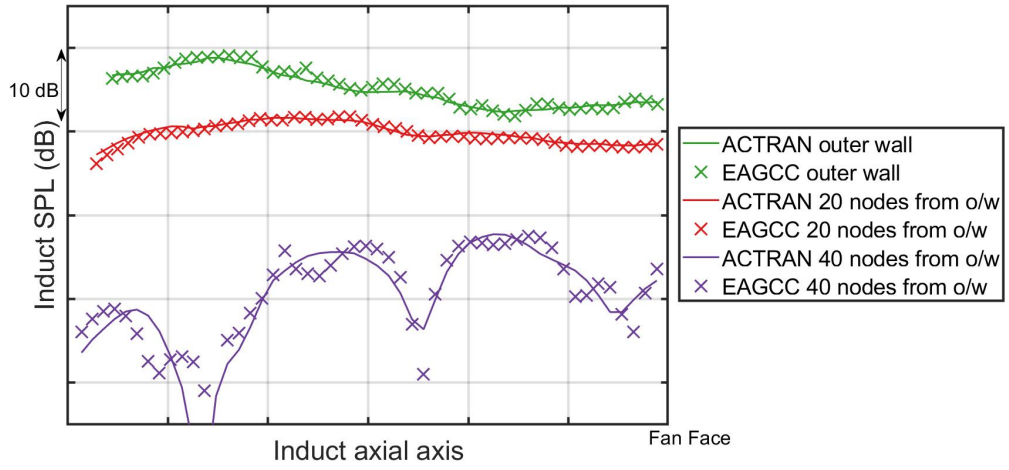

(A) 0 degrees

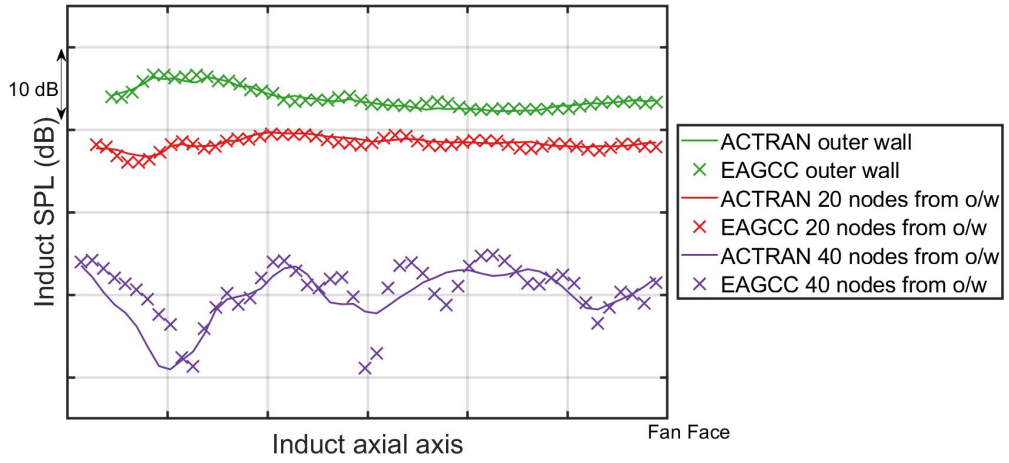

(B) 180 degrees

FIGURE 5.37: 3D non-axisymmetric hard wall intake.
SPL (dB) induct, plotted at radial positions relative to outer wall. Taken at fixed circumferential positions 0 and 180 degrees.

Fig. 5.39 shows the real part of the acoustic pressure viewed as circumferential cross-sections, given by taking cuts along axial mesh surfaces as shown in Fig. 5.38. The positions relate to the fan, the downstream and upstream end of the liner (in the lined case), the highlight and the near field, respectively. The position descriptor of these points corresponds to the outer wall position, but as cuts are taken along axial mesh lines and the mesh lines are not perpendicular to the axis, the position further in the duct will not necessarily correspond to this description as closely.

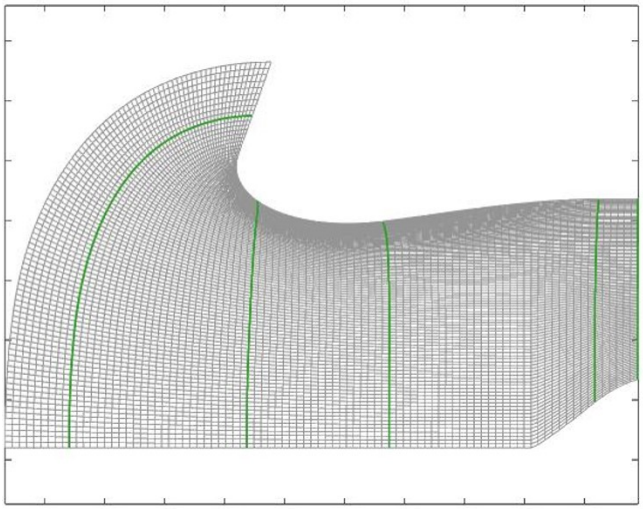

FIGURE 5.38: Mesh of reduced domain, side view of top (90 degrees), green lines indicate the axial positions of the cuts for the circumferential plots of Figs. 5.39 and 5.44.

In Fig. 5.39 the mean flow distortion due to the drooped non-axisymmetric geometry is shown to alter the sound field. The input mode, circumferential mode 24, is initially shown with 24 evenly shaped lobes seen at the source surface. The lobes start to twist anti-clockwise, as the wave travels upstream. This is well captured by the EAGCC result, with good agreement with ACTRAN/TM in phase and amplitude.

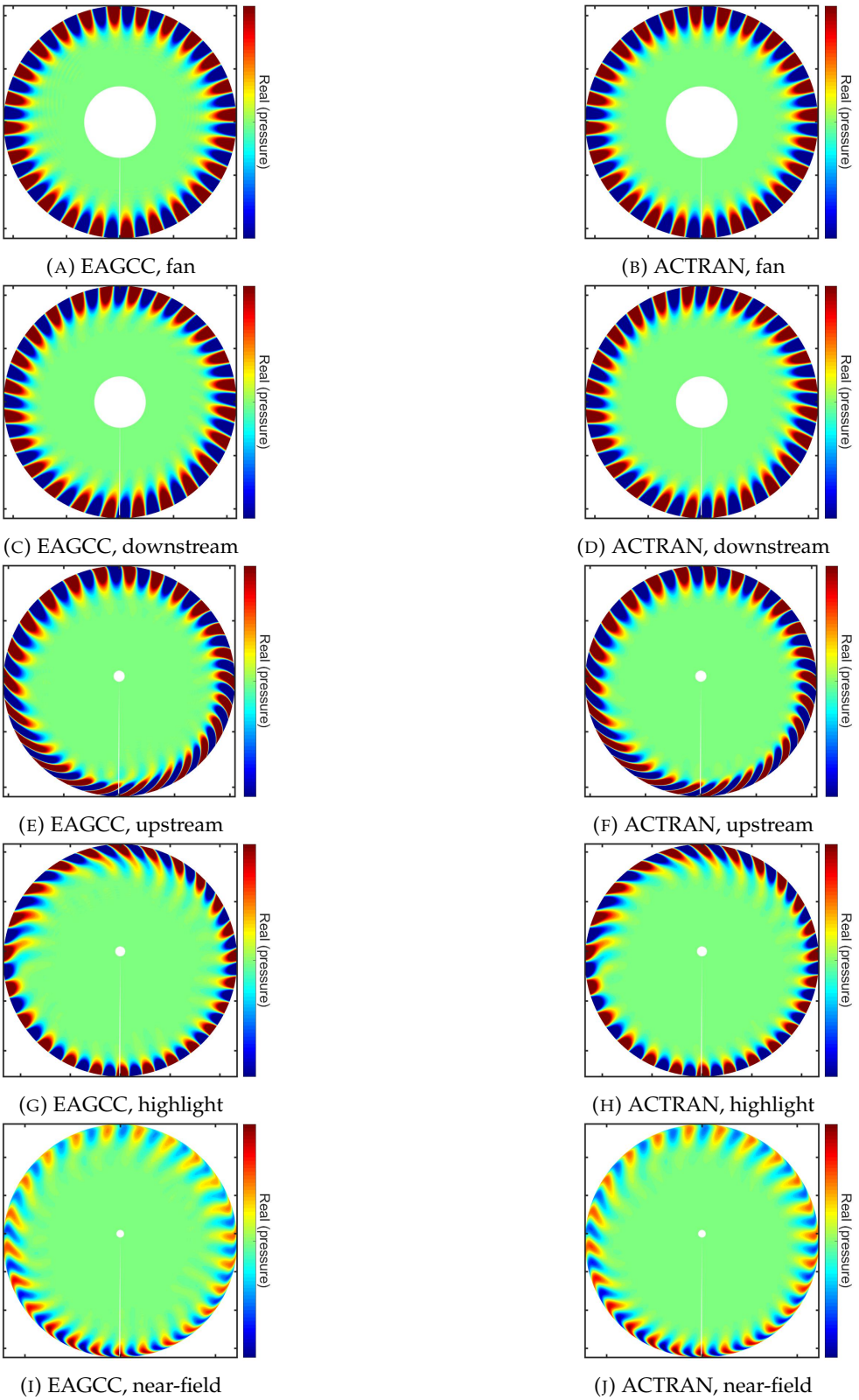

(A) EAGCC, fan (B) ACTRAN, fan

(C) EAGCC, downstream (D) ACTRAN, downstream

(E) EAGCC, upstream (F) ACTRAN, upstream

(G) EAGCC, highlight (H) ACTRAN, highlight

(I) EAGCC, near-field (J) ACTRAN, near-field

FIGURE 5.39: 3D non-axisymmetric hard wall intake. Real acoustic pressure. Cuts along axial mesh lines.

Fig. 5.40 shows the far-field directivity against polar angle at selected fixed circumferential positions. Unlike the axisymmetric case, for this intake the far-field

polar directivity is dependent on the circumferential angle, [34]. This is demonstrated in these approximate far-field results, where the profile and peak position are shown to vary circumferentially. The EAGCC and ACTRAN/TM results agree overall in amplitude within 2 dB, with the exception of low polar angles (maximum difference is less than 5dB). In all fixed circumferential positions, the general polar directivity is well captured. At 270 degrees and 0 degrees circumferentially, the peak positions of approx 92 degrees and 62 degrees are in agreement both in position and amplitude. For 180 degrees and 90 degrees, the peaks are within 1-2 dB in amplitude but there are some small differences in the profile particularly at the secondary peaks.

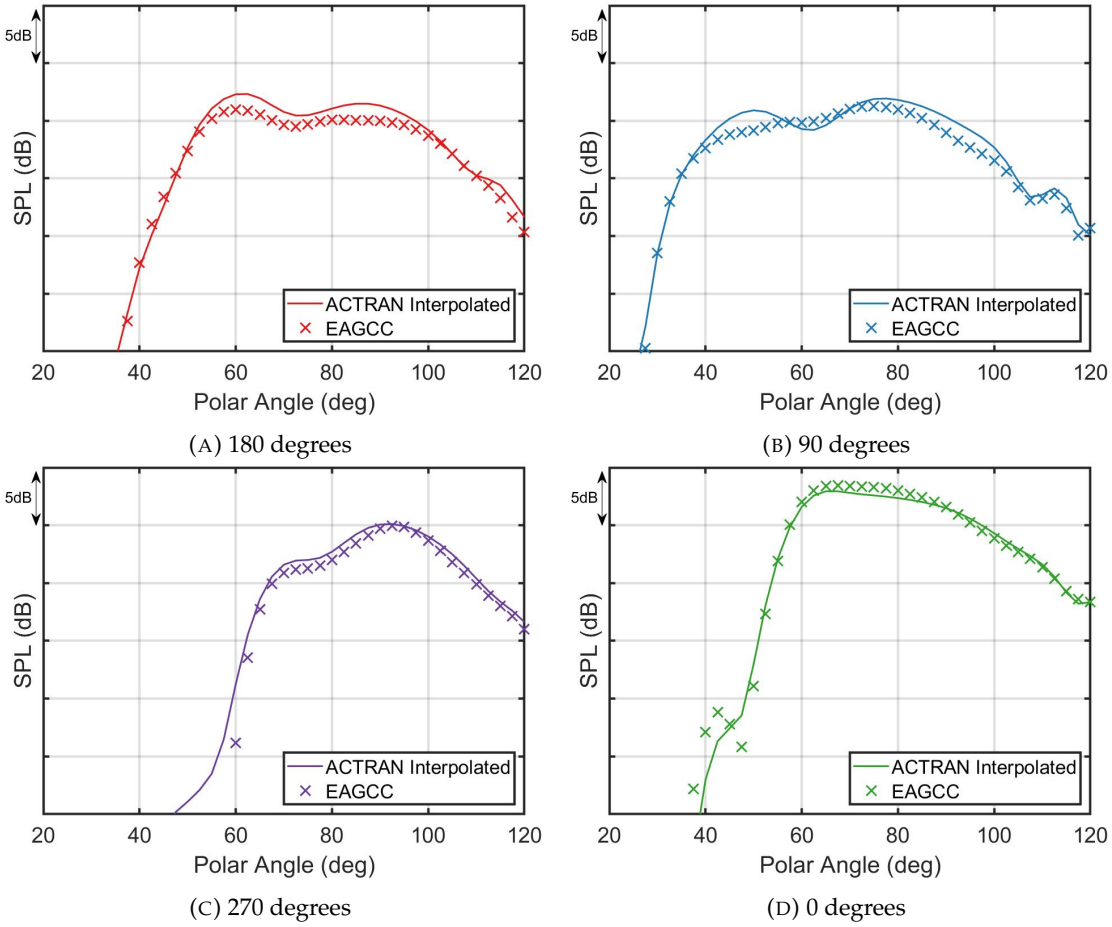

(A) 180 degrees

(B) 90 degrees

(C) 270 degrees

(D) 0 degrees

FIGURE 5.40: 3D non-axisymmetric hard wall intake. Far-field SPL (dB). Plots are at fixed circumferential positions.

5.3.3 Lined intake results

Fig 5.41 shows the real part of the unsteady pressure at cuts at constant circumferential position (ref. Fig. 5.21). The EAGCC result tends to be higher in amplitude compared to the ACTRAN/TM solution, this is seen upstream of the liner in the 90 degree cut and downstream of the liner in the 270 degree cut. The 0 degree view has the most noticeable disparity in amplitude, and at both 0 degrees and 180

degrees there are extra pressure fluctuations further away from the wall in the EAGCC result. In the 90 degree view there is less separation from the wall in the lined region. In the 270 degree cut there is some disparity in contour shape particularly downstream of the highlight, as well as extra pressure fluctuation further away from the wall. However, the disparities mentioned are small in magnitude.

Overall, Fig. 5.41 shows there is agreement between the two methods' results and the EAGCC result has successfully captured the effects of the liner including the movement of the maximum amplitudes of the lined modes away from the outer wall and the modal scattering upstream of the liner.

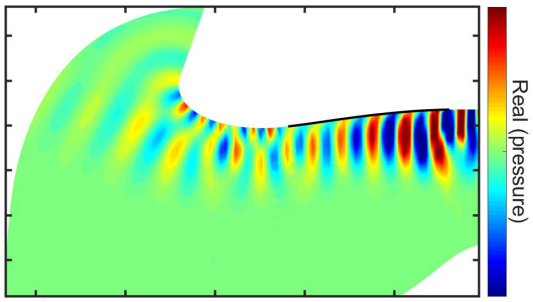

(A) EAGCC, cut at 90 degrees

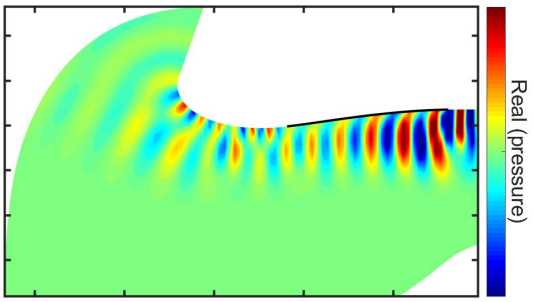

(B) ACTRAN/TM, cut at 90 degrees

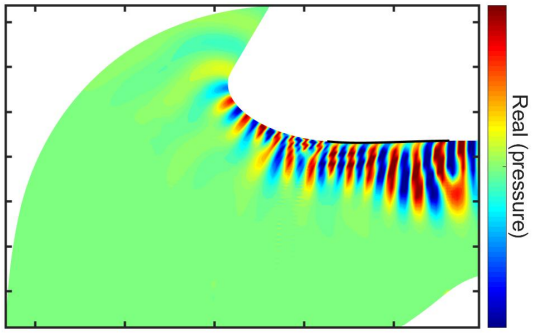

(C) EAGCC, cut at 270 degrees

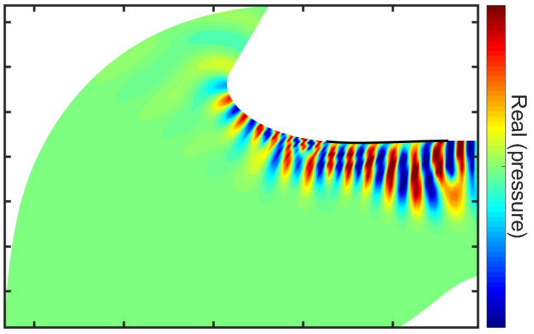

(D) ACTRAN/TM, cut at 270 degrees

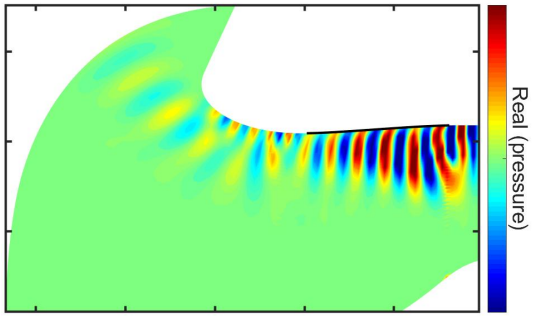

(E) EAGCC, cut at 0 degrees

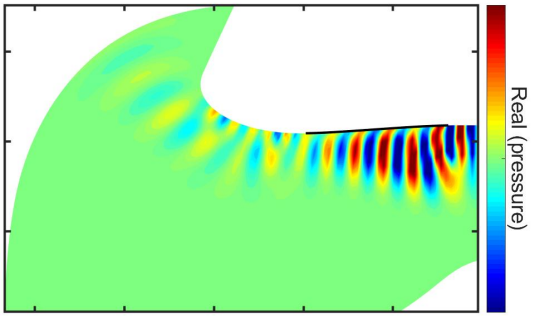

(F) ACTRAN/TM, cut at 0 degrees

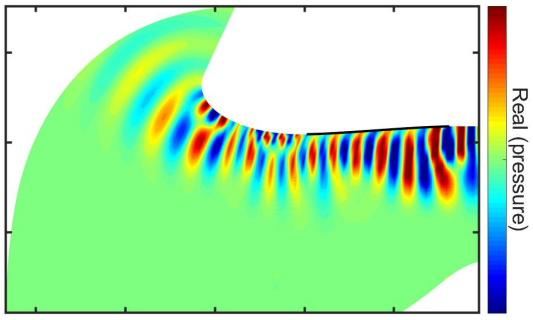

(G) EAGCC, cut at 180 degrees

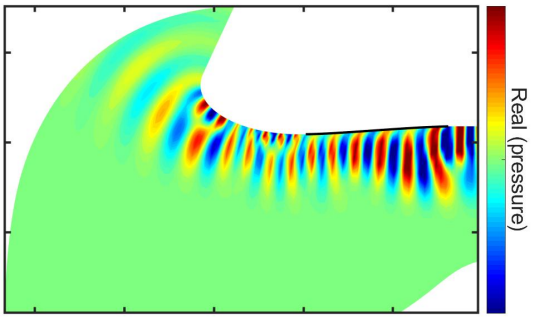

(H) ACTRAN/TM, cut at 180 degrees

FIGURE 5.41: 3D non-axisymmetric lined intake. Real part of acoustic pressure. Cuts taken at constant circumferential positions (ref. Fig. 5.21)

Fig. 5.42 shows the SPL along the outer wall for the induct region at fixed circumferential positions. At all circumferential positions the sharp attenuation caused by the liner is well captured by the EAGCC result. Further upstream in the liner the pressure fluctuations follow a similar profile in both but the EAGCC result is consistently 1-3dB higher and oscillates more than the ACTRAN/TM result. This is thought to be due to downstream reflections.

Overall, the EAGCC and ACTRAN/TM profiles are consistent but there is some difference in amplitude generally up to 5dB of each other. The greatest difference between the EAGCC and ACTRAN/TM results is seen at the upstream end of the liner at 270 degrees, where there is a 17 dB difference, however, this is only seen at this intersecting surface and is expected to be a result of the discontinuity caused by the liner.

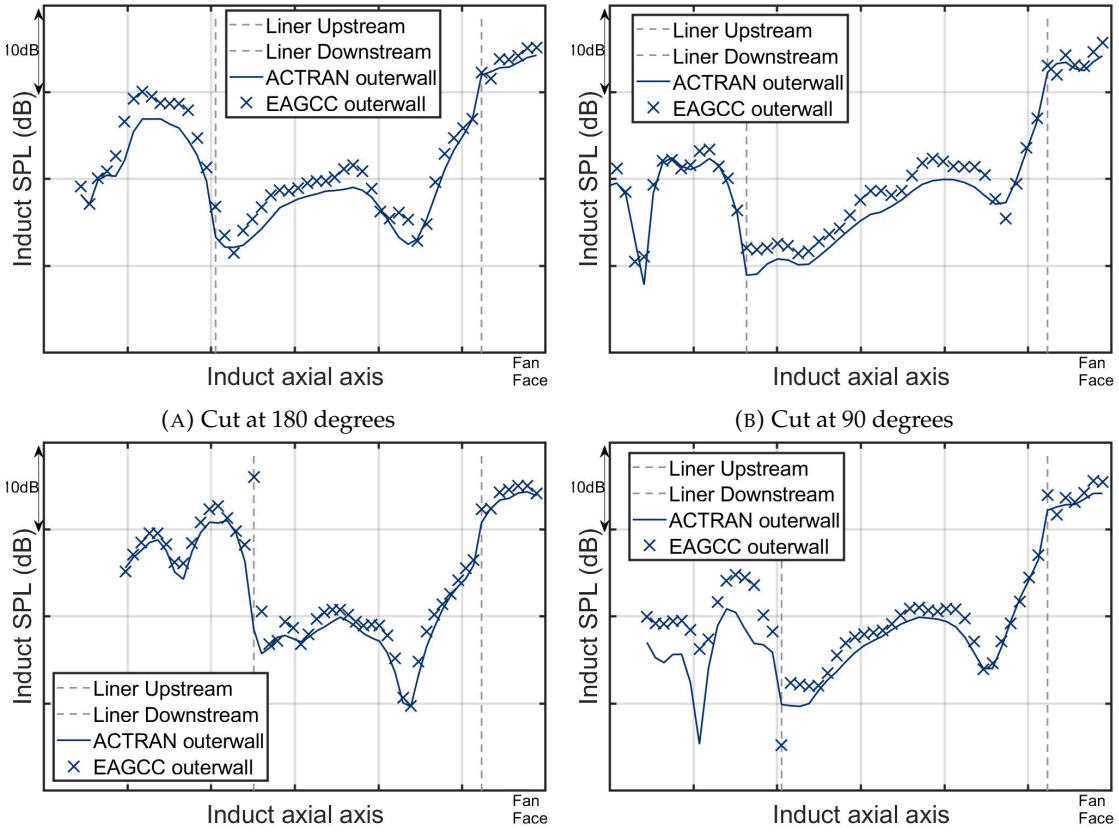

(A) Cut at 180 degrees

(B) Cut at 90 degrees

(C) Cut at 270 degrees

(D) Cut at 0 degrees

FIGURE 5.42: 3D non-axisymmetric lined intake. Induct SPL (dB). For induct region refer to Fig. 5.22.

Fig. 5.43 looks at the pressure away from the outer wall, it is shown that the large disparity present at the outer wall is not seen further into the duct. At radial positions 5, 10 and 20 points from the outer wall the results agree within 1-2 dB, for 40 points away there is a greater difference within 5 dB.

The sharp decrease in SPL seen at the outer wall, Fig. 5.42, at the downstream end of the liner is a result of the maximum pressure in the lined modes occurring further away from the wall as seen in Fig. 5.41. This is also seen in Fig. 5.43 where the magnitude of the attenuation from the downstream end of the liner is shown to decrease with distance from the outer wall.

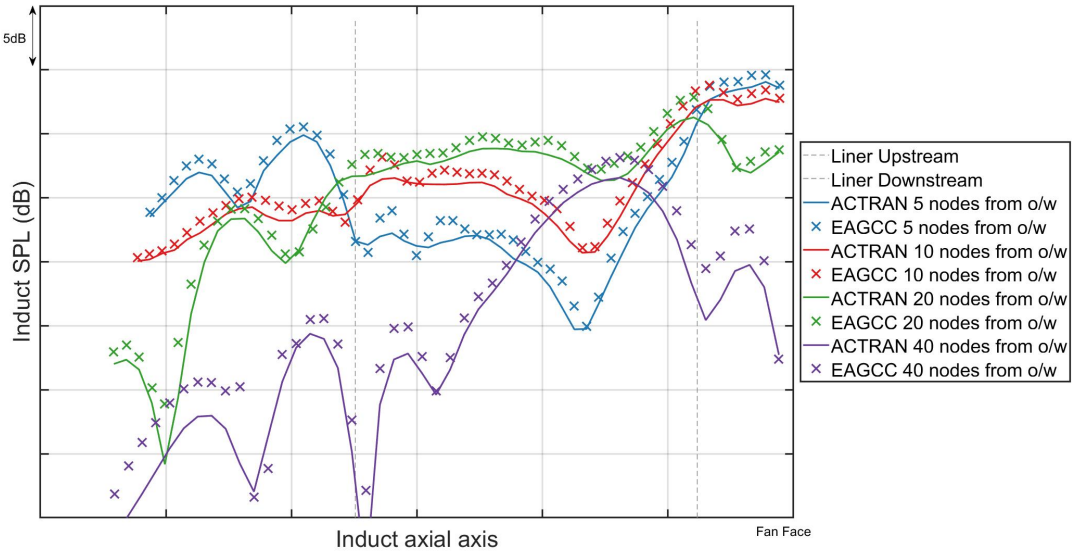

FIGURE 5.43: 3D non-axisymmetric lined intake. Induct SPL (dB) plotted at relative radial mesh positions to the outer wall (o/w).

Fig. 5.44 shows the circumferential variation in pressure at selected fixed axial slices, as described in Fig. 5.38. The EAGCC captures the same circumferential variation in the effect of the liner as ACTRAN/TM, including the higher attenuation at the upstream end of the liner in the 0 to 90 degree region (top right) and the modal scattering on the left side in the region close to the highlight. The EAGCC result is sometimes higher in amplitude and features some small erroneous pressure fluctuation, likely resulting from the inclusion of some high-order mode in the mode sorting.

There is a presence of false pressure changes shown at the inner wall at the downstream liner end which are thought to be caused by the existence of radial modes with pressure profiles that are high in amplitude at the inner wall. The current implementation of the boundary condition allows this, but this could be easily altered to remove this.

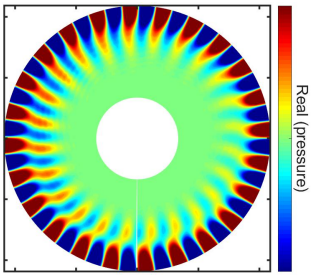

(A) EAGCC, fan

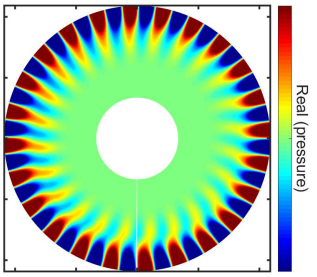

(B) ACTRAN, fan

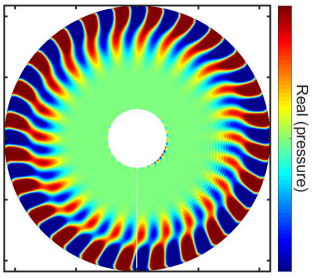

(C) EAGCC, downstream liner end

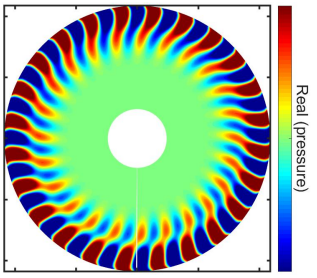

(D) ACTRAN, downstream liner end

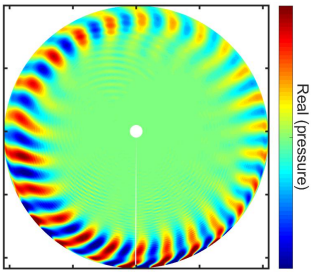

(E) EAGCC, upstream liner end

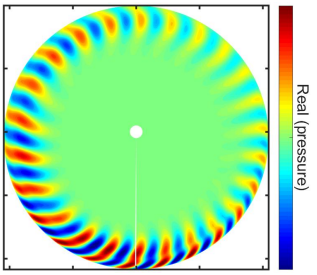

(F) ACTRAN, upstream liner end

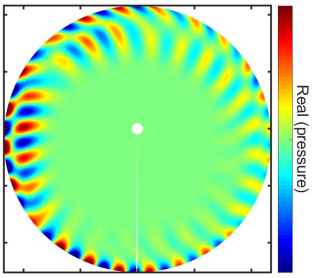

(G) EAGCC, highlight

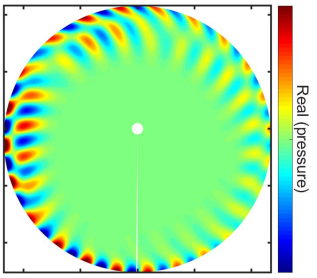

(H) ACTRAN, highlight

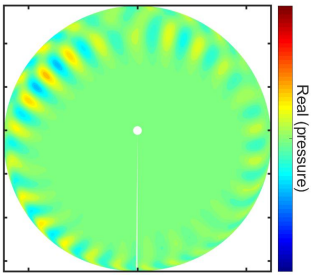

(I) EAGCC, near-field

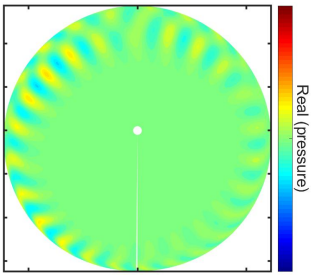

(J) ACTRAN, near-field

FIGURE 5.44: 3D non-axisymmetric lined intake. Real acoustic pressure. Cuts along axial mesh surfaces.

The far-field sound pressure level at four fixed circumferential positions is shown in Fig. 5.45. The circumferential variation in the polar directivity is more prominent in the lined case, and the EAGCC results capture this. The EAGCC far-field directivity at circumferential angle 0 degrees agrees well with the ACTRAN/TM result. The EAGCC results for the other three circumferential angles are within 3 dB of the reference solutions, and are generally consistent in profile, including polar position and amplitude of peaks and troughs.

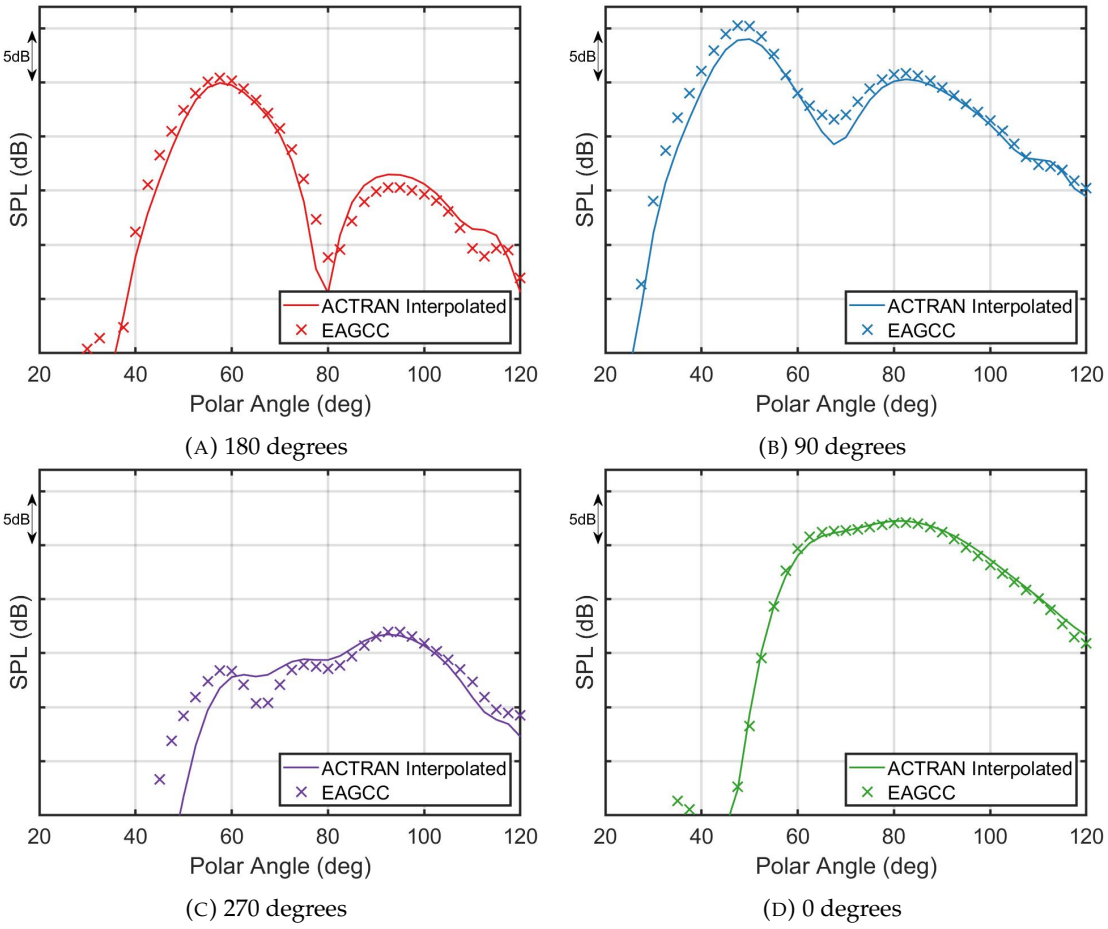

(A) 180 degrees

(B) 90 degrees

(C) 270 degrees

(D) 0 degrees

FIGURE 5.45: 3D non-axisymmetric lined intake. Far-field SPL (dB). Plots are at fixed circumferential positions.

5.4 Run time

An investigation has been carried out to characterise the expected run time and computational expense of applying the EAGCC method to 3D intakes.

All run-time values have been produced by running the EAGCC method on the computer cluster IRIDIS 5 at the University of Southampton. For the computations discussed below, the cluster is comprised of a large number of nodes, each with 40 CPUs and 192 GB of memory. The full list of properties of the cluster can be found at [150].

Fig. 5.46 shows the proportion of total elapsed wall time each step of the method takes. Note that this is without the additional parallelisation, as discussed in section 3.9.2, of the matriculate function.

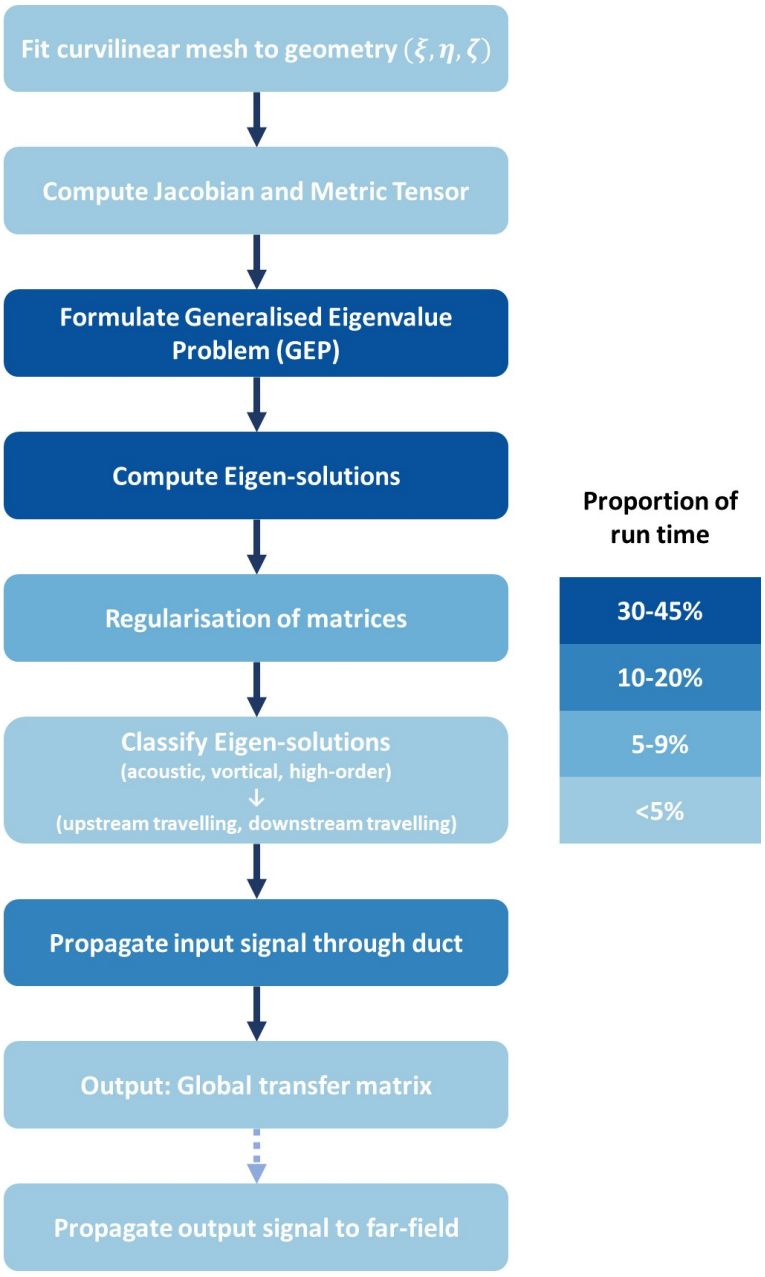

FIGURE 5.46: Flowchart of EAGCC code, coloured proportionally to elapsed run-time for 3d case presented.

The most computationally expensive steps in the method are: forming the generalised eigenvalue problem, computing the eigen solutions, and the propagation. The first two form the eigen-analysis which is set up to run in parallel as they only act on one axial surface at a time. The proportions shown in Fig. 5.46 assume these steps are run in parallel, each axial surface simultaneously. The propagation step, however, must be run in serial and scales with the number of axial surfaces in the propagation.

Looking at the eigen-analysis steps in more detail, the eigen-analysis function in the duct class includes the formation of the GEP (A and B matrices Eqn. 3.19) by the

'matriculate' function, the inclusion of the boundary conditions, and the computation of the eigen-solutions themselves using MATLAB's built in 'eig' function [145].

The proportion of computation time taken by these different stages, as part of the total eigen-analysis function, is shown in Fig. 5.47. Included in this function is a parfor loop (a loop in which the iterations are run in parallel) that loops through axial surfaces, and the two steps that take the longest within this parfor are the matriculate and eig functions.

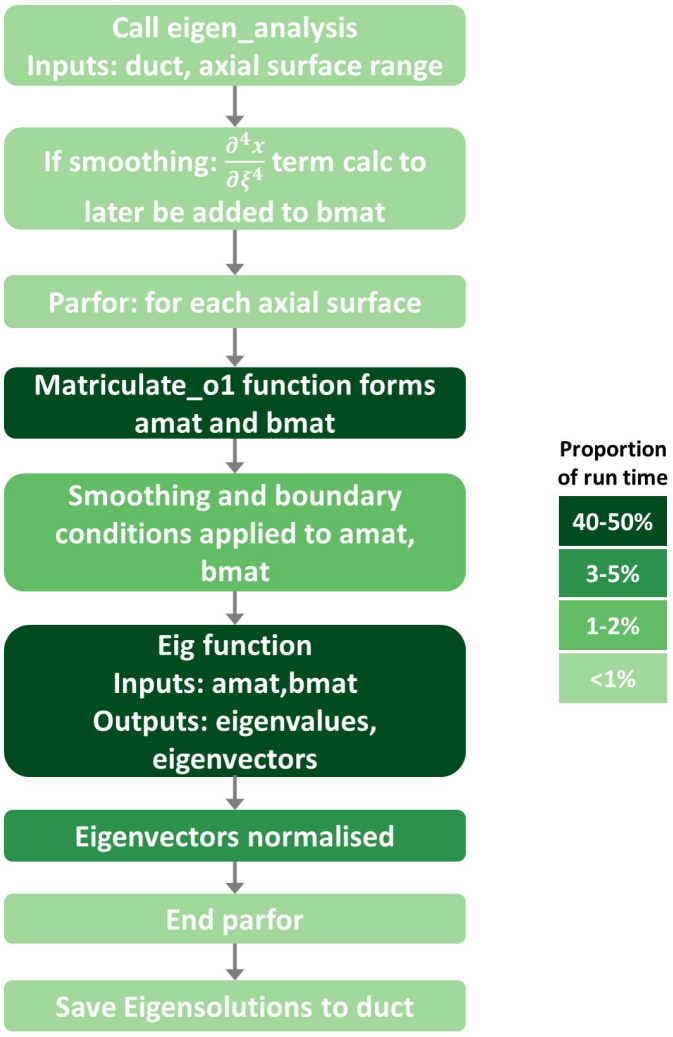

FIGURE 5.47: Flowchart of complete eigen-analysis function that includes forming GEP and computing eigen-solutions. Proportion applicable for most 3D cases.

The amount of time the eigen-solve and matriculate functions take to run is related to the size of the matrices in the GEP. This is a product of $(2 \times m + 1) \times 4 \times nr$ where m is the number of circumferential modes and nr is the number of radial points. Fig. 5.48 illustrates how the computation time scales with the matrix size. This was obtained by applying the EAGCC method to the hard wall 3D intake case presented in section 5.3 of this chapter. The number of circumferential harmonics included in the solution was adjusted to change the matrix size, before the eigen-analysis function was used to

compute the GEP and eigen-solutions for two surfaces, on two cores in parallel, on IRIDIS 5. The average wall-time for each matrix size is shown in Fig. 5.48.

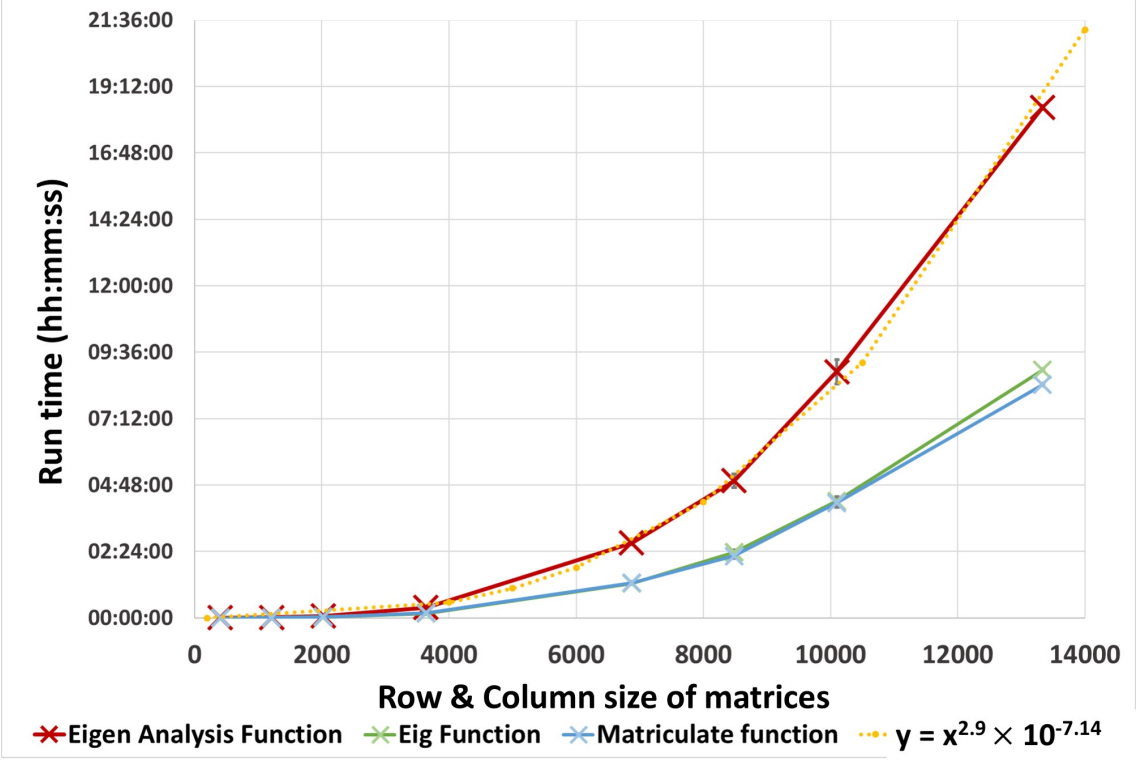

FIGURE 5.48: Wall time plotted against matrix size, two cores - one surface per core. Error bars show standard error for multiple runs.

Fig. 5.48 shows that the run time, y, of the total eigen analysis function is related to the row or column size of the matrix, x by

$$y = x^{2.9} \times 10^{-7.14}. \tag{5.1}$$

The eig and matriculate functions are both approximately half this time each. This is without any optimisation made to the matriculate function, however.

The parallelisation of the matriculate function, as discussed in section 3.9.2, leads to a reduction in computation time. This reduction is proportional to the size of the matrices in the GEP. For three-dimensional geometries, the row/ column size of the matrices will likely be great enough that a significant reduction in computation time is gained. Fig 5.49 shows the wall time of the original and parallelised matriculate functions for a range of matrix dimensions.

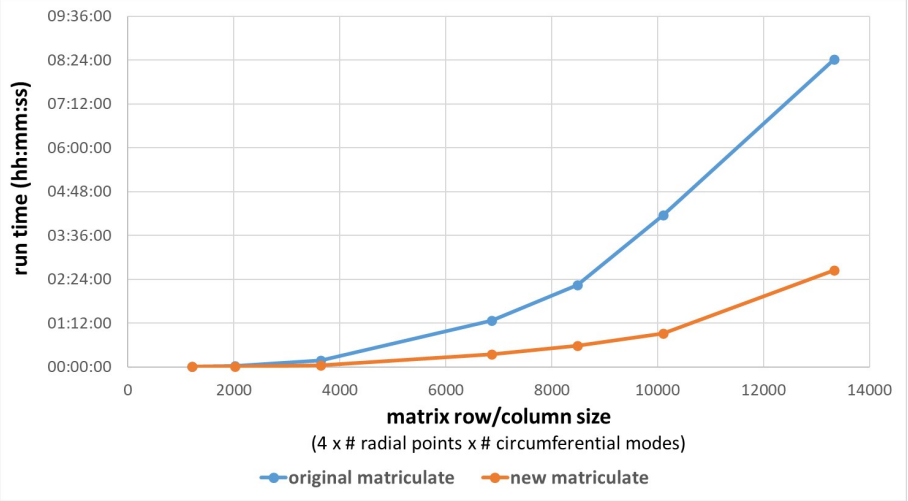

FIGURE 5.49: Wall time of the two matriculate functions plotted against matrix size.

5.4.1 Computational expense specific to example intake case

The expected wall time to produce the EAGCC solution for the intake presented in section 5.3 is approximately 6 hours 21 minutes. This would require 9 nodes, each using 147 GB RAM across 10 cores, one surface per core. This set up would have an expected core time of 18 days 15 hours (447 hours).

With the additional parallelisation of the matriculate function, this wall time would be expected to reduce to around 4 hours.

There are, however, practical computational limitations to consider. For example, access to four cores per surface and around 20 GB of RAM per surface is required so it may not be possible to run all surfaces in parallel at one time.

Other ways of utilising this reduction in computation time are possible, for example, if half of the surfaces were computed in parallel, at a time, this would still reduce the overall run-time of this case by around an hour.

The reference solutions computed by ACTRAN/TM were also produced on the computer cluster IRIDIS 5. The wall time for the lined 3D case, section 5.3.3, was 3 hours 15 mins. This was done by utilising 4 nodes, each using 1 core multi-threading (4 threads). The core time was 1 day 6 hours (30 hours), and 78GB of memory was used. This is around half to three-quarters of the expected wall time of the EAGCC method and considerably less expensive in terms of memory, processors and core time.

It is noted that as the geometry is symmetric about the vertical axis the ACTRAN/TM solution was computed using ACTRAN's sym-asym tool, which considerably reduced the amount of memory needed compared to running the full 3D version.

5.5 Summary

The investigation into run time discussed the relationship between matrix size and wall time for the EAGCC method and how the expected wall time increases with the matrix size. The matrix size itself is dependent on several factors including the extent of circumferential and radial mode scattering as a consequence of geometry and mean flow, as well as mesh resolution and input frequency.

The 3D non-axisymmetric intake presented in section 5.3 features non-axisymmetric geometry and mean flow distortion resulting in circumferential modal scattering. As a result, the matrix sizes are large and the computation time of the EAGCC solution is longer than that of the ACTRAN/TM. Furthermore, to compute the EAGCC solution in a time competitive to that of ACTRAN/TM the computational expense, in the way of memory requirements and accessible processors, is extensive and far greater than that needed by ACTRAN/TM for this specific case.

More generally, any given intake will have certain intricacies that affect the computational demands of either method. The number of circumferential modes required to capture the scattering will differ, which will have a significant effect on the computational expense of the EAGCC method. For cases at higher BPF, a wider range of circumferential modes will be required, but also an increased mesh resolution which will increase the computational expense of both EAGCC and ACTRAN/TM. Whereas some intake geometries will not be suitable for ACTRAN/TM sym-asym tool which would increase the memory requirement and the wall time.

One benefit of the EAGCC method is that the global transfer matrix can be re-used for different input signals without re-running the method and therefore little increase to the run time. For a case with significant modal scattering, such as the one featured in section 5.3, this has some limitations without including more circumferential modes in the original model. This could be a useful tool for considering multiple input modes, particularly in cases with less circumferential modal scattering.

At this stage of development of the EAGCC method, the indication from this validation exercise is that ACTRAN/TM is a more reliable and efficient tool for predicting the induct and far-field propagation for 3D intakes. However, the EAGCC method provides a useful analysis tool to break down these cases and explore the modal content. Furthermore, the EAGCC method has been shown to produce similar results to ACTRAN/TM for both hard wall and lined axisymmetric and non-axisymmetric intake geometries.

Chapter 6

Double Linear Approximation

The previous chapter demonstrated the applicability of the EAGCC method to fully three-dimensional intakes. However, it was also shown that it is computationally expensive compared to the finite element solver ACTRAN/TM.

With the parallelisation of the 'matriculate' function, the most computationally expensive part of the calculation is the computation of the eigen-solutions themselves. If the eigen-solve step in the EAGCC method is bypassed, the computational cost is expected to be significantly reduced. This chapter introduces an extension to the EAGCC method that employs such an idea.

6.1 Methodology

The scenario considered throughout this chapter is as follows:

1. The EAGCC method is applied to a given intake to produce a **base solution**
2. Small changes are made to the mean flow in a region of the intake
3. The 'double linear' extension is used to approximate the change in acoustic field resulting from the mean flow perturbation without recalculating the eigen-solutions.

This chapter looks solely at changes to axial mean flow.

Fig. 6.1 shows the flowchart of the EAGCC method seen in Chapter 3 (Fig. 3.1) with the addition of the proposed double linear extension in red, which is shown to bypass the eigen-solve stage of the original method.

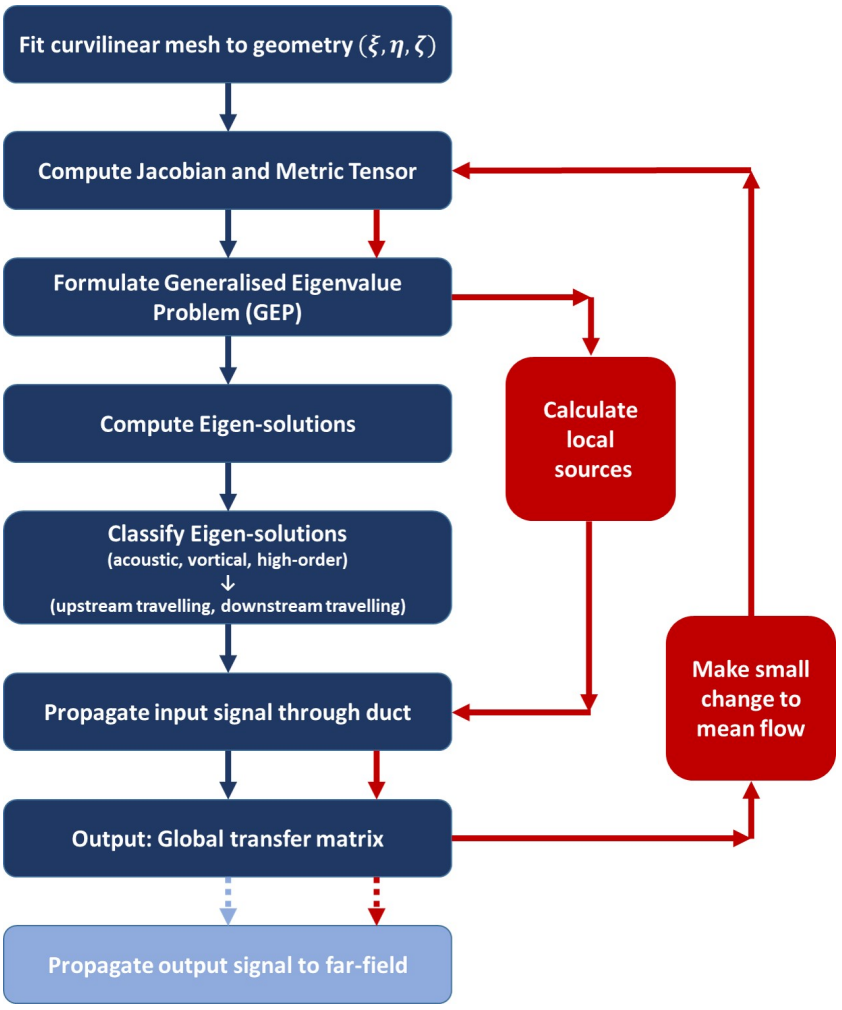

FIGURE 6.1: Flowchart of EAGCC process in blue with the proposed double linear extension in red.

6.1.1 Derivation

In the EAGCC method [6] the governing equations are formed into a generalized eigenvalue problem which is solved to give eigen-solutions. After propagating the input signals throughout the duct, the final solution $\mathbf{f}$, in the form of the eigenvectors multiplied by complex coefficients, is found such that

$$A\frac{\partial \mathbf{f}}{\partial \zeta} = B\mathbf{f} \tag{3.19}$$

where $\mathbf{f}$ here represents the solution vector of the system in the form $\mathbf{f} = \begin{pmatrix} u_\xi \\ u_\eta \\ u_\zeta \\ p \end{pmatrix}$ including values at each meshpoint. As seen in Chapter 3, A and B here denote

matrices formed by the linearised Euler equations discretised in the radial and circumferential direction.

Following the scenario introduced in the previous section, the base problem can be represented in the GEP form such that,

$$A_0 \frac{\partial f_0}{\partial \zeta} = B_0 f_0. \tag{6.1}$$

After small changes are made to the intake, the final problem is represented by Eqn. 3.19, with solution vector f. As the proposed changes to mean flow are considered small, it is assumed that the A and B matrices and solution vector can be expressed as a summation of the base problem/solution and a small perturbation resulting from the change to mean flow, such that

$$A = A_0 + A' \tag{6.2}$$

$$B = B_0 + B' \tag{6.3}$$

$$f = f_0 + f'. \tag{6.4}$$

Substituting the above equations into Eqn. 3.19

$$(A_0 + A')\frac{\partial}{\partial \zeta}(f_0 + f') = (B_0 + B')(f_0 + f') \tag{6.5}$$

When it is assumed the changes to the system are small, the $A'f'$, $B'f'$ terms are assumed sufficiently small to be neglected. Therefore, after expanding the brackets

$$A_0 \frac{\partial f_0}{\partial \zeta} + A_0 \frac{\partial f'}{\partial \zeta} + A' \frac{\partial f_0}{\partial \zeta} = B_0 f_0 + B_0 f' + B' f_0 \tag{6.6}$$

to first order in the perturbation variable. From Eqn. 6.1 it is known that

$$A_0 \frac{\partial f_0}{\partial \zeta} - B_0 f_0 = 0 \tag{6.7}$$

Hence,

$$A_0 \frac{\partial f'}{\partial \zeta} + A' \frac{\partial f_0}{\partial \zeta} = B_0 f' + B' f_0 \tag{6.8}$$

and therefore,

$$A_0 \frac{\partial f'}{\partial \zeta} - B_0 f' = A' \frac{\partial f_0}{\partial \zeta} - B' f_0. \tag{6.9}$$

Looking at the left-hand side of Eqn. 6.9, this has the same A_0, B_0 as the base problem (Eqn. 6.1) which means that the eigen analysis previously calculated for the base case can also be used to calculate the solution to the perturbed system. The right-hand side, on the other hand, is determined by the base solution (f_0) and the A' and B'

matrices that represent the changes to the problem resulting from the modifications to mean flow. Thus, the right-hand side can be viewed as 'virtual' or 'pseudo-sources' distributed along the duct.

If matrix A_0 is invertible [1] then it is convenient to rewrite Eqn. 6.9 as

$$\frac{\partial f'}{\partial \zeta} - A_0^{-1} B_0 f' = A_0^{-1}\left(A' \frac{\partial f_0}{\partial \zeta} - B' f_0\right) \tag{6.10}$$

in which case the local source terms are given by

$$\psi = A_0^{-1}\left(A' \frac{\partial f_0}{\partial \zeta} - B' f_0\right). \tag{6.11}$$

This method calculates a linear (based on the mean flow perturbation quantities) change to a linear (based on the linearised Euler equations) solution and hence is here called the double linear method.

6.1.2 Implementation

To implement the double linear approach within the EAGCC method, the source terms must be propagated within the existing EAGCC framework. This is achieved by propagating the local source terms ψ within the global transfer matrix calculation. The full derivation of the global transfer matrix is provided in Chapter 3 and can be seen in [65] by Wilson.

6.1.2.1 Methodology for Inverting Matrix A

Eqn. 6.11 denotes the local source terms.

$$\psi = A_0^{-1}\left(A' \frac{\partial f_0}{\partial \zeta} - B' f_0\right) \tag{6.11}$$

To include these source terms into the propagation they must be expressed with respect to the eigenvector basis. This is done by pre-multiplying Eqn. 6.11 by the inverse of the eigenvectors of the base solution, E_0^{-1}, such that

$$E_0^{-1} A_0^{-1}\left(A' \frac{\partial f_0}{\partial \zeta} - B' f_0\right). \tag{6.12}$$

The way the boundary conditions are imposed in the EAGCC method replaces the radial momentum equations in the eigenvalue problem at the inner and outer walls. This results in two rows of the A_0 matrix having entries of zero for all columns. In

[1] This is explored further in the next section

turn, this reduces the rank of A_0 from n to $n-2$ resulting in a large condition number and poorly defined inverse. To compensate the formulation below is proposed.

As introduced in section 3.7, f_0 is a product of the base eigen-solutions E_0 and some coefficient vector. The $A' \frac{\partial f_0}{\partial \zeta} - B' f_0$ term can be expressed as the product of some coefficient $\bar{c}$ and E_0 such that if

$$x = A' \frac{\partial f_0}{\partial \zeta} - B' f_0 \tag{6.13}$$

$$= E_0 \bar{c}, \tag{6.14}$$

then

$$E_0^{-1} x = \bar{c}. \tag{6.15}$$

Now, the local source terms can be written as

$$\psi = E_0^{-1} A_0^{-1} E_0 \bar{c} \tag{6.16}$$

and re-written as

$$\psi = \left(E_0^{-1} A_0 E_0\right)^{-1} \bar{c}. \tag{6.17}$$

This alone does not generally improve the result, as the condition number of matrix $E_0^{-1} A_0 E_0$ is still very large due to the rank of A_0. However, it is common that within the eigenvector matrices there are columns corresponding to infinite or very large eigenvalues (much larger than the other values and determined to be high-order modes so not used in the propagation). It is, therefore, proposed that the eigenvector matrix is reduced to the same column rank as that of the row rank of A_0 by removing the columns corresponding to the infinite, or largest, eigenvalues. This is denoted $\tilde{E_0}$ such that $\tilde{E_0}$ has dimensions $n \times (n-2)$ where n is the number of radial points and as a result has a rank of $n-2$.

As $\tilde{E_0}$ has a rank of $n-2$ a left inverse can be computed such that

$$\tilde{E_0}_L^{-1} = (E_0^T E_0)^{-1} E_0^T. \tag{6.18}$$

The left inverse is defined as

$$\tilde{E_0}_L^{-1} \tilde{E_0} = I, \tag{6.19}$$

where I is the identity matrix with dimensions $n-2$.

As the reduced eigenvector matrices have the same rank as A_0 then it is found that the condition number of $\tilde{E_0}_L^{-1} A_0 \tilde{E_0}$ is several orders of magnitude smaller than that of $E_0^{-1} A_0 E_0$.

Therefore, it is proposed that

$$\psi = \bar{E}^{-1} \left(\tilde{E_0}_L^{-1} A_0 \tilde{E_0}\right)^{-1} \bar{E} \bar{c}, \tag{6.20}$$

where $\bar{E}$ and $\bar{E}^{-1}$ are defined as

$$E_0 = \tilde{E_0}\bar{E}. \tag{6.21}$$

Therefore, $\bar{E}$ is a matrix of dimensions $(n-2) \times n$ and computed as

$$\tilde{E_{0_L}}^{-1} E_0 = \bar{E} \tag{6.22}$$

and

$$E_0^{-1} = \bar{E}^{-1} \tilde{E_{0_L}}^{-1}, \tag{6.23}$$

and $\bar{E}^{-1}$ is a matrix of dimensions $n \times (n-2)$ and computed as

$$E_0^{-1} \tilde{E_0} = \bar{E}^{-1}. \tag{6.24}$$

Therefore, it has been shown that

$$\bar{E}^{-1} \left(\tilde{E_{0_L}}^{-1} A_0 \tilde{E_0} \right)^{-1} \bar{E} \bar{c} = E_0^{-1} A_0^{-1} E_0 \bar{c}. \tag{6.25}$$

6.1.2.2 Adding source terms

Local source terms at the k^{th} axial surface, ψ_k (as shown in Eqn. 6.11), are added into the propagation process. Eqn. 3.66 that describes the local propagation between two adjacent surfaces (k and $k+1$) is now expressed as,

$$\begin{pmatrix} c_{(k+1)r} \\ c_{kl} \end{pmatrix} = \begin{pmatrix} Q_{rr} & Q_{rl} \\ Q_{lr} & Q_{ll} \end{pmatrix} \begin{pmatrix} c_{kr} \\ c_{(k+1)l} \end{pmatrix} + \begin{pmatrix} \psi_{(k+1)r} \\ \psi_{kl} \end{pmatrix}. \tag{6.26}$$

Similarly, re-introducing the transfer matrices for 1 to any k from Eqn. 3.65, and assuming the outgoing information can be expressed as a sum of the transfer matrix and the propagated source terms from 1 to k leads to

$$\begin{pmatrix} c_{kr} \\ c_{1l} \end{pmatrix} = \begin{pmatrix} P_{rr} & P_{rl} \\ P_{lr} & P_{ll} \end{pmatrix} \begin{pmatrix} c_{1r} \\ c_{kl} \end{pmatrix} + \begin{pmatrix} \Psi_{kr} \\ \Psi_{1l} \end{pmatrix}. \tag{6.27}$$

Eliminating the intermediate c_{kl} and c_{kr} terms from the two equations above gives rise to

$$\begin{pmatrix} c_{(k+1)r} \\ c_{1l} \end{pmatrix} = \begin{pmatrix} S_{rr} & S_{rl} \\ S_{lr} & S_{ll} \end{pmatrix} \begin{pmatrix} c_{1r} \\ c_{(k+1)l} \end{pmatrix} + \begin{pmatrix} \Psi_{(k+1)r} \\ \Psi_{1l} \end{pmatrix}. \tag{6.28}$$

This is derived by first expanding the linear systems

$$c_{(k+1)r} = Q_{rr}c_{kr} + Q_{rl}c_{(k+1)l} + \psi_{(k+1)r} \tag{6.29}$$
$$c_{kl} = Q_{lr}c_{kr} + Q_{ll}c_{(k+1)l} + \psi_{kl} \tag{6.30}$$
$$c_{kr} = P_{rr}c_{1r} + P_{rl}c_{kl} + \Psi_{kr} \tag{6.31}$$
$$c_{1l} = P_{lr}c_{1r} + P_{ll}c_{kl} + \Psi_{1l}, \tag{6.32}$$

then substituting the expression for c_{kl}, Eqn. 6.30, into the formula for c_{kr}, Eqn. 6.31,

$$c_{kr} = P_{rr}c_{1r} + P_{rl}c_{kl} + \Psi_{kr} \tag{6.33}$$
$$= P_{rr}c_{1r} + P_{rl}(Q_{lr}c_{kr} + Q_{ll}c_{(k+1)l} + \psi_{kl}) + \Psi_{kr} \tag{6.34}$$
$$\tag{6.35}$$

and expanding the brackets and moving the c_{kr} term to the left-hand side

$$(I - P_{rl}Q_{lr})^{-1}c_{kr} = P_{rr}c_{1r} + P_{rl}Q_{ll}c_{(k+1)l} + P_{rl}\psi_{kl} + \Psi_{kr} \tag{6.36}$$
$$c_{kr} = (I - P_{rl}Q_{lr})^{-1}(P_{rl}(Q_{ll}c_{(k+1)l} + \psi_{kl}) + P_{rr}c_{1r} + \Psi_{kr}). \tag{6.37}$$

Similarly, the expression for c_{kr}, Eqn. 6.31, is substituted into the formula for c_{kl} , Eqn. 6.30,

$$c_{kl} = Q_{lr}c_{kr} + Q_{ll}c_{(k+1)l} + \psi_{kl} \tag{6.38}$$
$$= Q_{lr}(P_{rr}c_{1r} + P_{rl}c_{kl} + \Psi_{kr}) + Q_{ll}c_{(k+1)l} + \psi_{kl} \tag{6.39}$$
$$= (I - Q_{lr}P_{rl})^{-1}(Q_{lr}(P_{rr}c_{1r} + \Psi_{kr}) + Q_{ll}c_{(k+1)l} + \psi_{kl}) \tag{6.40}$$

These equations are both used to substitute c_{kr} and c_{kl} in the formulas for $c_{(k+1)r}$, Eqn. 6.29, and c_{1l}, Eqn. 6.32, eliminating the intermediate terms

$$\begin{aligned} c_{(k+1)r} &= Q_{rr}c_{kr} + Q_{rl}c_{(k+1)l} + \psi_{(k+1)r} \\ &= Q_{rr}[(I - P_{rl}Q_{lr})^{-1}(P_{rl}(Q_{ll}c_{(k+1)l} + \psi_{kl}) + P_{rr}c_{1r} + \Psi_{kr})] + Q_{rl}c_{(k+1)l} + \psi_{(k+1)r} \\ &= Q_{rr}(I - P_{rl}Q_{lr})^{-1}P_{rr}c_{1r} + (Q_{rr}(I - P_{rl}Q_{lr})^{-1}P_{rl}Q_{ll} + Q_{rl})c_{(k+1)l} \\ &\qquad + Q_{rr}(I - P_{rl}Q_{lr})^{-1}P_{rl}\psi_{kl} + \Psi_{kr}) + \psi_{(k+1)r} \end{aligned}$$

and

$$c_{1l} = P_{lr}c_{1r} + P_{ll}c_{kl} + \Psi_{1l} \tag{6.41}$$
$$= P_{lr}c_{1r} + P_{ll}[(I - Q_{lr}P_{rl})^{-1}(Q_{lr}(P_{rr}c_{1r} + \Psi_{kr}) + Q_{ll}c_{(k+1)l} + \psi_{kl})] + \Psi_{1l} \tag{6.42}$$
$$= [P_{lr} + P_{ll}(I - Q_{lr}P_{rl})^{-1}(Q_{lr}P_{rr})]c_{1r} + P_{ll}(I - Q_{lr}P_{rl})^{-1}Q_{ll}c_{(k+1)l} \tag{6.43}$$
$$+ P_{ll}(I - Q_{lr}P_{rl})^{-1}(Q_{lr}\Psi_{kr} + \psi_{kl}) + \Psi_{1l}. \tag{6.44}$$

Therefore, in matrix form

$$\begin{pmatrix} c_{(k+1)r} \\ c_{1l} \end{pmatrix} = \begin{pmatrix} S_{rr} & S_{rl} \\ S_{lr} & S_{ll} \end{pmatrix} \begin{pmatrix} c_{1r} \\ c_{(k+1)l} \end{pmatrix} + \begin{pmatrix} \Psi_{(k+1)r} \\ \Psi_{1l} \end{pmatrix} \tag{6.45}$$

where the S_{rr},S_{rl},S_{lr},S_{ll} entries are the same as in shown in section 3.7 in the original EAGCC formulation, and the propagated source terms are

$$\Psi_{(k+1)r} = Q_{rr}(I - P_{rl}Q_{lr})^{-1}(P_{rl}\psi_{kl} + \Psi_{kr}) + \psi_{(k+1)r} \tag{6.46}$$

$$\Psi_{1l} \quad = P_{ll}(I - Q_{lr}P_{rl})^{-1}(Q_{lr}\Psi_{kr} + \psi_{kl}) + \Psi_{1l}. \tag{6.47}$$

The above calculation is for marching forward through axial surfaces 1 to N.

A similar process is followed for marching backwards, introducing a transfer matrix from surface N to any k such that

$$\begin{pmatrix} c_{Nr} \\ c_{kl} \end{pmatrix} = \begin{pmatrix} H_{rr} & H_{rl} \\ H_{lr} & H_{ll} \end{pmatrix} \begin{pmatrix} c_{(k+1)r} \\ c_{Nl} \end{pmatrix} + \begin{pmatrix} \Psi_{Nr} \\ \Psi_{(k+1)l} \end{pmatrix} \tag{6.48}$$

and using the same local transfer matrices as before between any adjacent surfaces k and $k+1$

$$\begin{pmatrix} c_{(k+1)r} \\ c_{kl} \end{pmatrix} = \begin{pmatrix} Q_{rr} & Q_{rl} \\ Q_{lr} & Q_{ll} \end{pmatrix} \begin{pmatrix} c_{kr} \\ c_{(k+1)l} \end{pmatrix} + \begin{pmatrix} \psi_{(k+1)r} \\ \psi_{kl} \end{pmatrix}. \tag{6.49}$$

The intermediate values $c_{(k+1)r}$ and $c_{(k+1)l}$ are eliminated to give

$$\begin{pmatrix} c_{Nr} \\ c_{kl} \end{pmatrix} = \begin{pmatrix} T_{rr} & T_{rl} \\ T_{lr} & T_{ll} \end{pmatrix} \begin{pmatrix} c_{(k+1)r} \\ c_{Nl} \end{pmatrix} + \begin{pmatrix} \Psi_{Nr} \\ \Psi_{kl} \end{pmatrix} \tag{6.50}$$

where T_{rr},$T_{rl}T_{lr}T_{ll}$ entries are the same as in the original EAGCC formulation, section 3.7, and the propagated source terms are

$$\Psi_{Nr} = H_{rr}(I - Q_{rl}H_{lr})^{-1}(Q_{rr}\Psi_{(k+1)l} + \psi_{(k+1)r}) + \psi_{Nr} \tag{6.51}$$

$$\Psi_{kl} = Q_{ll}(I - H_{lr}Q_{rl})^{-1}(H_{lr}\psi_{(k+1)r} + \Psi_{(k+1)l}) + \psi_{kl}. \tag{6.52}$$

To compute the global propagation of the source terms, the same step is followed as in the original EAGCC propagation derivation shown in Chapter 3 (Wilson [65]). Taking the transfer matrices from marching forward and backwards

$$\begin{pmatrix} c_{kr} \\ c_{1l} \end{pmatrix} = \begin{pmatrix} S_{rr} & S_{rl} \\ S_{lr} & S_{ll} \end{pmatrix} \begin{pmatrix} c_{1r} \\ c_{kl} \end{pmatrix} + \begin{pmatrix} \Psi_{kr} \\ \Psi_{1l} \end{pmatrix} \tag{6.53}$$

and

$$\begin{pmatrix} c_{Nr} \\ c_{kl} \end{pmatrix} = \begin{pmatrix} T_{rr} & T_{rl} \\ T_{lr} & T_{ll} \end{pmatrix} \begin{pmatrix} c_{kr} \\ c_{Nl} \end{pmatrix} + \begin{pmatrix} \Psi_{Nr} \\ \Psi_{kl} \end{pmatrix} \tag{6.54}$$

and eliminating c_{1l} and c_{Nr} in the same manner as before

$$c_{kr} = S_{rr}c_{1r} + S_{rl}c_{kl} + \Psi_{kr} \tag{6.55}$$
$$c_{1l} = S_{lr}c_{1r} + S_{ll}c_{kl} + \Psi_{1l} \tag{6.56}$$
$$c_{Nr} = T_{rr}c_{kr} + T_{rl}c_{Nl} + \Psi_{Nr} \tag{6.57}$$
$$c_{kl} = T_{lr}c_{kr} + T_{ll}c_{Nl} + \Psi_{kl} \tag{6.58}$$

substituting the formulas for c_{kr} and c_{kl} into the equations for c_{kl} and c_{kr}, respectively,

$$\begin{aligned} c_{kr} &= S_{rr}c_{1r} + S_{rl}c_{kl} + \Psi_{kr} && (6.59)\\ &= S_{rr}c_{1r} + S_{rl}[T_{lr}c_{kr} + T_{ll}c_{Nl} + \Psi_{kl}] + \Psi_{kr} && (6.60)\\ &= (I - S_{rl}T_{lr})^{-1}(S_{rr}c_{1r} + S_{rl}T_{ll}c_{Nl}) + (I - S_{rl}T_{lr})^{-1}(S_{rl}\Psi_{kl} + \Psi_{kr}) && (6.61) \end{aligned}$$

and

$$\begin{aligned} c_{kl} =& T_{lr}c_{kr} + T_{ll}c_{Nl} + \Psi_{kl} && (6.62)\\ =& T_{lr}[S_{rr}c_{1r} + S_{rl}c_{kl} + \Psi_{kr}] + T_{ll}c_{Nl} + \Psi_{kl} && (6.63)\\ =& (I - T_{lr}S_{rl})^{-1}(T_{lr}S_{rr}c_{1r}) + (I - T_{lr}S_{rl})^{-1}(T_{lr}\Psi_{kr} + \Psi_{kl}). && (6.64) \end{aligned}$$

The global transfer matrix is formed as it is in the original EAGCC propagation formulation, section 3.7. The product of the global transfer matrix and input coefficients are added to the propagated source terms to give the new solution to the new system. If the input coefficients are set to zero then this gives the solution to just the resultant change to the system, or the full solution can be found by inputting the original input coefficients.

$$\begin{aligned} \begin{pmatrix} c_{kr} \\ c_{kl} \end{pmatrix} &= \begin{pmatrix} I - S_{rl}T_{lr} & 0 \\ 0 & I - T_{lr}S_{rl} \end{pmatrix}^{-1} \begin{pmatrix} S_{rr} & S_{rl}T_{ll} \\ T_{lr}S_{rr} & T_{ll} \end{pmatrix} \begin{pmatrix} c_{1r} \\ c_{Nl} \end{pmatrix} \\ &\quad + \begin{pmatrix} I - S_{rl}T_{lr} & 0 \\ 0 & I - T_{lr}S_{rl} \end{pmatrix}^{-1} \begin{pmatrix} S_{rl}\Psi_{kl} + \Psi_{kr} \\ T_{lr}\Psi_{kr} + \Psi_{kl} \end{pmatrix} && (6.65)\\ &= G_k \begin{pmatrix} c_{1r} \\ c_{Nl} \end{pmatrix} + \begin{pmatrix} I - S_{rl}T_{lr} & 0 \\ 0 & I - T_{lr}S_{rl} \end{pmatrix}^{-1} \begin{pmatrix} S_{rl}\Psi_{kl} + \Psi_{kr} \\ T_{lr}\Psi_{kr} + \Psi_{kl} \end{pmatrix} && (6.66) \end{aligned}$$

6.1.3 Analytic Example in One Dimension

To demonstrate the method an equivalent analytic approximation for an example in one dimension is provided. This example concerns a one-dimensional duct of length L with uniform mean flow the Mach number is $M + 0.001 = 0.501$ in a small region defined by $0 \leq z \leq l$ and $M = 0.5$ otherwise.

Following Wilson [6], the governing equations can be formulated into an eigenvalue problem as shown in Eqn. 3.19, where matrices A and B, at each axial position, are defined as

$$A = \begin{pmatrix} M & 1 \\ 1 & M \end{pmatrix}, \quad B = \begin{pmatrix} -i\tilde{\omega} & 0 \\ 0 & -i\tilde{\omega} \end{pmatrix} \tag{6.67}$$

and the solution vector

$$\mathbf{f} = \begin{pmatrix} u_\zeta \\ p \end{pmatrix}. \tag{6.68}$$

Matrix A is invertible and

$$A^{-1}B = \frac{i\tilde{\omega}}{1-M^2} \begin{pmatrix} M & -1 \\ -1 & M \end{pmatrix}. \tag{6.69}$$

The eigenvalues can then be calculated as

$$\lambda_r = \frac{-i\tilde{\omega}}{1+M}, \quad \lambda_l = \frac{i\tilde{\omega}}{1-M} \tag{6.70}$$

where subscripts r and l denote right and left travelling. The corresponding eigenvectors are

$$\mathbf{e}_r = \begin{pmatrix} 1 \\ 1 \end{pmatrix}, \quad \mathbf{e}_l = \begin{pmatrix} -1 \\ 1 \end{pmatrix}. \tag{6.71}$$

Consider a downstream travelling wave with complex pressure C at $z = 0$. The complex pressure along the whole duct is then

$$p = \begin{cases} Ce^{\lambda_r z}, \ z \leq 0 \\ Ce^{\lambda_{r_{mod}} z}, \ 0 \leq z \leq l \\ Ce^{\lambda_{r_{mod}} l} e^{\lambda_r (z-l)}, \ z \geq l \end{cases} \tag{6.72}$$

where $\lambda_{r_{mod}}$ is the eigenvalue of the right travelling wave in the modified region.

The eigenvalue in the modified region is

$$\lambda_{r_{mod}} = -\frac{i\tilde{\omega}}{1+M+0.001} \tag{6.73}$$

$$= -\frac{i\tilde{\omega}}{(1+M)(1+\frac{0.001}{1+M})} \tag{6.74}$$

$$\approx -\frac{i\tilde{\omega}}{1+M}\Big(1-\frac{0.001}{1+M}\Big). \tag{6.75}$$

For the downstream region $z \geq l$

$$p_{z \geq l} = Ce^{\lambda_{r_{mod}} l} e^{\lambda_r (z-l)} = Ce^{(\lambda_{r_{mod}} - \lambda_r) l} e^{\lambda_r z}. \tag{6.76}$$

From Eqn. 6.73 the pressure can be approximated analytically as

$$p_{z\geq l} = Ce^{\left(\frac{-i\tilde{\omega}}{1+M+0.001} - \frac{-i\tilde{\omega}}{M+1}\right)l} e^{\lambda_r} \tag{6.77}$$

$$\approx Ce^{\left(\frac{0.001i\tilde{\omega}}{(1+M)^2}\right)l} e^{\lambda_r} \tag{6.78}$$

$$\approx Ce^{\lambda_r}\Big(1 + \frac{0.001i\tilde{\omega}l}{(1+M)^2}\Big). \tag{6.79}$$

Comparing this to the double linear method, in the modified region

$$A' = \begin{pmatrix} 0.001 & 0 \\ 0 & 0.001 \end{pmatrix}, \quad B' = 0, \tag{6.80}$$

the local source terms are given by

$$\psi = A_0^{-1}\Big(A'\frac{\partial f_o}{\partial \zeta} - B' f_0\Big). \tag{6.81}$$

As shown previously, $\mathbf{f}_0 = \alpha \begin{pmatrix} 1 \\ 1 \end{pmatrix} e^{\lambda_r z}$, therefore

$$\frac{\partial \mathbf{f}_0}{\partial z} = \lambda_r \alpha \begin{pmatrix} 1 \\ 1 \end{pmatrix} e^{\lambda_r z} = \frac{-i\tilde{\omega}}{M_1}\alpha \begin{pmatrix} 1 \\ 1 \end{pmatrix} e^{\lambda_r z} \tag{6.82}$$

The inverse of matrix A

$$A_0^{-1} = \frac{1}{M^2 - 1}\begin{pmatrix} M & -1 \\ -1 & M \end{pmatrix}. \tag{6.83}$$

Therefore from Eqn. 6.77 the right-travelling (downstream) source is given by

$$\psi_r = \begin{cases} -0.001\frac{-i\tilde{\omega}}{(1+M)^2}\alpha \begin{pmatrix} 1 \\ 1 \end{pmatrix} e^{\lambda_r z},\ 0 \leq z \leq l \\ 0,\ \textit{otherwise}. \end{cases} \tag{6.84}$$

To approximate the solution for the whole new system, f, the local source terms are propagated from 0 to l

$$\mathbf{f} = \mathbf{f}_0 + \mathbf{f}' \tag{6.85}$$

$$= \alpha \begin{pmatrix} 1 \\ 1 \end{pmatrix} e^{\lambda_r z} - \alpha \begin{pmatrix} 1 \\ 1 \end{pmatrix} \int_0^1 0.001 e^{\lambda_r \zeta}\Big(-\frac{i\tilde{\omega}}{(1+M)^2}\Big) e^{\lambda_r (z-\zeta)}\, \partial\zeta \tag{6.86}$$

$$= \alpha \begin{pmatrix} 1 \\ 1 \end{pmatrix} e^{\lambda_r z}\Big(1 + \frac{0.001i\tilde{\omega}l}{(1+M)^2}\Big). \tag{6.87}$$

It can be seen from Eqn. 6.77 and Eqn. 6.87 that the double linear approach gives the same solution, to first order in the perturbation variables, as computed analytically.

6.2 One Dimensional Test-cases

A set of one-dimensional test cases similar to the analytical example case given in section 6.1.3 have been conducted. The base solution consists of a unit (pressure) amplitude plane wave at frequency 5312rad/s (freefield wavenumber 16) travelling upstream in a 1m long duct with uniform mean flow at Mach number 0.5, calculated with the EAGCC method with 100 equispaced mesh points along the duct.

A total of 35 calculations have been performed in accordance with the test matrix shown in Table 6.1. In each test-case the mean flow is perturbed from the base value over a certain fraction of the duct length. Note that the duct fractions and fractional flow increases include some large values, well beyond those in which we would expect the approximate double linear method to be accurate, in order to demonstrate the limits of applicability.

For each case, the result is calculated first using the double linear method, and then a reference solution is calculated using the full EAGCC method without the double linear approximation.

Note that in this simple one-dimensional case, the computation of the eigen-solutions represents only a small proportion of the solution time: the benefit of using the approximate solution will only become apparent in large three-dimensional calculations.

TABLE 6.1: Test matrix for one-dimensional test-cases.

Parameter	Values
Length of duct with different mean flow	0.05, 0.1, 0.2, 0.4, 0.8
Percentage increase to mean flow	0.25%, 0.5%, 1%, 2%, 4%, 8%, 16%

6.2.1 One-dimensional Test-cases: Expected Behaviour

Before looking at the results, it is important to consider the expected behaviour. One key feature of this one-dimensional test case is that the pressure/velocity relationship in the eigenmodes is independent of the Mach number. That is, the eigenmodes remain unchanged throughout the duct, although the eigenvalues, representing the rate of change of phase with axial distance, and hence the phase velocity of the wave along the duct, do change in the region where the mean flow Mach number has been increased.

The fact that the eigenmodes do not change means that an upstream travelling wave just downstream of the Mach number discontinuity remains an upstream travelling wave just upstream of the discontinuity: that is, we should not expect any *reflection* of the input wave at the interfaces.

The change in phase speed at the discontinuity carries a change of amplitude with it such that acoustic energy flux remains constant.

In the absence of reflections, the acoustic intensity must be the same in both sections of the duct. Hence the amplitude of the wave in the perturbed section differs from that in the unperturbed section, with an abrupt change in amplitude, equal and opposite, at each of the two discontinuities in the duct.

In addition to this abrupt change, the changed phase velocity in the perturbed region leads to a progressively increasing difference in phase between the original solution and the perturbed solution.

These effects are illustrated in Figures 6.2 and 6.3 below, which show the pressure amplitude and phase difference along the duct of the reference solution for several test cases all with a change region of $0.2m$ of the duct length, $Mn+$ denotes the percentage increase in Mach number.

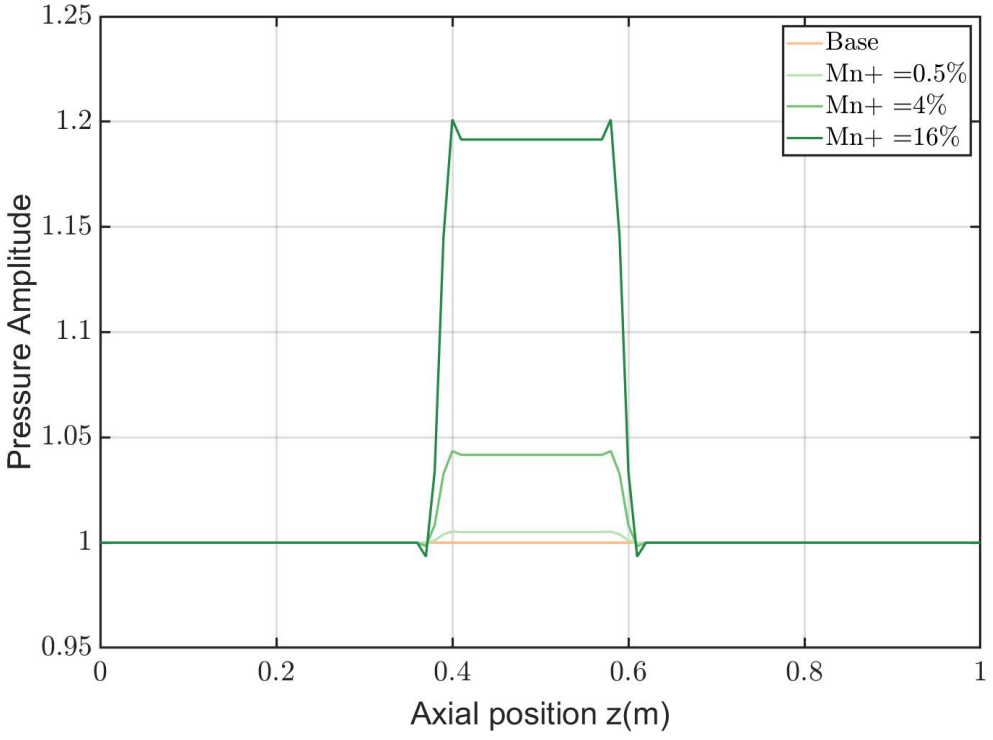

FIGURE 6.2: Pressure amplitude against axial position z(m) for 1D test cases with a changed region of 0.2m. Mn+ denotes the percentage increase in Mach number.

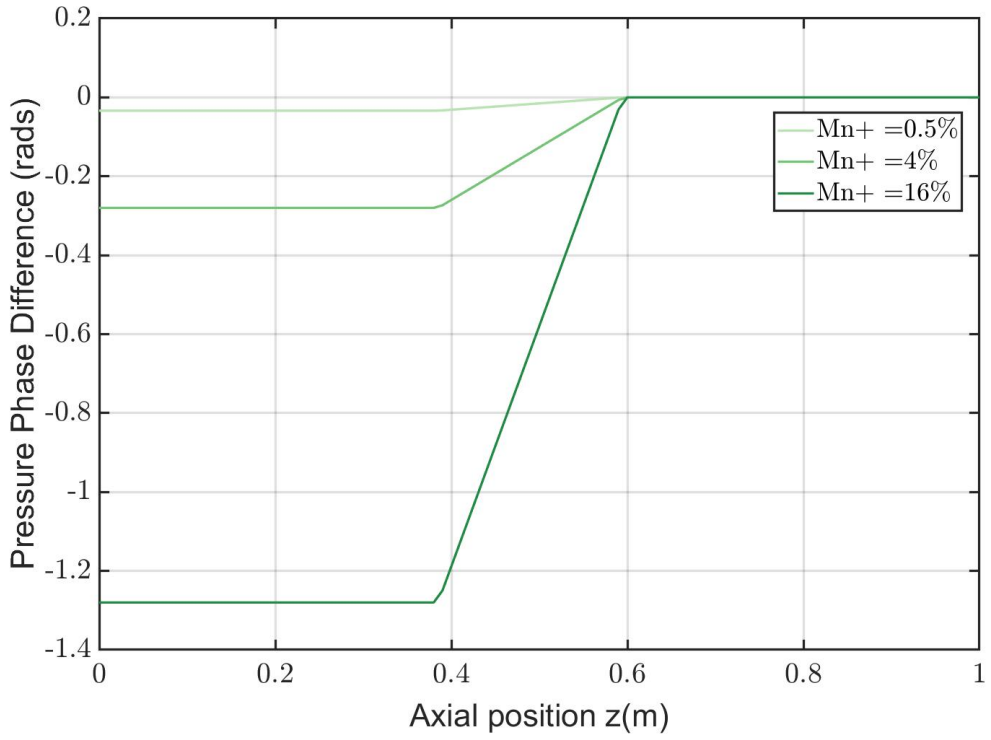

FIGURE 6.3: Pressure phase difference (rads) against axial position z(m) for 1D test cases with a changed region of 0.2m. Mn+ denotes the percentage increase in Mach number.

6.2.2 One-Dimensional Test-cases: Results

The results for the full test matrix are summarised in relation to the *difference* between the outgoing wave in the double linear calculation and the base solution, compared to the 'actual' *difference* seen between the outgoing wave given by the full EAGCC (reference) solution and the base solution. To demonstrate this, let us look at a specific case from the test matrix in close detail before discussing all the results.

6.2.2.1 Example 1D case

The example case considered is that of a 4% increase in Mach number (0.5 to 0.52) over a 0.2m region of the duct model. The cases considered throughout consist of inputting a single upstream travelling radial harmonic at the downstream end of the duct.

Fig. 6.4 shows the amplitude of the pressure along the duct of the reference, base, and double linear solutions. As shown previously, the reference solution increases in amplitude in the changed region but returns to the same amplitude as the base solution upstream of the changed region. The amplitude of the double linear solution, however, remains higher than the reference and base solutions upstream of the changed region thus this is an error in the amplitude of the double linear solution.

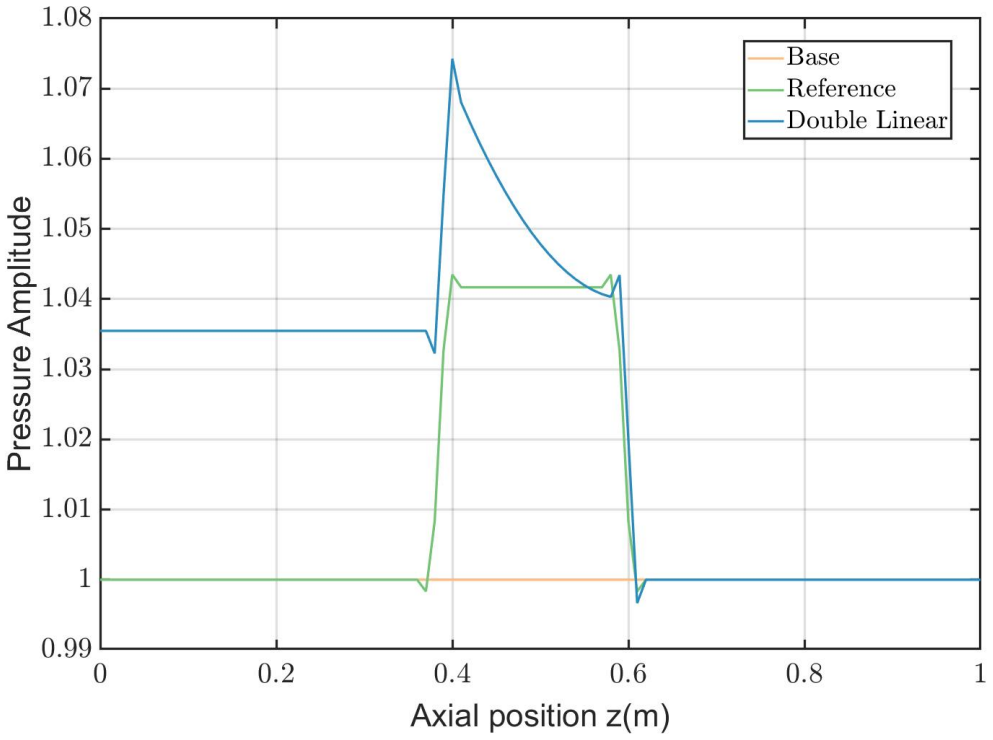

FIGURE 6.4: Pressure amplitude of base, reference, and double linear solutions, for 1D case with 4% increase in Mach number over 0.2m region.

Fig. 6.5 shows the phase difference from the base solution of the reference and double linear solutions. It can be seen that there is an error in the phase difference of the double linear solution. Therefore, although the change in mean flow only results in a change in phase at the outlet of the duct and not in amplitude, the double linear solution erroneously predicts a change in both.

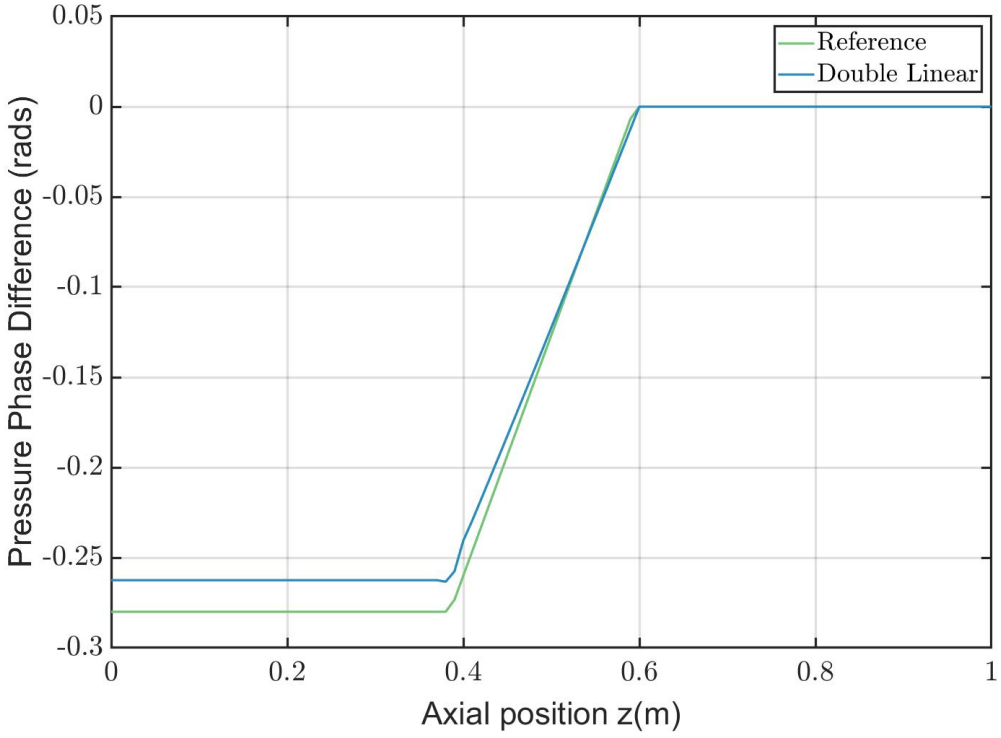

FIGURE 6.5: Phase difference from the base solution, for reference and double linear solutions.

The original intention was to generate an error metric based on the amplitude of the outgoing wave. However, it has been shown that the flow perturbation used in this test series affects mainly the phase not the amplitude and that there is error in the double linear solution in amplitude and phase.

The pressure amplitude coefficients are complex numbers, Fig. 6.6 plots the output pressure coefficients at the upstream end of the duct ($z = 0$) on an argand diagram.

It can be seen that the amplitudes of the differences between the double linear and base solution and between the reference and base solutions are similar, as shown in Fig. 6.6. Therefore, the chosen error metric is the fractional error in the change due to the perturbation.

$$\begin{aligned} Error_{frac} &= \frac{|(reference - base) - (double\ linear - base)|}{|reference - base|} \\ &= \frac{|reference - double\ linear|}{|reference - base|} \end{aligned} \tag{6.88}$$

For this example case, the fractional error is 0.14 which denotes that the amplitude of the error in the double linear solution is 14% of the amplitude of the expected change.

The error in the predicted change can lead to an error in either amplitude or phase of the full solution. If the fractional error is small then the error in both phase and

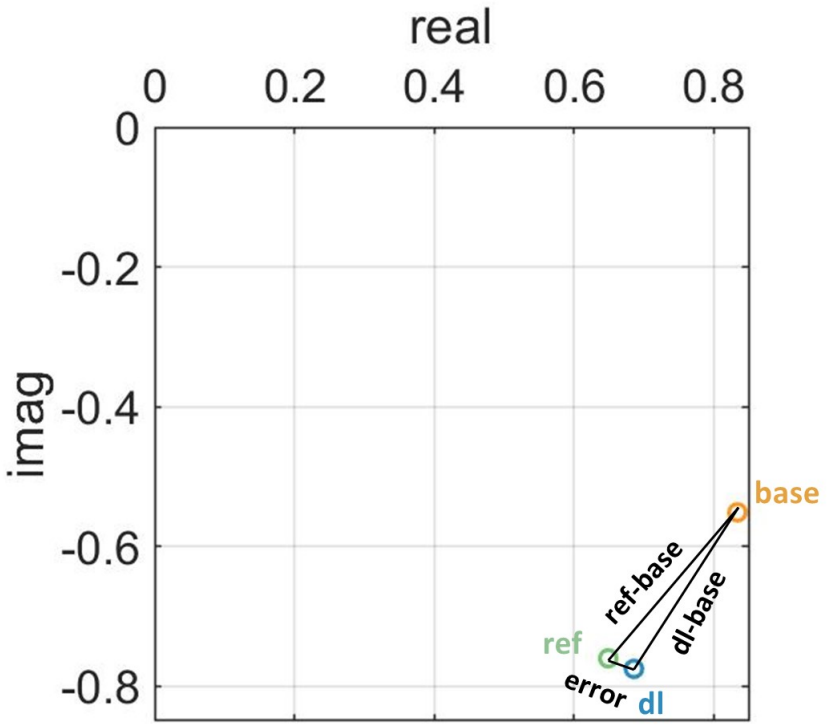

FIGURE 6.6: Coefficients of upstream travelling input mode at output, for case with 4% increase in Mach number over 0.2m of the duct. Base solution (orange), reference solution (green) and double linear solution (blue), plotted on an argand diagram. The horizontal is the real part of the coefficient and the vertical is the imaginary part.

amplitude will be small compared to the amplitude of the change from the base solution.

6.2.2.2 Full test matrix

Fig. 6.7 shows the error for all 1D test cases with a fractional error of 20% or below. It can be seen that, for a fixed modified region length, if the fractional increase to the Mach number doubles the error also approximately doubles. Similarly, if the modified region length doubles this results in the error roughly doubling from (1.5 to 1.9 times bigger).

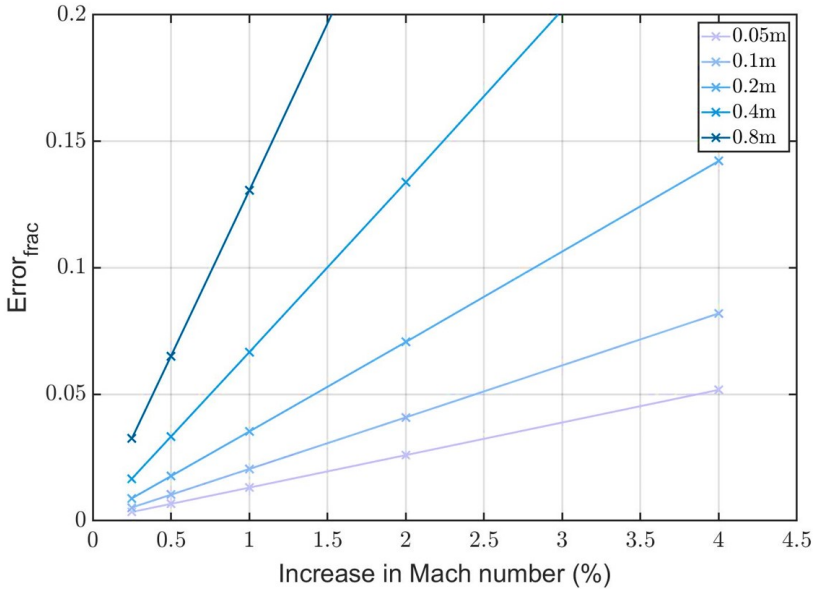

FIGURE 6.7: Fractional error (for 1D cases with error of 20% or less). Percentage increase in mach number on the horizontal axis, line colours denote the length of the modified region.

Fig. 6.8 shows the fractional error for all 1D cases. Dashed contour lines have been added at fractional error levels of 0.01 and 0.1 to aid clarity. The double linear approximation is accurate at the lowest perturbation magnitude but reduces in accuracy with the increase in magnitude of the perturbation.

The level of acceptable error will of course vary by application. In general less accuracy is required when calculating sensitivities than absolute values, and obtaining the difference to within 20% may be acceptable, but this requires further consideration based on the application. If, however, greater accuracy is needed, for instance 1% error, then Figs. 6.7 and 6.8 show that the double linear method is restricted in these cases to mean flow changes of less than 1% in a modified region of 0.2m of the duct length.

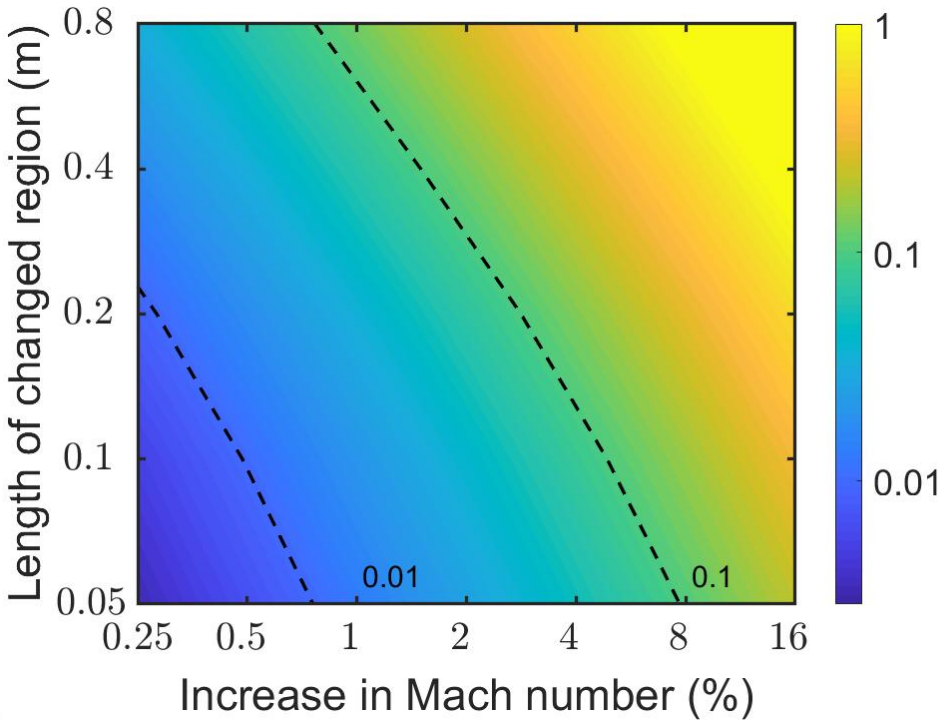

FIGURE 6.8: Contour plot of the fractional error for all 1D test cases.

6.3 Three-dimensional Axisymmetric Cylindrical Annular Duct Test-cases

In this section a number of axisymmetric test cases similar to those demonstrated in one-dimension are introduced. The base geometry for these test cases is an annular duct with outer radius $R_1 = 0.432$ and inner radius $R_0 = 0.2$. Wilson [6] used a duct of the same size to validate the EAGCC method for predicting acoustic propagation, comparing against analytical Bessel-Fourier modes. Similarly to the one-dimensional cases, the length of the modified region and percentage increase to Mach number are two parameters considered. Additional parameters include base Mach number and cut-on ratio. The input mode is of circumferential mode 18, with a frequency defined in proportion to the cut-on ratio, α, and radial order, μ.

$$\tilde{\omega} = (\sqrt{1 - M^2})\mu\alpha. \tag{6.89}$$

The test matrix is shown in Table 6.2.

TABLE 6.2: Test matrix for three-dimensional test-cases.

Parameter	Values
Length of modified region (m)	0.04, 0.08, 0.16, 0.32, 0.64
Percentage increase to mean flow Mach number	0.25, 0.5, 1, 2, 4
Mode cut-on ratio	1.1, 1.3
Mach number in base problem	0.1, 0.2, 0.3, 0.4, 0.5

Similarly to the one-dimensional cases the solution with the perturbed flow was calculated both with the double linear approximation, and using the full EAGCC method without approximation.

6.3.1 Annular Duct Test-cases: Results

Fig. 6.9 shows the fractional error, calculated as shown in Eqn. 6.88, for cases with fixed base Mach numbers of 0.1, 0.3, and 0.5. It shows that the error increases with Mach number, as well as the percentage increase in Mach number($Mn+$) and length of modified region, (L_m).The cut-on ratio has limited effect on the error. However, for any given case fixed in: base Mach number; fractional Mach increase; and length of modified region, the case with the higher cut-on ratio has a slightly higher error value.

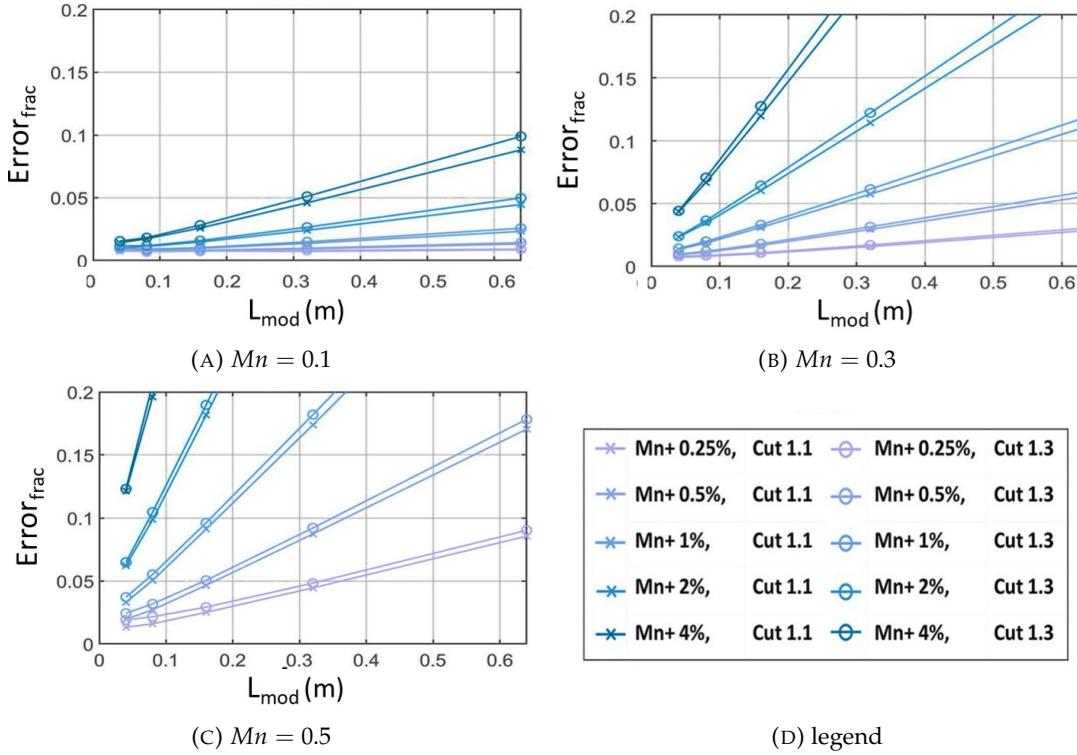

(A) $Mn = 0.1$ (B) $Mn = 0.3$

(C) $Mn = 0.5$ (D) legend

FIGURE 6.9: Error vs Length of modified region,L_{mod}. Fixed Mach number. Coloured lines denote percentage increase to Mach number ($Mn+$), symbols denote cut-on ratio: x - 1.1, and o - 1.3.

Taking a closer look at the relationship between the error and Mach number, Fig. 6.10 shows that the error is close to proportional to the Mach number squared. However, this proportionality increases with the fractional mach increase. If instead the increase to Mach number is considered as the magnitude of the change (the product of base Mach number and the fractional increase, $\Delta Mn = Mn \times \%Mn+$) then it can then be seen that the fractional error is linearly proportional to the magnitude change in Mach number. Fig. 6.10 demonstrates that overall the fractional error is proportional to the product of the Mach number and the magnitude increase of the Mach number.

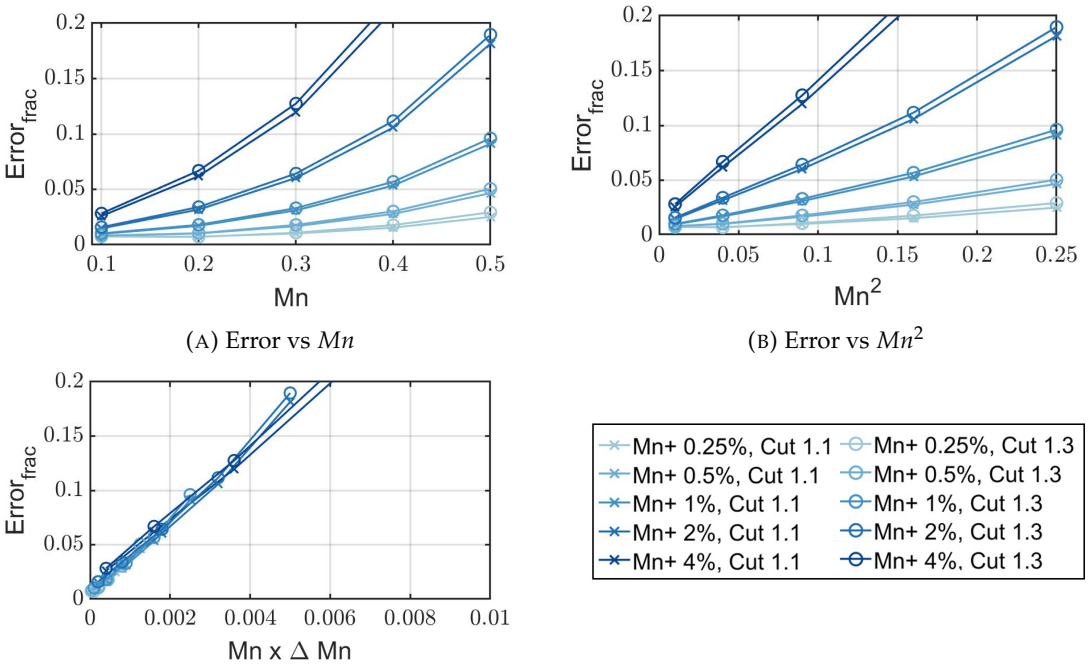

(A) Error vs Mn

(B) Error vs Mn^2

(C) Error vs $Mn \times \Delta Mn$

(D) legend

FIGURE 6.10: Test cases with fixed length of modified region, L_{mod} of 0.16m. Fractional error on vertical axis. Coloured lines denotes percentage increase in Mach number, symbols denotes cut-on ratio.

Considering all cases, at fixed lengths of the modified region it can be seen in Fig. 6.11 that the proportionality between $Mn \times \Delta Mn$ and fractional error also grows with the length of modified region. Thus by including the length of modified region into the product on the horizontal axis, Fig. 6.11 shows this reduces all the cases to approximately one constant of proportionality.

The predicted constant of proportionality is 225. It is noted that the data does not exactly go through the origin, but this is thought to be due to the normalisation of the fractional error by the $|reference - base|$ which is very small in the majority of cases with low fractional error.

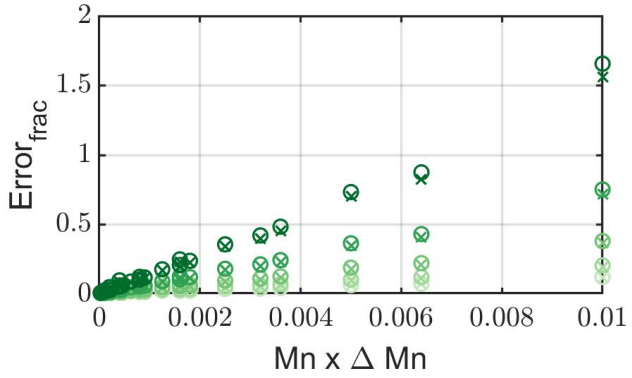

(A) Error vs $Mn \times \Delta Mn$

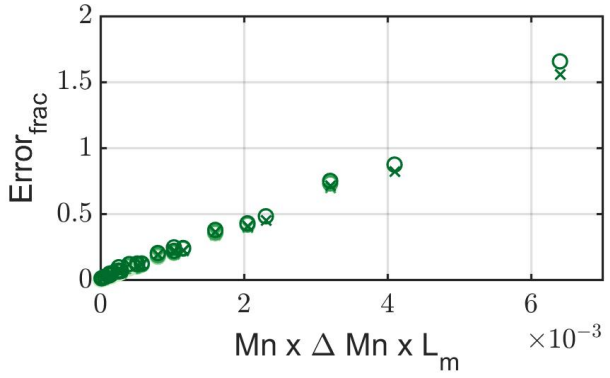

(B) Error vs $Mn \times \Delta Mn \times L_m$

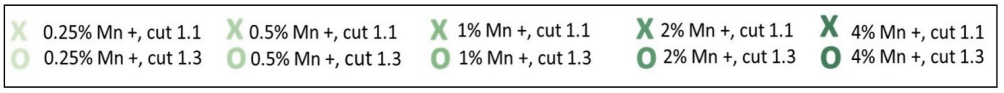

(C) legend

FIGURE 6.11: Fractional Error for all cases. Colour of symbols denotes length of modified region and symbol denotes cut-on ratio.

6.4 Axisymmetric Intake

In this section, the double linear method is applied to the same axisymmetric aero-engine intake as in Chapter 5 section 5.2.2 taken from Xiong and Sugimoto [34].

For the perturbation, the axial velocity in the mean flow is increased by 1% over a region of length approximately 0.15m, in the middle of the duct. Fig. 6.12 shows the change to the mean flow induct.

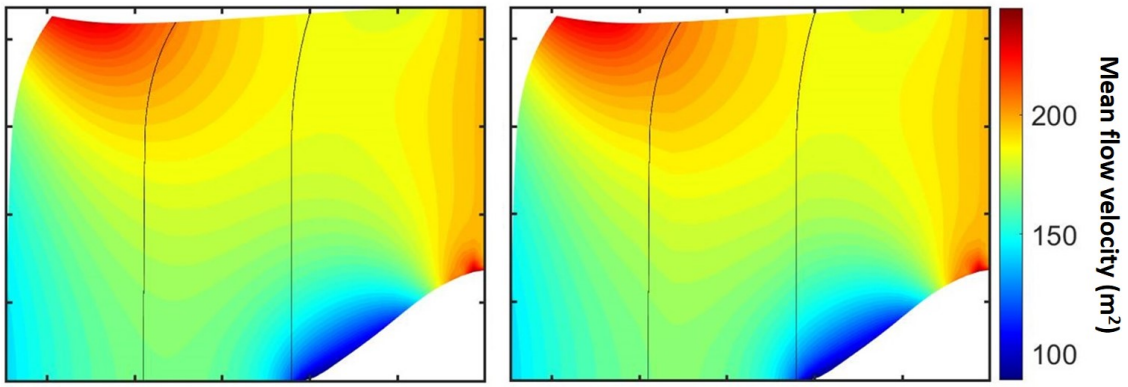

FIGURE 6.12: Real part of the mean flow velocity. Base (left) and modified (right), black lines show modified region.

6.4.1 Three-Dimensional Axisymmetric Intake: Results

6.4.1.1 Full solution results

Before considering the error in the sensitivity, it is useful to look at the full solutions first. Fig. 6.13 shows the difference between the perturbed and base solutions.

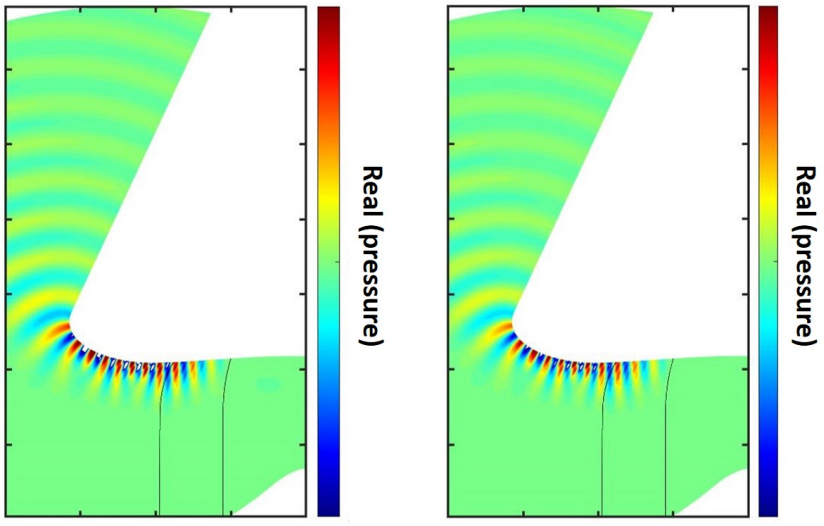

FIGURE 6.13: Real part of the acoustic pressure. Reference - base (left) and double linear - base (right), black lines show modified region.

It can be seen that the 1% change in mean flow does not have a large effect overall on the base solution. Furthermore, the double linear approximation broadly agrees with the reference solution although some small differences in pressure amplitude can be seen even at this level.

Looking at the pressure along the outer wall, Fig. 6.14 shows there is no change to the outer wall pressure downstream of the modified region and thus all three solutions agree here. Inside the modified region the outer wall pressure in the reference solution

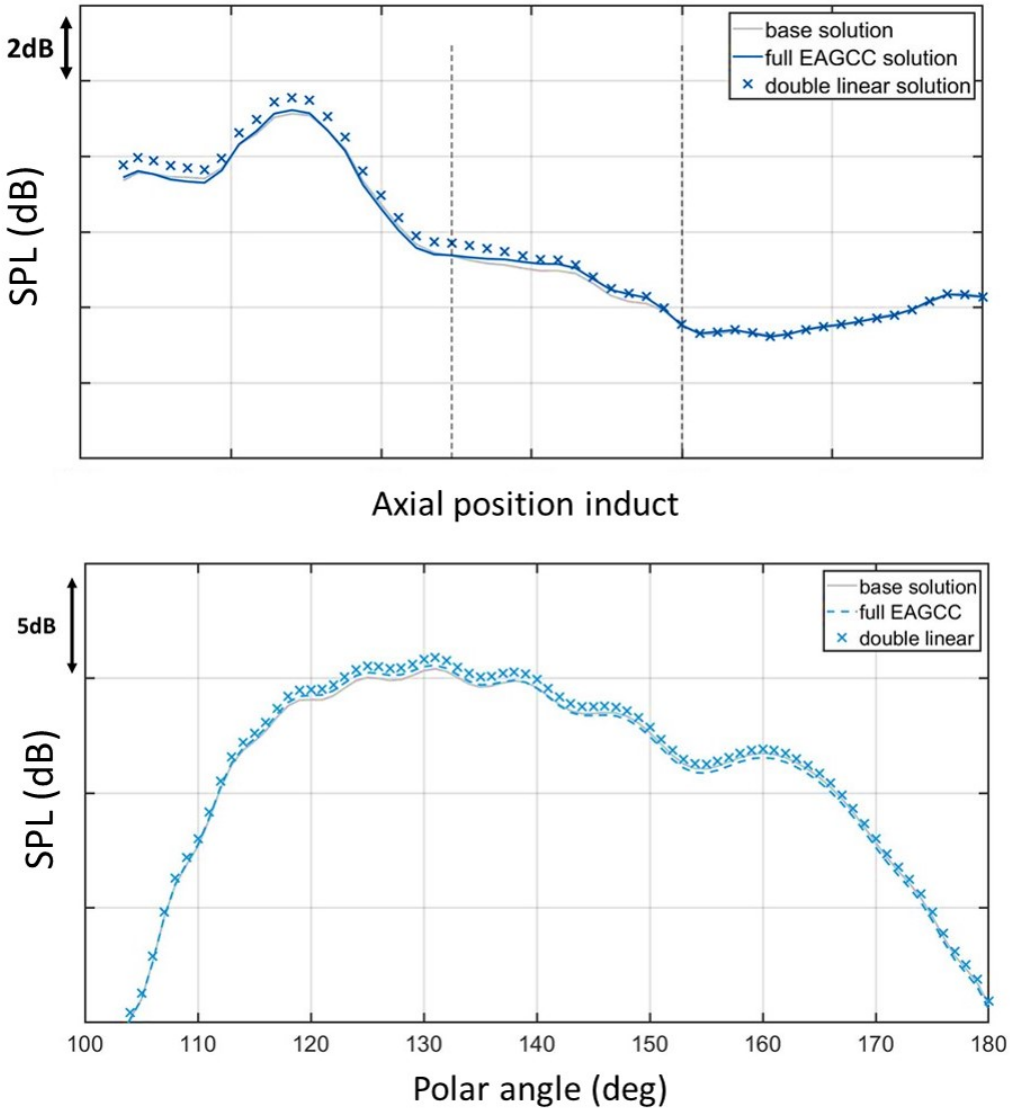

FIGURE 6.14: Induct SPL (dB) along outer wall (top). Far-Field SPL (dB) (bottom)

differs from that of the base solution. The double linear solution agrees with the reference solution in the downstream half of the modified region but not in the upstream half, where a consistent difference of approximately 1/3 dB is seen between the reference and double linear solutions. This change is also reflected in the far-field. As with the previous test cases, the major effect of the mean flow changes is to change the phase of the outgoing wave rather than the amplitude. The change in amplitude predicted by the full EAGCC solution is negligible, whereas the double linear solution predicts an erroneous small change in amplitude.

6.4.1.2 Perturbation results

In this test case there are two 'cut-on' propagating upstream travelling modes, they are of first and second radial order denoted 'usr1' and 'usr2'. Considering first the amplitude coefficients of these two modes, Fig. 6.15 plots the absolute value of the amplitude coefficients for all three solutions, and Fig. 6.16 plots the absolute difference, $|reference - base|$ and $|double\ linear - base|$, at each axial position induct. As seen in Fig. 6.14 the amplitude coefficients are the same downstream of the modified region. For the first radial harmonic, usr1, the coefficients of the reference and base solution are also the same upstream of the modified region but there is a consistent difference between those and the double linear coefficient, equivalent to the 1/3 dB difference seen previously. The absolute value of the coefficients of the second radial harmonic remains different in the reference solution to the base and the double linear appears to agree.

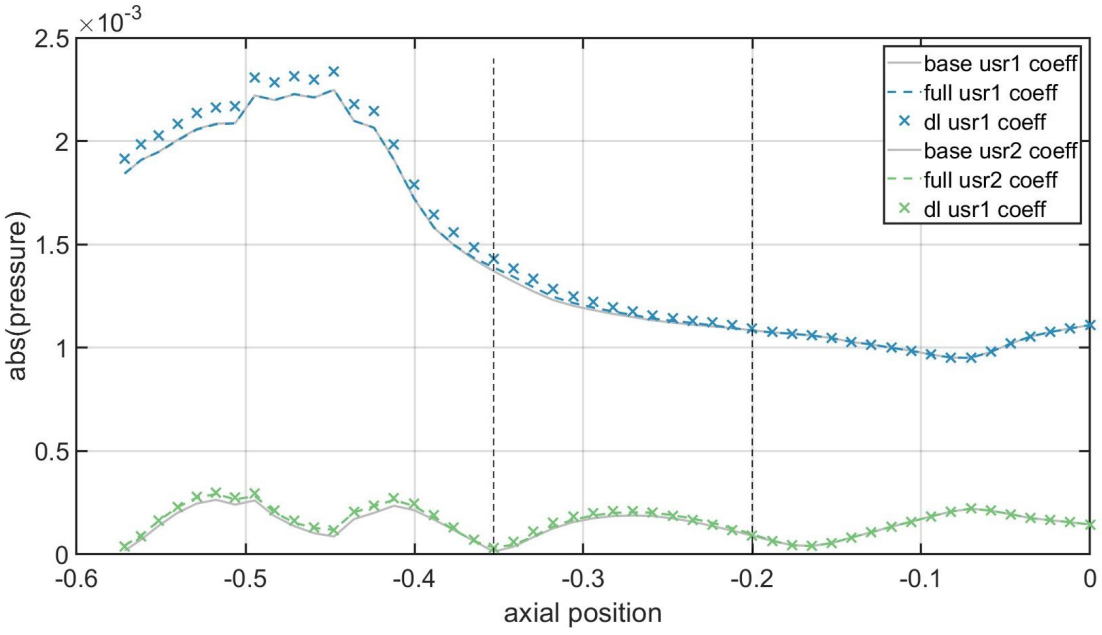

FIGURE 6.15: Absolute value of the amplitude coefficients of the first two upstream travelling radial harmonics, usr1 and usr2 respectively, at each axial position for the full base, reference and base solutions.

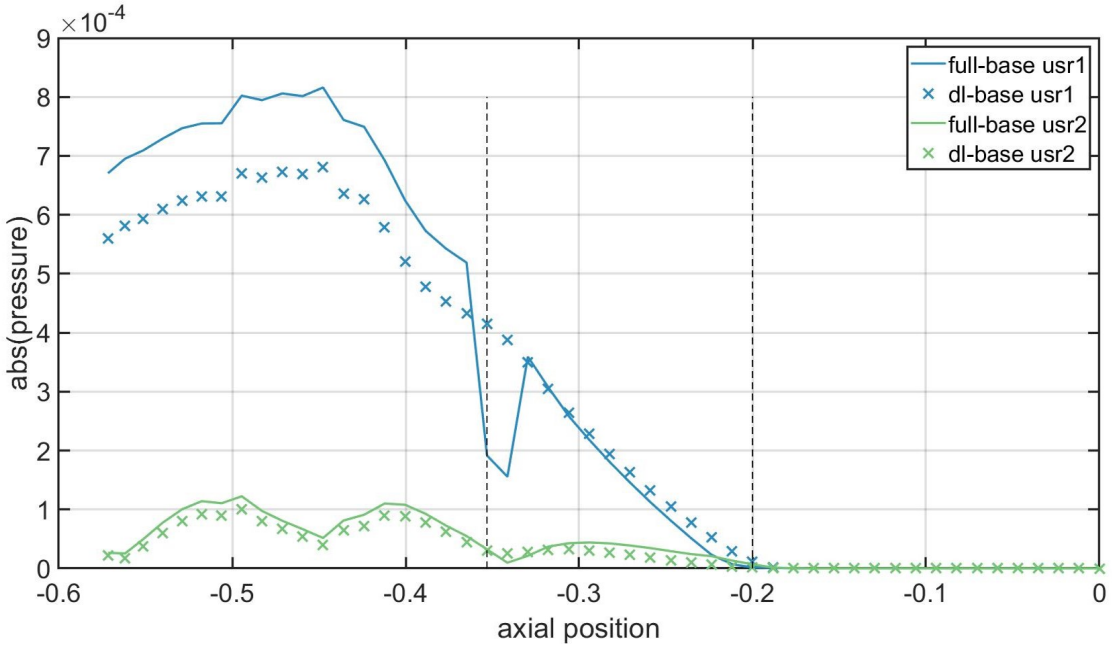

FIGURE 6.16: Absolute value of the difference in amplitude coefficients of the first two upstream travelling radial harmonics, usr1 and usr2 respectively, at each axial position for the full-base and double linear - base.

It was shown in section 6.2 that neither the amplitude of the full solution nor the amplitude of the difference is a suitable error metric. Here, therefore, the error metric is defined as the amplitude of the error in the coefficient of the first and second radial harmonics normalised by the predicted change in the respective coefficient due to the perturbed mean flow.

Fig. 6.17 plots the fractional error in the two coefficients upstream of the modified region. It is shown that the error in the first harmonic is consistently 22% upstream of the modified region in duct.

The error induct is also consistent with the error in the far-field. Fig. 6.18 shows that the fractional error in the far-field approximation is approximately 23% at the peak.

Based on the correlation provided in section 6.3 , for a cylindrical annulus, the expected error would be approximately 17%. This accounts for the majority of the observed error here.

6.5 Discussion

The results of the three sets of test cases included in this chapter show consistency in the parameters associated with error in the double linear approximation. The errors in

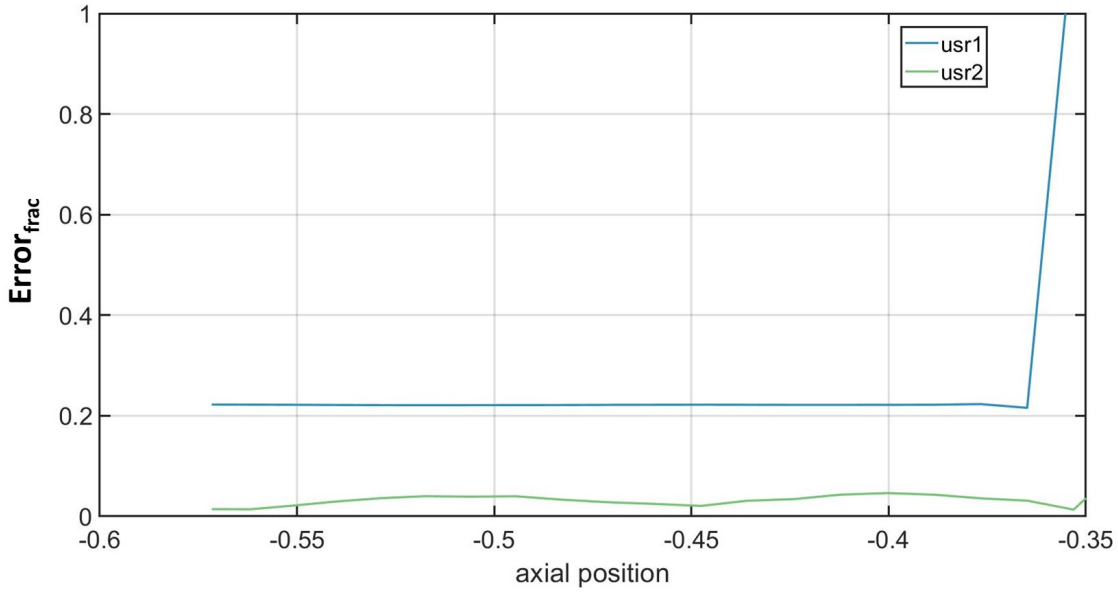

FIGURE 6.17: Fractional error in the amplitude coefficients of the first two upstream travelling radial harmonics, usr1 and usr2 respectively, at each axial position upstream of the modified region.

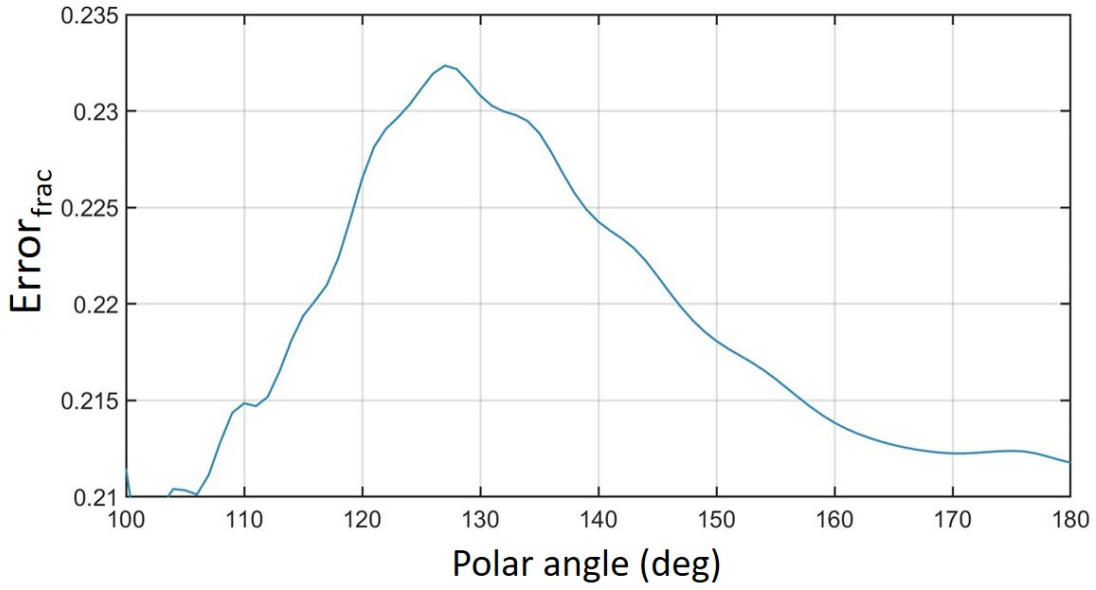

FIGURE 6.18: Fractional error in the far-field pressure.

each case are shown to be related to a single parameter

$$\Gamma = M \times \Delta Mn + \times L_{mod} \tag{6.90}$$

The change to Mach number has been shown to cause a change in the phase of the propagating waves, which can be considered as pseudo-sources that are propagated at the unperturbed Mach number. The base Mach number will change the wave angle

relationship between the perturbed and unperturbed flow in the modified region. The phase difference of the pseudo sources will grow with the length of the modified region. Overall the error is proportional to both the length of the modified region and the magnitude of the change in Mach number.

All the cases included in this chapter only consider changes to axial velocity applied uniformly in circumferential and radial directions, therefore the perturbed solutions result in a change in phase rather than amplitude. Errors in the double linear solution can manifest themselves as errors in amplitude, which are generally small but can appear large if only the amplitude is considered. For this reason, an error metric was selected taking into account both amplitude and phase (Eqn. 6.88). If this error metric is small then both the amplitude and phase errors are small.

For axisymmetric ducts it has been shown that the method works well for small changes in Mach number over a limited region of the duct. From Eqn. 6.88 a change of 3% in mean flow Mach number over an axial length of 0.1 outer wall radii with a base Mach number of 0.5, is expected to have a fractional error of 0.07 (7%). Note this refers to 7% of the change from the base to the perturbed solutions, not 7% of the full solution. As the error increases with larger changes it is felt that the benefit to this approximation method would be to calculate sensitivities to small step changes within a wider optimisation scheme, such as a hill-climbing routine. This is a similar idea to the way adjoint, another linear approximation method, has been used in aero-acoustics optimisation applications [151].

6.6 Conclusions

A computationally fast approximate eigen-based method has been developed for calculating sensitivities of acoustic propagation in ducts to small changes in geometry and mean flow.

The method has been extensively validated for small changes in mean flow in one-dimensional and axisymmetric ducts.

The error has been quantified and related to a single parameter, Γ, combining the base flow Mach number, the length of the modified region, and the change in Mach number.

The errors are more significant with modest to large changes in Mach number, or large perturbed regions. This is primarily due to the linear error terms (pseudo-sources) radiating with the unperturbed mean flow. This behaviour is not unique to this method, but can be expected from any linear perturbation analysis (for instance adjoint analysis).

Further work is required to extend the application of this approximation method. Given this limitation, it is felt that the method cannot be used for assessing widely different duct designs but is better suited to numerical optimisation and robust design. This could be achieved by incorporating it into wider optimisation schemes to predict the sensitivities to small changes in mean flow.

Chapter 7

Conclusions and Future Work

7.1 Conclusions

This thesis comprises three main chapters of work. The following section sets out the main conclusions for each.

7.1.1 Error Analysis

An investigation into mesh-related error, caused by axial discretisation, has been undertaken in one dimension.

- There are three competing error terms at the highest order of error, all related to successive derivatives of the Jacobian matrix.
- These error terms feature in two equations describing the (spatially) local error at each analysis surface.
- This error analysis has been validated, including the influence of each of the error terms individually, using a range of numerical test-cases.
- A full error analysis in three dimensions would be prohibitive, but guidance is provided [Chapter 4] to apply the understanding from the one-dimensional analysis to mesh definition in three dimensions.

7.1.2 Validation of EAGCC against ACTRAN/TM

A validation of the EAGCC method against ACTRAN/TM has demonstrated the method is applicable to non-axisymmetric 3D intakes, with and without an acoustic liner.

- The EAGCC method was found to be more computationally expensive than the ACTRAN/TM finite element approach.
- Applying the EAGCC method to fully three-dimensional geometries involves classifying a large number of modes. This has highlighted the issue of mode classification, which currently requires significant manual input.
- Further work is required to automate the mode classification routine in a robust manner before the EAGCC method can be considered for industrial application.

The validation led to several developments to the EAGCC method itself.

- An improved method has been devised for applying EAGCC to three-dimensional ducts which helps with mode classifiation. This includes the division of domains into axial sections; the inclusion of more high-order modes, than previously thought necessary, in the acoustic modal sum; and the use of wave-splitting between adjacent surfaces.
- A new implementation approach has been developed for applying acoustic liners to fully three-dimensional ducts, with improved handling of discontinuities at the liner junction.
- Parallelisation of the 'matriculate' function within the EAGCC method has reduced the run time for large three-dimensional ducts by around 30%.

7.1.3 Double Linear Approximation

The double linear approach, in conjunction with the extended parallelisation of the 'matriculate' function, provides an approximate eigen-based method for calculating sensitivities of acoustic propagation in ducts to small changes in mean flow.

- The combined methods considerably reduce the computation time of the equivalent EAGCC computation. Firstly by around half by cutting out the eig solver, then by around a further three-quarters by parallelising the matriculate function.
- The method has been extensively validated for changes in mean flow in one-dimensional and axisymmetric three-dimensional ducts.
- The application is limited to small changes in Mach number over small regions of the duct. For example: an increase of 3% in mean flow Mach number over an axial length of 0.1 of the outer wall radii.
- The error in the double linear method has been quantified and related to a single parameter, Γ, combining the base flow Mach number, the length of the modified region, and the change in Mach number.

7.2 Future Work

- Further investigation is needed to understand the modal behaviour in non-axisymmetric geometry and mean flow. This should lead onto the development of a robust mode sorting routine, reducing the human intervention required to implement the EAGCC method.
- Further investigation is required to characterise the relationships between mesh definition; derivatives of the Jacobian matrix; and the mechanisms through which mesh-related error is created in three dimensions. This could ultimately inform the formulation of an automated meshing routine, optimised to reduce the discretisation error.
- Other boundary conditions such as the Ingard-Myers [45], and Brambley [152] boundary conditions should be integrated into the method to broaden the potential applicability of the EAGCC method including high Mach number flows.
- Validate the 'double linear' approximation for fully 3D intakes.
- Extend the 'double linear' approximation to small changes in geometry or liner impedance.
- Optimisation of the EAGCC code to reduce the computation time would broaden the range of applications. The most computationally expensive aspect of the method at present is the eigensolve. Further work to explore ways of reducing this, such as through the use of GPU, should be considered.

References

[1] A. P. Dowling and Y. Mahmoudi, "Combustion noise," in *Proceeding of the Combustion Institute 35*, (San Francisco, California), Elsevier Inc. on behalf of The Combustion Institute, August 2014.

[2] R. J. Astley, "Propulsion system noise: Turbomachinery," *Encyclopedia of Aerospace Engineering*, 2010.

[3] S. Moreau, "Turbomachinery noise predictions: Present and future," *Acoustics*, vol. 1 (1), p. 92–116, January 2019.

[4] R. Hawkins and A. G. Wilson, "A fast method for calculating sensitivities of acoustic propagation in ducts to small changes in geometry and mean flow," in *28th AIAA/CAES Aeroacoustics Conference*, no. AIAA 2022-3018, (Southampton, UK), American Institute of Aeronautics and Astronautics, June 2022.

[5] R. Hawkins and A. G. Wilson, "Error analysis for 1D propagation using eigen analysis in general curvilinear coordinates," in *AIAA AVIATION*, no. AIAA 2021-2298, American Institute of Aeronautics and Astronautics, July 2021.

[6] A. G. Wilson, "Propagation of acoustic perturbations in non-uniform ducts with non-uniform mean flow using eigen analysis in general curvilinear coordinate systems," *Journal of Sound and Vibration*, vol. 443, pp. 605–636, March 2019.

[7] "ICAO's annual report of the council," *International Civil Aviation Organisation*, 2018.

[8] I. A. T. Association, "Press release: IATA forecast predicts 8.2 billion air travelers in 2037," *The IATA 20-year Passenger Forecast, developed by IATA and Tourism Economics*, 2018.

[9] ICAO, "Effects of novel coronavirus (COVID-19) on civil aviation: Economic impact analysis," *International Civil Aviation Organisation*, May 2020.

[10] P. Suau-Sanchez, A. Voltes-Dorta, and N. Cuguero-Escofet, "An early assessment of the impact of COVID-19 on air transport: Just another crisis or the end of aviation as we know it?," *Journal of Transport Geography*, vol. 86, June 2020.

[11] M. Basner, C. Clark, A. Hansell, J. Hileman, S. Janseen, K. Shepherd, and V. Sparrow, "Aviation noise impacts: State of the science," *Noise and Health*, vol. 19 (87), pp. 41–50, March-April 2017.

[12] S. Stansfeld, C. Clark, B. Berglund, I. Lopez-Barrio, P. Fischer, E. Öhström, M. Haines, J. Head, S. Hygge, I. van Kamp, and B. Berry, "Aircraft and road traffic noise and children's cognition and health: a cross-national study," *Lancet*, vol. 365 (9475), pp. 1942–1949, June 2005.

[13] S. Hygge, G. W. Evans, and M. Bullinger, "A prospective study of some effects of aircraft noise on cognitive performance in schoolchildren," *Psychological Science*, vol. 13 (5), pp. 469–474, September 2002.

[14] K. Jones, "Aircraft noise and sleep disturbance: A review," *Civil Aviation Authority*, April 2009.

[15] L. Anna, M. Blangiardo, L. Fortunato, S. Floud, K. De Hoogh, D. Fecht, R. E. Ghosh, H. E. Laszlo, C. Pearson, L. Beale, S. Beevers, J. Gulliver, N. Best, S. Richardson, and P. Elliot, "Aircraft noise and cardiovascular disease near Heathrow airport in London: Small area study," *BMJ (Online)*, vol. 347 (7928), pp. 1–10, October 2013.

[16] C. D. Zevitas, J. D. Spengler, B. Jones, E. McNeely, B. Coull, X. Cao, S. M. Loo, A. Hard, and J. G. Allen, "Assessment of noise in the aeroplane cabin environment," *Journal of Exposure Science and Environmental Epidemiology*, vol. 28, p. 568–578, 2018.

[17] S. Pennig, J. Quehl, and V. Rolny, "Effects of aircraft cabin noise on passenger comfort," *Ergonomics*, vol. 55, pp. 1252–1265, 2012.

[18] A. Rodríguez-Díaz, B. Adenso-Díaz, and P. L. González-Torre, "A review of the impact of noise restrictions at airports," *Transportation Research Part D: Transport and Environment*, vol. 50, pp. 144–153, January 2017.

[19] "Getting to grips with aircraft noise.," *Flight Operations Support and Line Assistance, Airbus Customer Services*, 2003.

[20] D. Casalino, F. Diozzi, R. Sannino, and A. Paonessa, "Aircraft noise reduction technologies: A bibliographic review," *Aerospace Science and Technology*, vol. 12 (1), pp. 1–17, January 2008.

[21] M. Smith, *Aircraft Noise*, ch. 3, pp. 41–119. Cambridge University Press, 1989.

[22] M. J. Lighthill, "On sound generated aerodynamically I. general theory," *Proceedings of The Royal Society London*, vol. 211, 1952.

[23] W. Eversman, "Theoretical models for duct acoustic propagation and radiation," in *NASA. Langley Research Center, Aeroacoustics of Flight Vehicles: Theory and Practice. Volume 2: Noise Control*, NASA, August 1991.

[24] S. Glegg and W. Devenport, *Aeroacoustics of Low Mach Number Flows: Fundamentals, Analysis, and Measurement*. Elsevier Science, 2017.

[25] G. F. Pickett and T. G. Sofrin, "Multiple pure tone noise generated by fans at supersonic tip speeds," *Pratt and Whitney Aircraft, NASA Technical Reports*, 1974.

[26] J. Tyler and T. Sofrin, "Axial flow compressor noise studies," *Transactions of the Society of Automotive Engineers*, vol. 70, pp. 309–332, 1962.

[27] S. W. Rienstra, *Fundamentals of Duct Acoustics*. Technische Universiteit Eindhoven, 2015.

[28] R. J. Astley, R. Sugimoto, I. M. Achunche, M. F. Kewin, P. Mustafi, and E. P. Deane, "A review of CAA for fan duct propagation and radiation, with application to liner optimisation," in *IUTAM Symposium on Computational Aero-Acoustics for Aircraft Noise Prediction*, pp. 143–152, Procedia Engineering, June 2010.

[29] C. K. W. Tam, "Computational aeroacoustics: Issues and methods," *American Institute of Aeronautics and Astronautics*, vol. 33, pp. 1788–1796, 1995.

[30] Z. Cheng, J. Fang, C. Shu, and M. Zhang, "Assessment of aeroacoustic resolution properties of DG schemes and comparison with DRP schemes," *Journal of Computational Physics*, vol. 399, 2019.

[31] S. K. Lele and J. W. Nichols, "A second golden age of aeroacoustics?," *Philosophical Transactions of the Royal Society*, vol. 372 (2022), 2014.

[32] M. Daroukh, S. Moreau, N. Gourdain, J. F. Boussuge, and C. Sensiau, "Effect of distortion on turbofan tonal noise at cutback with hybrid methods," *International Journal of Turbomachinery, Propulsion and Power*, vol. 2 (3), 2017.

[33] T. T. Akhtar, X. Li, and X. Tang, "Hybrid CFD-CAA numerical simulation of rotor stator interaction tonal noise," in *Proceedings of 16th International Bhurban Conference on Applied Sciences and Technology (IBCAST)*, pp. 697–702, January 2019.

[34] L. Xiong and R. Sugimoto, "Effects of turbofan engine intake droop and length on fan tone noise," in *25th AIAA/CAES Aeroacoustic Conference*, no. AIAA 2019-2581, (Delft, The Netherlands), American Institute of Aeronautics and Astronautics, May 2019.

[35] R. J. Astley, R. Sugimoto, G. Gabard, E. Norde, E. J. Grift, and M. Bocquier, "The effect of steady flow distortion on mode propagation in a turbofan intake," in *20th AIAA/CAES Aeroacoustic Conference*, no. AIAA 2014-3113, (Atlanta, Georgia), American Institute of Aeronautics and Astronautics, June 2014.

[36] P. Moin and K. Mahesh, "Direct numerical simulation: a tool in turbulence research," *Annual review of fluid mechanics*, vol. 30 (1), pp. 539–578, 1998.

[37] F. Hindenlang, G. J. Gassner, C. Altmann, A. Beck, M. Staudenmaier, and C. D. Munz, "Explicit discontinuous Galerkin methods for unsteady problems," *Computers and Fluids*, vol. 61, pp. 86–93, May 2012.

[38] C. Bogey, C. Bailly, and D. Juvé, "Noise investigation of a high subsonic, moderate reynolds number jet using a compressible large eddy simulation," *Theoretical and Computational Fluid Dynamics*, vol. 16 (4), pp. 273–297, March 2003.

[39] G. Brés, F. Pérot, and D. Freed, "A Ffowcs Williams - Hawkings solver for Lattice-Boltzmann based computational aeroacoustics," in *16th AIAA/CEAS Aeroacoustic Conference*, no. AIAA 2010-3711, (Stockholm, Sweden), American Institute of Aeronautics and Astronautics, June 2010.

[40] Z. Rarata, G. Gabard, R. Sugimoto, J. Coupland, R. J. Astley, H. Namgoong, and P. J. G. Schwaller, "Integrating CFD source predictions with time-domain CAA for intake fan noise prediction," in *20th AIAA/ CAES Aeroacoustics Conference*, no. AIAA 2014-2456, (Atlanta, Georgia), American Institute of Aeronautics and Astronautics, June 2014.

[41] R. Sugimoto, A. O. James, A. McAlpine, and R. J. Astley, "CFD/CAA coupling for the prediction of fan tone noise propagation and radiation through a drooped intake," in *28th AIAA/CAES Aeroacoustic Conference*, no. AIAA 2022-3100, (Delft, The Netherlands), American Institute of Aeronautics and Astronautics, June 2022.

[42] J. Coupland, A. G. Wilson, N. Pollard, S. Uellenberg, C. Breard, and J. Diamond, "Demonstration of a CFD-CAA methodology to predict buzz-saw noise propagation to the aircraft," in *13th AIAA/CAES Aeroacoustic Conference*, no. AIAA 2007-3517, (Rome, Italy), American Institute of Aeronautics and Astronautics, May 2007.

[43] S. W. Rienstra and A. Hirschberg, *An introduction to acoustics. Extended and Revised Edition of Report IWDE92-06*. Technische Universiteit Eindhoven, 2018.

[44] K. U. Ingard, "Influence of fluid motion past a plane boundary on sound reflection, absorption and transmission," *Journal of the American Chemical Society*, vol. 31(7), pp. 1035–1036, 1959.

[45] M. Myers, "On the acoustic boundary condition in the presence of flow," *The Journal of Sound and Vibration*, vol. 71 (3), pp. 429–434, August 1980.

[46] M. Van Dyke, "Slow variations in continuum mechanics," *Advances in Applied Mechanics*, vol. 25, pp. 1–45, 1987.

[47] A. H. Nayfeh and D. P. Telionis, "Acoustic propagation in ducts with varying cross sections," *The Journal of the Acoustical Society of America*, vol. 54, pp. 1654–1661, 1973.

[48] A. H. Nayfeh, D. P. Telionis, and S. G. Lekoudis, "Acoustic propagation in ducts with varying cross-sections and sheared mean flow," *Progress in Astronautics and Aeronautics: Aeroacoustics: Jet and Combustion Noise; Duct Acoustics*, vol. 37, pp. 333–351, 1975.

[49] S. W. Rienstra, "Contribution to the theory of sound propagation in ducts with bulk-reacting lining," *Journal of Acoustical Society of America*, vol. 77, pp. 1681–1685, 1985.

[50] S. W. Rienstra, "Sound transmission in a slowly varying lined flow duct," *Nieuw Archief voor Wiskunde*, vol. 4, part 6 no. 1-2, pp. 157–167, 1988.

[51] S. W. Rienstra, "Sound transmission in slowly varying circular and annular lined ducts with flow," *Journal of Fluid Mechanics*, vol. 380, pp. 279–296, February 1999.

[52] S. W. Rienstra and W. Eversman, "A numerical comparison between multiple-scales and FEM solution for sound propagation in lined flow ducts," *Journal of Fluid Mechanics*, vol. 437, pp. 367–384, June 2001.

[53] S. W. Rienstra, "Sound propagation in slowly varying lined flow ducts of arbitrary cross-section," *Journal of Fluid Mechanics*, vol. 495, pp. 157–173, November 2003.

[54] N. Peake and A. J. Cooper, "Acoustic propagation in ducts with slowly varying elliptic cross-section," *Journal of Sound and Vibration*, vol. 243 (3), pp. 381–401, June 2001.

[55] A. J. Cooper and N. Peake, "Propagation of unsteady disturbances in a slowly varying duct with mean swirling flow," *Journal of Fluid Mechanics*, vol. 445, pp. 207–234, October 2001.

[56] E. J. Brambley and N. Peake, "Sound transmission in strongly curved slowly varying cylindrical ducts with flow," *Journal of Fluid Mechanics*, vol. 596, pp. 387–412, January 2008.

[57] N. C. Ovenden, "A uniformly valid multiple scales solution for cut-on cut-off transition of sound in flow ducts," *Journal of Sound and Vibration*, vol. 286 (1-2), pp. 403–416, August 2005.

[58] N. C. Ovenden, W. Eversman, and S. Rienstra, "Cut-on cut-off transition in flow ducts: comparing multiple-scales and finite-element solutions," in *10th AIAA/CAES Aeroacoustic Conference*, no. AIAA 2004-2945, (Manchester, UK), American Institute of Aeronautics and Astronautics, May 2004.

[59] S. W. Rienstra, "A classification of duct modes based on surface waves," *Wave motion*, vol. 37, no. 2, pp. 119–135, 2003.

[60] A. F. Smith, N. C. Ovenden, and R. I. Bowles, "Flow and geometry induced scattering of high frequency acoustic duct modes," *Wave Motion*, vol. 49, pp. 109–124, 2012.

[61] A. F. Stevenson, "Exact and approximate equations for wave propagation in acoustic horns," *Journal of Applied Physics*, vol. 22 (12), pp. 1461–1463, December 1951.

[62] V. Pagneux, N. Amir, and J. Kergomard, "A study of wave propagation in varying cross-section waveguides by modal decomposition part one. theory and validation," *The Journal of the Acoustical Society of America*, vol. 100 (4), pp. 2034–2048, October 1996.

[63] V. Pagneux and S. Félix, "Sound propagation in rigid bends: A multimodal approach," *The Journal of the Acoustical Society of America*, vol. 110 (3), pp. 1329–1337, September 2001.

[64] S. Félix and V. Pagneux, "Multimodal analysis of acoustic propagation in three-dimensional bends," *Wave Motion*, vol. 36 (2), pp. 157–168, August 2002.

[65] A. G. Wilson, "Calculation of acoustic transfer functions for smooth ducts of varying cross section and non-uniform mean flow using eigen analysis in general curvilinear coordinates," in *24th AIAA/CAES Aeroacoustic Conference*, no. AIAA 2018-3776, (Atlanta, Georgia), American Institute of Aeronautics and Astronautics, June 2018.

[66] S. Félix and V. Pagneux, "Sound attenuation in lined bends," *The Journal of the Acoustical Society of America*, vol. 116 (4), pp. 1921–1931, October 2004.

[67] W. P. Bi, V. Pagneux, D. Lafarge, and Y. Aurégan, "Modelling of sound propagation in a non-uniform lined duct using a multi-modal propagation method," *Journal of Sound and Vibration*, vol. 289 (4-5), pp. 1091–1111, February 2006.

[68] A. Maurel, J. F. Mercier, and V. Pagneux, "Improved multimodal admittance method in varying cross-section waveguides," *Proceedings of the Royal Society A*, vol. 470 (2164), April 2014.

[69] A. Maurel, J. F. Mercier, and S. Félix, "Propagation in waveguides with varying cross-section and curvature: a new light on the role of supplementary modes in multi-modal methods," *Proceedings of the Royal Society A*, vol. 470 (2166), June 2014.

[70] S. Félix, A. Maurel, and J. F. Mercier, "Improved multimodal methods for the acoustic propagation in waveguides with finite wall impedance," *Wave Motion*, vol. 54, pp. 1–10, April 2015.

[71] J. F. Mercier and A. Maurel, "Improved multimodal method for the acoustic propagation in waveguides with a wall impedance and a uniform flow," *Proceedings of the Royal Society*, vol. 472 (2190), June 2016.

[72] P. Moinier and M. Giles, "Eigenmode analysis for turbomachinery applications," *Journal of Propulsion and Power*, vol. 21, pp. 973–978, 2005.

[73] K. Kousen, "Eigenmode analysis of ducted flows with radially dependent axial and swirl components," in *1st AIAA/CEAS Joint Aeroacoustics Conference*, no. AIAA 1995-160, (Munich, Germany), pp. 1085–1094, 1995.

[74] A. L. P. Maldonado, R. J. Astley, J. Coupland, G. Gabard, and D. Sutliff, "Sound propagation in lined annular ducts with mean swirling flow," in *21st AIAA/CEAS conference*, no. AIAA 2015-2522, American Institute of Aeronautics and Astronautics, June 2015.

[75] R. J. Astley, G. Gabard, X. Zhang, and X. Chen, "IUTAM symposium on computational aero-acoustics for aircraft noise prediction time-domain computation of multimode propagation in an aeroengine duct," *Procedia Engineering*, vol. 6, pp. 173–182, 2010.

[76] X. Chen, X. Huang, and X. Zhang, "Sound radiation from a bypass duct with bifurcations," *AIAA Journal*, vol. 47 (2), pp. 429–436, February 2009.

[77] S. K. Richards, X. Chen, X. Huang, and X. Zhang, "Computation of fan noise through an engine exhaust geometry with flow," *International Journal of Aeroacoustics*, vol. 6 (3), p. 223–241, September 2007.

[78] C. Tam and J. Webb, "Dispersion-relation-preserving finite difference schemes for computational acoustics," *Journal of Computational Physics*, vol. 107, pp. 262–281, 1993.

[79] C. K. W. Tam, J. C. Webb, and Z. Dong, "A study of the short wave components in computational acoustics," *Journal of Computational Acoustics*, vol. 1, pp. 1–30, 1993.

[80] A. Jameson, W. Schmidt, and E. Turkey, "Numerical solutions of the Euler equations by finite volume methods using Runge-Kutta time stepping schemes," in *AIAA*, American Institute of Aeronautics and Astronautics, June 1981.

[81] J. Von Neumann and R. D. Richtmyer, "A method for the numerical calculation of hydrodynamic shocks," *Journal of Applied Physics*, vol. 21, pp. 232–237, 1950.

[82] C. K. W. Tam, J. C. Webb, and Z. Dong, "Wall boundary conditions for high order finite difference schemes in computational aeroacoustics," *Theoretical and computational fluid dynamics*, vol. 8, pp. 303–322, 1994.

[83] K. A. Kurbatskii and C. K. W. Tam, "Curved wall boundary conditions for high-order finite difference schemes on acoustic wave scattering problems," *Bulletin of the American Physical Society*, vol. 39, 1993.

[84] C. K. W. Tam and K. A. Kurbatskii, "A wavenumber based extrapolation and interpolation method for use in conjunction with high-order finite difference schemes," *Journal of Computational Physics*, vol. 157, pp. 588–617, 2000a.

[85] C. K. W. Tam and K. A. Kurbatskii, "Multi-size-mesh multi-time-step dispersion-relation-preserving scheme for aeroacoustics problems," *Journal of Computational Physics*, vol. 17 (2), pp. 119–132, 2003.

[86] N. Schoenwald, L. Panek, C. Richter, and F. Thiele, "Simulation of the rearward propagation of fan noise through a long cowl aero-engine," in *14th AIAA/CAES Aeroacoustic Conference*, no. AIAA 2008-2820, (Vancouver, Canada), American Institute of Aeronautics and Astronautics, May 2008.

[87] N. Schoenwald, L. Panek, C. Richter, and F. Thiele, "Investigation of sound radiation from a scarfed intake by CAA-FWH simulations using overset grids," in *13th AIAA/CAES Aeroacoustic Conference*, no. AIAA 2007-3524, (Rome, Italy), American Institute of Aeronautics and Astronautics, May 2007.

[88] S. K. Lele, "Compact finite difference schemes with spectral-like resolution," *Journal of Computational Physics*, vol. 103, pp. 16–42, 1992.

[89] J. W. Kim and D. J. Lee, "Optimized compact finite difference schemes with maximum resolution," *AIAA Journal*, vol. 34 (5), pp. 887–893, 1996.

[90] R. Hixon, "A new class of compact schemes," in *36th AIAA Aerospace Sciences Meeting and Exhibit*, no. AIAA 1998–0367, (Reno, Nevada), American Institute of Aeronautics and Astronautics, Janauary 1998.

[91] G. Ashcroft and X. Zhang, "Optimised prefactored compact schemes," *Journal of Computational Physics*, vol. 190 (2), pp. 459–477, September 2003.

[92] X. Zhang, X. Chen, C. L. Morfey, and P. A. Nelson, "Computation of spinning modal radiation from an unflanged duct," *AIAA Journal*, vol. 42 (9), pp. 1795–1801, September 2004.

[93] S. Richards, X. Zhang, and X. Chen, "Acoustic radiation computation from an engine inlet with aerodynamic flow field," in *10th CEAS/AIAA Aeroacoustics Conference*, no. AIAA 2004-0848, (Manchester, UK), American Institute of Aeronautics and Astronautics, May 2004.

[94] S. K. Richards, X. Chen, and X. Zhang, "Parallel computation of 3D acoustic radiation from an engine intake," in *11th AIAA/CEAS Aeroacoustics Conference*, no. AIAA 2005-2947, (Monterey, California), American Institute of Aeronautics and Astronautics, May 2005.

[95] P. C. M. Lau, "Curvilinear finite difference method of potential problems," *Civil Engineering Department, University of Western Australia*, 1977.

[96] P. C. M. Lau, "Curvilinear finite difference method for 3D potential problems," *Journal of Computational Physics*, vol. 32, pp. 325–344, 1979.

[97] H. Daiguji and B. R. Shin, "Some numerical schemes using curvilinear coordinate grids for incompressible and compressible Navier-Stokes equations," *Sādhanā*, vol. 18, pp. 431–476, 1993.

[98] M. R. Visbal and D. V. Gaitonde, "On the use of higher-order finite-difference schemes on curvilinear and deforming meshes," *Journal of Computational Physics*, vol. 181, pp. 155–185, 2002.

[99] M. R. Visbal and D. V. Gaitonde, "Very high order spatially implicit schemes for computational acoustics on curvilinear meshes," *Journal of Computational Acoustics*, vol. 9(4), pp. 1259–1286, 2001.

[100] M. R. Visbal and D. P. Rizzetta, "Large eddy simulations on curvilinear grids using compact differencing and filtering schemes," *Journal of Fluids Engineering*, vol. 124(4), pp. 836–847, December 2002.

[101] O. C. Zienkiewicz, "The birth of the finite element method and of computational mechanics," *International Journal for Numerical Methods in Engineering*, vol. 60, pp. 3–10, 2004.

[102] O. C. Zienkiewicz, R. L. Taylor, and J. Z. Zhu, *The Finite Element Method: Its Basis and Fundamentals*. Butterworth-Heinemann, 7 ed., 2013.

[103] P. P. Rao and P. J. Morris, "Use of finite element methods in frequency domain aeroacoustics," *AIAA Journal*, vol. 44, pp. 1643–1652, 2018.

[104] R. J. Astley and W. Eversman, "Finite element formulations for acoustical radiation," *Journal of Sound and Vibration*, vol. 88 (1), pp. 47–64, May 1983.

[105] R. J. Astley, "A finite element wave envelope formulation for acoustical radiation in moving flows," *Journal of Sound and Vibration*, vol. 103 (1), pp. 471–485, May 1985.

[106] A. V. Parrett and W. Eversman, "Wave envelope and finite element approximations for turbofan noise radiation in flight," *AIAA Journal*, vol. 24 (5), May 1986.

[107] W. Eversman, "Mapped infinite wave envelope elements for acoustic radiation in a uniformly moving medium," *Journal of Sound and Vibration*, vol. 224 (4), pp. 665–687, July 1999.

[108] R. J. Astley, G. J. Macaulay, J. P. Coyette, and L. Cremers, "Three-dimensional wave-envelope elements of variable order for acoustic radiation and scattering. part I. formulation in the frequency domain," *Journal of the Acoustical Society of America*, vol. 103, pp. 49–63, January 1998.

[109] R. J. Astley and J. A. Hamilton, "Modelling tone propagation from turbofan inlets - the effect of extended lip liners," in *8th AIAA/CAES Aeroacoustic Conference*, no. AIAA 2002-2449, (Breckenridge, Colorado), American Institute of Aeronautics and Astronautics, June 2002.

[110] G. Gabard, R. J. Astley, and M. B. Tahar, "Stability and accuracy of finite element methods for flow acoustics. I: general theory and application to one-dimensional propagation," *International Journal for Numerical Methods in Engineering*, vol. 63 (7), pp. 947–973, March 2005.

[111] *Actran 19.1 User's Guide - Volumes 1 and 2*. Belgium: Free Field Technologies, www.fft.be, May 2019.

[112] W. Möhring, "A well-posed acoustic analogy based on a moving acoustic medium," in *Proceedings 1st Aeroacoustic Workshop (in connection with the German research project SWING*, (Dresden, Germany), 1999.

[113] R. Sugimoto and R. J. Astley, "Modelling of flow effects on propagation and radiation from bypass ducts," in *11th AIAA/CAES Aeroacoustic Conference*, no. AIAA 2005-3011, (Monterey, California), American Institute of Aeronautics and Astronautics, May 2005.

[114] R. Sugimoto, R. J. Astley, L. De Mercato, K. R. Holland, and V. Jurdic, "Prediction methods for propagation in bypass ducts and comparison with measured data," in *11th AIAA/CAES Aeroacoustic Conference*, no. AIAA 2005-3059, (Monterey, California), American Institute of Aeronautics and Astronautics, May 2005.

[115] R. Sugimoto, R. J. Astley, G. Gabard, and N. Tsuchiya, "Three-dimensional effects of geometries and acoustic treatments on bypass-duct noise," in *13th AIAA/CAES Aeroacoustic Conference*, no. AIAA 2007-3549, (Rome, Italy), American Institute of Aeronautics and Astronautics, May 2007.

[116] C. McAleer, R. J. Astley, K. Holland, R. Sugimoto, and A. Kempton, "Fan noise propagation within curved bypass ducts with 3D features," in *14th AIAA/CAES Aeroacoustic Conference*, no. AIAA 2008-2878, (Vancouver, Canada), American Institute of Aeronautics and Astronautics, May 2008.

[117] I. Achunche, R. J. Astley, R. Sugimoto, and A. Kempton, "Prediction of forward fan noise propagation and radiation from intakes," in *15th AIAA/CAES Aeroacoustic Conference*, no. AIAA 2009-3239, (Miami, Florida), American Institute of Aeronautics and Astronautics, May 2009.

[118] A. Mosson, "New advances in the use of ACTRAN/TM for nacelle simulations and optimisation of IBM clusters for ACTRAN parallel computations," in *12th AIAA/CEAS Aeroacoustics Conference*, no. AIAA 2006-2588, (Cambridge, Massachusetts), American Institute of Aeronautics and Astronautics, May 2006.

[119] B. V. Antwerpen, R. Leneveu, S. Caro, and P. Ferrante, "New advances in the use of ACTRAN/TM for nacelle simulations," in *14th AIAA/CEAS Aeroacoustics Conference*, no. AIAA 2008-2827, (Vancouver, Canada), American Institute of Aeronautics and Astronautics, May 2008.

[120] R. Astley, I. Achunche, and R. Sugimoto, "Validation of CAA prediction of noise radiated from turbofan intakes," vol. 4, (Krakow, Poland), pp. 2072–2079, July 2009.

[121] R. Sugimoto, P. Murray, A. McAlpine, and R. Astley, "Prediction of in-duct and near-field noise for a fan rig intake," No. 2013-2022, (Berlin, Germany), May 2013.

[122] A. Prinn, R. Astley, and R. Sugimoto, "Predicting the effect of flow distortion on in-duct acoustic propagation," 22nd International Congress on Sound and Vibration, July 2015.

[123] A. G. Prinn, R. Sugimoto, and R. J. Astley, "The effect of steady flow distortion on noise propagation in turbofan intakes," in *22th AIAA/CAES Aeroacoustic Conference*, no. AIAA 2016-3028, (Lyon, France), American Institute of Aeronautics and Astronautics, June 2016.

[124] J. Winkler, C. A. Reimann, R. A. Reba, and J. Gilson, "Turbofan inlet distortion noise prediction with a hybrid CFD-CAA approach," in *20th AIAA/CAES Aeroacoustic Conference*, no. AIAA 2014-3102, (Atlanta, Georgia), American Institute of Aeronautics and Astronautics, June 2014.

[125] W. H. Reed and T. R. Hill, "Triangular mesh methods for the neutron transport equation," *Los Alamos Scientific Laboratory, N. Mex. (USA)*, October 1973.

[126] H. L. Atkins and C. W. Shu, "Quadrature-free implementation of the discontinuous galerkin method for hyperbolic equations," *AIAA Journal*, vol. 36 (5), pp. 775–782, 1998.

[127] H. Atkins and D. P. Lockard, "A high-order method using unstructured grids for the aeroacoustic analysis of realistic aircraft configurations," in *5th AIAA/CEAS Aeroacoustic Conference and Exhibit*, no. AIAA 99-1945, (Bellevue, WA), American Institute of Aeronautics and Astronautics, May 1999.

[128] D. Stanescu, H. M. Y., and F. F., "Aircraft engine noise scattering by fuselage and wings: a computational approach," *Journal of Sound and Vibration*, vol. 263 (2), pp. 319–333, February 2003.

[129] L. Liu, X. Li, and F. Q. Hu, "Nonuniform time-step Runge–Kutta discontinuous Galerkin method for computational aeroacoustics," *Journal of Computational Physics*, vol. 229 (19), pp. 6874–6897, September 2010.

[130] B. Seny, J. Lambrechts, T. Toulorge, V. Legat, and J. F. Remacle, "An efficient parallel implementation of explicit multirate Runge–Kutta schemes for discontinuous Galerkin computations," *Journal of Computational Physics*, vol. 256 (1), pp. 135–160, January 2014.

[131] L. Wang and D. J. Mavriplis, "Implicit solution of the unsteady Euler equations for high-order accurate discontinuous Galerkin discretizations," *Journal of Computational Physics*, vol. 225 (2), pp. 1994–2015, August 2007.

[132] A. Kanevsky, M. H. Carpenter, D. Gottlieb, and J. S. Hesthaven, "Application of implicit–explicit high order Runge–Kutta methods to discontinuous Galerkin schemes," *Journal of Computational Physics*, vol. 225 (2), pp. 1753–1781, August 2007.

[133] P. Houston and E. Süli, "hp -adaptive discontinuous Galerkin finite element methods for first-order hyperbolic problems," *SIAM Journal on Scientific Computing*, vol. 23, pp. 1226–1252, 2001.

[134] M. Alhawwary and Z. J. Wang, "Fourier analysis and evaluation of DG, FD and compact difference methods for conservation laws," *Journal of Computational Physics*, vol. 373, p. 835–862, 2018.

[135] R. Leneveu, B. Schiltz, S. Laldjee, and S. Caro, "Performance of a DGM scheme for LEE and applications to aircraft engine exhaust noise," in *14th AIAA/CEAS Aeroacoustics Conference*, no. AIAA 2008-2884, (Vancouver, Canada), American Institute of Aeronautics and Astronautics, May 2008.

[136] K. Y. Fung and H. Ju, "Time-domain impedance boundary conditions for computational acoustics and aeroacoustics," *International Journal of Computational Fluid Dynamics*, vol. 18 (6), pp. 503–511, 2004.

[137] N. Chevaugeon, J. F. Remacle, X. Gallez, P. Ploumhans, and S. Caro, "Efficient discontinuous galerkin methods for solving acoustic problems," in *11th AIAA/CEAS Aeroacoustics Conference*, no. AIAA 2005-2823, (Monterey, California), American Institute of Aeronautics and Astronautics, May 2005.

[138] J. Manera, R. Leneveu, S. Caro, and J. Mardjono, "Broadband turbomachinery noise: exhaust noise computations with ACTRAN/TM and ACTRAN/DGM," in *15th AIAA/CAES Aeroacoustic Conference*, no. AIAA-2009-3292, (Miami, Florida), American Institute of Aeronautics and Astronautics, May 2009.

[139] B. Schiltz, R. Leneveu, S. Caro, Y. Druon, and A. Mosson, "Exhaust noise prediction of realistic 3d lined turbofans submitted to strong shear layers," in *15th AIAA/CAES Aeroacoustic Conference*, no. AIAA-2009-3416, (Miami, Florida), American Institute of Aeronautics and Astronautics, May 2009.

[140] R. Leneveu, B. Schiltz, S. Laldjee, and S. Caro, "Performance of a DGM scheme for LEE and applications to aircraft engine exhaust noise," in *14th AIAA/CAES Aeroacoustic Conference*, no. AIAA-2008-2884, (Vancouver, Canada), American Institute of Aeronautics and Astronautics, May 2008.

[141] A. G. Wilson, "Eigen analysis in general curvilinear coordinates for prediction of noise propagation in aeroengine inlets," in *23rd AIAA/CEAS Aeroacoustics Conference*, no. AIAA 2017-3704, (Denver, Colorado), June 2017.

[142] A. G. Wilson, "Non-linear acoustic propagation in circumferentially non-uniform mean flow," in *25th AIAA/CAES Aeroacoustic Conference*, no. AIAA 2019-2448, (Delft, The Netherlands), American Institute of Aeronautics and Astronautics, May 2019.

[143] D. C. Kay, *Schaum's Outline of Tensor Calculus*. Schaum's, 2011.

[144] B. Spain, *Tensor Calculus, third edition*. Oliver and Boyd Ltd, 1960.

[145] The MathWorks, Inc. eig (matlab function) R2021b. Accessed: February 07, 2022 [Online]. Available: https://uk.mathworks.com/help/matlab/ref/eig.html.

[146] The MathWorks, Inc. Linear Algebra (matlab documentation) R2021b. Accessed: February 07, 2022 [Online]. Available: https://uk.mathworks.com/help/matlab/linear-algebra.html.

[147] A. Najafi-Yazdi, G. A. Brés, and L. Mongeau, "An acoustic analogy formulation for moving sources in uniformly moving media," *Proceedings of The Royal Society A*, vol. 467 (2125), pp. 144–165, June 2011.

[148] P. Schwaller, N. Baker, D. Tomlinson, P. Sijtsma, and R. Hemmings, "Noise validation of model fan rig with engine," in *12th AIAA/CAES Aeroacoustic*

Conference, no. AIAA 2006-2479, (Cambridge, Massachusetts), American Institute of Aeronautics and Astronautics, May 2006.

[149] The MathWorks, Inc. scatteredInterpolant (matlab function) R2021b. Accessed: February 07, 2022 [Online]. Available: https://uk.mathworks.com/help/matlab/ref/scatteredinterpolant.html.

[150] "The IRIDIS computer cluster."

[151] L. Wu, A. G. Wilson, and J. W. Kim, "Low-noise blade design optimisation for a transonic fan using adjoint-based approach," *AIAA Journal*, vol. 60 94), April 2022.

[152] E. Brambley, "A well-posed modified myers boundary condition," in *16th AIAA/CEAS Aeroacoustic Conference*, no. AIAA 2010-3942, (Stockholm, Sweden), American Institute of Aeronautics and Astronautics, June 2010.